January 2022

Atomic Layer Deposition (ald) Of Lanthanide Oxide Films: Synthesis, Characterization, And Precursor Property Evaluation Of New Classes Of Lanthanide Complexes And Thermal Ald Of Erbium Oxide Thin Films

Navoda Amali Jayakodiarachchi
Wayne State University

ATOMIC LAYER DEPOSITION (ALD) OF LANTHANIDE OXIDE FILMS: SYNTHESIS, CHARACTERIZATION, AND PRECURSOR PROPERTY EVALUATION OF NEW CLASSES OF LANTHANIDE COMPLEXES AND THERMAL ALD OF ERBIUM OXIDE THIN FILMS

by

NAVODA AMALI JAYAKODIARACHCHI

DISSERTATION

Submitted to the Graduate School

of Wayne State University,

Detroit, Michigan

in partial fulfillment of the requirements

for the degree of

DOCTOR OF PHILOSOPHY

2022

MAJOR: CHEMISTRY (Inorganic)

Approved By:

_____

Advisor Date

_____

_____

_____

_____

DEDICATION

I dedicate this dissertation to my beloved parents, Indrani Abeygunasekara and Nihal Jayakodiarachchi, my loving husband, Dr. Upendra Amal Rathnayake, and my siblings Charith Nilanka, Dakshitha Udari, and Shashi Hemal.

"The one who falls and gets up is stronger than the one who never tried. Do not fear failure but rather fear not trying."

-Roy T. Bennett

"Follow your bliss and the universe will open doors where there were only walls."

-Joseph Campbell

ACKNOWLEDGEMENTS

The pursuit of my doctorate has been an experience like none other; the tedium of failed experiments and long days in the lab punctuated by the occasional small step forward. In short, it has been a difficult, yet rewarding journey filled with excitement. As I reflect upon the fond memories of the past several years, I acknowledge all those who were a part of my journey so far.

First and foremost, I would like to thank my advisor, Professor Charles H. Winter, for introducing me to the fascinating field of atomic layer deposition (ALD) and for guiding me to be an independent scientist. Professor Winter has been an outstanding mentor, and it has been a privilege to learn from someone of his talent and character. His patience, understanding, and feedback encouraged my creativity and increased my faith in my potential. Every challenge I have faced turned into a beginning of something new and interesting because of your instincts and directions. I am so proud of what I have accomplished under your guidance.

Next, I want to thank Professor Stanislav Groysman, Professor Sarah Trimpin, and Dr. Thomas Knisley for serving as my dissertation committee members from the beginning of my Ph.D. and for their kind comments, guidance, and helpful suggestions throughout this journey. I want to express my sincere gratitude to Dr. Thomas Knisley from Applied Materials for his kind approval to access multiple instruments in his lab throughout my Ph.D. career.

Five or six years in our life is a long period. I want to thank all of the past and current Winter group members for making these years a wonderful set of years filled with joy. All of you have helped me come this far and achieve my goals by making a very pleasant lab environment. Even how stressful some days were, it felt really exciting to come early morning to the lab and spend the time with you all and I am going to miss you all very much. Without any doubt, I could say these six years are the best years spent in my academic life so far.

There are no words for me to thank all the personnel in the Department of Chemistry at Wayne State University for giving me this remarkable opportunity to pursue a Ph.D. in the USA and supporting me during each step on the way to completion of my Ph.D. Especially, I want to thank our department chair Professor Matthew Allen, graduate academic service officer Melissa Rochon, administrative assistants Jackie Kennedy and Kim Miller, and accounting assistant Mishad Ahmed for making this journey a smooth one. Further, I want to convey my heartful gratitude to all of the staff in the Lumigen Instrument Center, Science Stores, Chemistry Main Office, and Office of International Students and Scholars for their technical assistance. Special thanks should go to Dr. Cassie Ward for working so enthusiastically on solving the crystal structures of my complexes and Dr. Zhi Mei (Mike), Dr. Sameera Perera, Mr. Dennis Anderson, Dr. Philip Martin, Nestor Ocampo, Jason Parizon, and Elizabeth Ries (Liz) for all their support.

My sincere thank goes to all of the collaborators in the MRSEC (Materials Research Science and Engineering Centers) IRG-2 group in the University of Wisconsin-Madison for the great time and valuable discussions we had and for providing funding all these years. Especially, I should thank Professor Paul G. Evans, Prof. Donald Savage, and Dr. Rui Liu for their time and efforts in conducting XRR and AFM experiments and providing useful suggestions, and making an excellent environment to bring our collaboration work to success.

Last but not least I want to thank all my family members for all of their love and support to come this far. Especially, I am grateful to my husband, for his moral support, trust, and guidance throughout these years, without whom this journey would not be as beautiful and relaxing as it is.

TABLE OF CONTENTS

LIST OF TABLES

LIST OF FIGURES

LIST OF ABBREVIATIONS

ABBREVIATION	LONG FORM
ALD	Atomic Layer Deposition
AFM	Atomic Force Microscopy
CVD	Chemical Vapor Deposition
Cp	Cyclopentadienyl
CBO	Conduction Band Offset
2 DEG	2 Dimensional Electron Gas
IC	Integrated Circuit
IR	Infrared Spectroscopy
MOSFET	Metal-Organic Semiconducting Field Effect Transistor
NMR	Nuclear Magnetic Resonance
PV	Photovoltaic
PVD	Physical Vapor Deposition
RMS	Root Mean Square
SEM	Scanning Electron Microscopy
SOFC	Solid Oxide Fuel Cell
TGA	Thermogravimetric Analysis
thd	2,2,6,6-tetramethyl-3,5-heptanedionato
XPS	X-Ray Photoelectron Spectroscopy
XRD	X-Ray Diffractometry
XRF	X-Ray Fluorescence Spectroscopy
XRR	X-Ray Reflectivity

LIST OF SCHEMES

CHAPTER 1

Introduction

1.1 Lanthanides

Lanthanides (Ln) are the fifteen elements in the periodic table from lanthanum through lutetium (La, Ce, Pr, Nd, Pm, Sm, Eu, Gd, Tb, Dy, Ho, Er, Tm, Yb, and Lu), with atomic numbers from 57 to 71. These lanthanides, along with the group IIIB elements yttrium (Y) and scandium (Sc), are collectively known as the rare earth elements.[1, 2] Due to the gradual filling of valence electrons into the 4*f* orbitals across the series with the increase of the atomic number, lanthanides are also recognized as 4*f* elements.[2, 3] In general, all of the lanthanides exhibit +3 as the most common oxidation state, along with a few elements also having +2 and +4 valence states. As presented in Table 1, the adoption of +2 and +4 stable oxidation states is believed to be governed by the stability of the final electron configuration of the corresponding lanthanide ion (Ln^{n+}).[2, 4] Accordingly, Ln^{n+} with empty ($4f^{0}$), half-filled ($4f^{7}$), or completely filled ($4f^{14}$) 4*f* levels show stable +4 and +2 oxidation states with the exception of Pr^{4+} and Sm^{2+}.[2, 3]

Another important behavior of lanthanides is the steady decrease of the Ln^{3+} ionic radii across the series from La through Lu. This is known as lanthanide contraction. Owing to the shapes of the f orbitals, 4f electrons themselves and outer 5s and 5p electrons are less shielded from the increased nuclear charge, and hence are attracted more towards the nucleus, decreasing the radii as the nuclear charge increases.[1, 3, 4] As a consequence, the ionic radius of Y^{3+} has a resemblance to those of Ho^{3+} and Er^{3+}, leading to similar chemistries.[3] The 4f valence electrons of Ln^{3+} are located inside the $5s^2$ and $5p^6$ electrons. Therefore, the involvement of 4f orbitals in covalent bonding with ligand orbitals is minimal and the bonding in lanthanide complexes is largely ionic.[2, 4] Accordingly, lanthanide ions (most commonly +3) and ligands can be considered as oppositely

charged particles where electrostatic interactions take place to make ionic bonds.[2, 4] As a result of these electrostatic interactions, coordination numbers and the geometry of the lanthanide complexes are mainly determined by the steric factors of the ligands and the resulting complexes usually possess a wide range of coordination numbers (generally ~3-12) and irregular coordination geometries.[5, 6] Further, ionic bond strengths of Ln^{3+} complexes increase moving from La^{3+} to Lu^{3+} as a result of the increased charge density caused by the decrease in ionic radii. Additionally, lanthanide ions are strongly Lewis acidic and have a strong affinity towards ligands containing highly electronegative donor atoms such as O and F.[2, 5, 7, 8] Further, Ln^{3+} ions are oxophilic. Hence, lanthanide complexes with Ln-X bonds where X is a non-oxygen atom tend to react rapidly to make Ln-O bonds.[9]

Table 1. Electronic configurations of lanthanide ions.

Lanthanide	Electron configuration			
	Ln	Ln^{3+}	Ln^{4+}	Ln^{2+}
La	[Xe] $5d^1\ 6s^2$	[Xe] $5d^0\ 6s^0$		
Ce	[Xe] $4f^2\ 6s^2$	[Xe] $4f^1\ 6s^0$	[Xe] $4f^0\ 6s^0$	
Pr	[Xe] $4f^3\ 6s^2$	[Xe] $4f^2\ 6s^0$	[Xe] $4f^1\ 6s^0$	
Nd	[Xe] $4f^4\ 6s^2$	[Xe] $4f^3\ 6s^0$		
Pm	[Xe] $4f^5\ 6s^2$	[Xe] $4f^4\ 6s^0$		
Sm	[Xe] $4f^6\ 6s^2$	[Xe] $4f^5\ 6s^0$		[Xe] $4f^6\ 6s^0$
Eu	[Xe] $4f^7\ 6s^2$	[Xe] $4f^6\ 6s^0$		[Xe] $4f^7\ 6s^0$
Gd	[Xe] $4f^7\ 5d^1\ 6s^2$	[Xe] $4f^7\ 6s^0$		
Tb	[Xe] $4f^9\ 6s^2$	[Xe] $4f^8\ 6s^0$	[Xe] $4f^7\ 6s^0$	
Dy	[Xe] $4f^{10}\ 6s^2$	[Xe] $4f^9\ 6s^0$		
Ho	[Xe] $4f^{11}\ 6s^2$	[Xe] $4f^{10}\ 6s^0$		
Er	[Xe] $4f^{12}\ 6s^2$	[Xe] $4f^{11}\ 6s^0$		
Tm	[Xe] $4f^{13}\ 6s^2$	[Xe] $4f^{12}\ 6s^0$		
Yb	[Xe] $4f^{14}\ 6s^2$	[Xe] $4f^{13}\ 6s^0$		[Xe] $4f^{14}\ 6s^0$
Lu	[Xe] $4f^{14}\ 5d^1\ 6s^2$	[Xe] $4f^{14}\ 6s^0$		

1.2 Properties of Lanthanide Oxides

The characteristic valence state of all the lanthanides in the series is +3. These trivalent lanthanides make lanthanide sesquioxides (Ln_2O_3) with a 1:1.5 lanthanide to oxygen ratio. Lanthanides oxides with 1:1 (LnO) and 1:2 (LnO_2) Ln:O ratios are also known with +2 and +4

oxidation states, respectively.[10] Lanthanide oxides are hygroscopic in nature, and readily react with ambient moisture (equation 1).[11-14] This reactivity of lanthanide oxides with water decreases across the series, where La_2O_3 has the highest reactivity and Lu_2O_3 has the lowest reactivity. This behavior is attributed to the increase in electronegativity when moving from left to right.[15] Furthermore, Ln_2O_3 are strongly basic and tend to react with atmospheric CO_2 forming the corresponding carbonates (equation 2).[2, 11-13] Similar to the hygroscopicity, basicity also decreases when moving from La_2O_3 to Lu_2O_3.[3]

$$Ln_2O_3 + 2\ H_2O \longrightarrow Ln(OH)_3 + LnO(OH) \qquad (1)$$

$$Ln_2O_3 + 3\ CO_2 \longrightarrow Ln_2(CO_3)_3 \qquad (2)$$

Lanthanide sesquioxides (Ln_2O_3) are found in three distinct polymorphic forms denoted as (1) A-type Ln_2O_3 with a hexagonal crystal structure, (2) B-type with a monoclinic structure, and (3) C-type with a cubic crystal structure.[16, 17] Among the three polymorphs, A (hexagonal) and C (cubic) type are most commonly observed at low to medium temperatures. Moreover, hexagonal type structures are favored by early Ln_2O_3, whereas later Ln_2O_3 favors cubic crystal structures. [16, 17]

1.3 Potential Applications of Lanthanide Oxide Films

Ln_2O_3 possess some important properties which make them materials with wide application potential. Ln_2O_3 have high melting points in the range of 2230-2490 °C and are considered refractory materials.[18-20] Further, these oxides possess high dielectric constants (κ between 10 and 30),[21] large band gaps (between 2-6 eV),[22] large conduction band offset (CBO) values on Si (CBO of around 1.5-3.5 eV),[23] good thermal stability on Si up to about 1000 °C,[24] and high refractive indices (~1.9-2.0).[25, 26] Due to the aforementioned interesting properties of Ln_2O_3, they have gained

wide attention in a variety of fields such as optics, microelectronics, catalysis, and others. Herein, the major areas of potential application for lanthanide oxides are discussed briefly.

1.3.1 Photovoltaic Cells

Photovoltaic (PV) cells, commonly known as solar cells, are devices that directly convert sunlight into electricity. These devices are made of semiconductor materials such as silicon (Si) that absorb the energy photons from sunlight. The performance of PV cells depends on the number of photons absorbed by the semiconducting material. However, the efficiency of Si-based solar cells is low due to the reflection of the light that strikes the PV cell (Figure 1).[27] Hence, applying antireflection coatings on the working surface of PV cells is necessary.[28] Lanthanide oxides are promising candidates for this purpose owing to their high refractive index values and good thermal stability on Si.[25, 26] Several studies have proven the increased efficiency of Si-based PV cells with the use of Ln_2O_3 coatings (Ln = La, Ce, Er, Yb). [29-32]

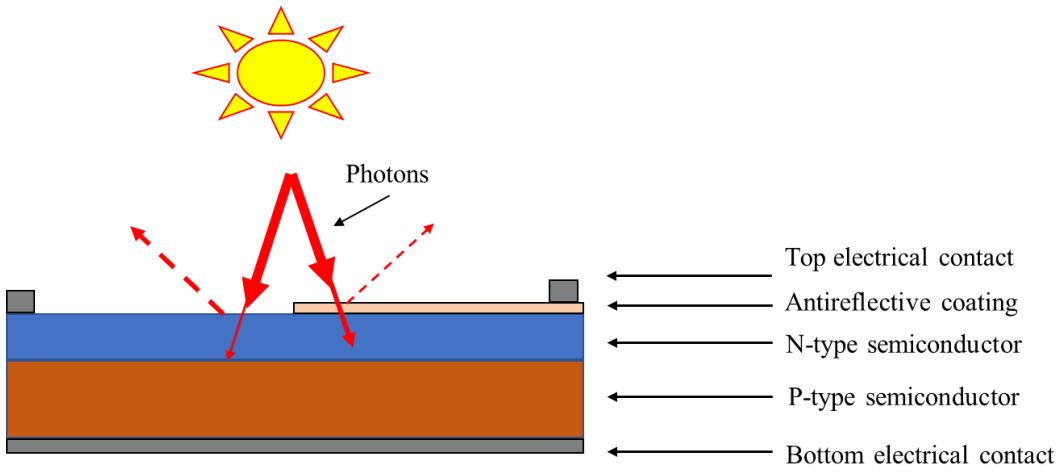

Figure 1. Basic view of a PV cell indicating the difference in photon absorption with and without an antireflection coating.

1.3.2 Metal-Oxide-Semiconductor Field Effect Transistors (MOSFETs)

Transistors are the building blocks of modern-day electronics. They act as small electrical switches that turn on and off the current and control the current flow and voltage in circuits. Hence, transistors are the most important components of electronic devices. MOSFET transistors consist of a gate which is a metal, a semiconductor channel that connects the source and the drain that allows passage of current, and a gate dielectric which is an insulator that covers the gate. SiO_2 is the gate dielectric that has been used since the invention of the MOSFET type transistors (Figure 2) due to its excellent electrical and thermal stability on Si. However, following Moore's prediction in 1965 (the number of transistors in a dense integrated circuit would double every two years), miniaturization of the transistors has occurred to build smaller, faster, cheaper, and less power consuming microelectronic devices.[33] To continue this shrinkage of devices, the physical thickness of the SiO_2 gate dielectric and the gate length in the transistors had to be decreased. However, in transistors below 100 nm, the thickness of the SiO_2 dielectric should reduce below 1.5 nm to achieve an effective dielectric constant (κ) value. Instead, the very thin SiO_2 gate dielectric resulted in leakage of current by direct tunneling of electrons through the gate dielectric.[34-37] This problem led to the investigation of new candidates as alternatives to replace SiO_2. Among other limited alternative oxide candidates such as HfO_2 and ZrO_2, lanthanide oxides are also under consideration due to their superior properties such as the high dielectric constant (κ between 10 and 30), large bandgap, good thermodynamic stability, and chemical stability on Si.[22, 38-41]

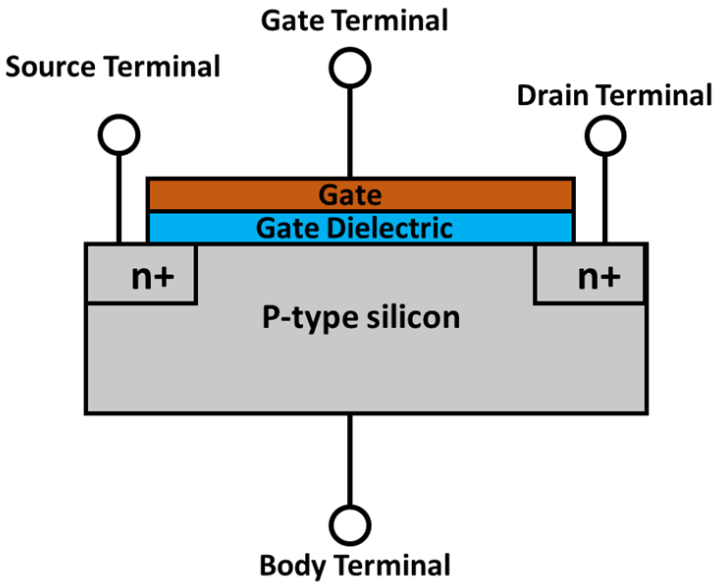

Figure 2. Schematic diagram of a cross sectional view of a MOSFET structure.

1.3.3 Solid Oxide Fuel Cells (SOFCs)

SOFCs are devices that generate electricity by oxidizing fuels (hydrogen or reformed hydrocarbons).[42] SOFCs are composed of three main components, a porous anode, a porous cathode, and a solid non-porous oxide electrolyte membrane that supports the porous electrodes (Figure 3).[42, 43] The cathode, which is also known as the air electrode, is composed of oxides and it catalyzes the reduction of oxygen to oxygen anions. The solid oxide electrolyte act as the mediator to diffuse these oxygen anions from cathode to anode.[42] At the anode, these oxygen anions are used to oxidize the fuels. All of the reactions in SOFCs take place at elevated temperatures of around 1000 °C.[43, 44]

Suitable oxide electrolytes in SOFCs must fulfill certain requirements. Major requirements include having large ionic conductivity, high heat resistivity, and stability in both oxidizing and reducing environments.[44] Most of the lanthanide oxides possess these properties and it has been found that incorporation of Ln_2O_3 increases the ionic conductivities of the electrolytes

considerably. Lanthanide-containing oxide materials such as yttria-stabilized zirconia (YSZ),[45] gadolinium or samarium-doped ceria (CGO or CSO),[46, 47] and strontium, magnesium-doped lanthanum gallate (LSGM)[48] are a few of the lanthanide oxide-containing electrolyte materials that have been widely investigated in SOFCs. Moreover, lanthanide oxide-doped materials are also being studied as cathode and anode materials for SOFCs.[49]

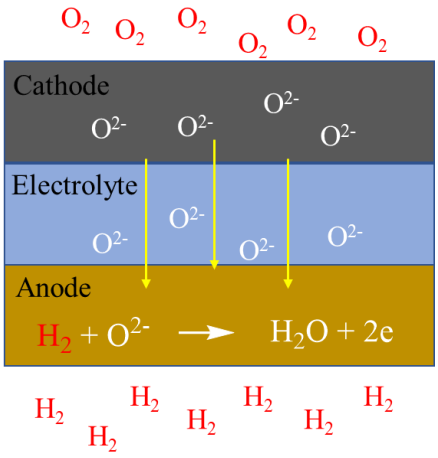

Figure 3. Schematic diagram of a typical SOFC adapted from ref. 43.

1.3.4 2-Dimensional Electron Gases (2-DEGs)

A 2-DEG is a structure that forms at the interface between two heterostructures with high electron density. These electrons can move freely along the interface but are confined to a few nanometers normal to the interface (2D movement).[50] Perovskite-type (ABO_3) oxide heterostructures have gained significant interest due to the large electron density observed (~$10^{14}/cm^2$) at the interface.[51] The first 2-DEG at oxide heterojunction was observed in the $LaAlO_3/SrTiO_3$ (Figure 4) system where dielectric $LaAlO_3$ films were grown epitaxially on a single crystalline $SrTiO_3$ substrate.[52] Extensive studies have shown the potential of this $LaAlO_3/SrTiO_3$ 2-DEG system for several novel applications, including pH sensors,[53] superconducting devices,[54, 55] and nanoelectronics.[56] Due to the interesting properties found in the

$LaAlO_3/SrTiO_3$ 2-DEG system, the interest in studying ternary oxides containing other early lanthanides (Ln = Pr, Nd) has increased.[57-59]

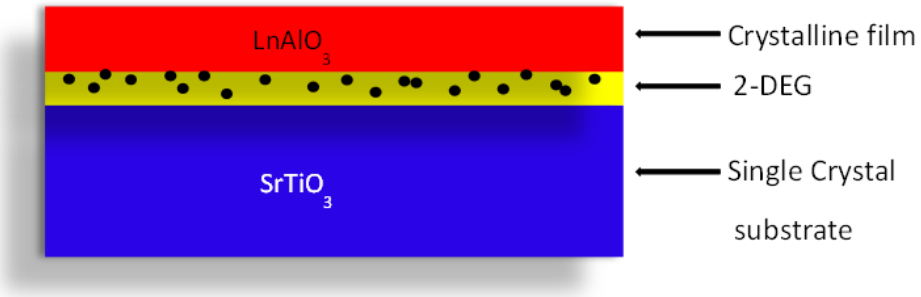

Figure 4. Structural illustration of a 2-DEG.

1.3.5 Protective Coatings

High melting points and enhanced phase stability of lanthanide oxide doped coatings at high temperatures make lanthanide oxides useful materials as thermal barrier coatings (TBC) and high-temperature corrosion resistant coatings.[18, 60-62] These TBCs should withstand strongly oxidative environments at high operating temperatures that are generally found in industrial applications such as chemical processing, petroleum refining, gas turbines, and jet engines. Also, these TBCs should have low thermal conductivities. Yttria stabilized zirconia (YSZ) is the most widely employed thermal barrier coating material with thermal conductivities around 1.2-1.8 $Wm^{-1}K^{-1}$ and new oxide coatings with thermal conductivities below the above value are being investigated for future high-temperature barrier coatings. It has been reported that the incorporation of lanthanide oxides such as Gd_2O_3, Sm_2O_3, and La_2O_3 into zirconia ($Ln_2Zr_2O_7$) results in higher melting points above 2000 °C and lower thermal conductivities than YSZ.[63]

Iron, cobalt, and nickel are the most commonly used metallic materials in industrial process equipments. The surface oxides layers formed by iron, cobalt, and nickel under oxidizing

conditions fail to provide protection to metal surfaces at high processing temperatures. Chromium alloy formation is an approach that has been used to protect these iron, nickel, and cobalt surfaces via the formation of thermally more stable oxides of chromium. These alloys of metals made with the combination of chromium are commonly known as chromia former alloys.[60] However, chromium(VI) oxides have been identified as toxic and carcinogenic materials. Incorporation of lanthanide oxides such as CeO_2 and Y_2O_3 has shown improved thermal barrier properties and adhesion properties of the protective coating along with reducing the amount of chromium needed for alloy formation.[18, 60]

In addition, lanthanide-doped oxides are reported to provide protection for metallic surfaces against corrosion and increase the adhesion properties of the protective coating to underlying metal substrates. Cerium-based oxide coatings have been largely investigated as corrosion-resistant coatings on various alloy systems including aluminum, magnesium, tin, zinc, and steel. Further, composite coatings of cobalt made with lanthanide oxides (Co-Nd_2O_3, Co-La_2O_3, Co-Y_2O_3, and Co-CeO_2) have shown superior corrosion resistance when compared to pure Co metal coatings.[64]

1.4 Thin Film Deposition of Binary and Ternary Lanthanide Oxides

As mentioned in previous paragraphs, binary lanthanide oxides (Ln_2O_3) and ternary analogues containing other metal ions ($LnMO_3$) are interesting groups of materials. These oxides are associated with a wide range of applications potential from protective coatings to microelectronic applications. Lanthanide oxides can be deposited using two major deposition techniques, known as physical vapor deposition (PVD) and chemical vapor deposition (CVD) (Figure 5).

In PVD, vapors of the target materials in the form of atoms, ions, or molecules are generated with the aid of physical processes such as evaporation or sputtering and then these vapors are transported to the substrate where they undergo condensation to form the coating. In PVD no chemical reaction takes place in the vapor phase and the type of the PVD method varies depending on the method used to generate vapors of the target material.[65] CVD is a process where chemical precursor vapors react or decompose on or near a heated substrate to produce the desired thin film material. In CVD, the reactions taking place between the precursors in the gas phase can lead to non-conformal film deposition. Metalorganic CVD (MOCVD) is a term used when metal-organic precursors such as metal β-diketonates and metal alkoxides are used as precursors.[66] Among the PVD techniques, molecular beam epitaxy (MBE),[67] sputtering,[68] electron beam evaporation,[69] and pulsed laser deposition (PLD)[70] are commonly used to deposit lanthanide oxides. MOCVD[71-76] and ALD[38] are the generally used CVD techniques for this purpose. PVD is a line-of-sight deposition technique and hence, it is difficult to control the thickness and achieve uniform films in high aspect ratio features. Both MOCVD and ALD techniques can deposit uniform films over large-surface areas on planar substrates. However, when it comes to high aspect ratio nanoscale features, only ALD has the ability to deposit highly conformal Angstrom level thin films with precise thickness control.[77]

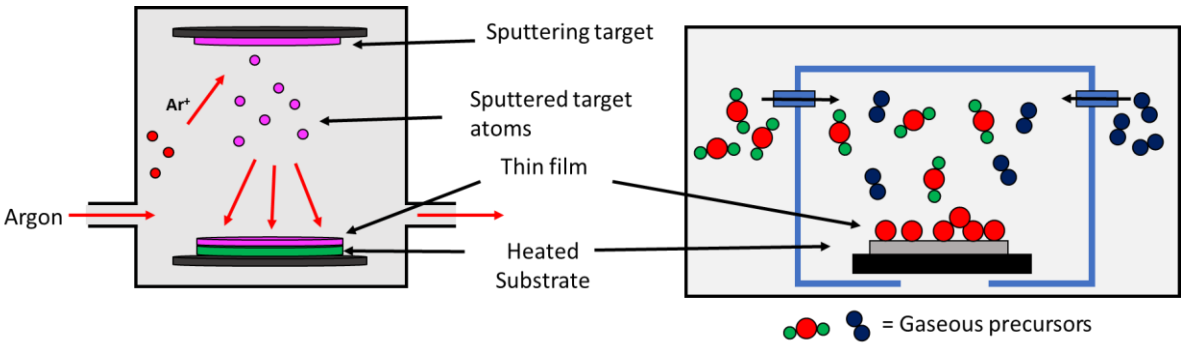

Figure 5. Schematic diagram of a film deposion by sputter PVD (left) and CVD (right).

1.4.1 Basic Principles of ALD

ALD is a vapor phase thin film deposition technique with the potential to deposit many materials, including metals, metal oxides, and metal nitrides on different substrates.[78,79] This technique is unique compared to other film deposition techniques due to its cyclic nature and the self-limiting surface reactions, which enable Angstrom level thickness control and highly conformal thin films in high-aspect-ratio features.[14, 78, 79] ALD was first introduced by Tuomo Suntola in 1974, by depositing zinc sulfide (ZnS) thin films for large-area electroluminescent displays.[80] Prior to the year 2000, the term atomic layer epitaxy (ALE) was used to describe ALD. Over the years, ALD has gained increased attention in the research and development sectors for thin film process development. This interest was further triggered in early 2000 when Intel announced the use of ALD to deposit high-κ dielectrics in complementary metal-oxide semiconductor (CMOS) transistor technology.[81] Especially, with the continuous need of scaling down microelectronic devices following Moore's law, ALD has become more and more important because of its ability to produce thin conformal films with precise atomic-level thickness control on nano-scale features.[79]

As depicted in Figure 6, an ALD process consists of four major steps. During the first step, gas phase molecules of the desired metal precursor are introduced into the reaction chamber where they react with the substrate surface reactive sites. In the second step, the reaction chamber is purged with an inert gas (N_2 or Ar) to remove excess precursor molecules and reaction byproducts from the reaction chamber. These two steps complete the first half cycle of the ALD process. During the third step, a vapor of a co-reactant is introduced into the reaction chamber and then reacts with the new surface reactive sites evolved from the first half cycle to form a monolayer of the desired material. For metal oxide ALD, usually this co-reactant is a small molecule containing

oxygen such as water, oxygen, or ozone. Finally, the reaction chamber is purged again with an inert gas to remove the excess co-reactants and reaction byproducts from the reaction chamber. These purge steps after each precursor pulse and co-reactant pulse in an ALD cycle are important to prevent any direct gas-phase reactions between the precursor and co-reactant before they reach the surface reactive sites, which can add uncontrolled CVD-like growth to the ALD process. Also, the removal of gaseous byproducts formed during the ALD half cycles through the purge step is important to avoid contamination of the resulting thin-film material.[82, 83]

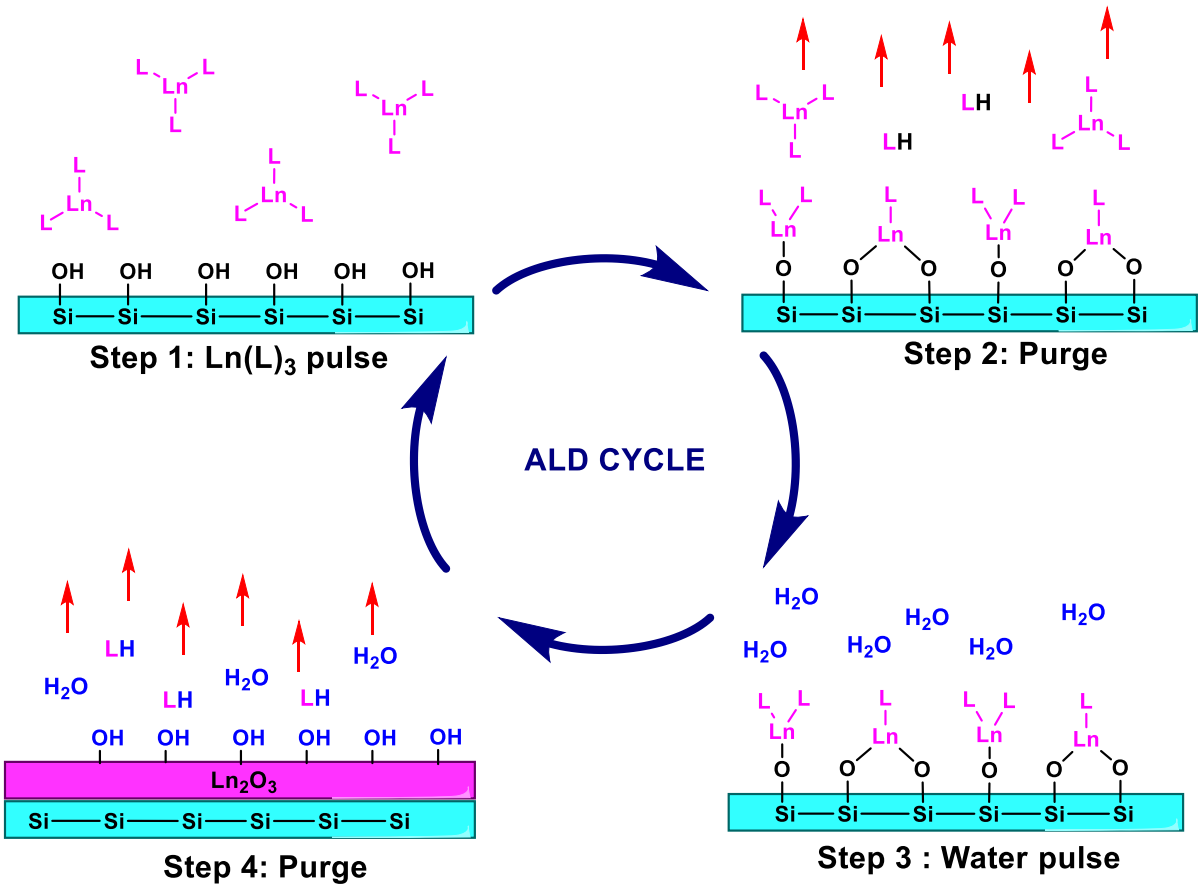

Figure 6. Schematic representation of a general ALD cycle.

1.4.2 Self-Limited Growth Behavior

An ideal ALD process consists of unique growth characteristics. As mentioned before, the key feature of ALD is the self-saturating or self-limited nature of the surface reactions, which give rise to conformal thin films with precise thickness control. Hence, when designing new ALD processes, it is very important to demonstrate the self-limiting behavior of each chemical precursor used. Generally, this is done by conducting several ALD runs under the same growth conditions with different amounts of metal precursor (or co-reactant) doses. In our ALD reactors, the amount of precursor dose injected into the reaction chamber is controlled by changing the precursor pulse times. Plotting the growth rate obtained from ALD runs against different precursor pulse lengths can determine whether the process shows self-limited growth or not. If the growth rate becomes constant for a plot after a particular pulse length as shown in Figure 7, that means the number of precursor molecules introduced within that period (y seconds) is sufficient to react with all the surface reactive groups on the growth surface. Beyond that pulse length, excess precursor molecules do not affect the film growth. As described herein, the precursor saturation plot is important to determine the amount of the precursor needed to obtain self-limited ALD growth behavior.[84]

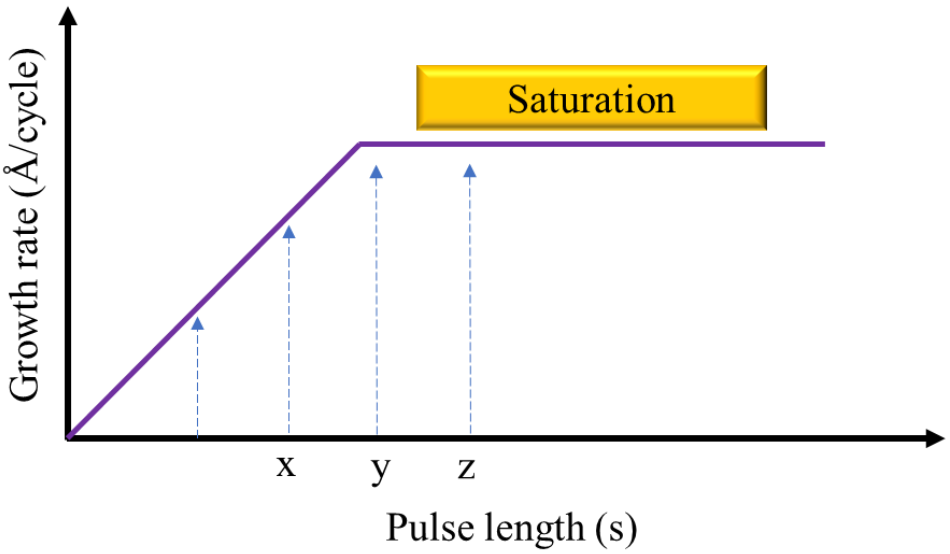

Figure 7. Plot of growth rate versus precursor pulse length illustrating self-limited growth behavior in ALD.

1.4.3 ALD Window

In ALD, the amount of energy required for surface reactions between the precursors and the co-reactants primarily depends on the type of the metal precursor, the co-reactant, and the type of the substrate being used.[85] For thermal ALD, this energy is supplied through the deposition temperature inside a heated reactor. Hence, for each thermal ALD process, deposition temperature can change from room temperature to several hundred degrees Celsius or more. Some ALD processes have a deposition temperature range in which a constant growth rate is maintained. This temperature range is known as the ALD window, where the growth rate is independent of the deposition temperature.[86] The requirement for an ALD process is that self-limited growth (Figure 6) is observed at one temperature. So, not all ALD processes will exhibit ALD windows. However, the presence of an ALD window is sometimes useful as it increases the reproducibility of the process.[85, 87]

As shown in Figure 8, at deposition temperatures below the ALD window, film growth rate tends to deviate either due to not having sufficient energy to overcome the activation energy for the surface reactions (growth rate decreases) or due to condensation of the precursor molecules and co-reactants on the film material (growth rate increases). At deposition temperatures above the ALD window, film growth rates can change either because of precursor decomposition inside the reaction chamber (growth rate increase) or due to partial desorption/removal of the surface reactive sites from the growth surface due to high temperature (growth rate decrease).

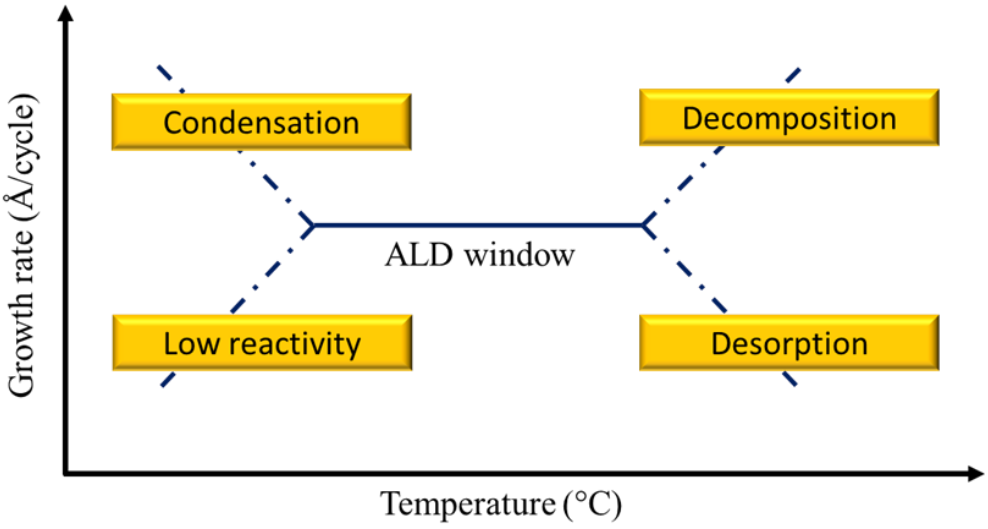

Figure 8. Plot of growth rate versus deposition temperature representing the ALD window and growth behavior outside the ALD window.

1.4.4 Linearity

The cyclic nature of the ALD process predicts a linear increase of film thickness with an increase in the number of ALD cycles. For an ideal ALD process, the plot of the thickness versus the number of cycles gives a straight line that passes through the origin as shown in Figure 9 (a). However, some ALD processes have exhibited dependence on the substrate surface chemistry, which either could enhance or inhibit the initial growth of the film up to a certain number of cycles as illustrated in Figure 9 (b). The slope of the thickness versus the number of cycle graphs in ALD

gives the self-limited growth rate for the process and the x- and y-intercepts of the extrapolated line give insights into the initial growth behavior of the film on the substrates.[85]

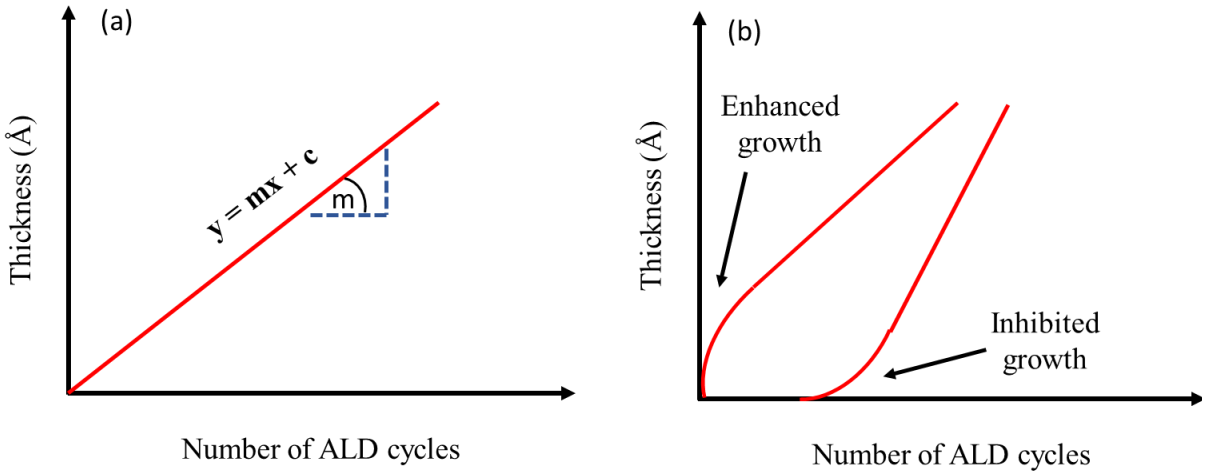

Figure 9. Plots of thickness versus the number of cycles illustrating linear growth with (a) and without (b) nucleation delay on the initial substrate surface during ALD.

1.4.5 ALD Precursor Requirements

1.4.5.1 Volatility

To be an ideal ALD precursor, chemical compounds (metal precursors and co-reactants) used in ALD should meet certain requirements. Volatility is a critical requirement. Since ALD is a vapor phase thin film deposition technique, chemical compounds used in ALD should be able to volatilize for efficient transport of the precursor molecules. Gaseous and liquid precursors are preferred because they usually provide a constant and repeatable flux of precursor vapors due to maintaining a constant surface area. The particle size of solid precursors may change during heating and from one batch to another. This may cause changes in the surface areas, hence solid precursors might fail to provide a constant flux of precursor vapors. Further, contamination of the precursor vapors with solid particles during sublimation can cause particle contamination to the growing film. The volatility of liquid and solid precursors is determined by vapor pressure. Vapor

pressure is the pressure generated by volatilized part of the molecules which are in dynamic equilibrium with the condensed phase. For ALD, 0.1 Torr is the typical acceptable lowest vapor pressure at the highest typical evaporation temperature of around 300 °C.[88] The volatility of a precursor is greatly influenced by the molecular weight and intermolecular interactions (hydrogen bonding, electrostatic interactions) between the molecules in the solid or liquid phase.[88, 89] Typically, substances with low molecular weights, and weaker/lesser intermolecular interactions are the most volatile.[86, 90] Accordingly, when pursuing metal precursors with the highest possible volatility, attention should be given to formation of monomeric complexes. If the target complex has polar bonds, ligands that can shield the metal-ligand bonds have to be selected to minimize intermolecular interactions. At the same time, a balance between the molecular weight of the ligand and shielding ability has to be maintained when selecting a suitable ligand to keep the molecular weight low while preventing the oligomerization of the complex. Particularly, in metal ions with large ionic radii, such as alkaline earth and lanthanides, metal-ligand bonds are highly polar due to the low electronegativity of these metal centers. Monomeric complexes of these metals are often coordinatively unsaturated due to the large ionic radii. These factors increase the tendency of these complexes to oligomerize and become more reactive with the surrounding environment.[91]

Saturation of the coordination sphere of large metal ions can be fulfilled by several strategies. The addition of neutral donor Lewis bases to make adduct complexes (Figure 10a), the use of multidentate ligands instead of monodentate ligands (Figure 10b), and the design of donor-functionalized ligands containing extra neutral donor atoms (Figure 10c) are the most common approaches. Coordinating donor atoms of the complexes made with these approaches can reduce the polarity of the metal-ligand bonds via the transfer of charge from the donor atom to the metal. This decrease in polarity of the metal-ligand bonds in the molecule can decrease the likelihood of

making intermolecular interactions. Hence, an increase in the volatility of the resulting complexes can be expected.[92] Further, volatility can be tuned by varying the ligand substituents. Ligands with aryl substituents tend to reduce the volatility because of higher molecular weights and π-stacking interactions that increase the intermolecular packing forces.[88, 93] Fluorinated ligand substituents can enhance the volatilities of compounds by reducing intermolecular interactions because of lone pair/lone pair repulsions between fluorine atom lone pairs of electrons.[94, 95] However, fluorinated ligands can have negative effects on film depositions, since they can afford corrosive and toxic HF, which can etch the film and the reactor parts.[88]

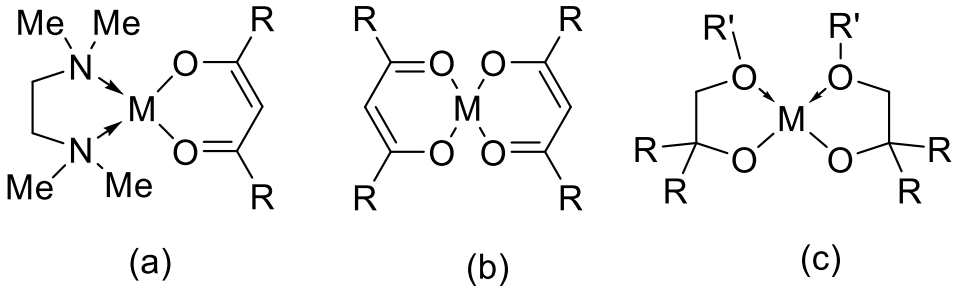

Figure 10. Schematic illustrations of metal complexes with a Lewis base adduct (a), multidentate ligands (b), and donor-functionalized ligands (c).

1.4.5.2 Thermal Stability

The second most important requirement for ALD precursors is thermal stability. The thermal stability of a compound can be defined as its resistance to change in the properties caused by heat.[88] The chemical precursors used in ALD should not undergo thermal decomposition at the vaporization temperatures (delivery temperature) and the deposition temperatures. Decomposition of the chemical precursors at the deposition temperature can lead to uncontrolled CVD-like growth, which eliminates the benefits of self-limited growth characteristics of ALD.

Multidentate ligands are known to provide better thermal stability over monodentate ligands via saturating the coordination sphere of the metal center with extra electron donor

atoms.[96, 97] Lewis base adduct complexes often tend to exhibit low thermal stabilities due to dissociation of the neutral Lewis base ligands at elevated temperatures.[6, 98] In general, complexes with strong metal to ligand bonds can be considered beneficial in designing thermally stable metal precursors. Fluorinated ligands and ligands with highly electronegative donor atoms such as oxygen make more thermally stable complexes by increasing the Lewis acidity of the metal center and thereby increasing the metal-ligand bond strengths.[88, 99]

Thermogravimetric analysis (TGA) is one of the most commonly used techniques to evaluate the suitability of chemical precursors for ALD in terms of their volatility and thermal stability. In TGA, the mass of a sample is measured continuously as a function of temperature or time, while the sample is heated using a controlled temperature program.[86] Results of the TGA experiment are displayed as a curve with temperature or time on the X-axis and weight percentage on the Y-axis (Figure 11). Depending on the stability of the precursor being analyzed, TGA can be carried out either inside a glove box (for air and moisture sensitive complexes) filled with inert gas (N_2 or Ar) or under ambient conditions (for air stable complexes). As depicted in the TGA curves shown in Figure 11, a 100% drop in the weight with a single step (curve A) with zero non-volatile residue indicates complete volatilization of the compound without undergoing any decomposition up to the temperature where the TGA curve hits zero mass percent. A compound that gives a single-step mass loss from the TGA curve but with a non-zero non-volatile residue (curve B) means the compound undergoes some thermal decomposition along with the volatilization.[86, 89]

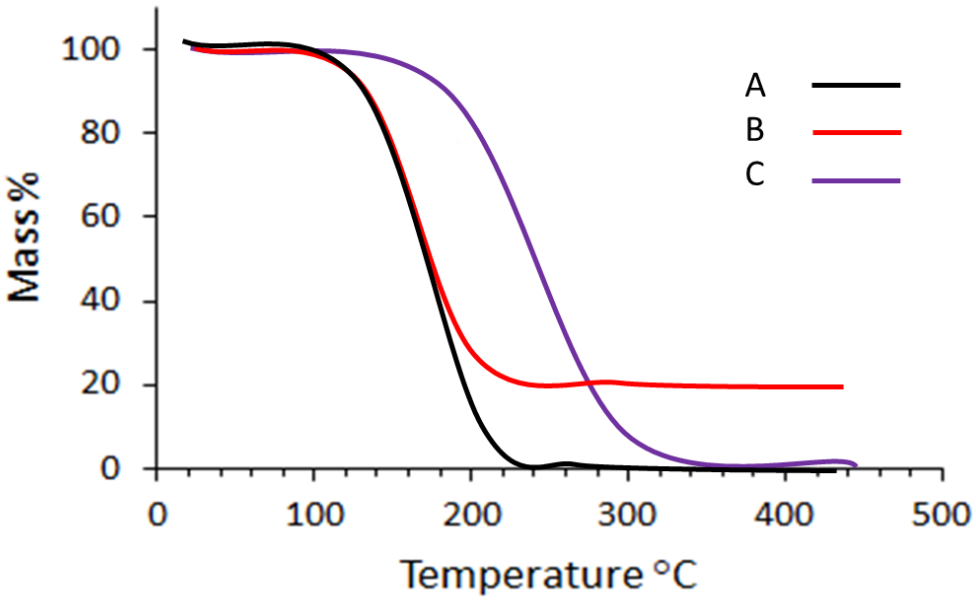

Figure 11. Representation of TGA traces of compounds with different volatilities and thermal stabilities.

Also, the temperature in the TGA curve where compounds start to lose/drop mass gives an idea about the volatility of the compound. For example, compound C in Figure 11 starts to lose mass at a relatively higher temperature than compounds A and B. Hence, compounds A and B are more volatile than complex C. The onset temperature of volatilization (T_1) for a compound can be more accurately calculated by extrapolating the TGA curve of that compound as shown in Figure 12. Another important detail that can be abstracted from the TGA trace is the temperature where 50% weight loss takes place (T_2). This temperature, T_2, is useful for a rough estimation of the delivery temperature of a compound during ALD. Generally, the temperature that is about 100 °C lower than the T_2 is approximately close to the delivery/volatilization temperature for that compound.

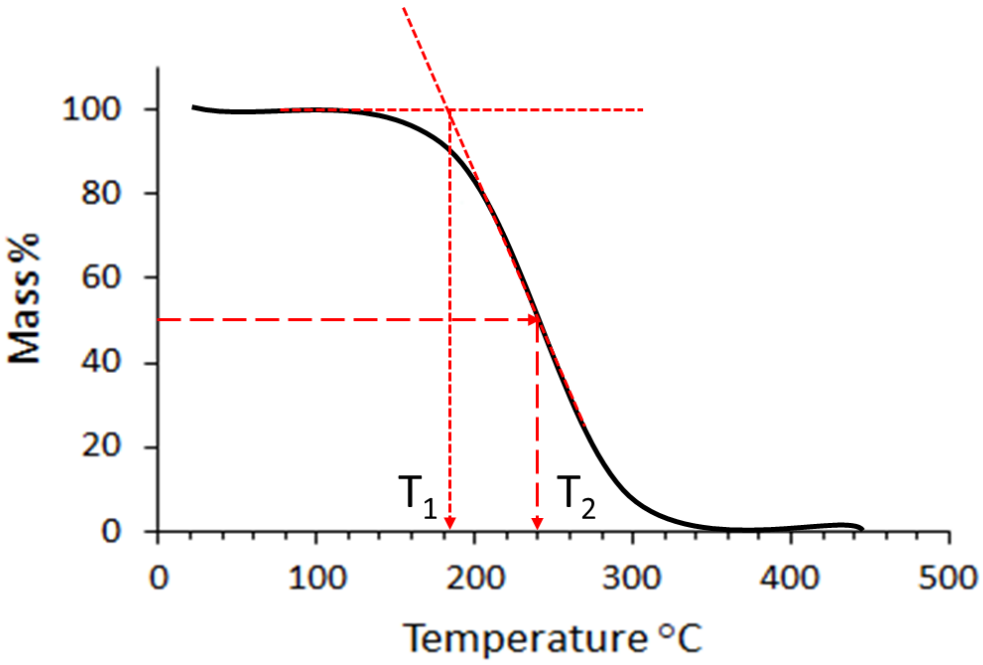

Figure 12. Obtaining onset of volatilization (T1) and temperature where 50% mass loss takes place (T2) from a TGA trace.

1.4.5.3 Reactivity

As mentioned before, ALD takes place through self-limited surface reactions. Hence, precursors being used in ALD must react with the surface reactive sites and with the co-reactants effectively, and must not react with themselves or self-decompose.[89] Reactivity of metal precursors during ALD can only be considered relative to the co-reactant being used. Metal to ligand bond strengths, relative pK_a values of both the metal complex and the co-reactant, steric factors, and the nature of the ligand substituents can be considered as the main factors that determine the reactivity of precursors during ALD.[100] Water is the most favorable co-reactant used in oxide ALD. Metal complexes with ligands that have higher pK_a values compared to that of water (pK_a~14-15) react with water and surface hydroxyl groups rapidly to give the corresponding metal oxides.[101] For example, the acetylacetone (acacH) ligand has a pK_a value of about 9, which is lower than the pK_a

of water (pK_a~14-15), and *tert*-butanol has a pK_a value of around 19 at 298 K[102] which is higher than the pK_a of water. Accordingly compared to water, Hacac is a stronger Bronsted acid (i.e., weak conjugate base) and *tert*-butanol is a weaker Bronsted acid (i.e., strong conjugate base). Hence, deprotonated *tert*-butoxide in metal complexes rapidly reacts with water to give metal oxide plus protonated *tert*-butanol ligand. In contrast, acetylacetonate (acac) metal complexes do not react with water, since weakly basic deprotonated acetylacetonates cannot abstract protons from relatively more basic water.[97, 103, 104] Ligands with electron withdrawing substituents such as CF_3 have relatively low pK_a values compared to the non-fluorinated versions. For instance, hexafluoroacetylacetone (hfacH) has a pK_a of ~5[105], which is lower than the pK_a of the non-fluorinated version, acacH (~9). Accordingly, metal complexes with electron-withdrawing ligand substituents are likely to have low reactivity with water compared to the complexes without electron-withdrawing groups.

As described above, high volatility, high thermal stability, and high reactivity towards surface reactive sites and co-reactants are the key requirements of ALD precursors. In addition, chemical substances used in ALD have to be of low toxicity, easy to handle, easy to synthesize and scale up, easily available, and the by-products formed during ALD have to be volatile so they can be purged out from the reaction chamber.[86]

1.5 Lanthanide ALD Precursors

There is only a handful of lanthanide precursors available for Ln_2O_3 ALD. These known lanthanide precursors can be categorized depending on the type of ligand being used to synthesize the complexes. Lanthanide complexes containing β-diketonate, cyclopentadienyl, bis(trimethylsilyl)amide, alkoxide, amidinate, and guanidinate ligands are the commonly

encountered precursors in Ln_2O_3 thin film deposition (Figure 13).[89, 106] The following section briefly describes the advantages and disadvantages of each of the above precursor classes.

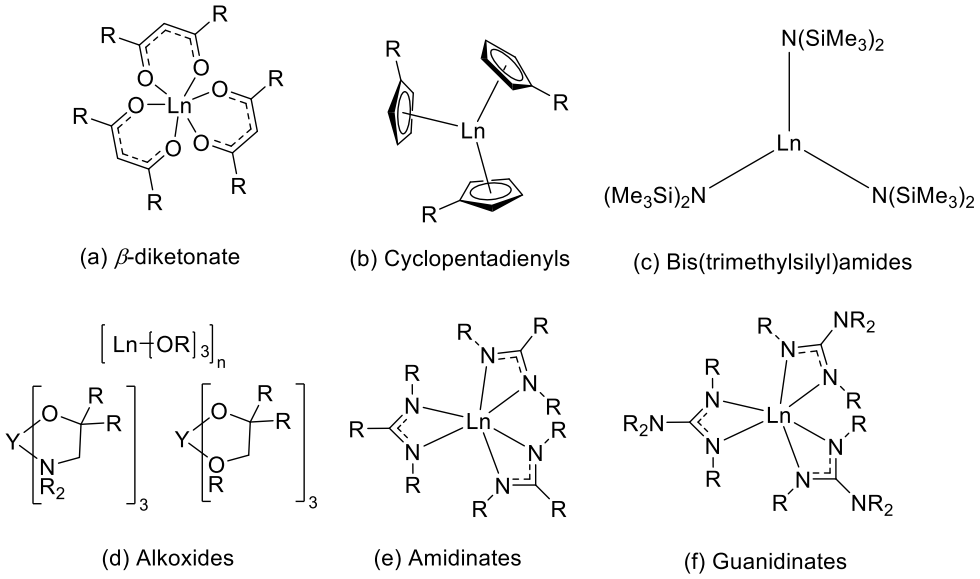

Figure 13. Volatile lanthanide precursors used for lanthanide oxide deposition by ALD.

1.5.1 *β*-Diketonate Ligands

Lanthanide complexes with *β*-diketonate ligands (Figure 13 (a)) have been studied extensively for lanthanide oxide film depositions. Acetylacetonate (acac) is the smallest *β*-diketonate ligand and three acac ligands fail to shield the large lanthanide centers effectively. Hence, lanthanide acac complexes are generally oligomeric and non-volatile. Monomeric lanthanide acac complexes can be achieved by the addition of Lewis bases such as bipyridyl (bipy) and phenanthroline (phen).[107] *tert*-Butyl substituted *β*-diketonate ligand (thdH) is more sterically demanding than acac ligands and provide better steric protection to the lanthanide center and make stable lanthanide complexes. Early and mid lanthanide(III) thd complexes crystalize as dimers.[107, 108] Lanthanide thd complexes possess high thermal stability, reasonable volatility, easy to synthesize, and are stable in air.[109, 110] Despite these favorable properties, $Ln(thd)_3$ shows no reactivity with water and requires strong oxidizing agents such as ozone for oxide ALD film

deposition.[111-113] This low reactivity of $[Ln(thd)_3]_x$ towards H_2O is attributed to the low basicity (thdH pK_a ~10) of the β-diketonate ligand compared to water (pK_a 14 or 15.7)[101] and strong Ln-O bonds.[13, 114] Hence, strong oxidizing agents such as ozone and high growth temperatures are required to afford oxide films.[13, 97, 115] These conditions could be detrimental for semiconductor device fabrication since strong oxidizing agents and high temperatures can damage the underlying substrates and increase the carbon impurities in films. As a result, the use of $[Ln(thd)_3]_x$ precursors for high-κ applications is limited.[13, 114] Further, the high melting points associated with these complexes could fail to provide a constant flux of precursor vapors during the ALD process owing to the constantly changing particle surface areas of solid precursors.[116]

1.5.2 Cyclopentadienyl (Cp) Ligands

Compared to lanthanide complexes with *β*-diketonate ligands, lanthanide complexes with cyclopentadienyl ligands (Figure 13 (b)) are highly reactive toward the water co-reactant. However, lanthanide complexes with unsubstituted Cp ligands ($Ln(C_5H_4R)$, R=H) tend to make oligomeric and polymeric species in the solid state through bridging Cp ligands. Hence, lanthanide complexes with unsubstituted Cp ligands are often less volatile and have high melting points.[117-119] The volatility of these complexes can be enhanced by introducing alkyl substituents on the Cp ring. Large alkyl substituents such as *iso*-propyl and *tert*-butyl groups can sterically block the bridging carbon atoms of the Cp rings and shield the lanthanide center effectively to favor monomeric lanthanide complex formation, which leads to higher volatilities.[120-122] When compared with the melting points of the homoleptic early lanthanide complexes reported in this chapter, early lanthanide cyclopentadienyl complexes with bulky substituents on the Cp ring have lower melting points. For instance, $La(C_5H_4iPr)_3$ and $Y(C_5H_4tBu)_3$ are liquids at room temperature and $Pr(C_5H_4iPr)_3$ and $Pr(C_5H_4Et)_3$ are low melting solids with melting points around 53-54 °C and

70-73 °C, respectively.[59, 122, 123] As mentioned before, having low melting points is advantageous to facilitate the constant flux of precursor vapor during ALD as they turn into liquids easily at the delivery temperatures. Lanthanide Cp complexes react rapidly with water during ALD to deposit Ln_2O_3, which can be attributed to the higher pK_a of Cp ligands (pK_a ~15.5 for C_5H_6)[124] compared to water (pK_a of 14 or 15.7) and oxophilic nature of Ln^{3+}. However, several Ln_2O_3 ALD processes using lanthanide Cp complexes have failed to provide self-limited growth behavior either for lanthanide Cp precursor or for water co-reactant.[59, 125] Further, some of the processes have reported higher carbon contaminations of the Ln_2O_3 films deposited with lanthanide Cp precursors.[126]

1.5.3 Bis(trimethylsilyl)amide Ligands

Owing to the relatively large size of Ln^{3+} ions, volatile lanthanide complexes with simple dialkylamido ligands are unknown. Instead, bis(trimethylsilyl)amide ligands (Figure 13 (c)) are bulkier and afford monomeric and volatile lanthanide complexes.[127] Tris[bis(trimethylsilyl)amide] lanthanide complexes ($Ln[N(SiMe_3)_2]_3$) can be easily synthesized using a halogen-free route by the treatment of lanthanide triflates instead of lanthanide chlorides with alkali earth bis(trimethylsilyl)amides.[128] Halogen free routes for synthesis of ALD precursors are advantageous since contamination of the final product with halides such as Cl^- and Br^- can be avoided. These halides contaminations in metal complexes can contaminate the films during film deposition process and further can etch the film and substrate through the formation acidic products such as HCl or HBr. $Ln[N(SiMe_3)_2]_3$ complexes have been used for lanthanide oxide thin film deposition with water as the co-reactant.[129-131] The higherreactivity of $Ln[N(SiMe_3)_2]_3$ complexes with water, compared to lanthanide complexes containing β-diketonate ligands, is attributed to the more reactive Ln-N bonds present in the $Ln[N(SiMe_3)_2]_3$ complexes and higher pK_a value of bis(trimethylsilyl)amine ligand (pK_a of $HN(SiMe_3)_2$ ~ 29)[132] compared to that of water

(pK_a of 14 or 15.7).[101] However, several reports have claimed Si and H contamination in the lanthanide oxide films deposited using $Ln[N(SiMe_3)_2]_3$ precursors. These Si and H contaminants are believed to occur due to the thermal decomposition of $Ln[N(SiMe_3)_2]_3$ precursors during ALD, since both Si and H are present in the precursor itself.[129-131] Some reports have also suggested that silanol (Me_3SiOH) can be formed due to the hydrolysis of Si-N bonds in bis(trimethylsilyl)amide ligand [$-N(SiMe_3)_2$] during the deposition processes, which can then react with surface-bound $M[N(SiMe_3)_2]_3$ precursors to form metal silicates (MSi_xO_y).[129] For instance, metal silicate films (MSi_xO_y, M = La and Hf) have been deposited with the combination of metal alkylamides ($M(NR_2)_4$) and alkoxysilanols, which suggests that Si contamination of Ln_2O_3 films with $Ln[N(SiMe_3)_2]_3$ precursors could possibly be due to lanthanide silicate formation by the reactions between silanols (possible hydrolyzed product of $Ln[N(SiMe_3)_2]_3$) and bis(trimethylsilyl)amide lanthanide precursors.[133, 134]

1.5.4 Alkoxides

Simple monodentate alkoxide ligands (-OR), such as *tert*-butoxide (OBu^t),[135] *iso*-propoxide (OPr^i),[136] and *neo*-pentoxie (ONep)[135], often form multinuclear lanthanide(III) complexes through bridging alkoxide ligand interactions (μ-OR) to saturate the coordination spheres of the large Ln^{3+} centers. Hence, most of the lanthanide complexes with simple alkoxide ligands are associated with low volatilities and thermal stabilities.[137] Tricoordinate monomeric Ln(III) alkoxide complexes can be achieved with bulky alkoxide ligands such as 2,6-di-*tert*-butyl phenoxide (DBP), but such complexes are presumably non-volatile due to the large molecular weight of the resulting complex and presence π-stacking interactions between the phenoxide groups.[138] To address the low volatilities of lanthanide complexes containing simple alkoxide ligands, donor functionalized alkoxide ligands (Figure 13(d)) have been designed to block the

vacant coordination sites on the lanthanide center via two or more donor atoms to minimize the tendency of oligomerization.[97, 139, 140] 1-Methoxy-2-methyl-2-propanol ($HOCMe_2CH_2OMe$, Hmmp) is a donor functionalized alcohol commonly used to synthesize lanthanide complexes. Late lanthanides form dimeric mmp complexes, where dimeric $[Lu(mmp)_3]_2$ has been characterized by single-crystal XRD.[139] It has been observed that early lanthanide mmp complexes undergo condensation to form oxo-bridged oligomers with low volatilities and thermal stabilities.[141] Hence, the use of $[Ln(mmp)_3]$ alkoxide precursors for conventional ALD is limited. Further, it has been also found that the formation of oxo bridges in early lanthanide mmp complexes can be suppressed by the addition of 3 mol equivalence of tetraglyme to one equivalence of $[Ln(mmp)_3]$ in toluene solution.[142] Hence, solutions of $[Ln(mmp)_3$•tetraglyme] have been used to deposit Ln_2O_3 films (Ln = La, Pr, Nd, Gd) using liquid injection MOCVD and ALD in which a solution of a metal precursor (usually in pentane, toluene, or THF) is used instead of the neat solid/liquid precursor.[74, 142, 143] In general, the strongly basic nature of alkoxide ligands (pK_a ~16-17)[144, 145] compared to water (pK_a of 14 or 15.7)[101] makes the reaction between water and the precursor feasible to deposit lanthanide oxides.

1.5.5 Amidinate and Guanidinate Ligands

Lanthanide complexes containing amidinate and guanidinate ligands (Figure 13 (e) and (f)) with the general formula $[RC(NR')_2]$ and $[R_2NC(NR')_2]$, respectively, are the most recent classes of precursors introduced for the ALD of lanthanide oxides. Both ligand systems afford Ln-N bonds and bidentate coordination to the Ln^{3+} center via two N atoms. Also, the volatility and thermal stability of these complexes can be tailored by varying the ligand substituents on C and N atoms in the ligand backbone.[146-148] Both amidine and guanidine ligands have higher pK_a values (pK_a ~27[149] for amidine and pK_a ~17[150] for guanidine) than that of water (pK_a of 14 or 15.7).[101] Hence,

lanthanide complexes with amidinate and guanidinate ligands have the potential to deposit Ln_2O_3 films with the mild oxygen source water.

The synthesis and characterization of a series of lanthanide complexes with the amidinate ligand [$MeC(N^tBu)_2$] have been reported.[151] These $Ln[MeC(N^tBu)_2]_3$ (Ln = Y, La, Ce, Nd, Eu, Er, Lu) amidinate complexes have revealed monomeric structures by single-crystal X-ray diffraction and high thermal stabilities above 300 °C. However, sublimation of these complexes requires high temperatures of around 180-200 °C at 0.05 Torr, indicating the low volatility of these complexes. Further, these precursors do not react with water to give Ln_2O_3 films during ALD and required strong oxidants such as ozone for the growth of Ln_2O_3 films.[151] On the contrary, lanthanide amidinate complexes with the formula $Ln[RC(N^iPr)_2]_3$, (R=H, CH_3, CH_2CH_3) have shown high reactivity towards the water during ALD to give Ln_2O_3 films.[152-154] However, some Ln_2O_3 ALD processes have not shown self-limited growth behavior with $Ln[RC(N^iPr)_2]_3$ amidinate precursors and water co-reactant.[155]

The ALD of Ln_2O_3 with guanidinate precursors is less studied so far. Lanthanide guanidinate complexes with the formula $Ln[Me_2NC(N^iPr)_2]_3$ ($Ln(DPDMG)_3$) are the most studied group of lanthanide guanidinates for ALD. The ALD of Ln_2O_3 films (Ln=Gd, Dr, Er, Y) has been reported recently with the use of $Ln(DPDMG)_3$ and water co-reactant.[103, 156, 157] The Ln_2O_3 films deposited with $Ln(DPDMG)_3$ precursors have given pure films, and the ALD processes have shown self-limited growth behavior for both water and $Ln(DPDMG)_3$ precursors.[103, 156, 157] The ALD windows of the Ln_2O_3 processes with $Ln(DPDMG)_3$ were reported to be 175-275 °C, 200-275 °C, 150-275 °C, and 175-250 °C for Gd_2O_3, Dy_2O_3, Er_2O_3, and Y_2O_3, respectively.[103, 156, 157] The upper temperature limit of the ALD window is often close to the decomposition temperature

of a precursor.[158, 159] Hence, it is safe to say that $Ln(DPDMG)_3$ complexes are thermally stable up to temperatures close to 250-275 °C.

1.6 Thesis Problem

As described earlier in this chapter, lanthanide oxide thin films have a wide range of potential applications in a vast variety of areas including microelectronics, optics, catalysis, and protective coatings. These applications are based on the fascinating properties associated with lanthanide oxide films such as high dielectric constants, large band gaps, large conduction band offset values on Si, good thermal stability on Si, and high refractive indices. Among the different application directions, the use of lanthanide containing oxides as alternative high dielectric gate oxide materials in transistors is the most compelling application.[69, 160, 161] With the continuous shrinkage of the dimensions of semiconductor devices, the topology of the transistors has evolved from traditional planar source and drain type architecture (Figure 2) to new three-dimensional (3D) topologies. Fabrication of defect-free uniform and thin gate dielectric materials on these new high-aspect-ratio nanoscale 3D topologies is challenging. Compared to the conventional thin film deposition techniques (PVD and CVD), ALD is a promising technique with the potential to produce pinhole-free thin films with high conformality and Angstrom level thickness control on high-aspect-ratio features, owing to the self-limited growth mechanism in ALD. Hence, increased attention is being given to the lanthanide oxide thin films grown by ALD.

However, the number of ALD processes reported for the deposition of lanthanide oxide thin films is limited due to the limited availability of suitable lanthanide ALD precursors. Even the limited number of lanthanide precursors that are currently available are associated with limitations such as low thermal stability, low volatility, need for strong oxidants such as ozone, Si contamination of films with Si-containing ligand systems, and lack of self-limited growth. Hence,

the development of new lanthanide ALD precursors is crucial for the advancement of Ln_2O_3 ALD and to expand the applications associated with Ln_2O_3 thin films. As previously mentioned in this chapter, for a chemical substance to be qualified as an ALD precursor, it should have high volatility, high thermal stability, and high reactivity towards co-reactants and surface reactive sites. The synthesis of lanthanide(III) complexes comprising all of the above mentioned properties is challenging due to the large ionic radii of Ln^{3+}. Many lanthanide(III) complexes tend to form non/less-volatile oligomers to saturate the large coordination spheres of the Ln^{3+} centers.

Hence, the main goal of this dissertation is to develop new classes of volatile, thermally stable, and reactive lanthanide complexes to afford high pure lanthanide oxide films via ALD with mild co-reactants such as water. To achieve this goal, priority was given to ligand systems with higher pK_a values than water to promote high reactivity with water during ALD and for bidentate ligand systems to endow appropriate thermal stability for the resulting lanthanide complexes. Accordingly, this dissertation introduces two new classes of lanthanide(III) complexes containing hydrazonate and enaminolate ligand systems. The structural aspects and ALD precursor properties of these new complexes were thoroughly evaluated.

Complexes were synthesized using a salt metathesis approach and were purified by sublimation and solvent crystallization. Characterization of the complexes was carried out using NMR, IR, single-crystal XRD, and elemental analysis. Precursor properties were evaluated using TGA, sublimation temperature, melting point, and thermal decomposition temperature studies. Er_2O_3 film deposition by ALD was carried out using a selected Er precursor to probe the suitability of the newly synthesized precursors for water-based ALD of Ln_2O_3. Films were characterized for thickness, crystallinity, roughness, density, and composition using spectroscopic ellipsometry,

scanning electron microscopy, grazing incident x-ray diffraction, x-ray reflectivity, atomic force microscopy, and x-ray photoelectron microscopy.

CHAPTER 2

Synthesis and Characterization of Lanthanide(III) Complexes Containing Hydrazonate Ligands, and Evaluation of Their Volatility and Thermal Stability

2.1 Introduction

The chemistry of new lanthanide complexes unveils more opportunities to explore the fascinating properties and applications associated with lanthanide-containing materials. Particularly, oxide films of lanthanides exhibit a wide variety of interesting applications ranging from catalysis to semiconductors.[19, 161-163] Fabrication of lanthanide oxide films through vapor phase deposition techniques, namely CVD and ALD, requires lanthanide complexes that are volatile and thermally stable. In general, ALD precursors must be more thermally stable than CVD precursors because CVD is often thought to involve the thermal decomposition of precursors to deposit films, whereas ALD does not. In addition to the volatility and thermal stability, ALD requires lanthanide complexes that have high reactivity with a second co-reactant to deposit lanthanide oxides. Halides of lanthanide complexes are non-volatile and hence cannot be used as precursors for film deposition. Volatile alkoxide complexes are known for lanthanides but their use in ALD is limited due to poor thermal stabilities.[139-141] Tris[bis(trimethylsilyl)amido]lanthanide(III) complexes have also been used in a few ALD studies.[129-131] These complexes show good reactivity with mild oxygen sources such as water to give oxides. However, several reports have demonstrated Si contamination in the films deposited with these silylamido precursors. The Si contamination is believed to arise from precursor decomposition during the film depositions due to the insufficient thermal stability.[114, 129] For lanthanide oxide ALD, the most commonly used precursors contain β-diketonate ligands. As indicated in the previous chapter, lanthanide complexes with β-diketonate ligands possess good thermal stability yet require strong oxidizing agents for the growth of oxide films. This low

reactivity may be attributed to the low pK_a (~10) of 1,3-diketones compared to water (pK_a 14 or 15.7).[101] The strong bonds between the highly electronegative oxygen donor atoms and strongly Lewis acidic Ln^{3+} centers in lanthanide β-diketonate complexes are predicted to lower the reactivity of these complexes further towards mild co-reactants.[164, 165]

The main objective of the work described in this chapter is to design and synthesize a new class of lanthanide complexes that can adequately address the limitations and drawbacks existing in currently available precursors. As mentioned in Chapter 1, owing to the large ionic radii of Ln^{3+} ions, simple monodentate ligands fail to encapsulate the Ln^{3+} centers. Hence, oligomerization of the complexes takes place through bridging ligands to saturate the coordination spheres of the Ln^{3+} centers, which often results in nonvolatile multi-nuclear complexes. With less sterically bulky ligands, solvent molecules often tend to coordinate to the Ln^{3+} centers, which can dissociate during heating, making the complexes thermally unstable.[166] Hence, the challenge is to discover a ligand system that can lead to volatile and thermally stable lanthanide complexes with appropriate reactivity towards mild co-reactants such as water. After screening a wide variety of ligand systems that did not provide desirable properties, attention was drawn towards hydrazonate ligands (RHNN=CR'CR"=O, R = *tBu*, R' = H, CH_3, R" = *tBu, iPr*) that our lab has previously studied. These hydrazone ligands have shown potential ALD precursor properties for complexes of the mid to late first-row transition metals, but no study has been conducted with lanthanides.[167]

Herein, the synthesis, structure, volatility, and thermal stability of lanthanide complexes that contain a *tert*-butyl hydrazone ligand (RHNN=CR'CR"=O, R = tBu, R' = H, R" = tBu) (Scheme 1) are described. This ligand makes a six-membered chelate ring via bidentate coordination to the lanthanide center through oxygen and nitrogen donor atoms. This six-membered chelating ring, along with the bulky *tert*-butyl substituent groups in the ligand

backbone, provides steric protection to the metal center, which could lead to volatile and thermally stable monomeric lanthanide complexes. The pK_a value for the hydrazone ligand reported here is not well documented. Hence, it is difficult to predict the reactivity of the proposed lanthanide hydrazonate complexes towards water co-reactant during ALD to deposit Ln_2O_3 based on the pK_a argument.

Scheme 1. Deprotonation of a *tert*-butyl hydrazone to obtain the anionic *tert*-butyl hydrazonate ligand used in this study.

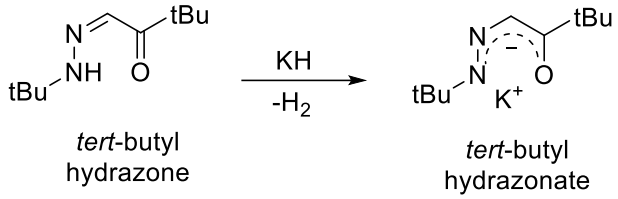

2.2 Results and Discussion

Synthetic Aspects

The *tert*-butyl hydrazone ligand ($L^{tBuHyd}H$) was synthesized by following a literature procedure that involves the treatment of *tert*-butyl glyoxal with *tert*-butyl hydrazine hydrochloride and potassium hydroxide.[167] The potassium salt of L^{tBuHyd} was prepared by treatment of one equivalent of $L^{tBuHyd}H$ with one equivalent of potassium hydride (KH) in tetrahydrofuran (THF). These freshly prepared solutions (3 equivalents) were treated directly with one equivalent of anhydrous $LnCl_3$ (Ln = La, Pr, Gd, Er, Lu, and Y) suspended in THF to afford complexes **1-6**, by the salt metathesis approach outlined in equation 3. Sublimation of the crude reaction mixtures obtained upon treatment of KL^{tBuHyd} (3 equiv) with $LnCl_3$ (Ln = La, Pr, Gd, Er, Lu, and Y) at 155−185 °C (0.5 Torr) afforded the homoleptic complexes **1**−**6** in 31−42% yields. Ln^{3+} ions were selected from early (La, Pr), mid (Gd), to late (Er, Lu) lanthanide ions to cover the lanthanide ions with different ionic radii in the lanthanide series. Additionally, Y^{3+} was also selected due to its

similarity in ionic radii and chemistry to later Ln^{3+} ions and the wide application potential of Y_2O_3 films.[1, 168-171]

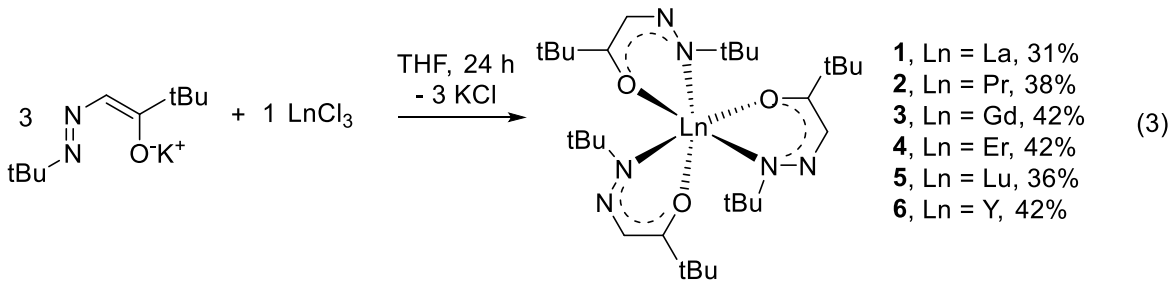

(3)

Complexes **1**–**6** were characterized by a combination of X-ray crystallography (**1**, **2**, **4**, **6**), ^{1}H nuclear magnetic resonance (NMR) spectroscopy (**1**, **5**, **6**), $^{13}C\{^1H\}$ NMR spectroscopy (**1**, **5**, **6**), infrared spectroscopy, melting points, and CHN microanalyses. The X-ray crystal structures are presented below, and the line drawings in equation 3 represent the molecular structures that were observed for **1**, **2**, **4**, and **6**.

The ambient temperature ^{1}H and $^{13}C\{^1H\}$ NMR spectra of diamagnetic lanthanide hydrazonate complexes **1**, **5**, and **6** in benzene-d_6 showed the expected resonances for the L^{tBu}Hyd ligands. The L^{tBu}Hyd ligands in **1**, **5**, and **6** share common vinyl C-H and *tBu* moieties. The vinyl C-H resonances were observed as a broad singlet in each spectrum between δ 7.65 and 7.70. ^{1}H NMR resonances of the *tBu* groups attached to the N atoms of the ligands (N-*tBu*) appeared as a broad singlet in each spectrum in the narrow range of δ 1.38 to 1.42, while the *tBu* groups on the carbonyl carbon atoms (C-*tBu)* appeared as a broad singlet in each spectrum in the narrow range of δ 1.13 to 1.14. The ^{1}H and $^{13}C\{^1H\}$ NMR spectra of **1, 5,** and **6** are shown in Figures 12, 13, and 14.

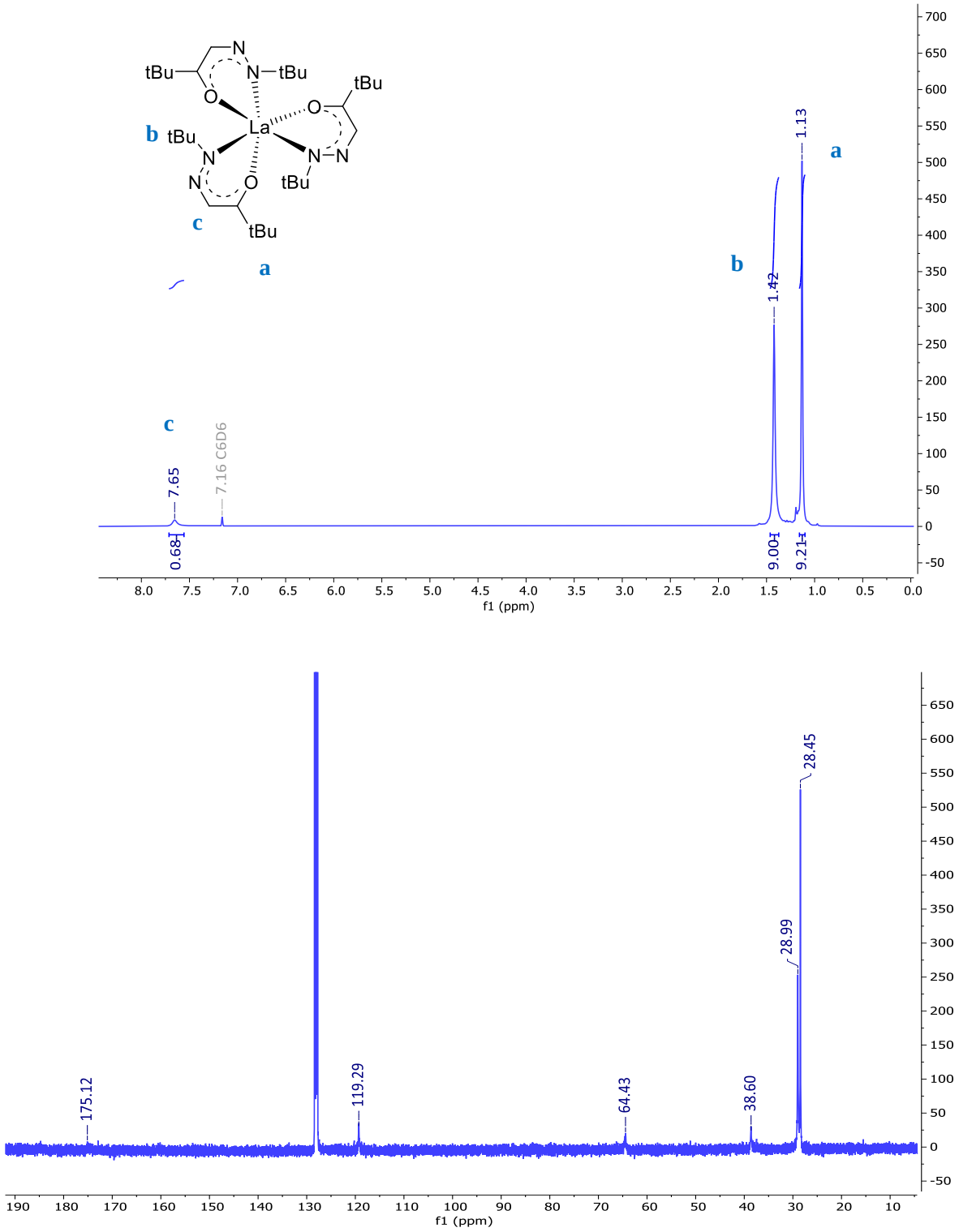

Figure 14. Room temperature ^{1}H (top) and $^{13}C\{^{1}H\}$ (bottom) NMR spectra of lanthanum complex **1** in benzene-d_6**.**

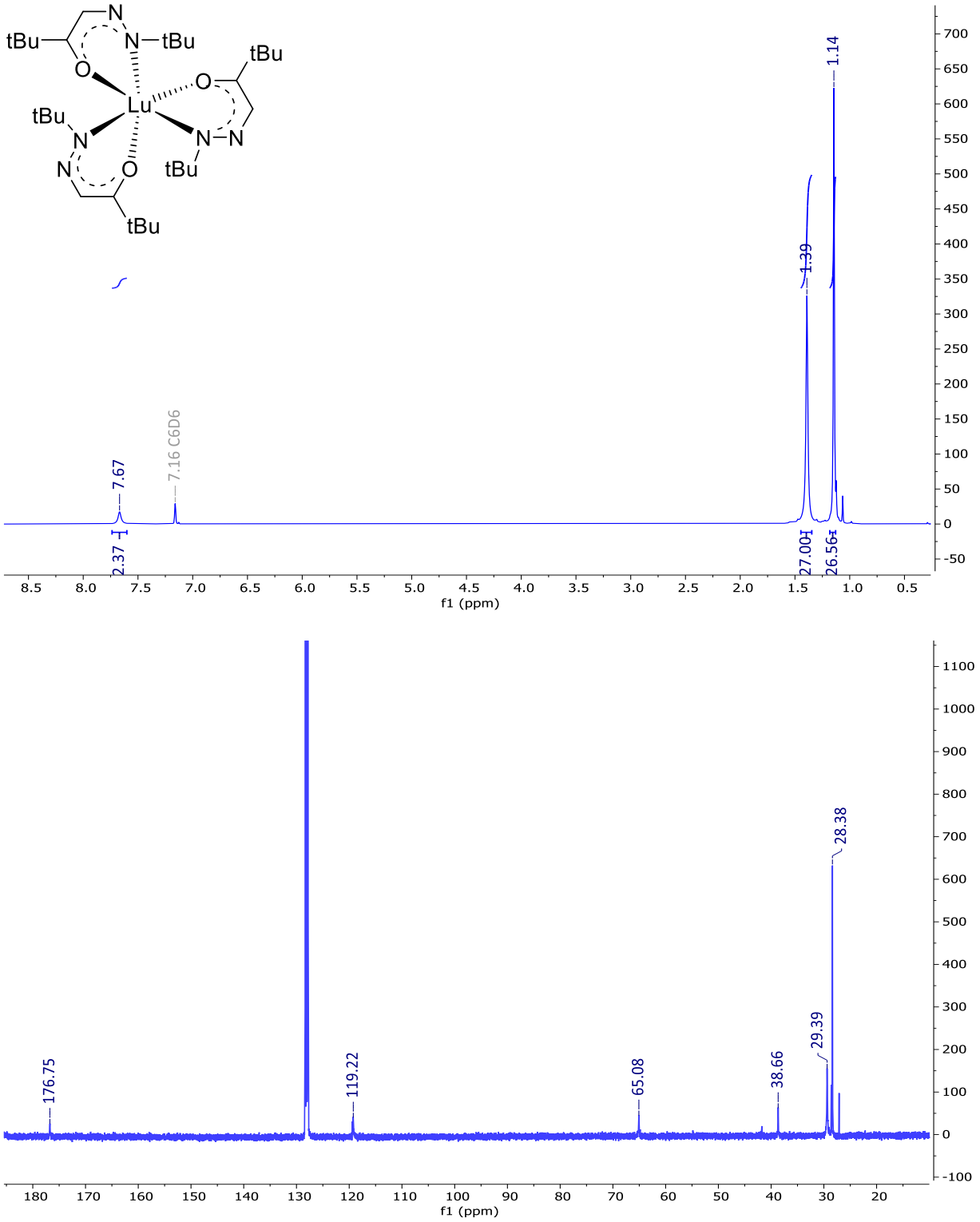

Figure 15. Room temperature ^{1}H (top) and $^{13}C\{^{1}H\}$ (bottom) NMR spectra of lutetium complex **5** in benzene-d_6.

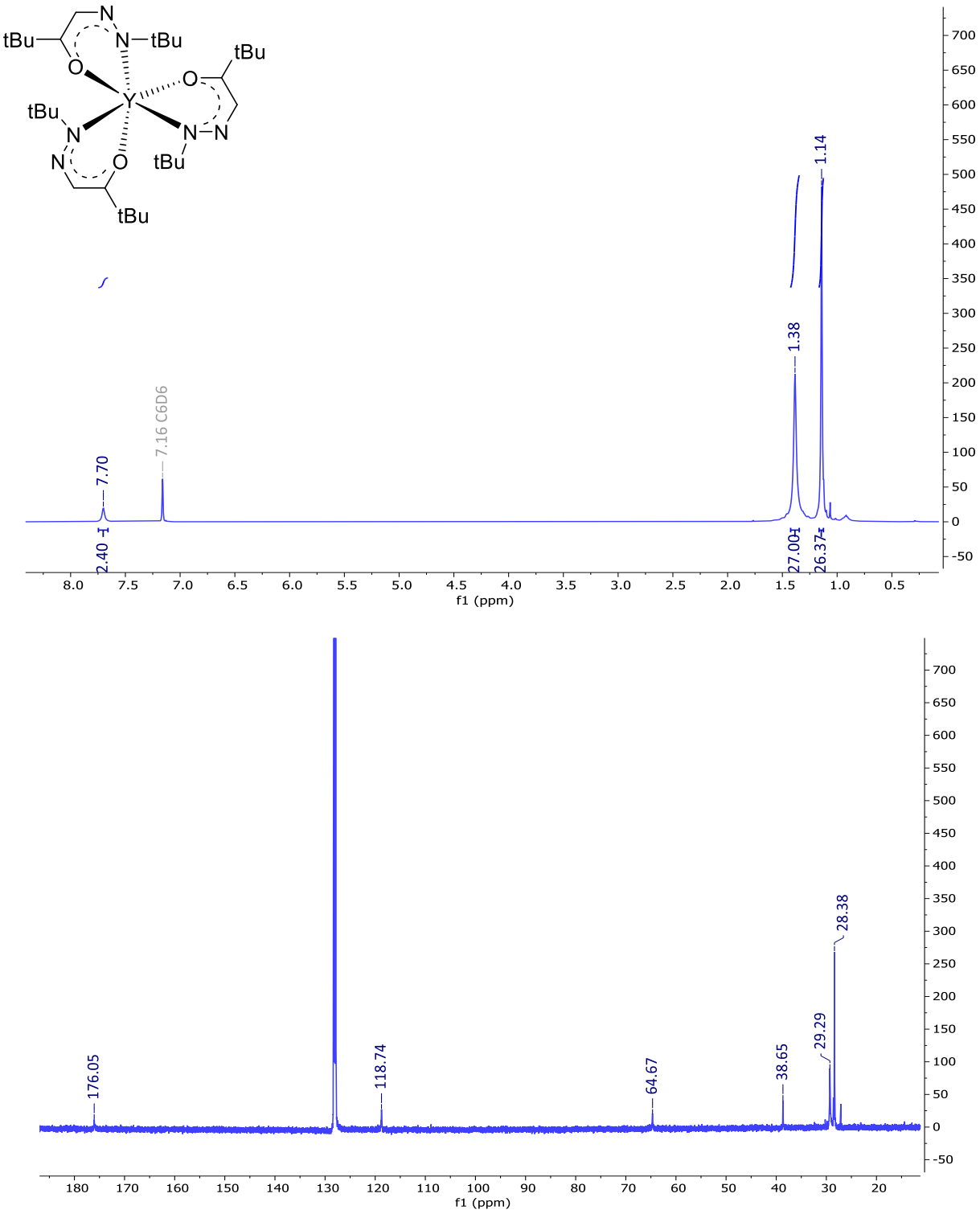

Figure 16. Room temperature ^{1}H (top) and $^{13}C\{^{1}H\}$ (bottom) NMR spectra of yttrium complex **6** in benzene-d_6.

Variable Temperature (VT) ^{1}H NMR Studies

Broadening of the ^{1}H NMR resonances was observed with diamagnetic lanthanide hydrazonate complexes **1**, **5**, and **6** in the spectra recorded at room temperature (23 °C). This behavior could be attributed dynamic processes such as monomer-dimer equilibria, arm on-arm off equilibria in solution at a given temperature, or to the independent existence of two different species or structural isomers with approximately similar chemical shifts in the given solvent and at the given temperature. Hence, to further analyze the solution state behavior, variable temperature ^{1}H NMR spectra of the La (**1**) and Y (**6**) complexes in toluene-d_8 were carried out in the temperature range from -70 to +40 °C and the data are summarized below.

The behavior of La complex **1** was determined first (Figure 17). At 20 °C, the ^{1}H NMR spectrum of **1** recorded in toluene-d_8 exhibits resonances only for a single type of hydrazonate ligand at δ 7.60 (C-H), 1.41 (N-*tBu*), and 1.12 (C-*tBu*). When the ^{1}H NMR spectrum was recorded at 40 °C, resonances were observed at δ 7.55 (C-H), 1.39 (N-*tBu*), and 1.12 (C-*tBu*), which are very similar to the chemical shifts observed at 20 °C. However, when the temperature was decreased below 0 °C, the emergence of new resonances was visible. This observation remained approximately constant thoroughout the temperature range from -20 to -70 °C, and hence only the spectral data at -70 °C will be discussed in detail here. The ^{1}H NMR spectrum of **1** recorded at -70 °C (Figure 18) consisted of two N-*tBu* resonances at δ 1.45 and 1.36, and two C-*tBu* resonances at δ 1.20 and 1.13. The C-H resonance of **1** at -70 °C consisted of a less intense resonance at δ 7.49 and two slightly overlapped resonances at δ 7.77 and 7.78. The integration ratio between the resonances at δ 7.77 and 7.49 were close to 2:1.

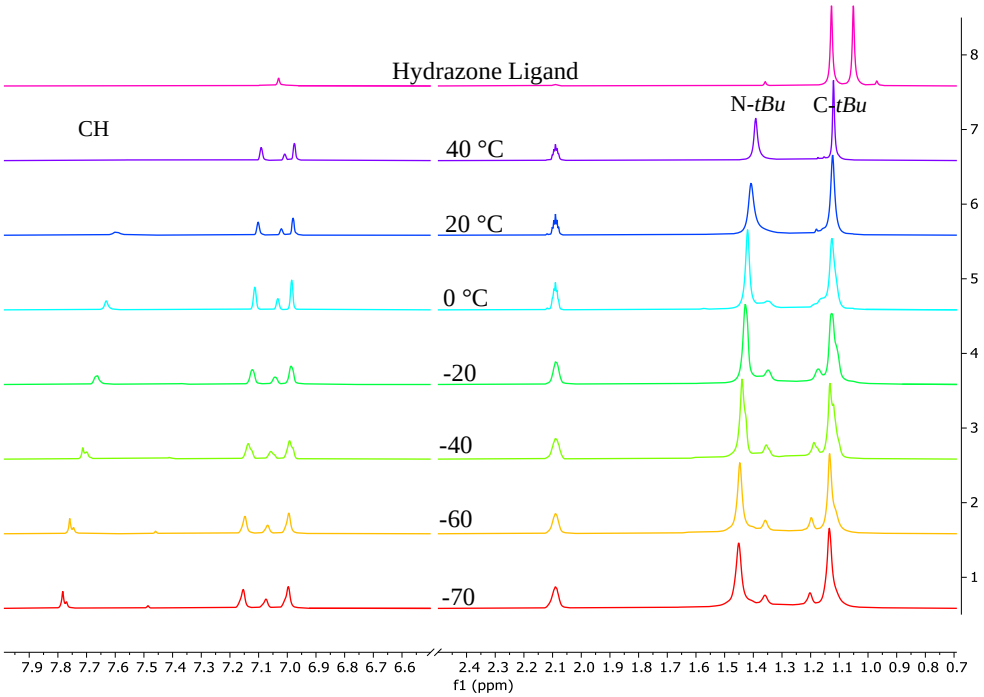

Figure 17. VT ^{1}H NMR spectrum of **1** in toluene-d_8. The resonances at around δ 7.2-7.0 and 2.09 are from toluene-d_8 solvent residual protons.

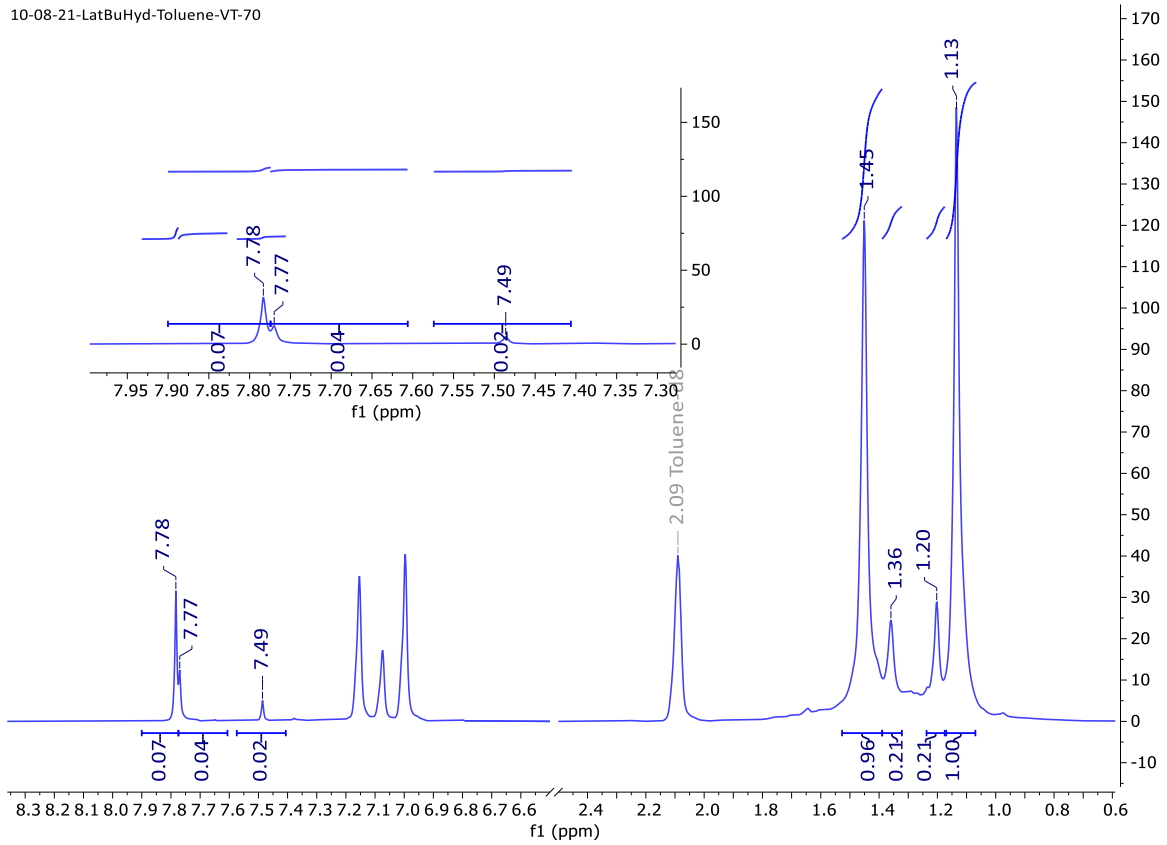

Figure 18. ^{1}H NMR spectrum of **1** recorded at -70 °C in toluene-d_8 with the zoomed-in CH resonance region. The resonances at around δ 7.2-7.0 and δ 2.09 are from toluene-d_8 solvent residual protons.

According to the single-crystal X-ray structure determination, the solid-state structure of **1** was determined to be a monomer with octahedral geometry around the La^{3+} center. In octahedral systems where the two donor sites within a bidentate ligand are dissimilar, the metal-centered coordination can result in the formation of two geometric stereoisomers, namely the meridional (*mer*) and facial (*fac*) isomers.[172] The final ratio of the *fac* and *mer* isomers are determined mainly by the change in the electronic behavior between the two donor atoms in the bidentate ligand, steric interactions, and secondary interactions.[172] Based on the variable temperature ^{1}H NMR spectral data described above and the solid-state structure of **1** being a monomer with octahedral geometry, it can be proposed that broadening of the ^{1}H NMR resonances occurs due to the presence of facial (*fac*) and meridional (*mer*) geometrical isomers of **1** in solution. The *mer* isomer has no

planes of symmetry, or axes of rotation, making the three coordinated ligands non-equivalent. The *fac* isomer has a C_3 axis of rotation giving full equivalence of all three ligands (Figure 19). Hence, in *fac* isomers, all three ligands show a single set of resonances and in *mer* isomers, each ligand shows a separate set of resonances.[172]

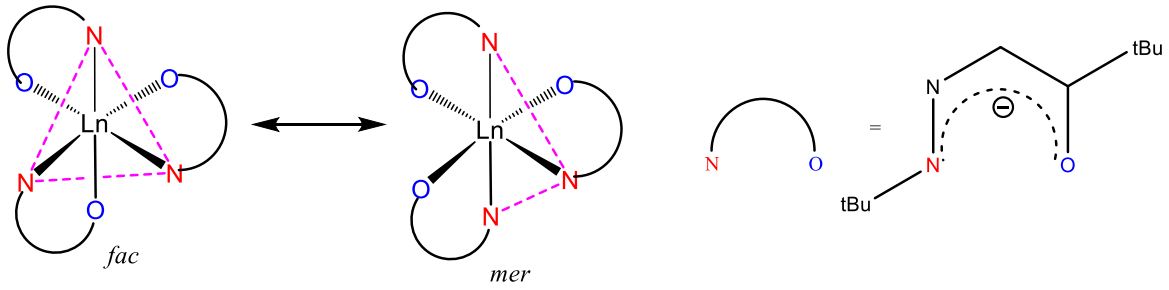

Figure 19. Schematic representation of *fac*/*mer* isomerism in octahedral complexes.

Based on the proposed *mer* and *fac* geometric isomers of **1** in solution, it can be suggested that resonances at δ 1.13, 1.45, and 7.78 at -70 °C represent the C-*tBu*, N-*tBu*, and C-H protons of the *fac* isomer, respectively. Proton resonances at δ 1.20 (C-*tBu)*, 1.36 (N-*tBu)*, 7.49 (C-H), and 7.77 (C-H) can be considered to emerge from the *mer* isomer. Ideally, as mentioned before, the *mer* isomer is expected to give three sets of resonances for each chemically non-equivalent ligand. However, the C-H protons of the proposed *mer* isomer of **1** gave only two resonances with the integration ratio of ~2:1 due to the overlapping of the C-H resonances of two of the ligands of the *mer* isomer with each other. Further, due to the less resolved and broadened nature of the NMR resonances, only one set of C-*tBu* and N-*tBu* resonances (δ 1.20, 1.36) of the *mer* isomer were distinguishable. The remaining two sets of C-*tBu* and N-*tBu* resonances of the *mer* isomer may be overlapped with the C-*tBu* and N-*tBu* proton resonances of the *fac* isomer located at δ 1.13, and 1.45, respectively. In 2016, Lima and coworkers reported the NMR spectra of *mer* isomers of two tris(8-hydroxyquinolinate)aluminum(III) complexes (Figure 20). They observed the presence of two sets of proton resonances for 8-hydroxyquinolinate ligands of the *mer* isomer with a 2:1

integration ratio, suggesting two of the resonances for the 8-hydroxyquinolinate ligands of the *mer* isomer are superimposed due to having similar chemical environments.[173] This observation is similar to what we observed for C-H resonances of the *mer* isomer of **1**. Additionally, the ratio between the proposed *fac* and *mer* isomers of **1** in toluene-d_8 remained constant (~1:1) within the -40 to -70 °C temperature range. This behavior suggests that at temperatures below 0 °C, the rate of interconversion between the *mer* and *fac* isomers of **1** becomes slow. As a result, separate proton resonances for proposed *mer* and *fac* isomers can be seen. When the solution is warmed to above 0 °C, the rate of *mer* and *fac* isomer interconversion becomes faster in the NMR time scale. Hence, only one set of broad resonances appears at temperatures above 0 °C.

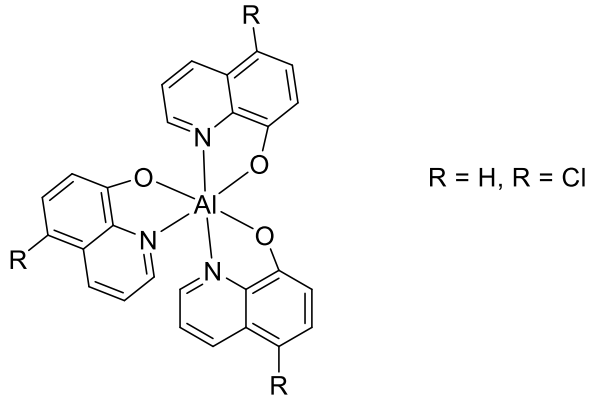

Figure 20. Structural representation of unsubstituted and chlorine substituted tris(8-hydroxyquinolinate)Al(III) complexes.

The variable temperature ^{1}H NMR spectra of yttrium complex **6** were studied next (Figures 21). The room temperature ^{1}H NMR spectrum of **6** recorded in benzene-d_6 exhibited broad resonances, especially for the proton resonance of N-*tBu* moiety. Similar to the lanthanum complex **1,** broadening of the NMR resonances for **6** can be explained based on the possibility of the presence of *fac* and *mer* geometrical isomers in solution. The ^{1}H NMR spectrum of **6** recorded at 20 °C in toluene-d_8 shows only one set of resonances at δ 7.63 (C-H), 1.36 (N-*tBu*), and 1.13 (C-

tBu), which are in close resemblance to the ^{1}H NMR resonances observed at 40 °C (δ 7.59 (C-H), 1.35 (N-*tBu*), 1.12 (C-*tBu*)). With the decrease of the temperature below 0 °C, the emergence of new resonances was evident. The ^{1}H NMR of **6** recorded at -60 °C in toluene-d_8 (Figure 22) consisted of four C-*tBu* resonances at δ 1.25, 1.21, 1.15, and 1.09 and three N-*tBu* resonances at δ 1.52, 1.43, and 1.34. The ligand backbone C-H groups of **6** showed four less well resolved C-H resonances at δ 7.85, 7.80, 7.73, and 7.41.

As mentioned earlier, the *fac* isomer should give one set of resonances for all of the three ligands, since they are equivalent. The *mer* isomer should give three sets of resonances for the three ligands, since they are chemically non-equivalent and spatially different. Hence, it can be proposed that resonances of **6** observed at -60 °C at δ 7.73 (C-H), 1.43 (N-*tBu*), and 1.15 (C-*tBu*) represent the *fac* isomer and C-H resonances observed at δ 7.85 (C-H), 7.80 (C-H), 7.41 (C-H), N-*tBu* resonances observed at δ 1.52, 1.34, and C-*tBu* observed at δ 1.25, 1.21, and 1.09 represent the *mer* isomer. As expected for the *mer* isomer of **6**, three sets of resonances were observed for C-H and C-*tBu* protons for the three chemically non-equivalent $L^{tBu\text{Hyd}}$ ligands. However, for N-*tBu* groups only two resonances were distinguishable due to the broad and less resolved nature of the N-*tBu* region. It can be speculated that the remaining N-*tBu* resonance of the mer isomer is overlapped with the N-*tBu* resonance of the fac isomer that appeared at δ 1.43. Further, due to the broad and overlapped nature of the proton resonances, accurate integration of the proton resonances of the *mer* and *fac* isomers were difficult. However, approximate integration values suggest ~1:2 *mer* to *fac* integration ratio in solution.

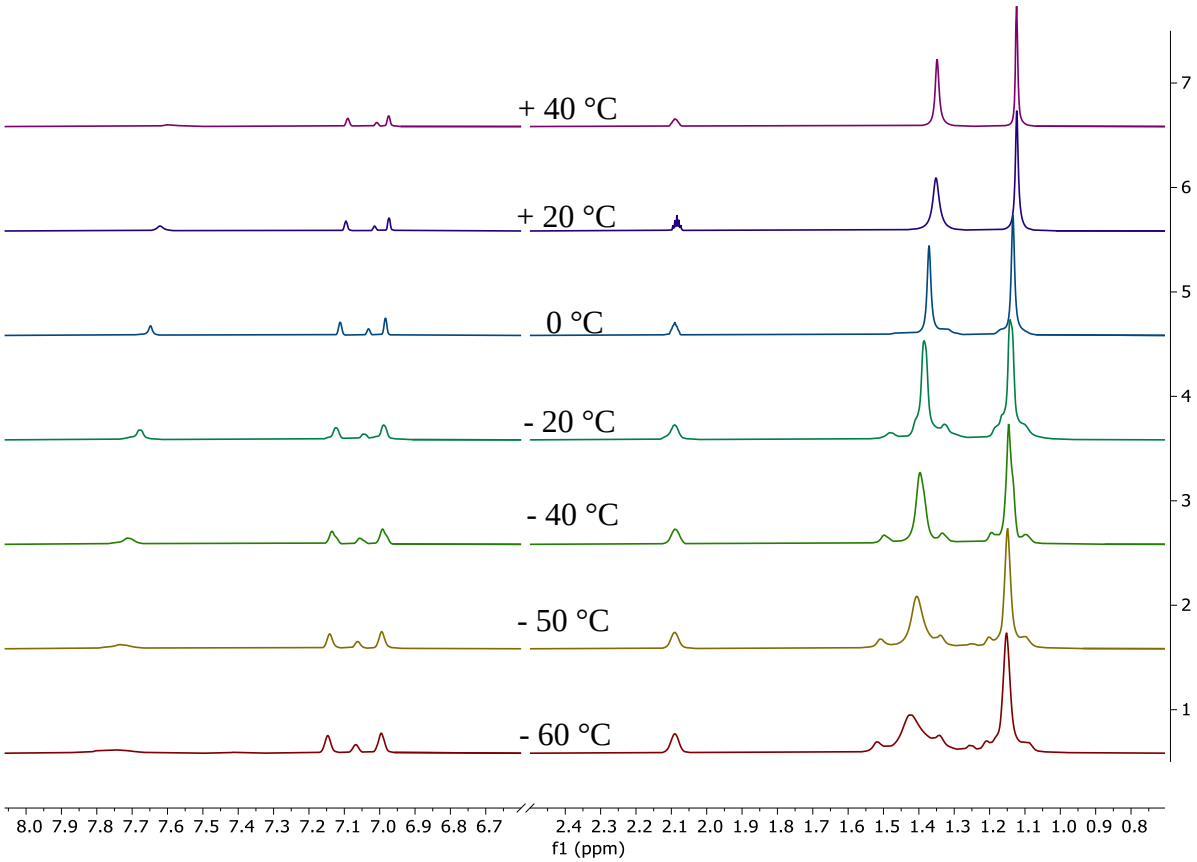

Figure 21. VT ^{1}H NMR spectra of complex **6** in toluene-d_8. The resonances at around δ 7.2-7.0 and 2.09 are from toluene-d_8 solvent residual protons.

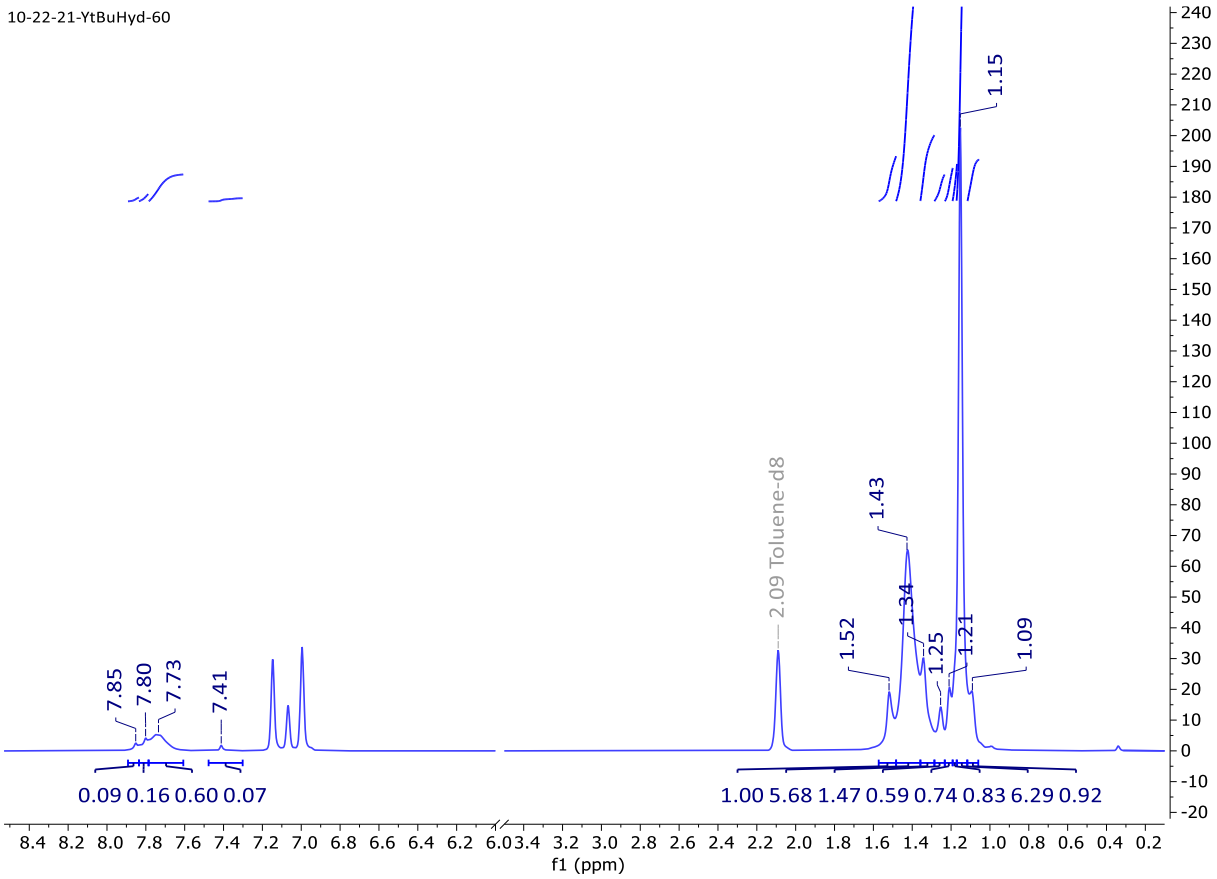

Figure 22. ^{1}H NMR spectrum of **6** recorded at -60 °C in toluene-d_8. The resonances at around δ 7.2-7.0 and 2.09 are from toluene-d_8 solvent residual protons.

Elemental Analysis

The elemental analysis results of **1−6** were evaluated to determine the bulk purity and compositions of these new lanthanide hydrazonate complexes. Complexes **2-6** gave H and N values that were within ±0.4% of the calculated values. However, the C microanalysis values for **1−3** and **6** were slightly lower than the calculated values. The lower C values in microanalyses could arise from refractory metal carbide formation, which has been previously observed for lanthanide complexes with oxygen-containing ligands.[139, 141, 174-176] Infrared spectra of **1-6** show medium to strong absorptions between 1481-1514 cm^{-1} for C=C bonds and 1327-1333 cm^{-1} for the C−O single-bond stretches in hydrazonate ligand.

Structural Analysis

Single crystal X-ray diffraction studies were carried out for **1**, **2**, **4**, and **6**. Crystals were obtained either by sublimation or slow evaporation in hexane under argon atmosphere at room temperature. According to the single-crystal X-ray structure determination data collected, **1**, **2**, **4**, and **6** showed similar diffraction patterns, and the *tert*-butyl groups of the hydrazonate ligands were highly disordered.

Complex **4** (Figure 23) crystallizes as a six-coordinate monomer with three κ^2-*tert*-butyl hydrazonate ligands coordinated to the Er center in an octahedral geometry. The molecular structure of the crystallized complex **4** exists as the *mer* isomer, in which the two axial positions of the octahedron are occupied only by N atoms. The hydrazonate ligands of **4** were highly disordered over several sites making overall eight possible conformations of the *mer* isomer (Figure 24) and all of the eight conformations are equally likely. Hence, the overall crystal structure of **4** is a combination of all eight conformations. As a result, several constraints and restraints on bond lengths and angles were imposed in order to refine the final structure. Bond lengths and angles of the cobalt(II) version of this complex already published in the Cambridge Crystallographic Database (Ref. NIQKOP) were used for this purpose.[167] Hence, bond lengths and angles obtained for **4** do not give exact values for this particular complex. However, Er-O and Er-N bond lengths are unique for this complex but cannot say definitively to which isomer these values belong. Qualitatively, the Er-N bond lengths (2.443(12), 2.450(12), 2.486(14) Å) and Er-O bond lengths (2.118(10), 2.115(10), 2.125(11) Å) for **4** are in good agreement with the Er-N (2.545 (6), 2.615 (6), 2.532 (6) Å) and Er-O (2.150 (5), 2.141 (5), 2.141 (5) Å) bond lengths observed for the six coordinate piperidine substituted Er-enaminolate complex (Figure 25) described in the Chapter 3.[176] Figure 23 illustrates the ORTEP image of one of the eight possible isomer

confirmations obtained for **4**. Similarly, **1**, **2**, and **6** also gave highly disordered structures and are six coordinate monomers with three κ^2-*tert*-butyl hydrazonate ligands bound to the Ln^{3+} center.

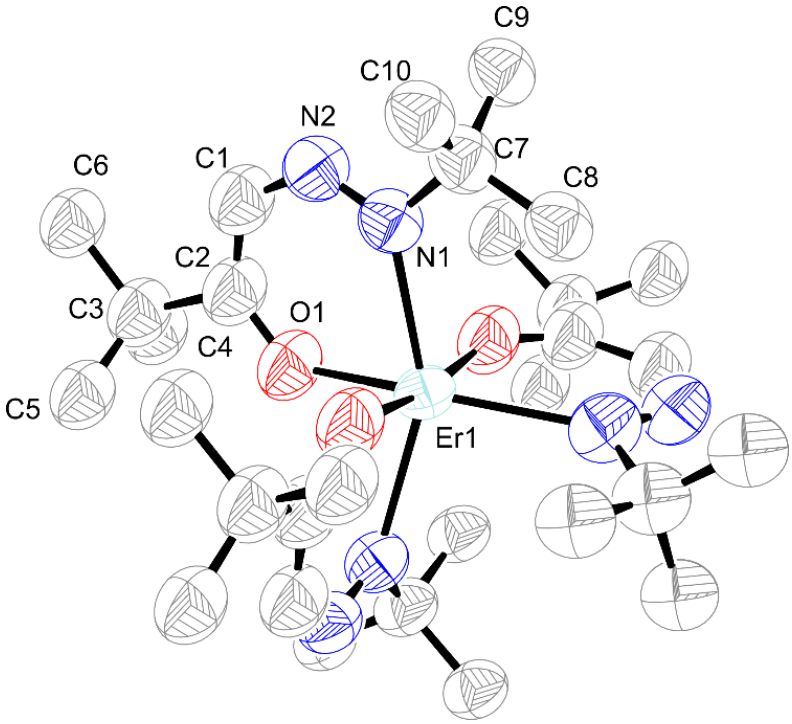

Figure 23. ORTEP image of Er(^{tBu}Hyd)$_3$ (**4**) with displacement ellipsoids at the 50% level showing only one of the eight possible isomer conformations.

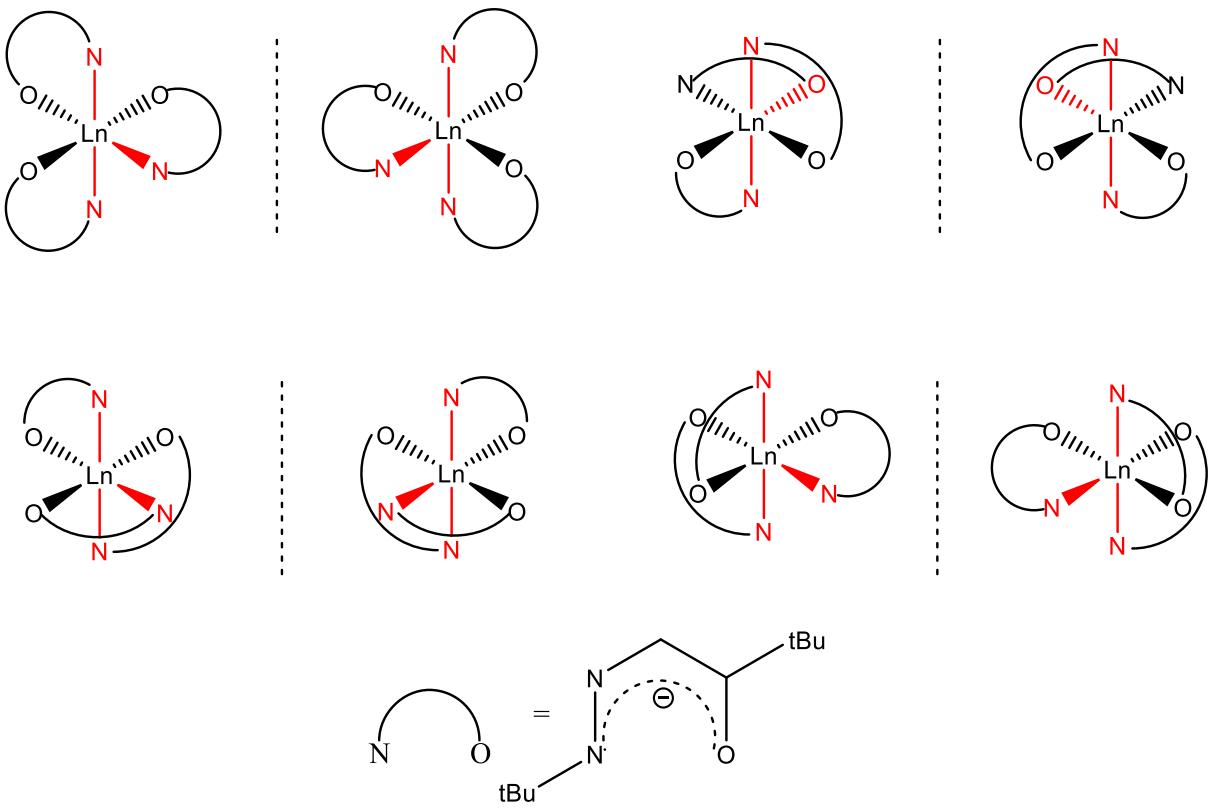

Figure 24. Schematic representation of different possible conformations of the *mer* isomers of **4** in solid-state.

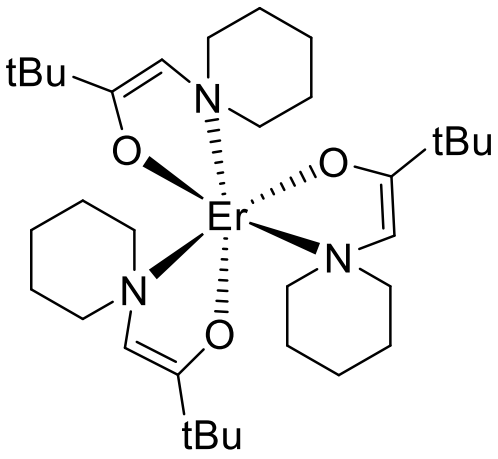

Figure 25. Line drawing of the structure of piperidine substituted Er-enaminolate complex reported in Chapter 3.

Precursor Properties

The primary goal in synthesizing these new lanthanide hydrazonate complexes was to use them as precursors for lanthanide oxide film depositions, especially by ALD. As described in detail in Chapter 1, ALD precursors must fulfill key requirements such as sufficient volatility, sufficient thermal stability, and high reactivity with co-reactants and surface reactive sites. Accordingly, the volatility and thermal stability of **1-6** were examined using sublimation and solid-state decomposition temperature measurements, respectively. As summarized in Table 2, **1-6** sublimed between 155-185 °C at 0.5 Torr to afford yellow to orange products, indicating the volatility of the complexes. A general trend is that the volatility decreases with the increasing molecular weights of the complexes.[177] However, **1** and **2** have slightly higher sublimation temperatures despite having lower molecular weights than **3-6**. These higher sublimation temperatures of **1** and **2,** compared to **3-6,** can be explained based on the size of the Ln^{3+} center and the bulkiness of the $L^{tBu\text{Hyd}}$ ligand. La^{3+} and Pr^{3+} have larger ionic radii than the Gd^{3+}, Er^{3+}, Lu^{3+}, and Y^{3+} ions. Hence, the $L^{tBu\text{Hyd}}$ ligand may not have the correct steric profile to shield the large La^{3+} and Pr^{3+} metal centers completely from the surroundings. As a result, the tendency of La^{3+} and Pr^{3+} in **1** and **2** to make intermolecular interactions with the neighboring molecules is higher than in **3-6**. These intermolecular interactions can decrease the volatility of **1** and **2**, making their sublimation temperatures higher than **3-6**.

Table 2. Sublimation temperatures and decomposition temperatures for **1-6**

Complex	Sublimation temperature (°C, 0.50 Torr)	Decomposition temperature (°C)	Molecular Weight of $Ln(^{tBu}Hyd)_3$ (g/mol^{-1})
1, $La(^{tBu}Hyd)_3$	185	259	688.73
2, $Pr(^{tBu}Hyd)_3$	170	293	690.73
3, $Gd(^{tBu}Hyd)_3$	160	290	707.08
4, $Er(^{tBu}Hyd)_3$	165	289	717.08
5, $Lu(^{tBu}Hyd)_3$	170	276	724.79
6, $Y(^{tBu}Hyd)_3$	155	285	638.73

Thermal decomposition temperatures of **1-6** were determined by heating a few milligrams of each complex in a sealed capillary tube, using a melting point apparatus with a ramp of 5 °C/min. The complexes were then visually examined for signs of decomposition upon heating. Complexes **2-6** turned reddish-brown between 275 and 290 °C, indicating their gradual thermal decomposition, while La complex **1** showed the same color change at a slightly lower temperature (~260 °C). The lower thermal stability observed for La complex **1**, compared to **2-6**, could arise due to the differences in the charge to size ratio of Ln^{3+} in **1-6**. As mentioned before, La^{3+} has the largest ionic radius across the lanthanide series and Lu^{3+} has the smallest ionic radius. For Ln^{3+}, the charge to size ratio increases from La^{3+} to Lu^{3+}. Hence, Lewis acidity of Ln^{3+} increases across the lanthanide series from La^{3+} to Lu^{3+}. As a result, for $Ln(^{tBu}Hyd)_3$ complexes, the metal to ligand bond strengths can be expected to increase from La^{3+} to Lu^{3+}. Accordingly, the Ln-$L^{tBu}Hyd$ bonds in $La(^{tBu}Hyd)_3$ **1** are expected to be weaker and longer than the Ln-$L^{tBu}Hyd$ bonds in **2-6**, making **1** less thermally stable than **2-6**. This gradual decrease of Ln-X (X=Lewis basic donor atom such as

O and N) distance across the lanthanide series from La^{3+} to Lu^{3+} is expected for lanthanide complexes due to the lanthanide contraction and has been confirmed by a few studies with different classes of lanthanide complexes.[178, 179] Further, ligands that do not have the correct steric profile to shield the Ln^{3+} ions can also lead to less stable complexes. As mentioned earlier, the inability of the L^{tBu}Hyd ligand to protect the La^{3+} center from interacting with the neighboring molecules can increase the decomposition of the **1** at low temperatures.[180] Complexes **2-6** possess decomposition temperatures that are about 100 °C above their corresponding sublimation temperatures. This is a favorable sign that these complexes have the potential to be delivered into the deposition chamber during ALD with minimal or no thermal decomposition.

To obtain more insights into the volatility and thermal behavior of **1-6**, TGA analyses were carried out inside an argon-filled glove box with a ramp of 10 °C/min using a few milligrams of each complex obtained by sublimation. Representative TGA traces recorded for **1-6** are given in Figure 26. The TGA traces show clean volatilizations of **1-6** with single-step weight losses. Volatilizations start at around 250 °C and result in low nonvolatile residual masses (**1**, 11%, **2**, 10%, **3**, 12%, **4**, 8%, **5** and **6**, 10%) after 500 °C. As previously mentioned in the introduction chapter of this thesis, the presence of a single step weight loss is important for an ALD precursor since it indicates the volatilization of one type of a species (preferably the targeted metal complexes). Volatilization without decomposition is helpful to prevent contamination of the films from other volatile products and to maintain self-limited ALD growth. Table 3 summarizes the percent of nonvolatile residues after 500 °C, the onset of volatilization where complexes start to lose weight at atmospheric pressure, and the temperatures where 50% weight losses take place ($T_{50\%}$) for **1-6**. The 50% weight losses of **1-6** take place at a temperature of around 270 °C. This temperature is important in calculating the delivery temperature for the ALD process development

as previously explained in the introduction chapter, and for **1-6**, a delivery temperature in the ALD reactor of around 170 °C can be suggested.

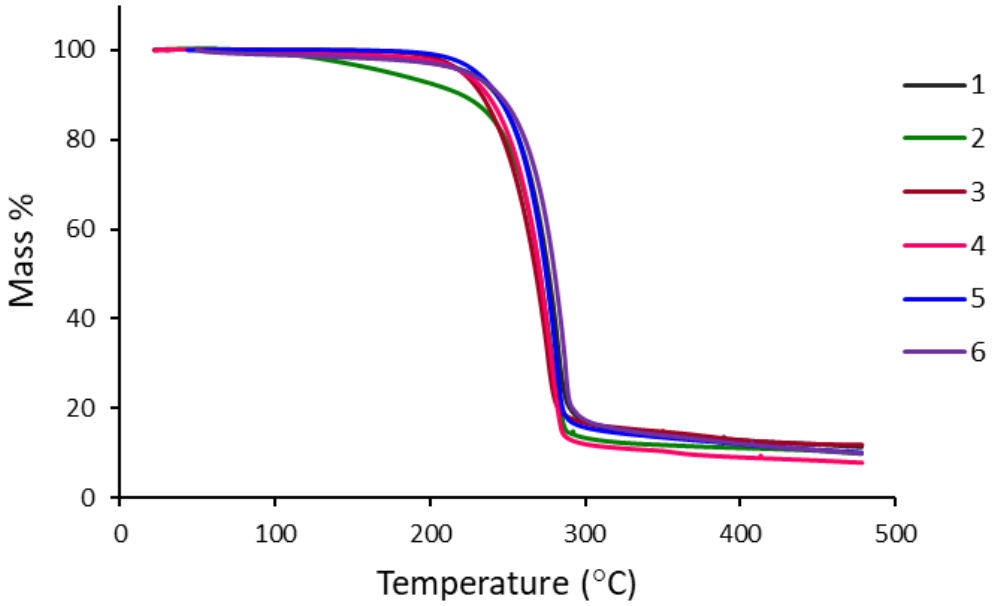

Figure 26. TGA Traces of lanthanide *tert*-butyl hydrazonate complexes **1-6.**

Table 3. Percent nonvolatile residue, onset temperature of volatilization, and temperature at 50% weight loss for **1-6.**

Complex	Residual mass %	Onset of volatilization (°C)	Temp. where 50% mass loss takes place (°C)
1, La(^{tBu}Hyd)$_3$	11	250	278
2, Pr(^{tBu}Hyd)$_3$	10	250	270
3, Gd(^{tBu}Hyd)$_3$	12	240	268
4, Er(^{tBu}Hyd)$_3$	8	245	270
5, Lu(^{tBu}Hyd)$_3$	10	250	275
6, Y(^{tBu}Hyd)$_3$	10	255	280

To broaden the understanding of the thermal behavior of these lanthanide hydrazonates, **1** (La(^{tBu}Hyd)$_3$) and **6** (Y(^{tBu}Hyd)$_3$) were subjected to heating for 24 h in sealed glass ampoules at two temperatures: a) corresponding sublimation temperatures at low pressure and b) upper limit of the ALD delivery temperature in our ALD system (190 °C). To evaluate the complex stability, ^{1}H NMR spectra were recorded before and after each heat experiment and observed for any changes in the chemical shifts or emergence of new resonances due to thermal decomposition. Accordingly, **1** and **6** were heated under atmospheric pressure for 24 h at 180 °C and 160 °C, respectively, which are close to their sublimation temperatures. Complex **6** was also heated for 24 h at 190 °C, which is close to the upper temperature limit of the precursor delivery system in our ALD reactor. Interestingly, as depicted in Figure 27, the ^{1}H NMR spectra of **6** recorded before and after heating did not show any significant changes in the chemical shifts or in the number of proton resonances at both temperatures. These observations suggest that **6** can maintain a good thermal stability for a long period of time at its expected delivery temperature of ~170 °C in an ALD reactor. By contrast, La complex **1** was completely decomposed after heating for 24 h at 180 °C, showing no proton resonances corresponding to the parent compound (Figure 28).

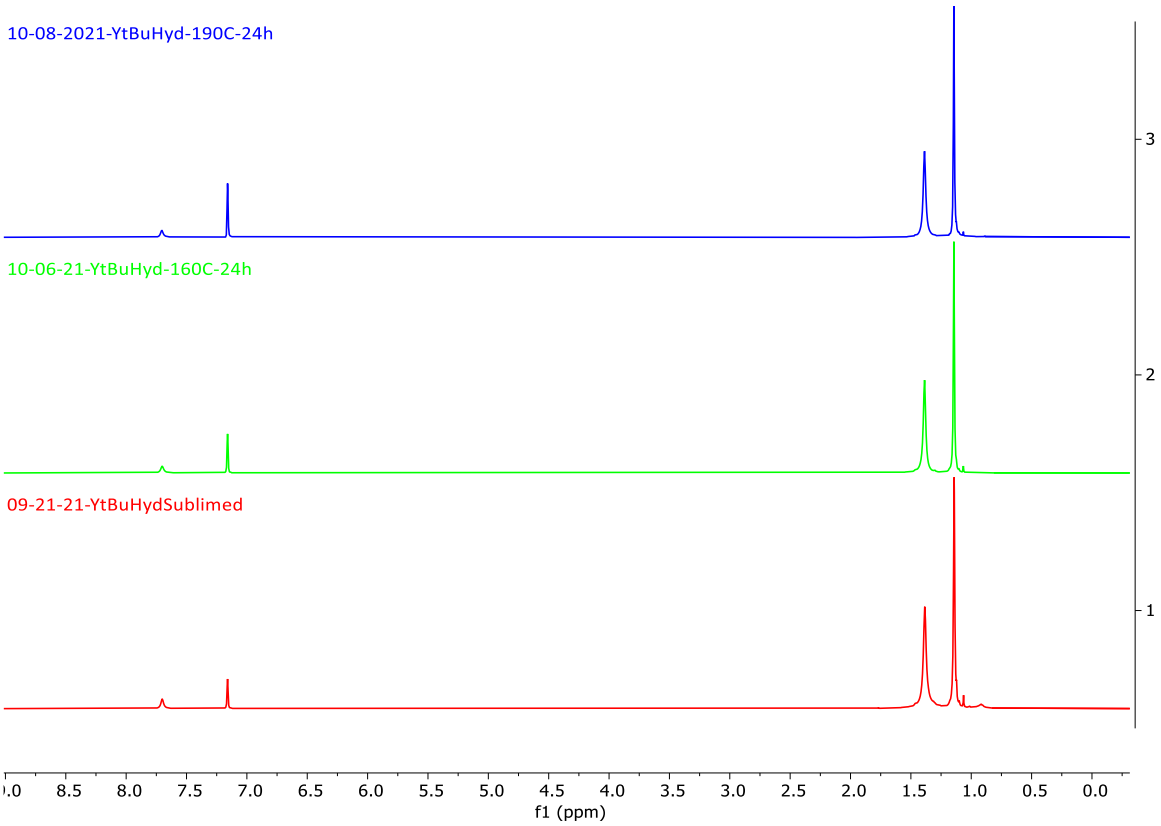

Figure 27. ^{1}H NMR spectra of **6** before and after heating for 24 h at 160 and 190 °C. The resonance at around δ 7.16 is from the benzene-d_6 solvent residual protons.

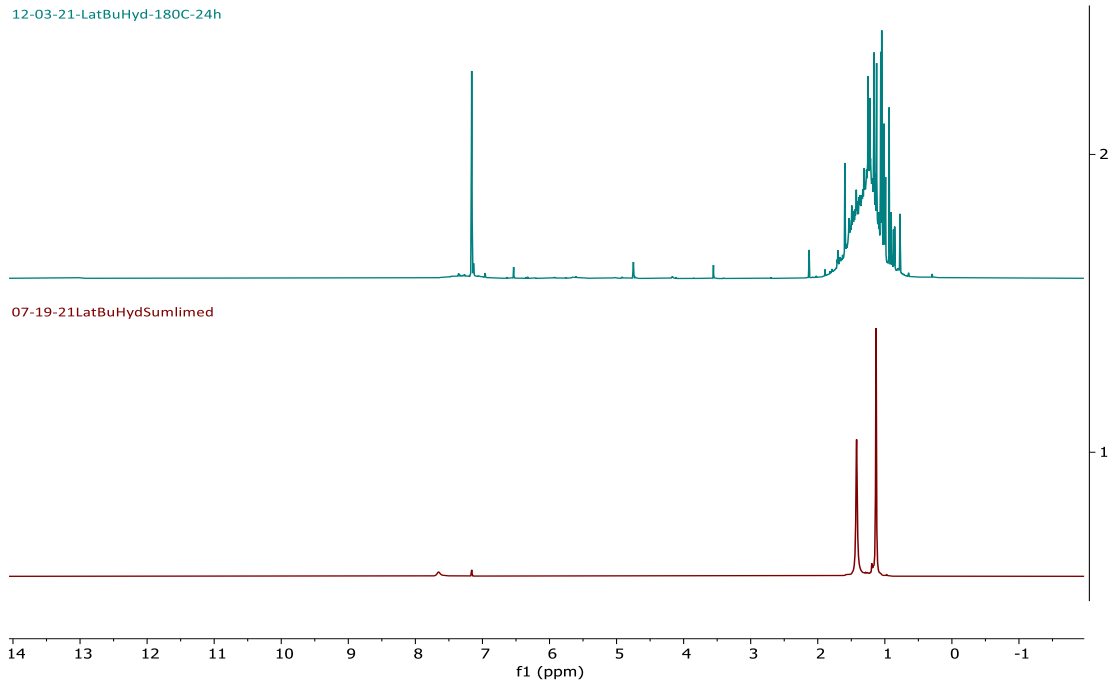

Figure 28. ^{1}H NMR spectra of **1** before and after heating for 24 h at 180 °C. The resonance at around δ 7.16 is from the benzene-d_6 solvent residual protons.

Since Y complex **6** showed a good thermal stability at its delivery temperature, we sought to evaluate its long-term thermal stability at 275 °C for 1 h, which is a common ALD deposition temperature for Ln_2O_3 thin films in the literature.[97, 129, 181, 182] During the heating process, **6** underwent a slight color change from bright yellow to pale orange. However, the ^{1}H NMR of **6** (Figure 29) remained unchanged before and after the heat treatment. This observation further confirms the possibility of using **6** as a precursor for yttrium oxide ALD.

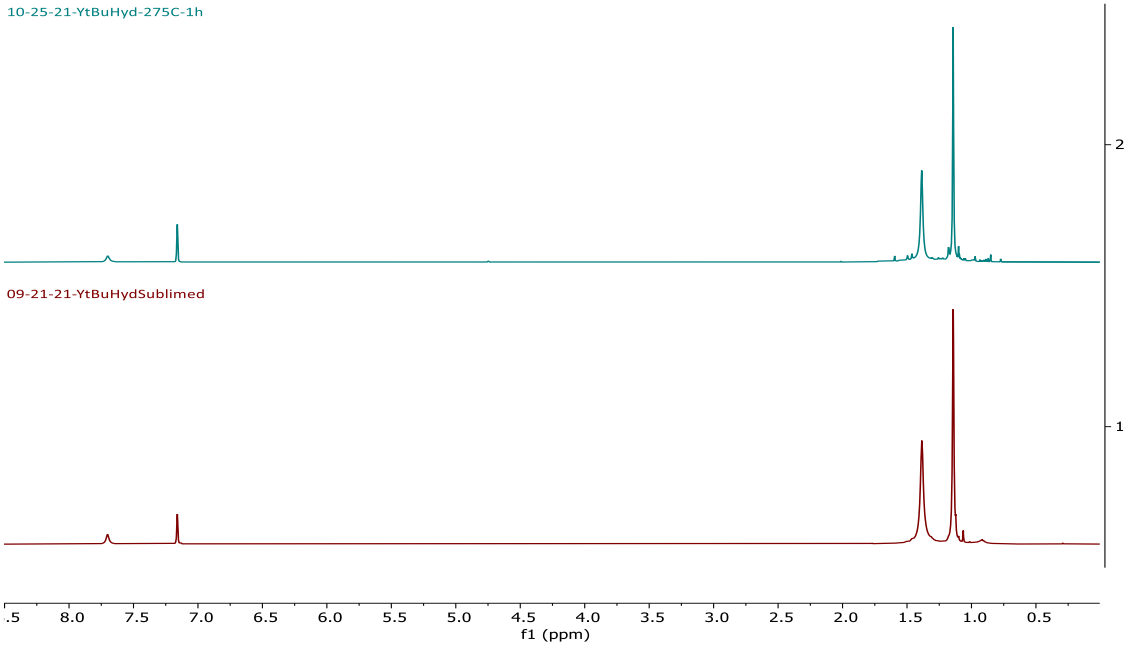

Figure 29. ^{1}H NMR spectra of **6** before and after heating for 24 h at 275 °C. The resonance at around δ 7.16 is from the benzene-d_6 solvent residual protons.

2.3 Conclusions

This chapter introduces a new class of lanthanide complexes containing *tert*-butyl hydrazonate ligands. La, Pr, Gd, Er, Lu, and Y complexes were synthesized to cover the whole lanthanide series, representing early, mid, and late lanthanides. Complexes **1-6** sublimed in the 155-185 °C temperature range at 0.5 Torr, demonstrating their volatility at reduced pressure. TGA traces of **1-6** show single-step weight losses with <12% non-volatile residues, indicating clean volatilization and minimal thermal decomposition. Compared to lanthanide *β*-diketonate complexes, which are stable in air, **1-6** are reactive in the presence of air and moisture, suggesting their possible reactivity towards mild oxygen sources such as water for the ALD of Ln_2O_3. Further, the absence of unwanted atoms such as Si and F in the *tert*-butyl hydrazone ligand backbone is another advantage of these precursors, because complexes with Si containing ligands can incorporate Si impurities into the films and complexes with F containing ligands can form HF that can etch the films and reactor parts.[129, 130] Hence, these lanthanide *tert*-butyl complexes will be a

useful addition to the limited volatile lanthanide ALD precursors available so far to obtain high purity Ln_2O_3 films with enhanced electrical properties.

2.4 Experimental Section

General Consideration

All reactions and manipulations for the synthesis of lanthanide complexes included in this chapter were carried out under an inert atmosphere of argon or nitrogen using standard Schlenk and glove box techniques, except that the hydrazone ligand was synthesized under ambient atmosphere. Tetrahydrofuran and diethyl ether were distilled from purple colored solutions of sodium/benzophenone ketyl under an argon atmosphere and hexane was distilled from sodium under an argon atmosphere. Anhydrous powders of $LaCl_3$, $GdCl_3$, $ErCl_3$, $LuCl_3$, and YCl_3 were purchased from Strem Chemicals, Inc. and anhydrous $PrCl_3$ was purchased from Sigma Aldrich and ProChem Inc. The anhydrous lanthanide chlorides were used as received. Potassium hydride (30 wt % dispersion in mineral oil) was purchased from Sigma Aldrich and was washed with hexane and dried under reduced pressure before use. *Tert*-butyl hydrazine hydrochloride and pinacolone were purchased from Across Organics, and SeO_2 was purchased from Sigma Aldrich. 3,3-Dimethyl-2-oxobutanal (*tert*-butyl glyoxal) was prepared following a published procedure, except that a neat reaction mixture of pinacolone and SeO_2 was refluxed for 24 h without adding methanol and water as solvents.[183]

^1H and $^{13}C\{^1H\}$ NMR spectra were recorded using an Agilent 400 MHz spectrometer at 400 and 100 MHz, respectively, in benzene-d_6 or toluene-d_8. NMR spectra were referenced to the residual proton and carbon resonances of the corresponding NMR solvent. All spectra were recorded at ambient temperature unless otherwise noted. Infrared spectra were acquired using a Shimadzu IRTracer-100 spectrometer. Melting points and solid-state thermal decomposition

temperatures were determined using an Electrothermal-IA-9000 series digital melting point apparatus with a heating rate of 5 °C/min. TGA data were obtained using a TA Instruments TGA Q-50 apparatus inside an argon-filled glovebox with a ramp of 10 °C/min. Elemental analyses were performed by Midwest Micro Lab, LLC., Indianapolis, IN.

Preparation of La($^{t\mathrm{Bu}}$Hyd)$_3$ (1).

A 100 mL Schlenk flask was charged with a magnetic stir bar, *tert*-butyl hydrazone LH$^{t\mathrm{Bu}}$Hyd (0.800 g, 4.34 mmol), and tetrahydrofuran (30 mL). The stirred solution at ambient temperature was slowly added to solid KH (0.209 g, 5.21 mmol), and the resulting mixture was stirred for 18 h at ambient temperature. The KL$^{t\mathrm{Bu}}$Hyd solution was then slowly added dropwise to a stirred suspension of anhydrous $LaCl_3$ (0.355 g, 1.45 mmol) in tetrahydrofuran (10 mL). The resultant bright yellow solution was stirred for 24 h at ambient temperature. The volatile components were removed under reduced pressure, and resultant yellow powder was subjected to sublimation at 185 °C/0.5 Torr to afford **1** as a yellow solid (0.309, 31%): mp 259 °C dec; ^{1}H NMR (benzene-d_6, 23 °C, δ) 7.65 (s, 3 H, C*H*), 1.42 (s, 27 H, NC(C*H*$_3$)$_3$), 1.13 (s, 27 H, C(C*H*$_3$)$_3$); ^{13}C{^{1}H} NMR (benzene-d_6, 23 °C, δ) 175.12 (s, *C*-O), 119.29 (s, *C*HN), 64.43 (s, N*C*(CH$_3$)$_3$), 38.60 (s, C*C*(CH$_3$)$_3$), 28.99 (s, NC(*C*H$_3$)$_3$), 28.45 (s, CC(*C*H$_3$)$_3$); IR (cm^{-1}) 2959 (m), 1481 (m), 1329 (s), 1179 (s), 1101 (s), 982 (m), 876 (m), 799 (m), 500 (s). Anal. Calcd for $C_{30}H_{57}LaN_6O_3$: C, 52.32; H, 8.34; N, 12.20. Found: C, 51.08; H, 7.70; N, 11.62.

Preparation of Pr($^{t\mathrm{Bu}}$Hyd)$_3$ (2).

In a fashion similar to the preparation of **1**, treatment of anhydrous $PrCl_3$ (0.358 g, 1.45 mmol) with a solution of KL$^{t\mathrm{Bu}}$Hyd (prepared from LH$^{t\mathrm{Bu}}$Hyd (0.800 g, 4.34 mmol) and KH (0.209 g, 5.21 mmol) in tetrahydrofuran (30 mL)) afforded **2** (0.377 g, 38%) as an orange solid upon sublimation at 170 °C/0.5 Torr: mp 293 °C dec; IR (cm^{-1}) 2959 (m), 1510 (m), 1333 (s), 1179 (s),

1101 (s), 984 (m), 876 (m), 799 (m), 501 (s), 422 (m). Anal. Calcd for $C_{30}H_{57}PrN_6O_3$: C, 52.16; H, 8.32; N, 12.16. Found: C, 51.46; H, 8.28; N, 11.98.

Preparation of Gd($^{t\mathrm{Bu}}$Hyd)$_3$ (3).

In a fashion similar to the preparation of **1**, treatment of anhydrous $GdCl_3$ (0.381 g, 1.45 mmol) with a solution of KL$^{t\mathrm{Bu}}$Hyd (prepared from LH$^{t\mathrm{Bu}}$Hyd (0.800 g, 4.34 mmol) and KH (0.209 g, 5.21 mmol) in tetrahydrofuran (30 mL)) afforded **3** (0.428 g, 42%) as an orange solid upon sublimation at 160 °C/0.5 Torr: mp 290 °C dec; IR (cm^{-1}) 2959 (m), 1512 (m), 1327 (s), 1179 (s), 1105 (s), 984 (m), 878 (w), 800 (m), 799 (m), 503 (s), 405 (m). Anal. Calcd for $C_{30}H_{57}GdN_6O_3$: C, 50.96; H, 8.12; N, 11.89. Found: C, 50.47; H, 8.05; N, 11.58.

Preparation of Er($^{t\mathrm{Bu}}$Hyd)$_3$ (4).

In a fashion similar to the preparation of **1**, treatment of anhydrous $ErCl_3$ (0.396 g, 1.45 mmol) with a solution of KL$^{t\mathrm{Bu}}$Hyd (prepared from LH$^{t\mathrm{Bu}}$Hyd (0.800 g, 4.34 mmol) and KH (0.209 g, 5.21 mmol) in tetrahydrofuran (30 mL)) afforded **4** (0.432 g, 42%) as an orange solid upon sublimation at 165 °C/0.5 Torr: mp 289 °C dec; IR (cm^{-1}) 2959 (m), 1514 (m), 1331 (s), 1177 (s), 1107 (s), 984 (m), 879 (w), 802 (m), 505 (s), 401 (m). Anal. Calcd for $C_{30}H_{57}ErN_6O_3$: C, 50.25; H, 8.01; N, 11.72. Found: C, 49.99; H, 8.00; N, 11.49.

Preparation of Lu($^{t\mathrm{Bu}}$Hyd)$_3$ (5).

In a fashion similar to the preparation of **1**, treatment of anhydrous $LuCl_3$ (0.407 g, 1.45 mmol) with a solution of KL$^{t\mathrm{Bu}}$Hyd (prepared from LH$^{t\mathrm{Bu}}$Hyd (0.800 g, 4.34 mmol) and KH (0.209 g, 5.21 mmol) in tetrahydrofuran (30 mL)) afforded **5** (0.374 g, 36%) as a yellow solid upon sublimation at 170 °C/0.5 Torr: mp 276 °C dec; ^{1}H NMR (benzene-d_6, 23 °C, δ) 7.67 (s, 3 H, C*H*), 1.39 (s, 27 H, NC(C*H*$_3$)$_3$), 1.14 (s, 27 H, C(C*H*$_3$)$_3$); ^{13}C{^{1}H} NMR (benzene-d_6, 23 °C, δ) 176.75 (s, *C*-O), 119.22 (s, *C*HN), 65.08 (s, N*C*(CH$_3$)$_3$), 38.66 (s, C*C*(CH$_3$)$_3$), 29.39 (s, NC(*C*H$_3$)$_3$), 28.38

(s, CC(CH_3)$_3$); IR (cm^{-1}) 2965 (m), 1514 (m), 1333 (s), 1173 (s), 1109 (m), 982 (w), 879 (w), 804 (m), 505 (s), 405 (m). Anal. Calcd for $C_{30}H_{57}LuN_6O_3$: C, 49.71; H, 7.93; N, 11.60. Found: C, 49.54; H, 7.89; N, 11.30.

Preparation of Y($^{t\mathrm{Bu}}$Hyd)$_3$ (6).

In a fashion similar to the preparation of **1**, treatment of anhydrous YCl_3 (0.283 g, 1.45 mmol) with a solution of KL$^{t\mathrm{Bu}}$Hyd (prepared from LH$^{t\mathrm{Bu}}$Hyd (0.800 g, 4.34 mmol) and KH (0.209 g, 5.21 mmol) in tetrahydrofuran (30 mL)) afforded **6** (0.386 g, 42%) as a yellow solid upon sublimation at 155 °C/0.5 Torr: mp 285 °C dec; ^{1}H NMR (benzene-d_6, 23 °C, δ) 7.70 (s, 3 H, C*H*), 1.38 (s, 27 H, NC(CH_3)$_3$) 1.14 (s, 27 H, C(CH_3)$_3$; ^{13}C{^{1}H} NMR (benzene-d_6,23 °C, δ) 176.05 (s, *C*-O), 118.74 (s, *C*HN), 64.67 (s, N*C*(CH$_3$)$_3$), 38.65 (s, C*C*(CH$_3$)$_3$), 29.29 (s, NC(*C*H$_3$)$_3$), 28.38 (s, CC(*C*H$_3$)$_3$); IR (cm^{-1}) 2965 (m), 1508 (m), 1333 (s), 1175 (s), 1086 (s), 1009 (m), 877 (w), 804 (m), 507 (s), 405 (m). Anal. Calcd for $C_{30}H_{57}YN_6O_3$: C, 56.41; H, 8.99; N, 13.16. Found: C, 55.94; H, 9.01; N, 12.93.

CHAPTER 3

Evaluation of Volatility and Thermal Stability in Monomeric and Dimeric Lanthanide(III) Complexes Containing Enaminolate Ligands

Reprinted (adapted) with permission from Jayakodiarachchi, N.; Evans, P. G.; Ward, C. L.; and Winter, C. H. *Organometallics* **2021**, *40,* 1270−1283.

3.1 Introduction

Binary lanthanide(III) oxide thin films and ternary analogs containing other metal ions are of interest for applications as high dielectric constant (κ) materials in transistors and memory devices, since their κ values can be higher than currently used materials such as HfO_2.[38, 184-187] Oxide thin films of the formula $LnAlO_3$ (Ln = La, Pr, Nd) grown on single crystal $SrTiO_3$ substrates have been studied in detail for their two-dimensional electron gas properties, where the electrical resistivities at the $LnAlO_3/SrTiO_3$ interfaces are very low.[52, 54, 57, 188-191] For both high-κ dielectric applications and two-dimensional electron gas materials, the interfaces between the oxide materials and the substrates need to be atomically smooth for optimum performance. [52, 54, 57, 188-192] Other applications of lanthanide-containing oxides include luminescent materials, optical materials, materials for quantum computing, superconductors, catalysis, and materials for advanced microelectronics.[193-199] While many methods can be used to deposit oxide films, atomic layer deposition (ALD) can afford films that are atomically smooth, in addition to providing Angstrom-level thickness control and perfect conformal coverage in high aspect ratio nanoscale features.[79, 161] Increasingly, synthesis and crystallization methods are taking advantage of three-dimensional nanoscale features in which conformality and thickness uniformity of ALD are advantageous. The scope of applications of oxides created using ALD includes a range of optical and electronic devices incorporating nanoscale crystalline features.[200] The conformality and precision are possible because of the self-limited growth mechanism in ALD.

ALD requires chemical precursors that are volatile, thermally stable at the deposition temperatures, and highly reactive toward a second reagent.[79, 161] Many different ligands have been employed to create volatile and thermally stable lanthanide precursors for film growth by ALD.[89] Ligands in previously reported precursors have included *β*-diketonate, [89, 201-203] cyclopentadienyl and substituted cyclopentadienyl,[89, 59, 126, 204, 205] bis(trimethylsilyl)amide,[89] alkoxide,[89,206] and amidinates and guanidinates.[89, 103, 125, 207, 208] Additionally, volatile lanthanide complexes containing N,N-dimethylaminodiboranate ligands have been recently reported, but have not been tested in ALD growth.[209-211] Currently available lanthanide precursors have exhibited several problems in ALD growth, including the low reactivity of *β*-diketonate precursors towards water as a co-reactant, substrate oxidation when using ozone as a co-reactant, low thermal stability, and lack of true self-limited growth. As a result, there is ongoing need for volatile, thermally stable lanthanide precursors for ALD that address these issues.

In envisioning new structures that might lead to new volatile and thermally stable lanthanide complexes, we focused our attention on bidentate ligands that contain very strong bonds within the ligand backbones to promote high thermal stability. Enaminolate ligands L^1-L^3 (scheme 2) are obtained upon deprotonation of *β*-amino ketones and contain a strong central C=C bond that should contribute high thermal stability to lanthanide complexes. The *tert*-butyl group is present to confer steric bulk, which should disfavor solvent coordination and may encourage monomeric complex formation. Moreover, there is only one acidic hydrogen atom site for enolate formation in ketones of the formula $tBuC(=O)CH_2NR_2$, thereby eliminating the formation of isomeric enolates. Finally, the *β*-amino ketone $PhC(=O)CH_2NMe_2$ has a p*K*a value of 23.55,[212] which ensures that the deprotonated enaminolates will react rapidly with water (p*K*a 14.00 or 15.7).[101] This situation should allow use of water as a co-reactant in ALD processes. There have been

several reports of structurally characterized K, Ni, Zr, Zn, and P complexes containing enaminolate ligands that are similar to L^1-L^3.[213-216] No lanthanide complexes containing enaminolate ligands have been described to date. Herein, we report the synthesis, structure, volatility, and thermal stabilities of lanthanide complexes containing enaminolate ligands.

Scheme 2. Enaminolate ligands used in this study.

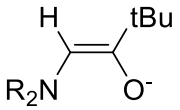

L^1, $NR_2 = NMe_2$
L^2, $NR_2 = N(CH_2)_4$
L^3, $NR_2 = N(CH_2)_5$

3.2 Results and Discussion

Synthesis of New Complexes.

The *β*-amino ketones L^1H-L^3H were prepared upon treatment of the bromomethyl ketone with secondary amines, as described in the experimental section. The potassium salts of L^1-L^3 (Scheme 2) were prepared by treatment of L^1H-L^3H with one equivalent of KH in THF. These freshly prepared solutions were treated directly with anhydrous $LnCl_3$ to afford complexes **7**-**21**, as outlined in equations 4-8 and in the experimental section.

Initial synthetic efforts explored the treatment of $PrCl_3$, $ErCl_3$, and YCl_3 with three equivalents of KL^1 in THF. Workup, followed by crystallization from diethyl ether, led to slow crystallization of the L^1H adducts **7**-**9** in low, variable yields, apparently through partial hydrolysis and then formation of highly crystalline **7**-**9**. After obtaining X-ray crystal structures (vide infra), the syntheses of **7**-**9** were optimized by treatment of KL^1 (3 equiv) and L^1H (1 equiv) with $LnCl_3$ (Ln = Pr, Er, Y) to afford **7**-**9** in 30-36% yields after crystallization from diethyl ether (equation 4). The yields of **7**-**9** are low because of their high solubilities in diethyl ether. By contrast, sublimation of the crude reaction mixtures obtained upon treatment of KL^1 (3 equiv) with $LnCl_3$

(Ln = Pr, Er, Y) at 100 to 120 °C (0.5 Torr) afforded the homoleptic complexes **10**-**12** in 36-56% yields. Complexes **10**-**12** were also accessed upon sublimation of **7**-**9** in 42-52% yields, with loss of coordinated L^1H, as shown in equation 5. Sublimation of **7**-**9** was also accompanied by some decomposition to afford non-volatile residues, thus leading to the moderate yields. The remaining complexes **13**-**21** were obtained in 37-56% yields upon treatment of KL^1, KL^2, or KL^3 (3 equiv) with $LnCl_3$ (Ln = La, Pr, Nd, Er, Lu, Y) in THF (eqs 4-8), followed by sublimation at the temperatures described in the experimental procedures.

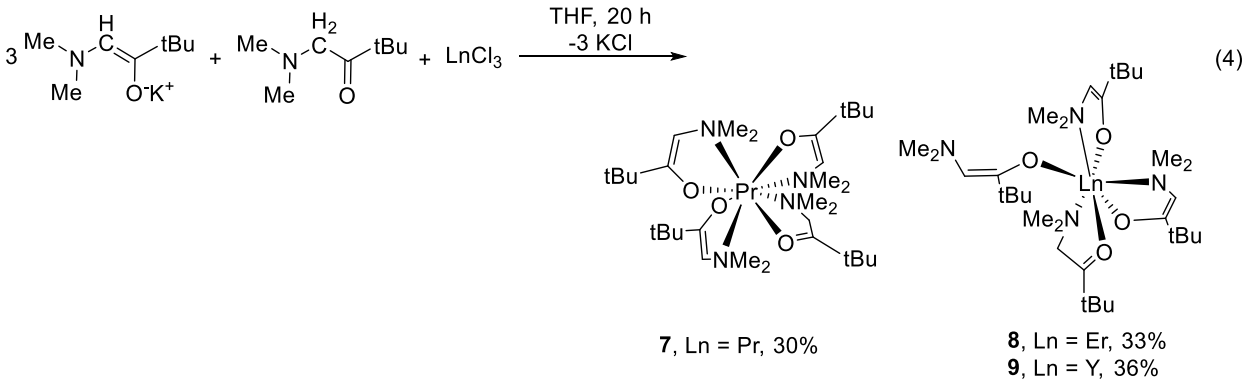

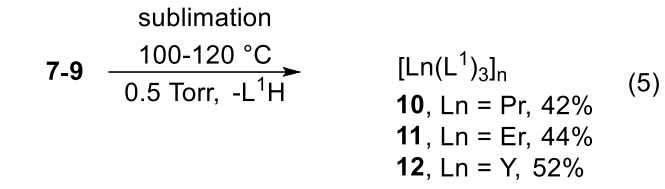

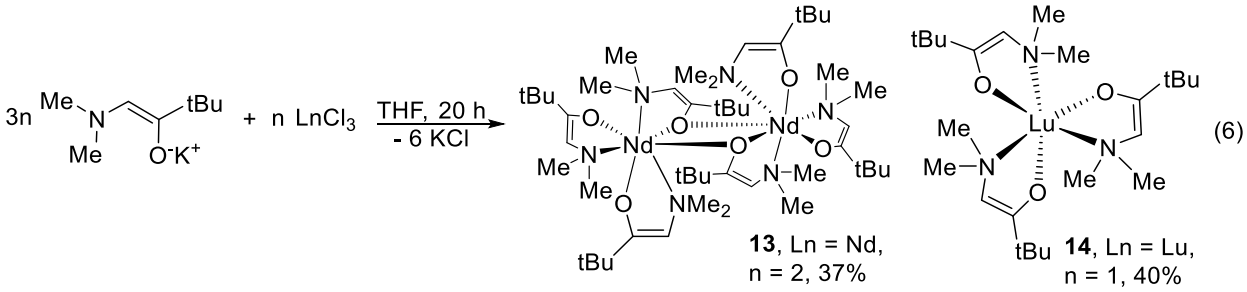

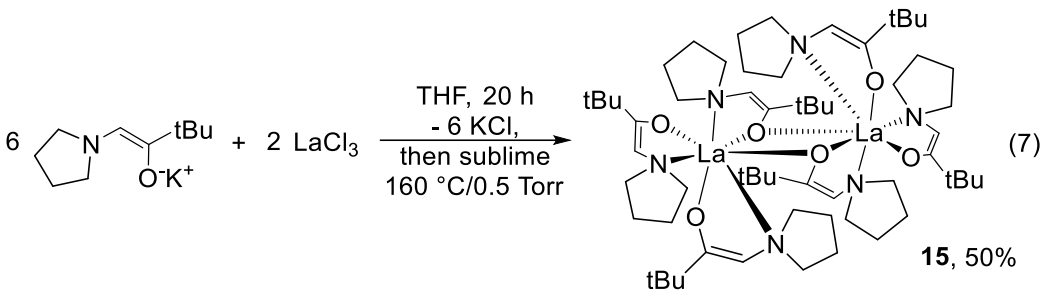

(7)

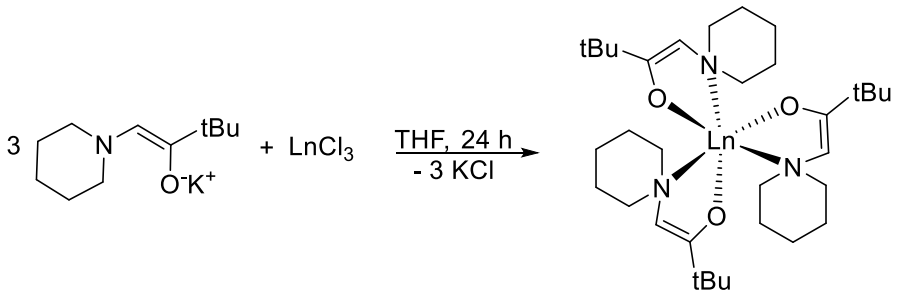

(8)

Complexes **7**-**21** were characterized by a combination of X-ray crystallography (**7**-**9**, **13**-**15**, **19**, **20**), ^{1}H nuclear magnetic resonance (NMR) spectroscopy (**9**, **12**, **14**-**16**, **20**, **21**), ^{13}C{^{1}H} NMR spectroscopy (**9**, **12**, **14**-**16**, **20**, **21**), infrared spectroscopy, melting points, and CHN microanalyses. The X-ray crystal structures are presented below and the line drawings in equations 4-8 represent the molecular structures that were observed for **7**-**9**, **13**-**15**, **19,** and **20**. ^{1}H and ^{13}C{^{1}H} NMR spectra of the diamagnetic La, Lu, and Y complexes **9**, **12**, **14**-**16**, **20,** and **21** at ambient temperature in benzene-d_6 showed the expected resonances for L^1, L^1H, L^2, or L^3 ligands, as appropriate (Figure 30 to 36). The L^1-L^3 ligands in **9**, **12**, **14**-**16**, **20,** and **21** share common vinyl C-H and *tBu* moieties. The vinyl C-H resonances were observed as a sharp singlet in each spectrum between δ 4.55 and 4.96. The *tBu* groups appeared as a sharp singlet in each spectrum in the narrow range of δ 1.24 to 1.29. In the ^{1}H NMR spectrum of **9** at ambient temperature, separate resonances were observed for the L^1 and L^1H ligands, in a 3:1 ratio (Figure 30).

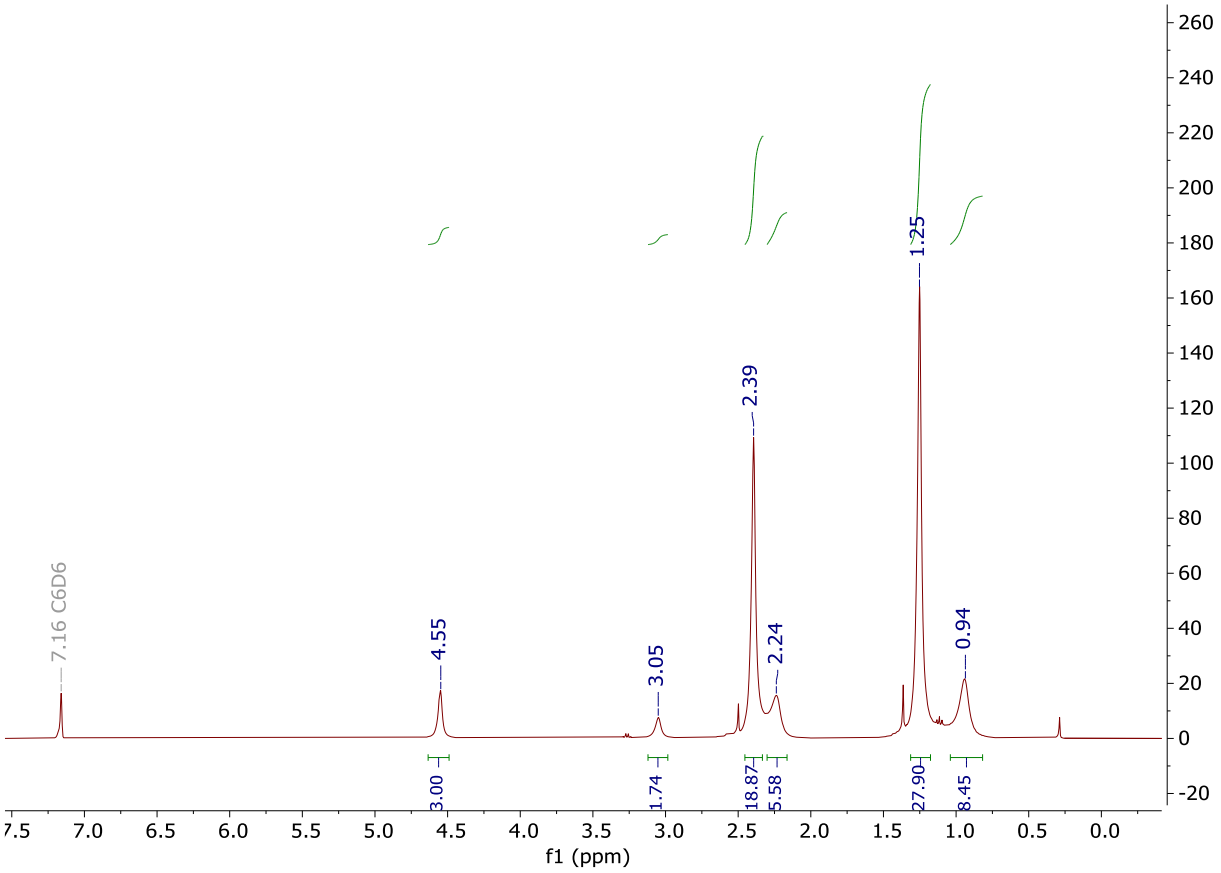

Figure 30. ^{1}H NMR Spectrum of **9** in benzene-d_6 at 23 °C.

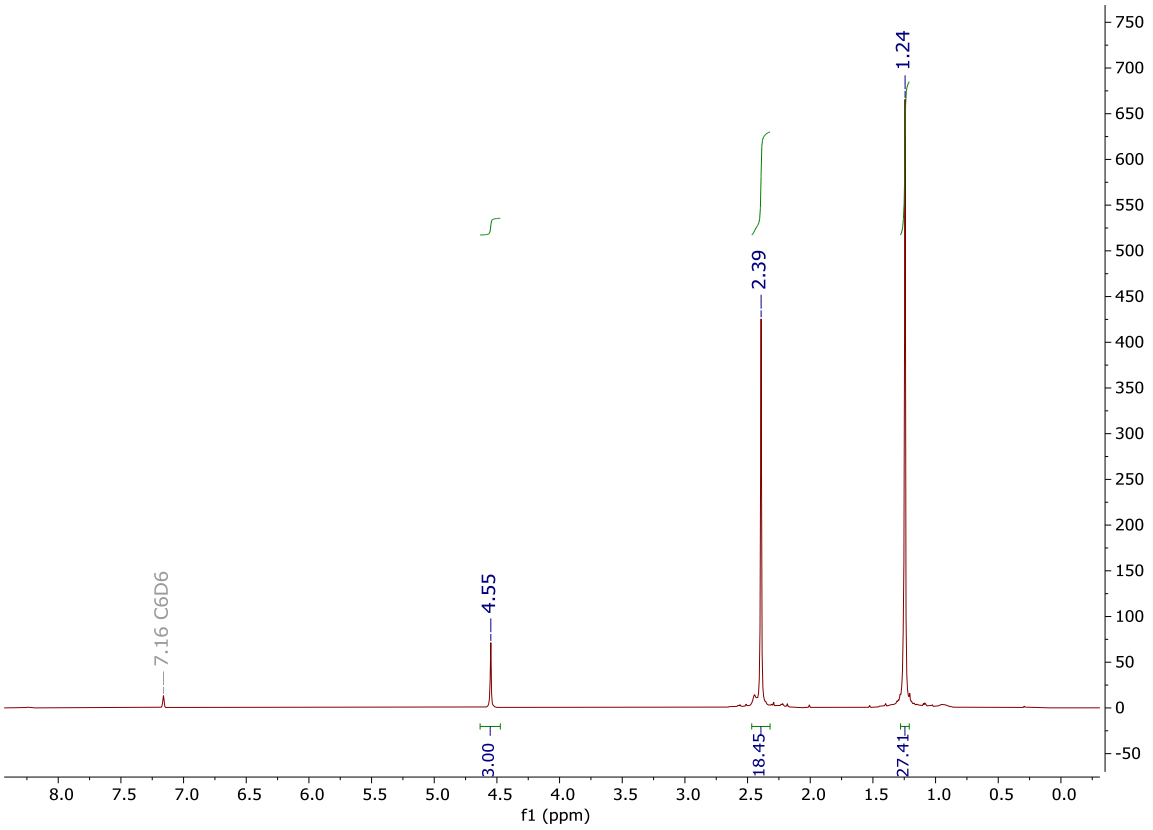

Figure 31.[1]H NMR Spectrum of **12** in benzene-d_6 at 23 °C.

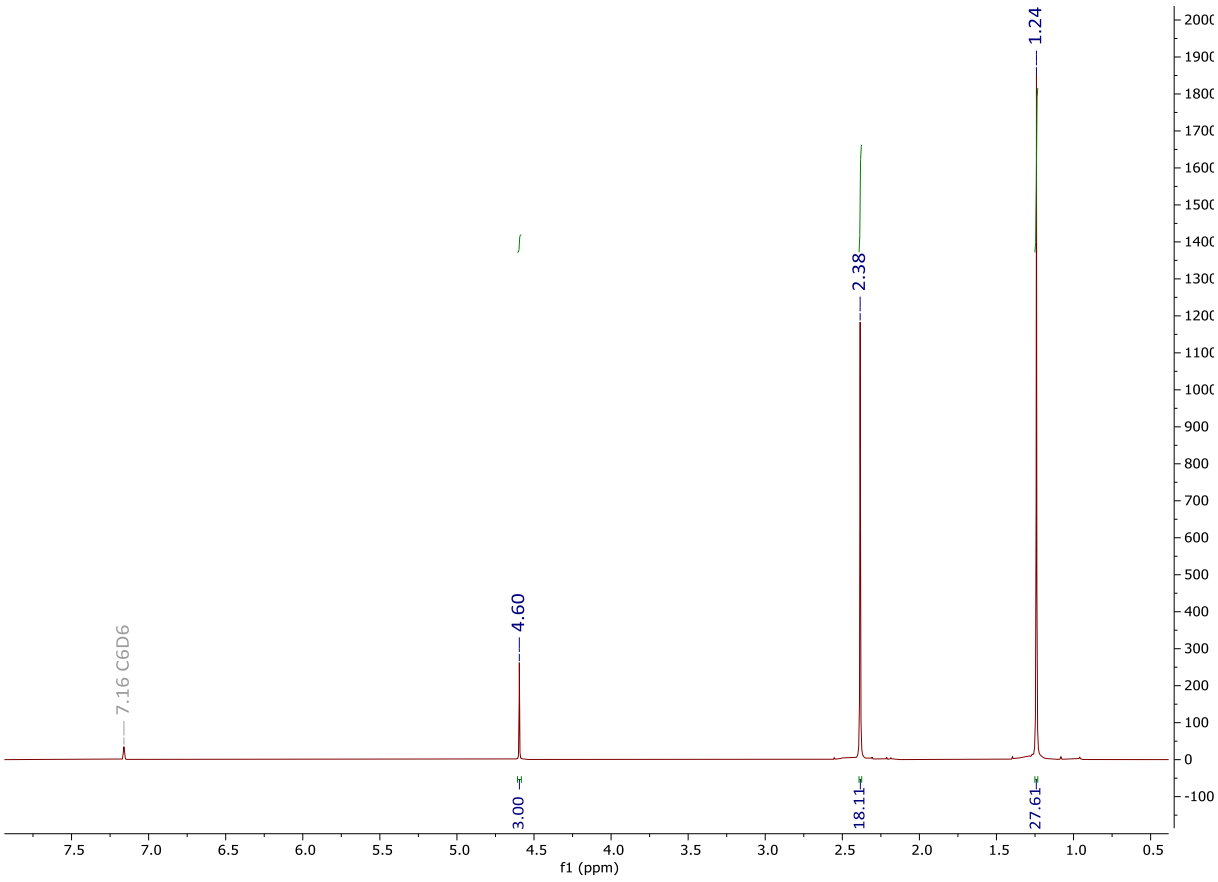

Figure 32. ^{1}H NMR Spectrum of **14** in benzene-d_6 at 23 °C.

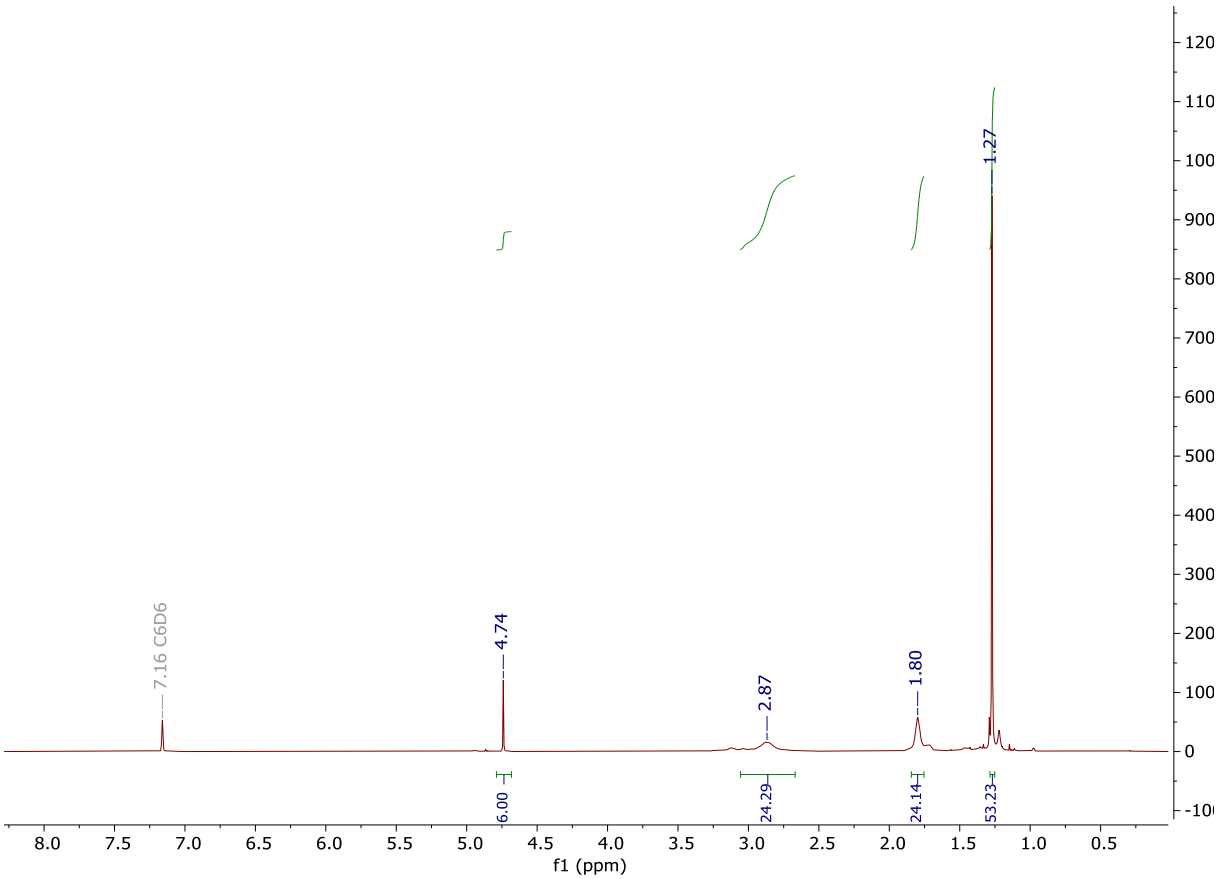

Figure 33. ^{1}H NMR Spectrum of **15** in benzene-d_6 at 23 °C.

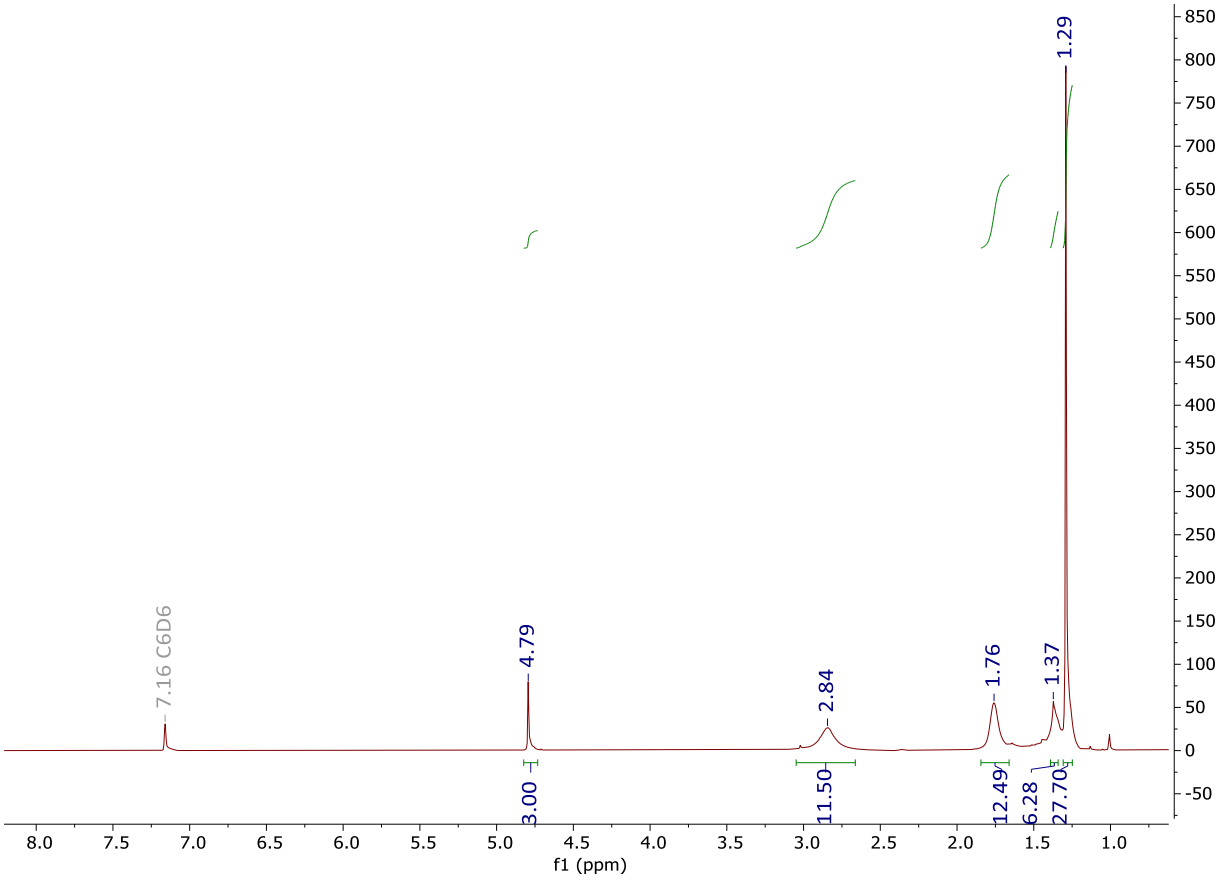

Figure 34. ^{1}H NMR Spectrum of **16** in benzene-d_6 at 23 °C.

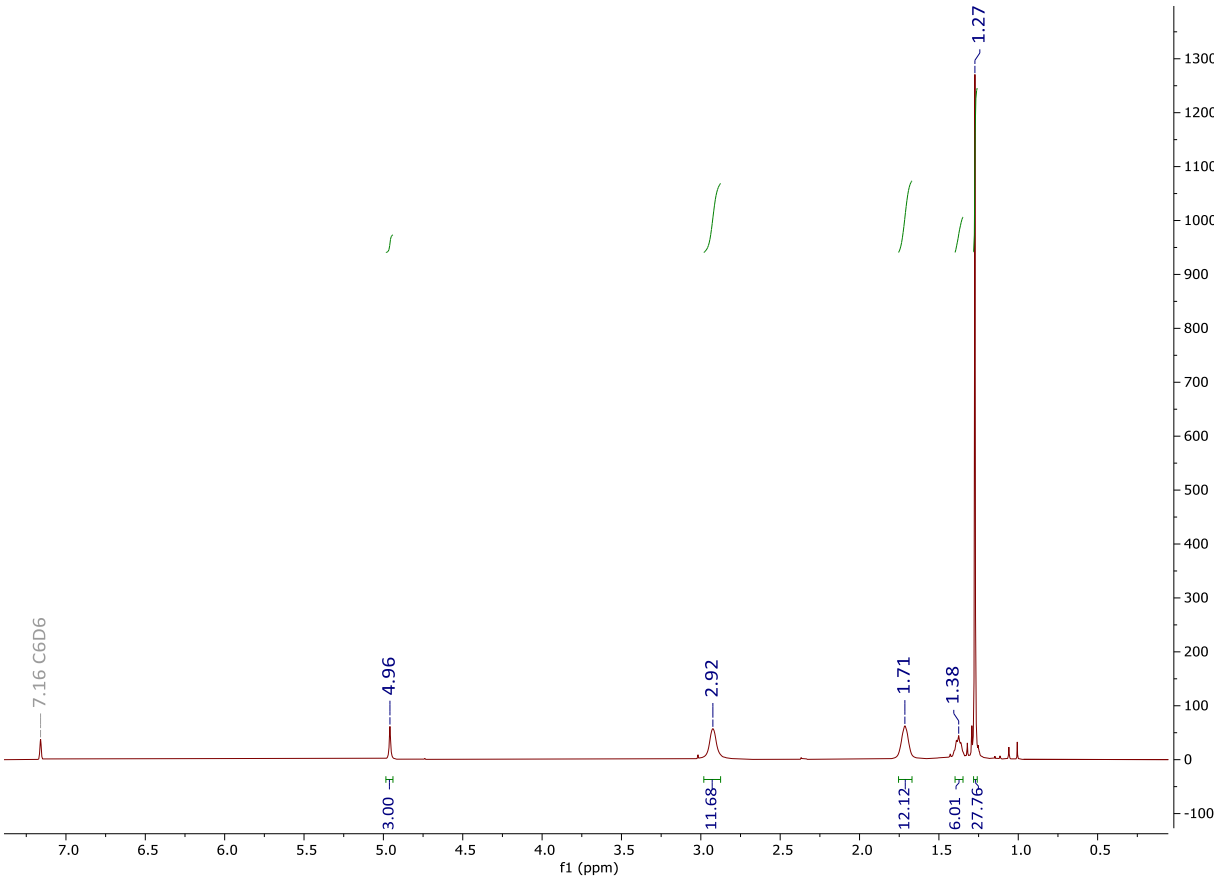

Figure 35. ^{1}H NMR Spectrum of **20** in benzene-d_6 at 23 °C.

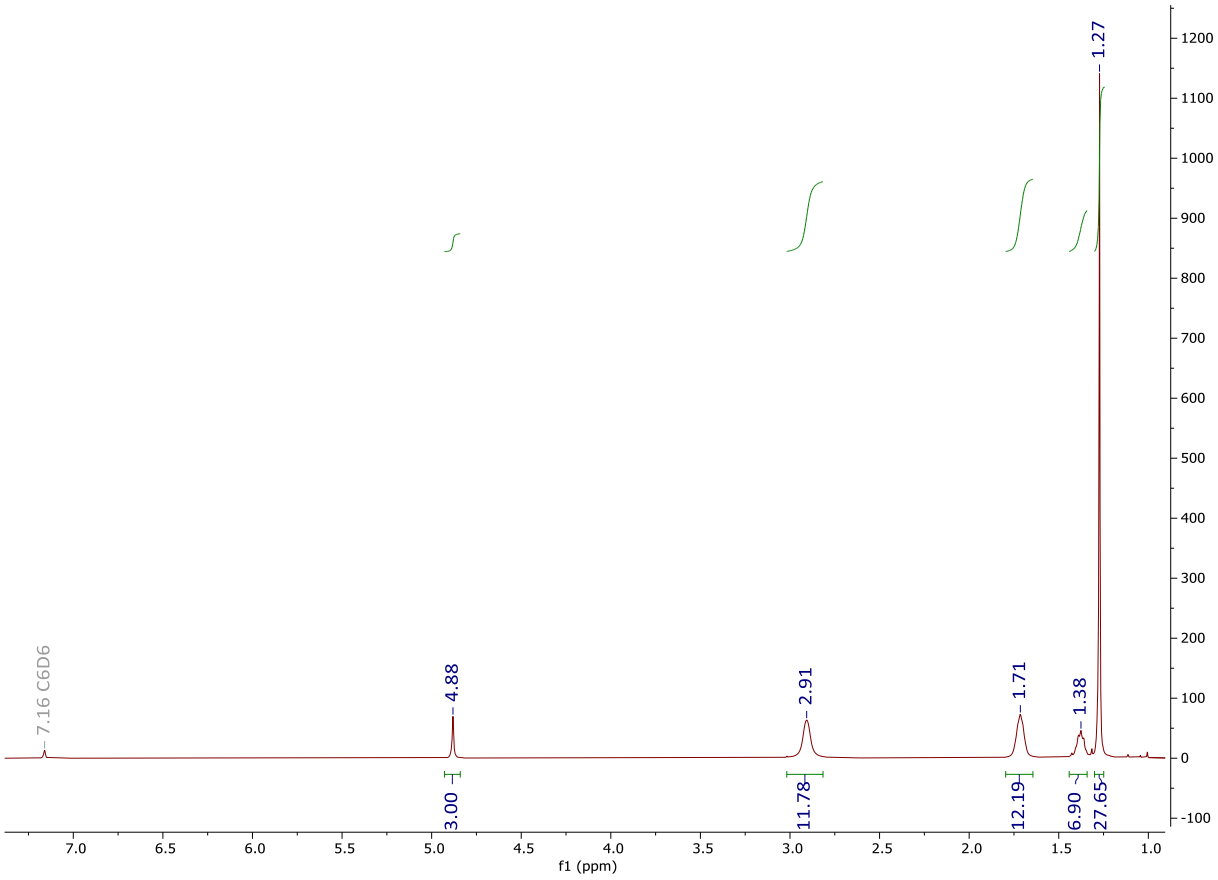

Figure 36. ^{1}H NMR Spectrum of **21** in benzene-d_6 at 23 °C.

The variable temperature ^{1}H NMR spectra of **9** are described below. The infrared spectra of **7-21** each show a medium to strong absorption between 1575 and 1618 cm^{-1} for the L^1, L^2, or L^3 C=C bonds and C-O single bond stretches between 1325 to 1337 cm^{-1}. For comparison, the C=O double bond stretches in L^1H-L^3H appear at 1717-1718 cm^{-1} and L^1H-L^3H do not show C=C or C-O single bond stretches. In addition to the L^1 C-O single bond stretches, the C=O double bond stretches for the coordinated L^1H ligands in **7-9** appear between 1678 and 1686 cm^{-1} (Figure 37). Complexes **7-16** and **18-21** gave H and N microanalysis values that were within ±0.4% of the calculated values. However, the C microanalysis values for **7-13**, **15**, **16**, and **18-21** were up to a few percent lower than the calculated values, despite multiple sample submissions and use of combustion enhancement. The lower C values in microanalyses might arise from refractory metal carbide formation. Several previous reports have reported similar low C microanalysis values in lanthanide complexes containing oxygen-based ligands.[139, 174, 175, 217, 218] Despite multiple submissions, **17** did not afford CHN microanalysis values that were within ±0.4% of the calculated values. To understand the solution structures of adducts **7-9**, variable temperature ^{1}H NMR spectra

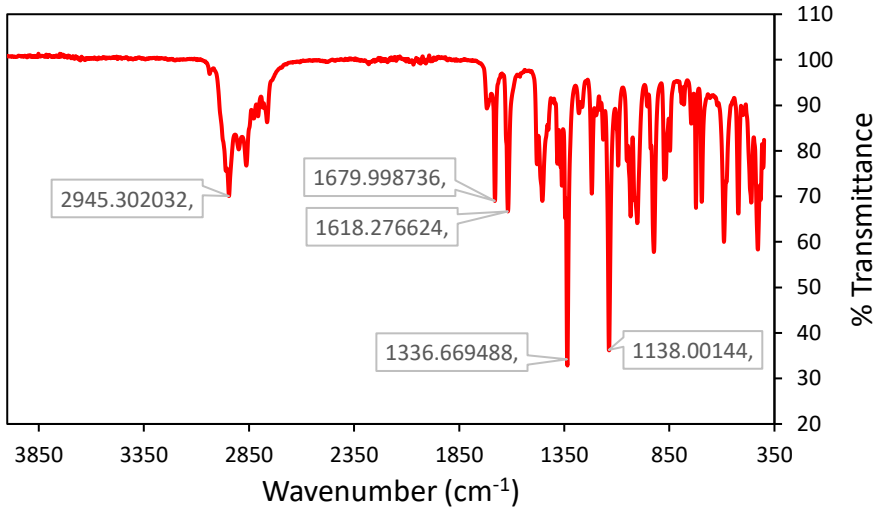

Figure 37. Infrared Spectrum of **7**.

were recorded for the diamagnetic Y complexes **9** and **12** in toluene-d_8. The behavior of **12** was determined first (Figure 38). At 20 °C, sharp singlets were observed at δ 4.52 (C-H), 2.39 (NMe_2), and 1.20 (*tBu*). The ^{1}H NMR spectrum at 60 °C revealed sharp singlets at δ 4.52 (C-H), 2.40 (NMe_2), and 1.17 (*tBu*), which are essentially identical to the chemical shifts at 20 °C. Upon cooling to -60 °C, the spectrum was very similar to those at 20 and 60 °C, with chemical shifts at δ 4.55 (C-H), 2.36 (NMe_2), and 1.31 (*tBu*). The solid state structure of **12** was not determined because X-ray quality crystals could not be grown, but it is likely a monomer (by analogy with **14**) or a dimer (by analogy with **13**). Observation of sharp resonances between −60 and +60 °C and minor chemical shift changes with temperature are consistent with either a monomeric structure or a dimeric structure where the exchange rate between the bridging and terminal L^1 ligands is rapid on the NMR time scale.

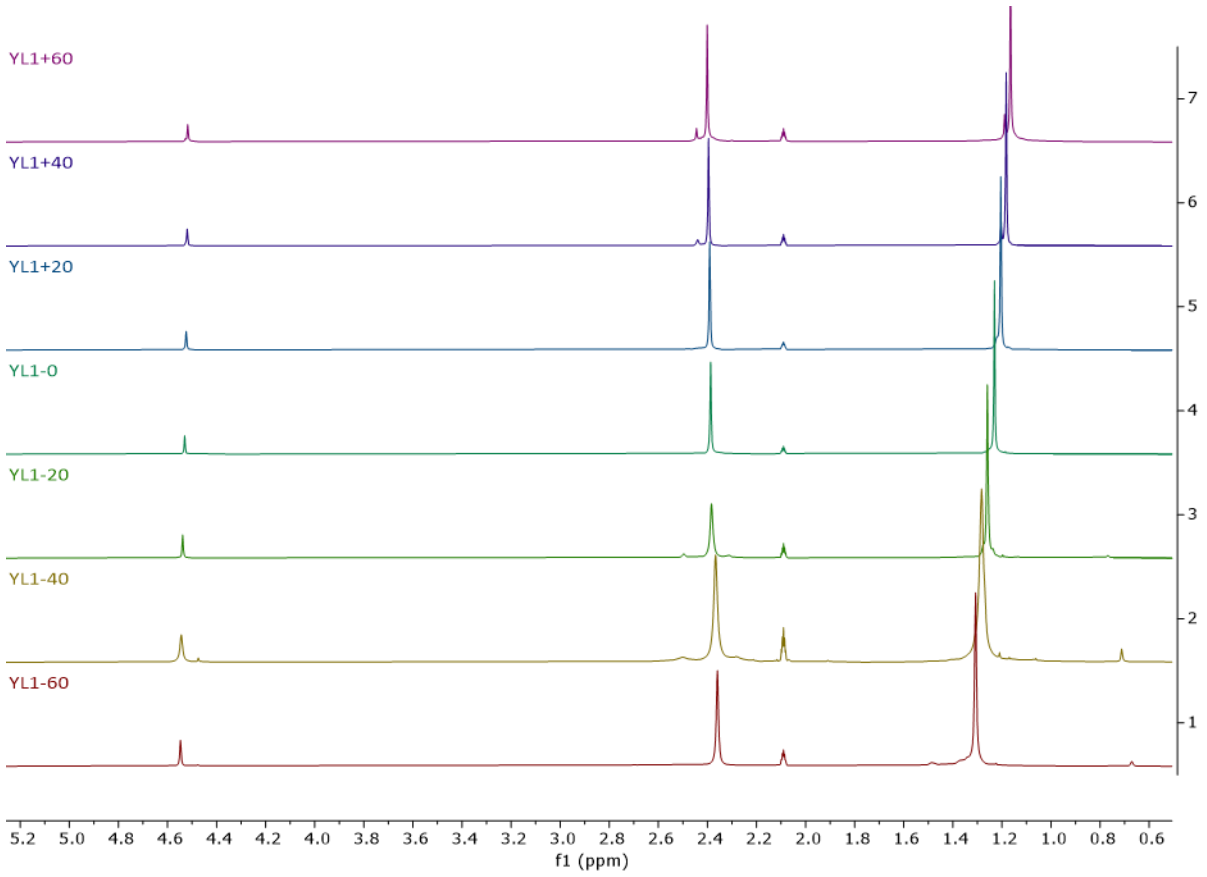

Figure 38. Variable Temperature ^{1}H NMR Spectra of **12** in toluene-d_8. The resonance at around δ 2.09 is from toluene-d_8 solvent residual protons.

The variable-temperature ^{1}H NMR spectra of **9** were explored next (Figure 39). At 20 °C in toluene-d_8, **9** exhibited resonances at δ 4.52 (C−H), 2.39 (NMe_2), and 1.21 (*tBu*) for the L^1 ligands and at δ 3.01 (CH_2), 2.21 (NMe_2), and 0.95 (*tBu*) for the L^1H ligand. The L^1:L^1H integration was 3:1. Interestingly, the L^1 resonances in **9** at 20°C had exactly the same chemical shifts as for **12** at the same temperature. Moreover, the chemical shifts of pure L^1H in toluene-d_8 at 20 °C (δ 2.98 (CH_2), 2.16 (NMe_2), and 0.96 (*tBu*)) were very close to those exhibited by the L^1H ligand in **9** at 20 °C. These chemical shift values suggest that L^1H is weakly bound to the Y ion in **9** at 20 °C and that the equilibrium **9** ↔ **12** +L^1H lies to the right under these conditions. Increasing the temperature to 60 °C led to resonances at δ 4.52 (C−H), 2.40 (NMe_2), and 1.16 (*tBu*) for the L^1 ligands and at δ 2.99 (CH_2), 2.18 (NMe_2), and 0.98 (*tBu*) for the L^1H ligand. These chemical shifts

are essentially identical to those observed at 20 °C. The ^{1}H NMR spectrum at −60 °C consisted of three *tert*-butyl resonances at δ 1.49, 1.37, and 0.67, in a 2:1:1 ratio. The resonance at δ 0.67 arose from the L^{1}H ligand and showed an upfield shift of δ 0.28 upon cooling from +20 to −60 °C. The resonances at δ 1.49 and 1.37 existed as a single resonance at δ 1.39 at −40 °C and coalesced into two resonances at −50 °C. The NMe_2 resonances at −60 °C consisted of a sharp resonance at δ 2.68 and broad resonances at δ 2.60 and 2.44. These resonances overlapped too much to allow an accurate relative integration. The enolate C−H resonance appeared at −60 °C as a slightly asymmetric singlet at δ 4.63. When these data are taken together, the ^{1}H NMR spectrum of **9** at −60 °C is consistent with the solid-state structure described below and shown in eq 4, since this structure would exhibit three *tert*-butyl resonances in a 2:1:1 ratio. When the temperature was increased to above −50 °C, the rate of exchange between the κ^2-L^{1} and κ^1-L^{1} ligands became rapid on the NMR time scale and only a single *tert*-butyl resonance was observed for the L^{1} ligands. The L^{1}H ligand retains separate resonances over the −60 to +60 °C temperature range.

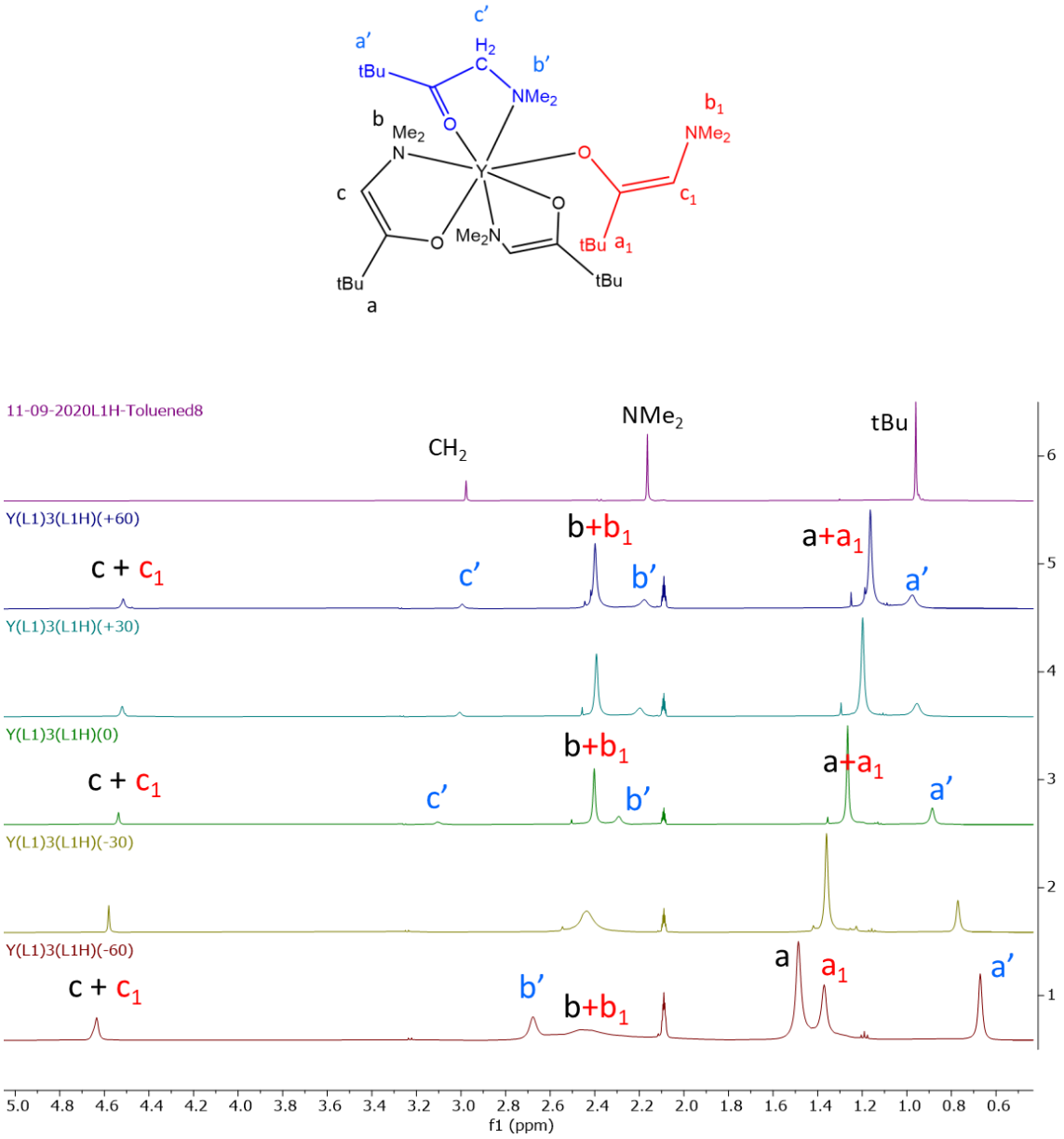

Figure 39. Variable Temperature ^{1}H NMR Spectra of **9** in toluene-d_8. The resonances at around δ 2.09 is from toluene-d_8 solvent residual protons.

3.3 X-ray Crystal Structures

X-ray crystal structures were determined for **7-9**, **13-15**, **19**, and **20** to understand the molecular structures (Figure 40 to 46). The data for **15** were of lower resolution and are not discussed herein but were sufficient to establish the overall dimeric structure and ligand connectivity. Crystallographic data are summarized in Tables 4 and 5.

Table 4. Crystal Data and Data Collection Parameters for **7-9** and **13-14**.

	7	**8**	**9**	**13**
Formula	$C_{32}H_{65}N_4O_4Pr$	$C_{32}H_{65}ErN_4O_4$	$C_{32}H_{65}N_4O_4Y$	$C_{48}H_{96}N_6Nd_2O_6$
FW	710.79	737.14	658.79	1141.78
space group	C2/c	$P2_1/n$	$P2_1/n$	$P2_1/n$
a (Å)	30.5956(19)	11.7598(4)	11.7855(5)	11.1563(12)
b (Å)	17.0132(8)	16.0023(6)	16.0308(6)	12.9057(14)
c (Å)	15.9490(8)	20.3810(7)	20.3944(7)	39.627(4)
V(Å^3)	7542.1(7)	3721.5(2)	3737.0(2)	5655.8(10)
Z	8	4	4	4
Temp (K)	100(1)	100(1)	100(1)	100(1)
ρ_{calcd} (g cm^{-3})	1.252	1.316	1.171	1.341
λ (Å)	0.71073	0.71073	0.71073	0.71073
μ (mm^{-1})	1.328	2.291	1.597	1.862
R(F)(%)	4.58	2.67	3.26	6.89
wR(F)(%)	11.60	5.27	7.09	11.81

$R(F) = \sum \| Fo | - | Fc \| / \sum | Fo |$; $wR(F) = [\sum w(Fo^2 - Fc^2)^2 / \sum w(Fo^2)^2]^{1/2}$ for $I > 2\sigma(I)$.

Table 5. Crystal Data and Data Collection Parameters for **14**, **15**, **19** and **20.**

	14	**15**	**19**	**20**
Formula	$C_{24}H_{48}LuN_3O_3$	$C_{60}H_{108}La_2N_6O_6$	$C_{33}H_{60}ErN_3O_3$	$C_{33}H_{60}LuN_3O_3$
FW	601.62	1287.34	714.10	721.81
space group	$P2_1/n$	C2/c	$P2_1$	$P2_1$
a (Å)	9.7510(6)	21.6485(9)	9.8447(7)	9.8745(5)
b (Å)	21.5897(13)	16.9744(8)	15.9493(11)	15.8943(8)
c (Å)	14.4442(8)	17.2690(8)	11.6776(8)	11.6918(6)
V(Å^3)	2889.8(3)	6316.3(5)	1729.8(2)	1732.24(15)
Z	4	4	2	2
Temp (K)	100(1)	100(1)	100(1)	100(1)
ρ_{calcd} (g cm^{-3})	1.383	1.1.354	1.371	1.384
λ (Å)	0.71073	0.71073	0.71073	0.71073
μ (mm^{-1})	3.441	1.385	2.460	2.883
R(F)(%)	2.16	9.27	4.10	2.94
wR(F)(%)	4.40	27.87	9.03	6.14
Flack Parameter			-0.012(9)	0.022(13)

$R(F) = \sum \| Fo | - | Fc \| / \sum | Fo |$; $wR(F) = [\sum w(Fo^2 - Fc^2)^2 / \sum w(Fo^2)^2]^{1/2}$ for $I > 2\sigma(I)$.

Figures 40−46 show representative perspective views of **7-9**, **13-15**, **19**, and **20**, respectively, as well as selected bond lengths and angles. Single crystals of sufficient quality for structure determinations could not be obtained for **10-12**, **16-18**, and **21**. Complex **7** crystallizes as an eight-coordinate monomer with three κ^2-L^1 ligands and one κ^2-L^1H ligand bonded to the Pr ion

(Figure 40). The κ^2-L^1 ligands are characterized by Pr−O bond distances of 2.332(3), 2.309(3), and 2.44(1) Å and Pr−N bond lengths of 2.846(4), 2.739(4), and 2.84(2) Å. The longer Pr−O1C distance may reflect steric crowding about the eight coordinate Pr ion. In contrast, the Pr−N distances fall within a narrow range of 2.74−2.85 Å. The κ^2-L^1H ligand has Pr−O and Pr−N bond lengths of 2.43(1) and 2.79(2) Å. The Pr−O4 distance is identical with that of Pr−O3 within experimental error. The Pr−N bond length is within the same range as those observed for the κ^2-L^1 ligands. The enolate C−C distances within the ligand backbones allow unambiguous assignment of the L^1 and L^1H ligands. Thus, the C1A−C2A, C1B−C2B, and C1C−C2C bond lengths are 1.339(7), 1.352(7), and 1.38(8) Å, respectively, and are close to the value expected for a C−C double bond (~1.32 Å). In contrast, the C1D−C2D distance is 1.47(2) Å, which is in the range for a C−C single bond.

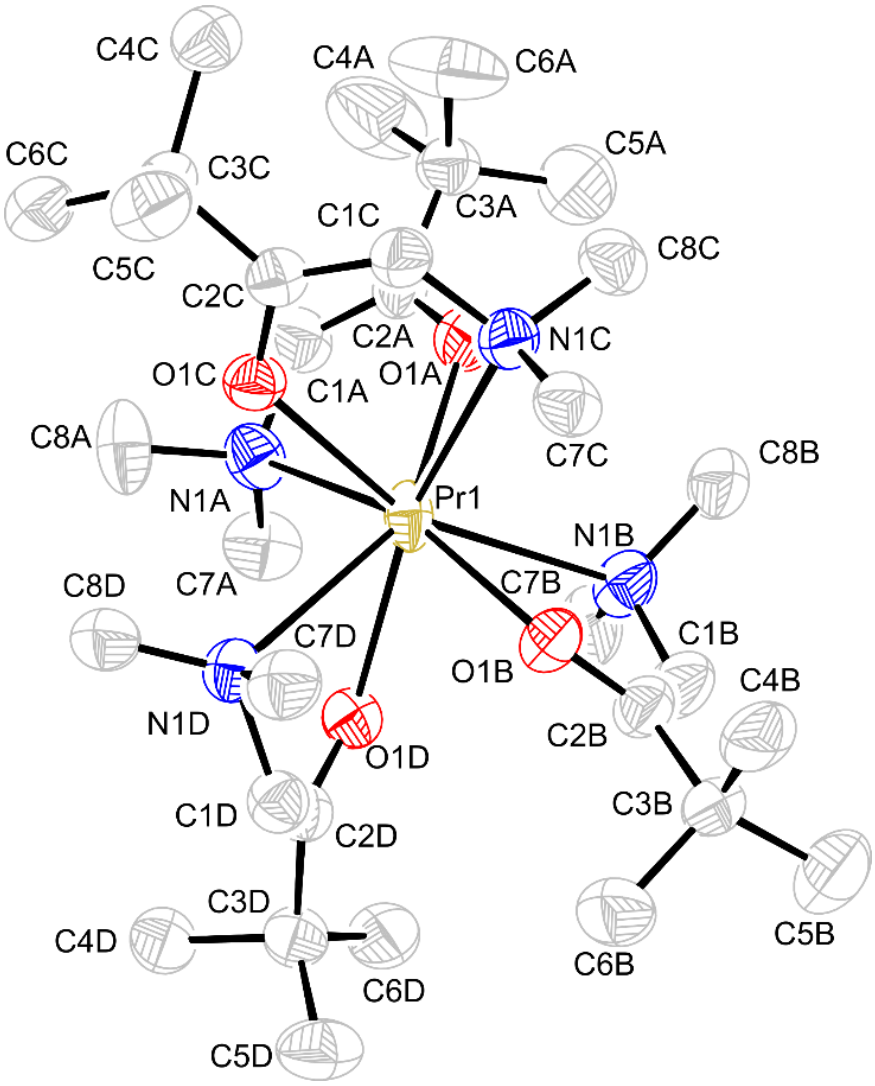

Figure 40. Perspective view of **7** with thermal ellipsoids at the 50% level.

Selected bond lengths (Å) and angles (°): Pr-O1A 2.332(3), Pr-O1B 2.309(3), Pr-O1C 2.44(1), Pr-O1D 2.43(1), Pr-N1A 2.846(4), Pr-N1B 2.739(4), Pr-N1C 2.84(2), Pr-N1D 2.79(2), C1A-C2A 1.339(7), C1B-C2B 1.352(7), C1C-C2C 1.38(2), C1D-C2D 1.47(2); O1A-Pr-O1B 124.9(1), O1A-Pr-O1C 88.6(3), O1A-Pr-O1D 124.9(3), O1B-Pr-O1C 116.6(3), O1B-Pr-O1D 83.2(3), O1C-Pr-O1D 122.6(5), O1A-Pr-N1A 63.6(1), O1A-Pr-N1B 75.7(1), O1A-Pr-N1C 75.7(4), O1A-Pr-N1D 153.3(3), O1B-Pr-N1A 156.6(1), O1B-Pr-N1B 64.7(1), O1B-Pr-N1C 75.7(3), O1B-Pr-N1D 79.5(3), O1C-Pr-N1A 83.5(3), O1C-Pr-N1B 159.2(3), O1C-Pr-N1C 61.8(4), O1C-Pr-N1D 68.9(4), O1D-Pr-N1A 75.4(3), O1D-Pr-N1B 78.0(3), O1D-Pr-N1C 157.1(4), O1D-Pr-N1D 62.6(4), N1A-Pr-N1B 101.1(1), N1A-Pr-N1C 100.5(4), N1A-Pr-N1D 98.5(3), N1B-Pr-N2C 100.5(4), N1B-Pr-N2D 129.3(3), N1C-Pr-N1D 104.1(5).

Complex **8** crystallizes as a seven-coordinate monomer that contains two κ^2-L^1 ligands, one oxygen-bound κ^1-L^1 ligand, and one κ^2-L^1H ligand (Figure 41). The lower coordination number of **8**, in comparison to **7**, is consistent with the smaller ionic radius of the Er^{3+} ion (0.890 Å) relative to the Pr^{3+} ion (0.990 Å).[38] The *tert*-butyl and dimethylamino groups are anti with respect to each other across the enolate C=C bond in the κ^1-L^1 ligand. The κ^2-L^1 ligands have Er−O bond distances of 2.183(2) and 2.200(2) Å and Er−N bond distances of 2.559(2) and 2.619(2) Å. The κ^1-L^1 ligand has an Er−O distance of 2.121(2) Å and is shorter than the related distances for the κ^2-L^1 ligands because of lower steric interactions. The Er−N distance is 4.594(2) Å for the κ^1-L^1 ligand and is clearly not a bonding interaction. The κ^2-L^1H ligand has Er−O and Er−N distances of 2.446(2) and 2.592(2) Å, respectively. The C−C distances within the L^1 ligand backbones are 1.331(4), 1.334(4), and 1.338(4) Å, which are consistent with C−C double bonds that are expected for enolate ligands. In contrast, the C−C distance for the L^1H ligand is 1.502(4) Å, which is in the range for a C−C single bond.

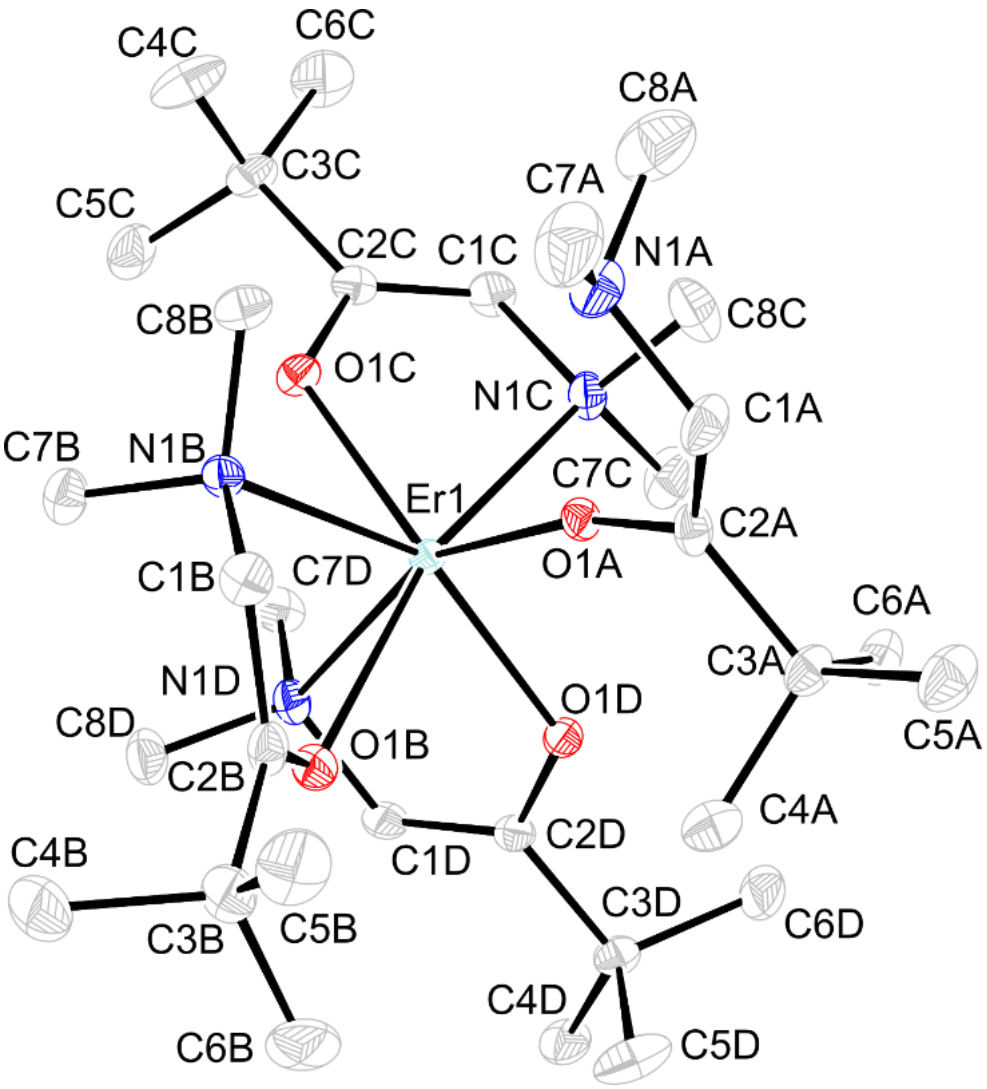

Figure 41. Perspective view of **8** with thermal ellipsoids at the 50% level.

Selected bond lengths (Å) and angles (°): Er-O1A 2.121(2), Er-O1B 2.446(2), Er-O1C 2.200(2), Er-O1D 2.183(2), Er-N1B 2.592(2), Er-N1C 2.559(2), Er-N1D 2.619(2), C1A-C2A 1.331(4), C1B-C2B 1.502(4), C1C-C2C 1.338(4), C1D-C2D 1.334(4); O1A-Er-O1B 86.63(7), O1A-Er-O1C 121.07(7), O1A-Er-O1D 91.62(7), O1B-Er-O1C 123.75(6), O1B-Er-O1D 81.52(6), O1C-Er-O1D 137.06(7), O1A-Er-N1B 80.89(7), O1A-Er-N1C 89.76(7), O1A-Er-N1D 157.31(7), O1B-Er-N1B 63.58(6), O1B-Er-N1C 166.00(7), O1B-Er-N1D 81.52(6), O1C-Er-N1D 137.06(7), N1B-Er-N1C 129.12(7), N1B-Er-N1D 107.65(7), N1C-Er-N1D 99.92(7).

Complex **9** adopts a seven-coordinate structure which is very similar to that of **8**, with two κ^2-L^1 ligands, one oxygen-bound κ^1-L^1 ligand, and one κ^2-L^1H ligand (Figure 42). Like **8**, the tertbutyl and dimethylamino groups are anti with respect to each other across the enolate C=C bond in the κ^1-L^1 ligand. The structural similarities of **8** and **9** are not surprising, given the similar ionic radii of Er^{3+} (0.890 Å) and Y^{3+} (0.900 Å).[58] The κ^2-L^1 ligands have Y−O bond distances of 2.206(1) and 2.187(1) Å and Y−N bond distances of 2.579(2) and 2.633(2) Å. The κ^1-L^1 ligand has a Y−O distance of 2.128(1) Å and is shorter than the related distances for the κ^2-L^1 ligands because of lower steric interactions. The nonbonding Y−N distance is 4.604(2) Å for the κ^1-L^1 ligand and is identical with the related value in **8**. The κ^2-L^1H ligand has Y−O and Y−N distances of 2.457(1) and 2.612(2) Å, respectively. The C−C distances within the L^1 ligand backbones are 1.337(3), 1.335(3), and 1.335(3) Å, which are identical with the values in **8** and are consistent with C−C enolate double bonds. The C−C single bond distance for the L^1H ligand is 1.501(3) Å, which is identical with the values in **7** and **8**.

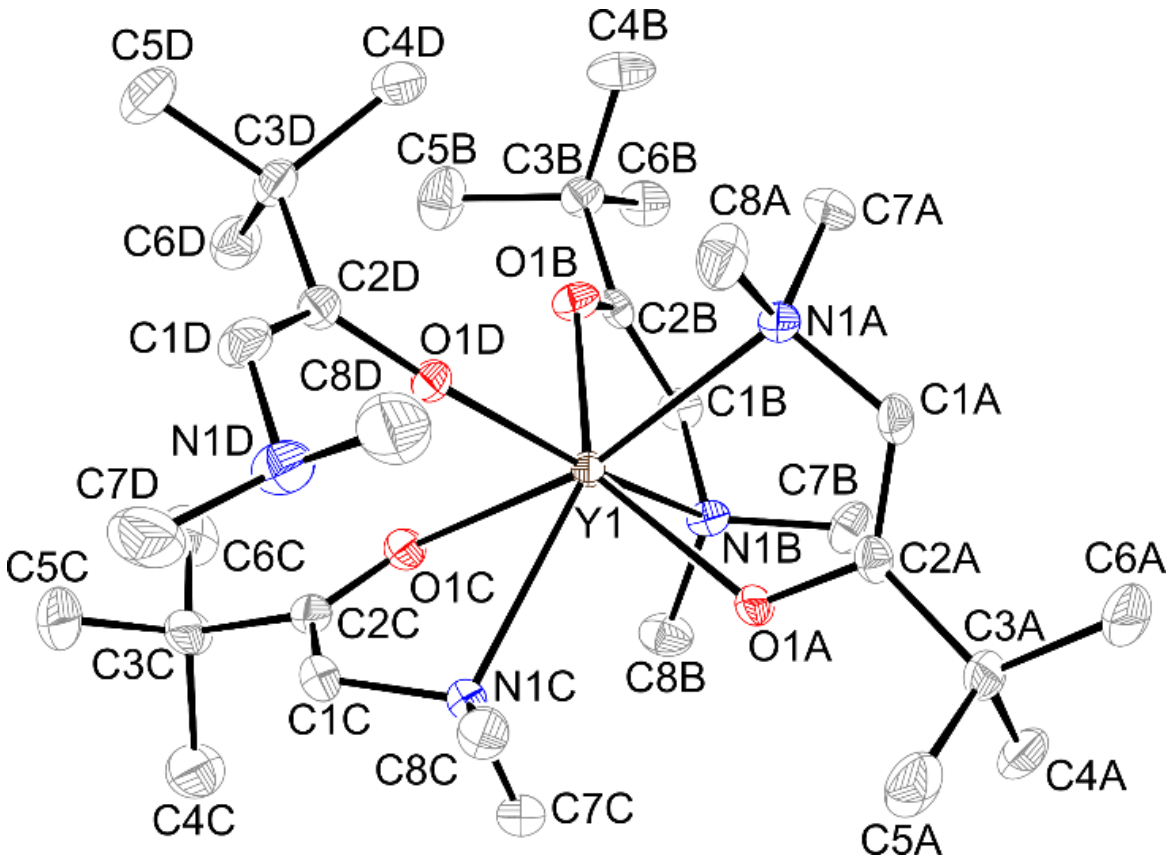

Figure 42. Perspective view of **9** with thermal ellipsoids at the 50% level.

Selected bond lengths (Å) and angles (deg): Y−O1A 2.206(1), Y−O1B 2.187(1), Y−O1C 2.457(1), Y−O1D 2.128(1), Y−N1A 2.579(2), Y−N1B 2.633(2), Y−N1C 2.612(2), C1A−C2A 1.337(3), C1B−C2B 1.335(3), C1C−C2C 1.501(3), C1D−C2D 1.335(3); O1A−Y−O1B 136.64(5), O1A−Y−O1C 123.80(5), O1A−Y−O1D 120.81(5), O1B−Y−O1C 81.93(5), O1B−Y−O1D 92.08(5), O1C− Y−O1D 86.70(5), O1A−Y−N1A 69.05(5), O1A−Y−N1B 81.88(5), O1A−Y−N1C 73.38(5), O1B−Y−N1A 85.07(6), O1B−Y−N1B 68.66(5), O1B−Y−N1C 144.84(5), O1C−Y−N1A 166.39(5), O1C−Y−N1B 79.01(5), O1C−Y−N1C 63.39(5), O1D−Y−N1A 89.78(6), O1D−Y−N1B 157.31(5), O1D−Y−N1C 80.88(5), N1A− Y−N1B 99.97(6), N1A−Y−N1C 128.95(6), N1B−Y−N1C 107.65(6).

Complex **13** adopts a dimeric structure which contains two L^1 ligands that bridge between the Nd ions through the oxygen atoms and then two κ^2-L^1 ligands that are bonded to each Nd ion (Figure 43). Each Nd ion is seven-coordinate. The Nd1−Nd2 distance is 4.0205(7) Å. The bridging L^1 ligands are characterized by Nd−O distances of 2.410(5), 2.470(6), 2.466(6), and 2.455(5) Å. These values are essentially identical, although the Nd1−O1 distance may differ slightly from the Nd1−O4 distance within experimental uncertainty. The Nd−N bond lengths associated with the bridging L^1 ligands are 2.595(7) and 2.610(7) Å. The Nd−O bond lengths for the terminal κ^2-L^1 ligands are 2.241(5), 2.256(8), 2.266(5), and 2.244(5) Å. These values are shorter than those for the bridging L^1 ligands, as expected. The Nd−N bond distances for the terminal κ^2-L^1 ligands are 2.852(9), 2.93(1), 2.819(7), and 2.848(7) Å. Interestingly, these values are 0.20−0.35 Å longer than those associated with the bridging L^1 ligands, which may arise from greater steric interactions upon forming Nd−N bonds in the terminal κ^2-L^1 ligands. The enolate C−C distances within the L^1 ligand backbones fall within the narrow range of 1.32(1)−1.33(2) Å, which are consistent with double bonds and are similar to the values in the L^1 ligands of **7-9**.

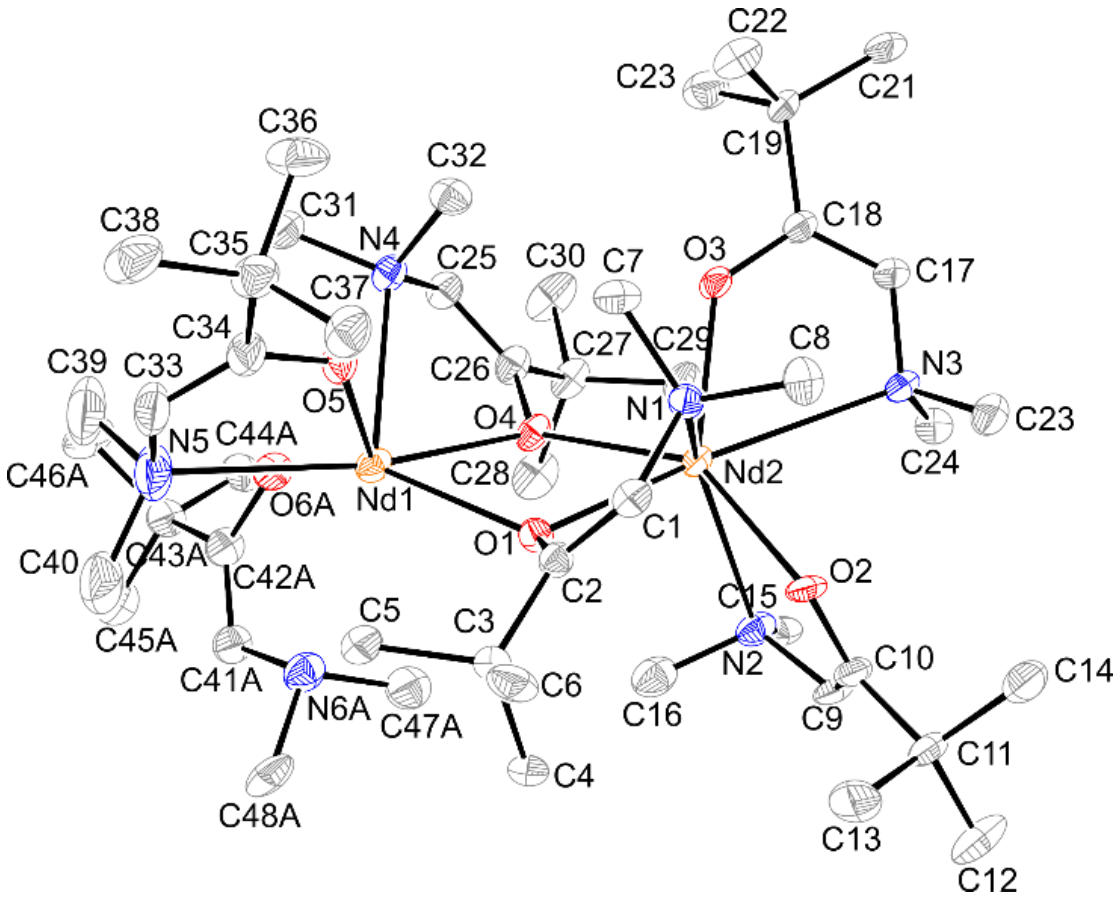

Figure 43. Perspective view of **13** with thermal ellipsoids at the 50% level.

Selected bond lengths (Å) and angles (deg): Nd1−Nd2 4.0205(7), Nd1−O1 2.410(5), Nd1−O4 2.470(6), Nd1−O5 2.241(5), Nd1−O6A 2.256(8), Nd2−O1 2.466(6), Nd2−O2 2.266(5), Nd2−O3 2.244(5), Nd2−O4 2.455(5), Nd1−N4 2.610(7), Nd1−N5 2.852(9), Nd1−N6A 2.928(2), Nd2−N1 2.595(7), Nd2−N2 2.819(7), Nd2−N3 2.848(7), C1−C2 1.33(1), C9−C10 1.32(1), C17−C18 1.33(1), C25−C26 1.33(1), C33−C34 1.33(1), C41A-C42A 1.33(2); O1−Nd1−O4 68.4(2), O1−Nd1−O5 88.0(2), O1−Nd1−O6A 94.3(2), O1−Nd2−O2 90.1(2), O1−Nd2− O3 118.3(2), O1−Nd2−O4 67.8(2), O4−Nd1−O5 119.8(2), O4− Nd1−O6A 92.9(3), O5−Nd1−O6A 75.4(3), O1−Nd2−O2 90.1(2), O1−Nd2−O3 118.3(2), O1−Nd2−O4 67.8(2), O2−Nd2−O3 129.9(2), O2−Nd2−O4 145.0(2), O3−Nd2−O4 85.1(2), Nd1− O1−Nd2 111.1(2), Nd1−O4−Nd2 109.4(2), O1−Nd1−N4 115.6(2), O1−Nd1−N5 125.8(2), O1−Nd1−N6A 94.3(2), O4− Nd1−N4 65.9(2), O4−Nd1−N5 165.7(2), O4−Nd1−N6A 103.3(3), O5−Nd1−N5 63.5(2), O5−Nd1−N6A 125.4(3), O6− Nd1−N6A 62.0(3), O1−Nd2−N1 65.5(2), O1−Nd2−N2 102.6(2), O1−Nd2−N3 164.4(2), N4−Nd1−N5 103.0(2), N4−Nd1−N6A 138.4(3), N5−Nd1−N6A 78.8(3), N1−Nd2−N2 140.8(2), N1− Nd2−N3 101.3(2), N2−Nd2−N3 82.1(2).

Complex **14** crystallizes as a six-coordinate monomeric complex that contains three κ^2-L^1 ligands (Figure 44). The geometry about the Lu ion is distorted octahedral. The lower coordination number in **14**, relative to **7-9** and **13**, arises from the smaller size of the Lu^{3+} ion (0.861 Å),[3] relative to the other ions. The Lu−O bond lengths are 2.115(2), 2.132(2), and 2.129(2) Å, which are identical within experimental uncertainty. The Lu−N bond distances are 2.459(2), 2.530(2), and 2.470(2) Å. The N atoms associated with the two shorter Lu−N bond lengths are mutually trans within the coordination sphere, whereas the N atom associated with the slightly longer Lu−N1B distance is trans to an O atom. The more strongly bonded O atom is likely responsible for the slight lengthening of the Lu−N1B bond. The enolate C−C distances within the L^1 backbones are 1.330(4), 1.336(4), and 1.336(4) Å. These values are consistent with C−C double bonds and are identical with the related values observed in the L^1 ligands of **7-9** and **13**.

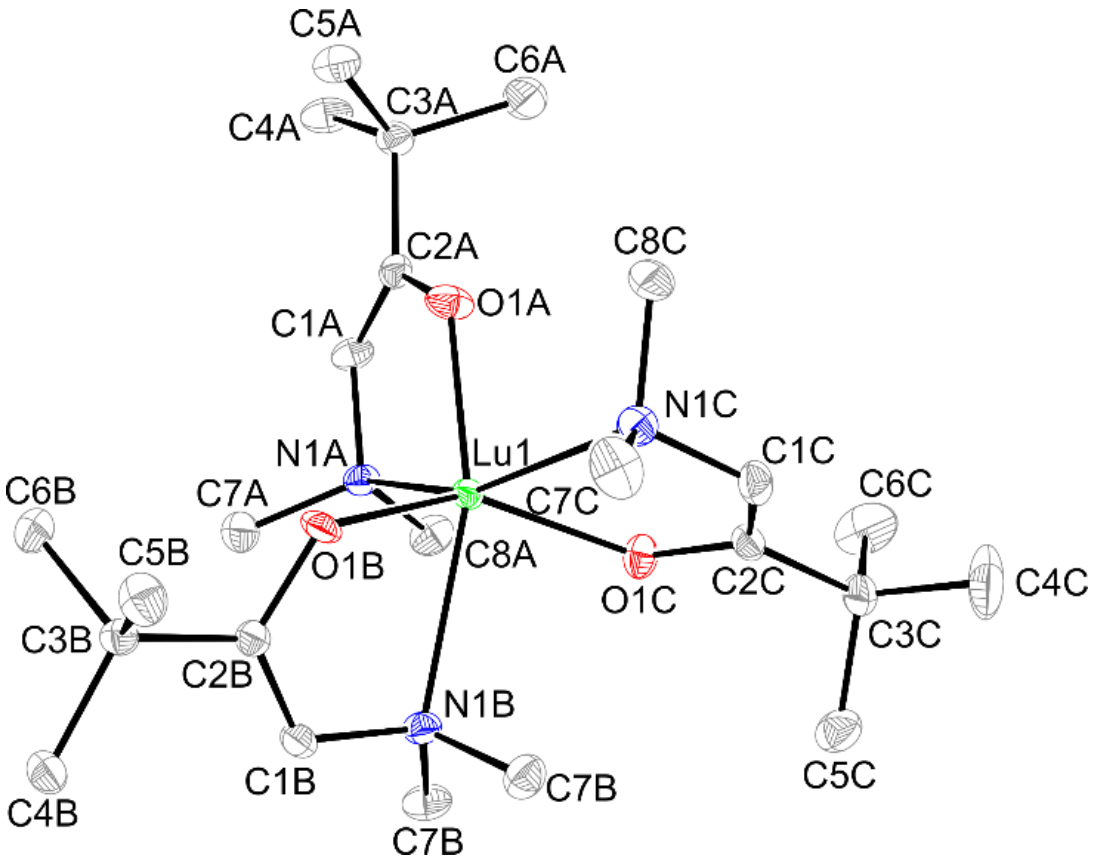

Figure 44. Perspective view of **14** with thermal ellipsoids at the 50% level.

Selected bond lengths (Å) and angles (deg): Lu−O1A 2.115(2), Lu−O1B 2.132(2), Lu−O1C 2.129(2), Lu−N1A 2.459(2), Lu−N1B 2.530(2), Lu−N1C 2.470(2), C1A-C2A 1.330(4), C1B−C2B 1.336(4), C1C−C2C 1.336(4); O1A−Lu−O1B 103.43(7), O1A− Lu−O1C 108.61(7), O1B−Lu−O1C 144.41(7), O1A−Lu−N1A 73.21(7), O1A−Lu−N1B 161.87(7), O1A−Lu−N1C 97.98(7), O1B−Lu−N1B 70.09(7), O1B−Lu−N1C 83.25(7), O1C−Lu− N1C 73.17(7), N1A−Lu−N1B 91.94(7), N1A−Lu−N1C 153.68(7), N1B−Lu−N1C 111.02(7).

Complex **19** crystallizes as a six-coordinate monomer that contains three κ^2-L^3 ligands (Figure 45). The geometry about the Er ion is distorted octahedral. The six-coordinate structure of **19** with three κ^2-L^3 ligands differs markedly from the seven coordinate structure of **8**, which contains two κ^2-L^1 ligands, one oxygen-bound κ^1-L^1 ligand, and one κ^2-L^1H ligand. The molecular structure of **19** is clearly affected strongly by the larger steric bulk of the piperidinyl substituent in L^3, in comparison to the dimethylamino group in L^1. The bulkier L^3 ligand blocks coordination of an L^3H ligand to the Er ion, but the L^3 ligand is not too bulky, and three κ^2-L^3 ligands can be accommodated. The Er−O bond lengths are 2.150(5), 2.141(5), and 2.141(5) Å, which are identical within experimental uncertainty. The Er−N bond distances are 2.545(6), 2.615(6), and 2.532(6) Å. As described for **14**, the N atoms associated with the two shorter Er−N bond lengths, Er−N1A and Er−N3, are mutually trans within the coordination sphere, whereas the N atom with the longer Er−N distance, Er−N2A, is trans to an O atom (O3). The stronger Er−O3 bond is likely responsible for the longer Er−N2A bond length. The enolate C−C distances within the L^3 ligand backbone are 1.315(9), 1.324(9), and 1.317(9) Å. These values are consistent with double bonds and are identical with the values for **7**-**9**, **13** and **14** within experimental uncertainty.

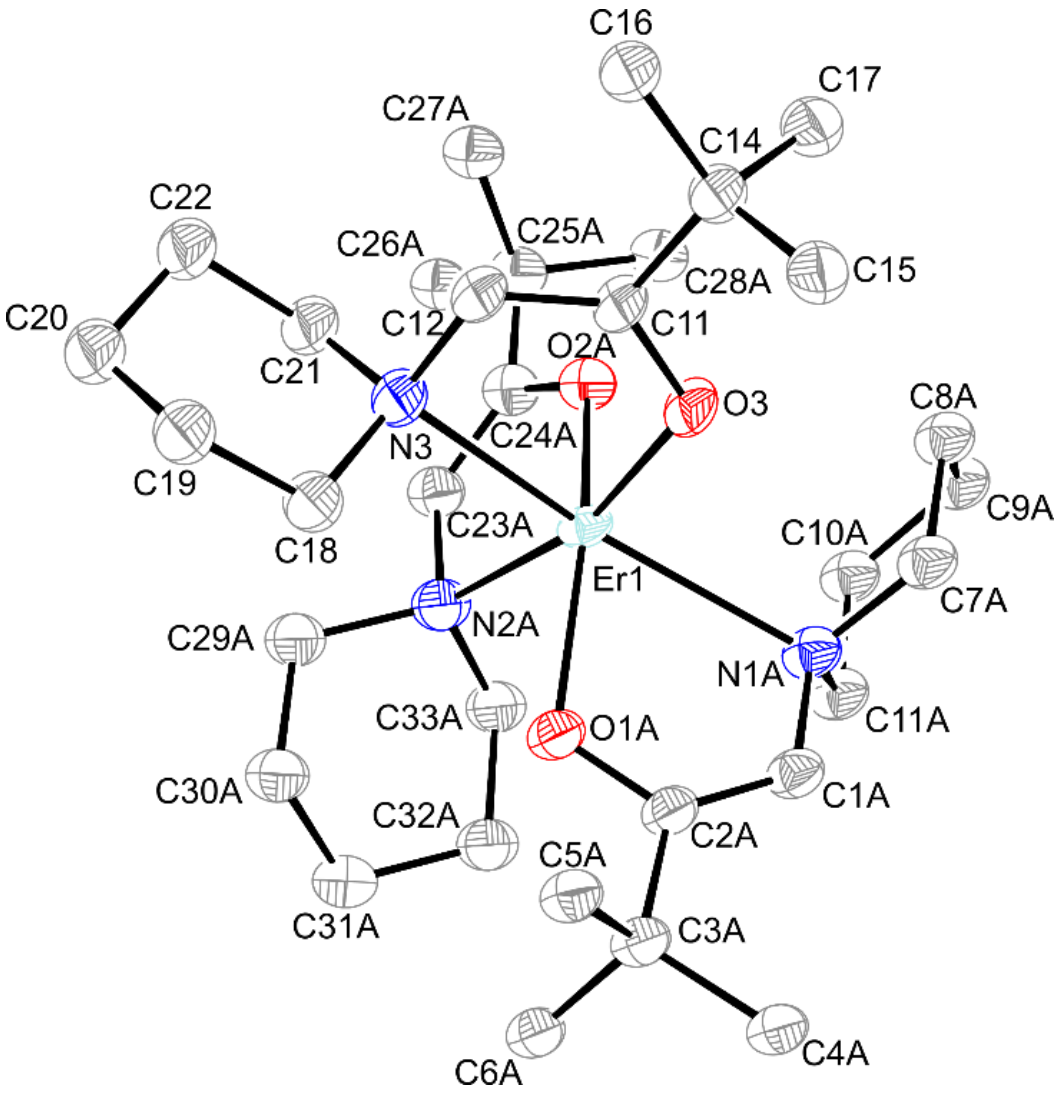

Figure 45. Perspective view of **19** with thermal ellipsoids at the 50% level.

Selected bond lengths (Å) and angles (deg): Er−O1A 2.150(5), Er−O2A 2.141(5), Er−O3 2.141(5), Er−N1A 2.545(6), Er−N2A 2.615(6), Er−N3 2.532(6), C1A−C2A 1.315(9), C23A−C24A 1.324(9), C11−C12 1.317(9); O1A−Er−O2A 151.8(3), O1A−Er− O3 107.4(3), O2A−Er−O3 100.0(3), O1A−Er−N1A 72.1(2), O1A−Er−N2A 85.3(3), O1A−Er−N3 99.8(2), O2A−Er−N2A 68.4(2), O2A−Er−N3 94.9(3), O3−Er−N3 72.0(2), N1A−Er− N2A 105.6(2), N1A−Er−N3 152.2, N2A−Er−N3 100.0(2).

Complex **20** adopts a six-coordinate monomeric molecular structure that is very similar to those found in **14** and **19** (Figure 46). The Lu−O bond lengths are 2.139(5), 2.117(5), and 2.112(5) Å, which are identical within experimental uncertainty. The Lu−N bond distances are 2.479(7), 2.458(5), and 2.40(2) Å. These distances are also identical within experimental error. The enolate C−C distances within the L^3 ligand backbone are 1.36(1), 1.351(9), and 1.35(1) Å. These values are consistent with double bonds and are identical with the values for **7-9**, **13**, **14**, and **19** within experimental uncertainty.

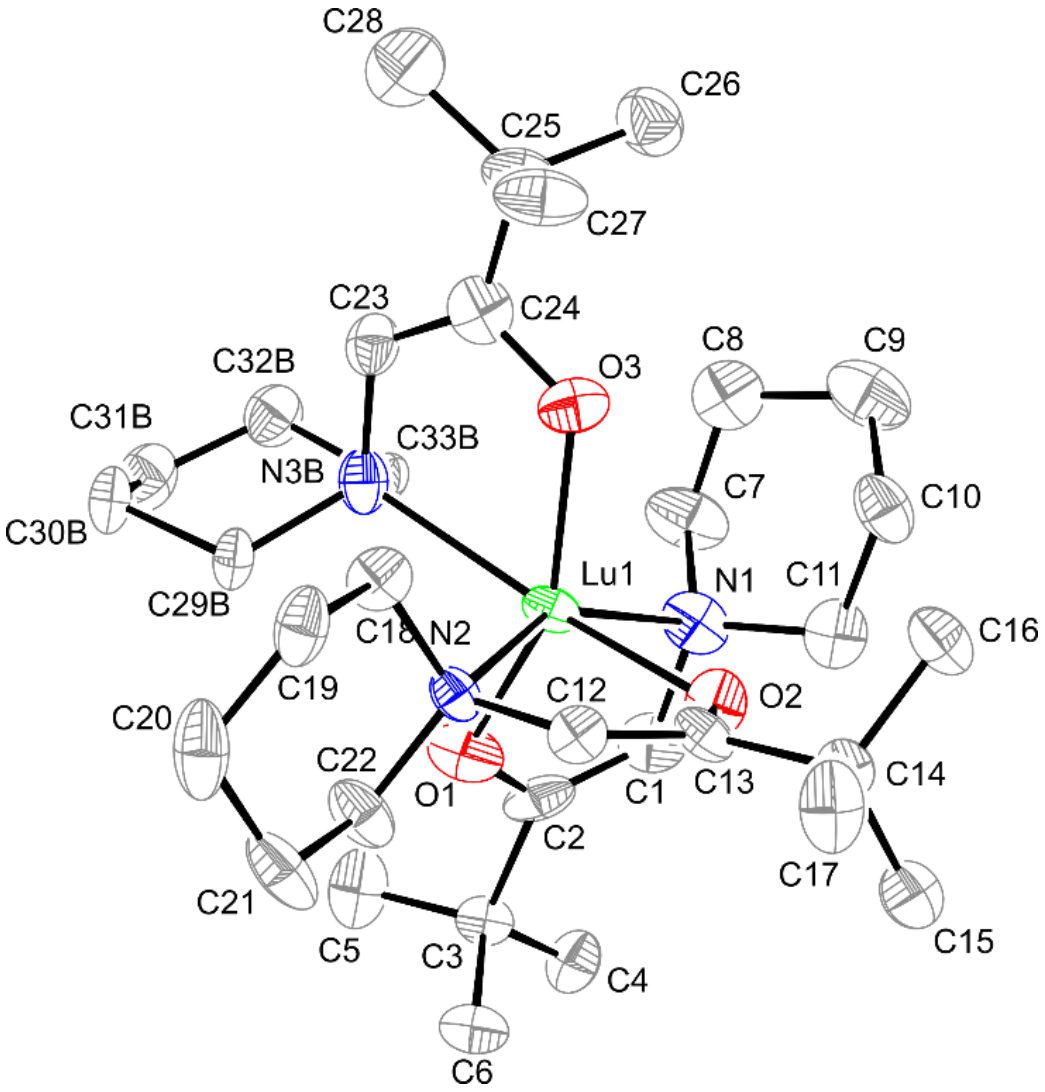

Figure 46. Perspective view of **20** with thermal ellipsoids at the 50% level.

Selected bond lengths (Å) and angles (°): Lu-O1 2.139(5), Lu-O2 2.117(5), Lu-O3 2.112(5), Lu-N1 2.479(7), Lu-N2 2.458(5), Lu-N3B 2.40(2), C1-C2 1.36(1), C12-C13 1.351(9), C23-C24 1.35(1); O1-Lu-O2 107.8(2), O1-Lu-O3 150.5(2), O2-Lu-O3 101.1(2), O1-Lu-N1 74.0(2), O1-Lu-N2 98.2(2), O1-Lu-N3B 82.5(3), O2-Lu-N1 85.0(2), O2-Lu-N2 73.6(2), O2-Lu-N3B 167.1(5), O3-Lu-N3B 69.9(3), N1-Lu-N2 153.8(2), N1-Lu-N3B 105.7(7), N2-Lu-N3B 97.7(7).

Comparison of Structure Data with Those of Related Complexes.

Only a few examples of lanthanide complexes containing enolate-based ligands have been structurally characterized. A common feature of previously reported complexes is that the enolate moieties are part of more complex chelating ligands.[219-222] The C=C double-bond lengths within the enolate fragments range from 1.33 to 1.37 Å.[219-222] These previously reported bond lengths are close to the values observed herein. A series of structurally characterized lanthanide(III) aryloxides provides Ln−O bond length comparisons with some of the complexes reported herein. The complexes $[Nd_2(O\text{-}C_6\text{-}2,4,6\text{-}Me_3H_2)_6(THF)_4]\cdot 2THF$ and $[Nd_2(O\text{-}C_6\text{-}2,4,6\text{-}Me_3H_2)_6(DME)_2]\cdot$(toluene) are dimeric with two bridging aryloxide ligands between the Nd ions and two terminal aryloxide ligands per Nd ion.[223] This dimeric structure is broadly similar to that of **13**. The bridging Nd−O bond lengths in $[Nd_2(O\text{-}C_6\text{-}2,4,6\text{-}Me_3H_2)_6(THF)_4]\cdot 2THF$ (2.410(2), 2.428(2) Å) and $[Nd_2(O\text{-}C_6\text{ -}2,4,6\text{-}Me_3H_2)_6(DME)_2]\cdot$(toluene) (2.357(1), 2.500(1) Å) are similar to those observed in **13** (2.410(5), 2.470(6) Å). The terminal Nd−O bond distances $[Nd_2(O\text{-}C_6\text{-}2,4,6\text{-}Me_3H_2)_6(THF)_4]\cdot 2THF$ (2.220(2), 2.216(2) Å) and $[Nd_2(O\text{-}C_6\text{-}2,4,6\text{-}Me_3H_2)_6(DME)_2]\cdot$(toluene) (2.204(2), 2.192(2) Å) are slightly shorter than the related values in **13** (2.241(5), 2.256(8), 2.266(5), 2.244(5) Å), consistent with a Nd ion coordination number of seven in **13** versus six in the Nd aryloxides. The complex $Er(O\text{-}C_6\text{-}2,4,6\text{-}Me_3H_2)_3(THF)_3$ has Er−O bond lengths of 2.082(6), 2.099(7), and 2.111(7) Å[223] and can be compared to the related values in **8** and **19**. In **8**, the Er−O distances associated with the anionic L^1 ligands are 2.121(2), 2.200(2), and 2.183(2) Å. The shortest of these distances corresponds to the κ^1-L^1 ligand, and this value is similar to the values for Er−O bond lengths in $Er(O\text{-}C_6\text{-}2,4,6\text{-}Me_3H_2)_3(THF)_3$. The two Er−O distances for the anionic κ^2- L^1 ligands are longer than the values in $Er(O\text{-}C_6\text{-}2,4,6\text{-}Me_3H_2)_3(THF)_3$, which likely arises from steric interactions associated with the bidentate coordination mode. The Er−O

bond length for the κ^2-L^1H ligand in **8** is 2.446(2) Å, which is in the range of the Er−O bond lengths for the THF ligands in $Er(O\text{-}C_6\text{-}2,4,6\text{-}Me_3H2)_3(THF)_3$ (2.434(7), 2.435(7) Å). The Er−O distances for the κ^2-L^3 ligands in **19** (2.150(5), 2.141(5), 2.141(5) Å) are longer than those in $Er(O\text{-}C_6\text{-}2,4,6\text{-}Me_3H_2)_3(THF)_3$, likely because of steric congestion in the coordination sphere caused by the piperidino substituents. Since the ionic radii of Er(III) and Y(III) are very similar, the Y−O bond length comparisons between $Er(O\text{-}C_6\text{-}2,4,6\text{-}Me_3H_2)_3(THF)_3$[223] and **9** are very close to those described above for $Er(O\text{-}C_6\text{-}2,4,6\text{-}Me_3H_2)_3(THF)_3$ and **8**. The reported crystal structures of $Pr(O\text{-}C_6H_3\text{-}2,6\text{-}iPr_2)_3(THF)_2$ and $Lu(OC_6H_3\text{-}2,6\text{-}iPr_2)_3(THF)_2$ offer bond length comparisons with **7**, **14**, and **20**.[224] The Pr−O aryloxide bond lengths in $Pr(O\text{-}C_6H_3\text{-}2,6\text{-}iPr_2)_3(THF)_2$ are 2.142(8), 2.158(9), and 2.216(9) Å, which are shorter than those observed for the κ^2-L^1 ligands in **7** (2.332(3), 2.309(3), 2.44(1) Å). The Pr−O bond distance for the κ^2-L^1H in **7** is 2.43(1) Å. The coordination numbers in $Pr(O\text{-}C_6H_3\text{-}2,6\text{-}iPr_2)_3(THF)_2$ and **7** are five and eight, respectively, which account for the differing Pr−O bond lengths. The Lu−O aryloxide bond lengths in $Lu(OC_6H_3\text{-}2,6\text{-}iPr_2)_3(THF)_2$ (2.041(4), 2.042(3), 2.048(4) Å) are also shorter than the related values in **14** (2.115(2), 2.129(2), 2.132(2) Å) and **20** (2.112(5), 2.117(5), 2.139(5) Å). The coordination number of five in $Lu(OC_6H_3\text{-}2,6\text{-}iPr_2)_3(THF)_2$ indicates less crowding, in comparison to the coordination number of six in **14** and **20**.

The Ln−N bond lengths in **7-9**, **13-15**, **19**, and **20** can be compared with those of selected complexes of similar coordination numbers containing the 1,10-phenanthroline (phen) ligand. The phen ligand was chosen as an analogue of the NR_2 fragments in L^1 and L^3 ligands, since all are neutral donors and because there are sufficient previously reported structures containing phen ligands to compare with the structures herein. The Pr−N bond lengths in $Pr(acac)_3(phen)$ (acac = 2,4-pentanedionate) are 2.659(5) and 2.690(6) Å,65 which are shorter than the related values in **7**

(2.739(4), 2.79(2), 2.84(2), 2.846(4) Å), although the differences are at the edge of experimental uncertainty. The longer Pr−N distances in **7** may reflect increased steric crowding due to accommodation of the NMe_2 groups, relative to the situation with the phen ligand in $Pr(acac)_3(phen)$. The Nd−N bond lengths in eight-coordinate $Nd(pfnp)_3(phen)$ (pfnp = 4,4,5,5,5-pentafluoro-1-(2-naphthyl)-1,3-butanedionate) range between 2.61 and 2.67 Å,[66] which are similar to the shortest Nd−N bond lengths in **13** (2.610(7), 2.595(7) Å). The longer Nd−N bond lengths in **13** (2.82−2.93 Å) probably reflect considerable steric crowding in the coordination spheres of the Nd ions. The Er−N bond distances in $Er(pfnp)_3(phen)$[225] are between 2.49 and 2.55 Å, which are similar to or slightly shorter than the related values in **8** (2.592(2), 2.559(2), 2.619(2) Å) and **19** (2.532(6), 2.545(6), 2.615(6) Å), despite the coordination numbers of eight in $Er(pfnp)_3(phen)$ and seven and six in **8** and **19**, respectively. Again, the bulky nature of the L^1, L^1H, and L^3 ligands in **8** and **19** create steric congestion about the Er ions that likely leads to a slight lengthening of the Er−Ndistances. The complex$Y(TTA)_3(phen)$ (TTA = 4,4,4-trifluoro-1-(2-thienyl)-1,3-butanedionate) has Y−N bond lengths of 2.535(6) and 2.558(5) Å,67 which are similar to or slightly shorter than the analogous values found in seven-coordinate **9** (2.579(2), 2.612(2), 2.633(2) Å). The slightly longer Y−N bond lengths in **9**, in comparison to $Y(TTA)_3(phen)$, can likely be attributed to the steric congestion about the Y ion that occurs through coordination of the L^1 and L^1H NMe_2 groups. The eight coordinate complex $Lu(acac)_3(phen)$ has Lu−Nbond distances of 2.50(2) and 2.521(6) Å,[226] which are similar to or slightly longer than the Lu−N values in six-coordinate **14** (2.459(2), 2.470(2), 2.530(2) Å) and **20** (2.40(2), 2.458(5), 2.479(7) Å). The slightly longer Lu−N distances in $Lu(acac)_3(phen)$, in comparison to **14** and **20**, can be attributed to the differences in coordination numbers of these complexes.

Precursor Properties.

Melting point determinations, preparative sublimations, decomposition temperature measurements, and thermogravimetric analyses (TGA) were carried out to determine the suitability of **7-21** for use as ALD precursors. Table 6 summarizes the melting points and sublimation and decomposition temperatures for **7-21**. Liquid precursors in ALD are highly desirable, because the surface areas of liquids are constant, thereby leading to constant gas-phase precursor concentrations. In contrast, the surface areas of solid precursors may not be constant during vapor transport, which may afford gas-phase precursor concentrations that change with precursor loading. Among **7-21**, **8**, **11**, **13**, **16**−**18**, and 2**1** have melting points that are lower than their sublimation temperatures and thus undergo vapor transport from the liquid state. Clear trends are apparent in the sublimation temperatures.

Table 6. Melting points, sublimation temperatures, and decomposition temperatures for **7-21**.

Complex	mp (°C)	Subl. Temp. at 0.5 Torr (°C)	Dec. Temp. (°C)
7, $Pr(L^1)_3(L^1H)$	128-130	120	206
8, $Er(L^1)_3(L^1H)$	107-110	110	229
9, $Y(L^1)_3(L^1H)$	120-123	100	180
10, $[Pr(L^1)_3]_n$	133-136	120	220
11, $[Er(L^1)_3]_n$	93-95	110	265
12, $[Y(L^1)_3]_n$	111-115	100	188
13, $[Nd(L^1)_3]_2$	73-76	120	210
14, $Lu(L^1)_3$	112-116	95	255
15, $[La(L^2)_3]_2$	171	160	180
16, $La(L^3)_3$	140-144	155	255
17, $Pr(L^3)_3$	124-128	150	280
18, $Nd(L^3)_3$	144-148	160	280
19, $Er(L^3)_3$	155-158	140	290
20, $Lu(L^3)_3$	167-172	140	272
21, $Y(L^3)_3$	152-155	160	280

The complexes containing L^1 ligands (**7-14**) sublime at the lowest temperatures among the series, likely because they have the lowest molecular weights. Complexes **7-9** sublime with loss of L^1H between 100 and 120 °C, and these sublimation temperatures are the same as those exhibited by **10-12**. Nd complex **13** is dimeric in the solid state but sublimes at 120 °C at 0.5 Torr. Since **13** is a liquid at 120 °C, it is possible that there is a monomer−dimer equilibrium present and vapor transport may occur from the monomers. The dimeric La complex **15** has the highest

sublimation temperature, which may arise from its dimeric structure and melting point that is higher than the sublimation temperature. Complexes **16-21** contain L^3 ligands and sublime at 140−160 °C at 0.5 Torr. These higher sublimation temperatures likely occur because the L^3 complexes have the highest molecular weights among the monomeric complexes.

Decomposition temperatures were determined in sealed capillary tubes containing a few milligrams of **7-21** that were heated at 5 °C/min until a color change to orange or red was observed. Complexes containing L^3 ligands (**16-21**) showed the highest decomposition temperatures (255−290 °C), while the dimeric La complex **15** containing L^2 ligands decomposed at 180 °C. Complexes containing L^1 ligands (**7-14**) exhibited intermediate thermal stabilities (180−265 °C). The thermal stability trends may arise from differences in the steric bulk of the ligand substituents. Complexes containing the L^3 ligand may be large enough to protect the metal ions from intramolecular and intermolecular decomposition reactions better than complexes containing L^1 and L^2 ligands. Interestingly, decomposition temperatures of **7-9** in sealed capillary tubes were 8−46 °C lower than those of the analogous complexes **10-12** that do not contain L^1H. It is likely that the presence of L^1H in liquid **7-9** leads to decomposition at lower temperatures than for pure **10-12**.

The thermal behavior and volatility of **7-21** were further investigated by TGA. Figure 47 and 48 show the representative TGA plots for complexes **7-12** and **16−21**, respectively. TGA traces for **13-15** are presented in Figure 49 and Table 7 gives the onsets of volatilization and percent residual masses for **7-21**. The TGA traces of **7-9** show two-step weight losses, with the first weight loss of about 20% beginning at around 80 °C, consistent with the evolution of loosely coordinated L^1H. For comparison, the weight percentages of L^1H are 23.3% (**7**), 19.4% (**8**), and 21.7% (**9**). Another weight loss event occurs between 120 and 180 °C with nonvolatile residues

after heating to 500 °C of 15%, 19%, and 7% for **7-9**, respectively. The TGA traces of **10-12** show single-step weight losses starting at about 140 °C. Interestingly, the percent nonvolatile residues for **10-12** upon reaching 500 °C are lower than those observed for **7-9** (e.g., nonvolatile residues of **10** < **7**, **11** < **8**, **12** ≤ **9**). This observation is consistent with the lower decomposition temperatures of **7-9** in comparison to **10-12** and is likely related to enhanced decomposition of **7-9** in the presence of L^1H. Complexes **16-21** show single-step weight losses up to their decomposition temperatures (272−290 °C). The 50% weight loss temperatures for **16-21** (~260−280 °C) are more positive than those for **10-12** (~220−230 °C), suggesting lower volatility of **16-21**. This trend is consistent with the sublimation temperatures for **10-12** and **16-21** shown in Table 6. The TGA traces of **13-15** also show single-step weight losses (Figure 49), but the nonvolatile residues (~20−30%) are higher than those of **7-12** and **16-21**.

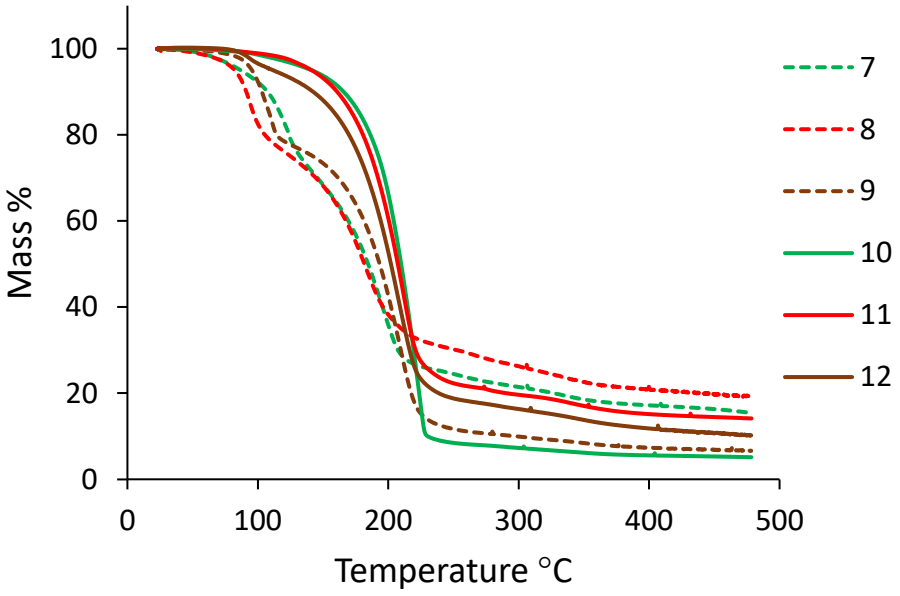

Figure 47.TGA traces of L^1-containing complexes **7-12**.

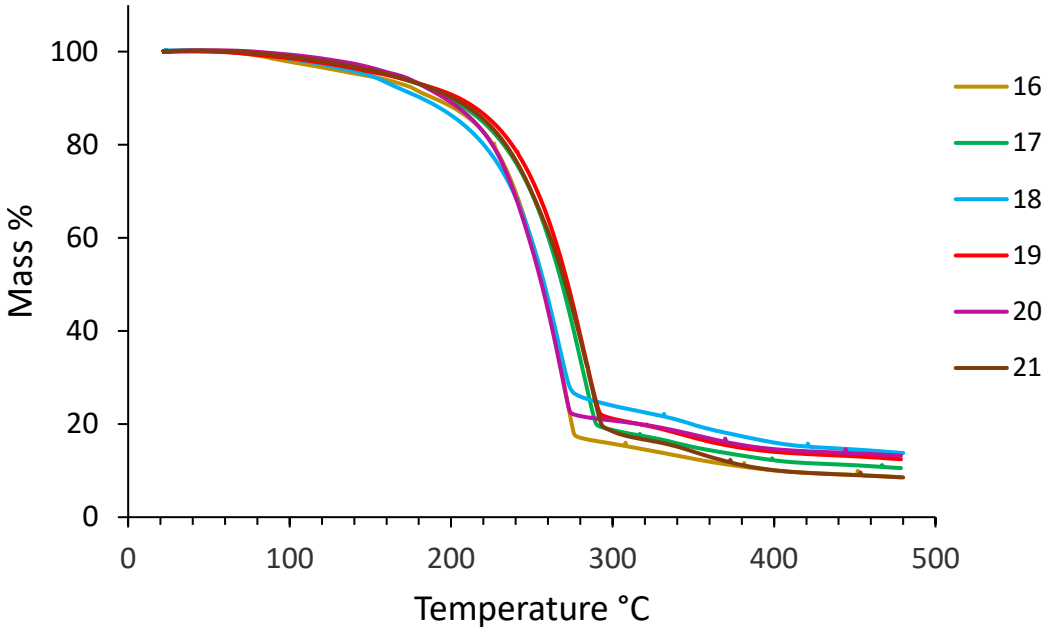

Figure 48. TGA traces of L^3 containing complexes **16-21**.

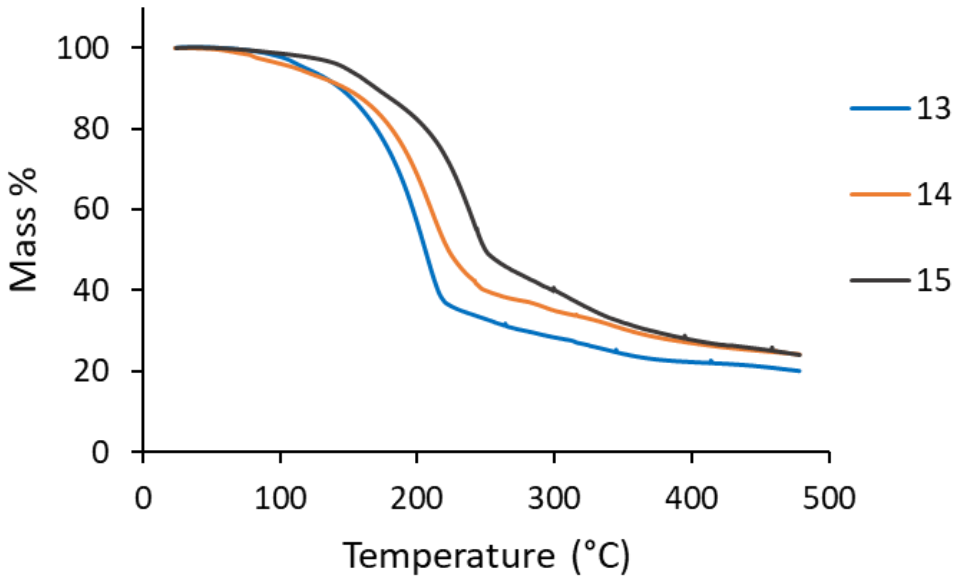

Figure 49. TGA traces of complexes **13-15**.

Table 7.Onset of volatilization and residual mass at 500 °C in the thermogravimetric analysis of **7-21**.

Compound	Onset of volatilization (°C)	Residual mass %
7, $Pr(L^1)_3(L_1H)$	96	15
8, $Er(L^1)_3(L_1H)$	80	19
9, $Y(L^1)_3(L_1H)$	92	7
10, $[Pr(L^1)_3]_n$	176	5
11, $[Er(L^1)_3]_n$	160	14
12, $[Y(L^1)_3]_n$	158	10
13, $[Nd(L^1)_3]_2$	153	20
14, $Lu(L^1)_3$	158	24
15, $[La(L^2)_3]_2$	186	24
16, $La(L^3)_3$	220	9
17, $Pr(L^3)_3$	225	10
18, $Nd(L^3)_3$	215	14
19, $Er(L^3)_3$	230	12
20, $Lu(L^3)_3$	220	13
21, $Y(L^3)_3$	225	9

The thermal stability of **12** was probed further by preparative sublimations. As noted above, sublimation of **9** gave a moderate yield of **12** (52%) and was accompanied by the formation of a nonvolatile residue. A sample of **12** that was purified by sublimation was resublimed at 100 °C and 0.5 Torr and afforded an 86% recovery of **12**. There was a small amount of nonvolatile residue left after the sublimation, suggesting some decomposition during the vaporization process. Moreover, a 25 mg sample of **12** was sealed in a glass ampule under argon and was heated in a

furnace at 130 °C for 24 h. The sample of **12** was initially a pale yellow solid and became a red-orange oil after heating for 24 h. ^{1}H NMR analysis (Figure 50) of the red-orange oil revealed a complex spectrum, in which the resonances for **12** were absent. Accordingly, **12** decomposed completely after heating at 130 °C for 24 h and thus has low thermal stability at this temperature. It is likely that the L^{1} ligand lacks sufficient steric bulk to protect the Ln−O and Ln−N bonds from decomposition reactions.

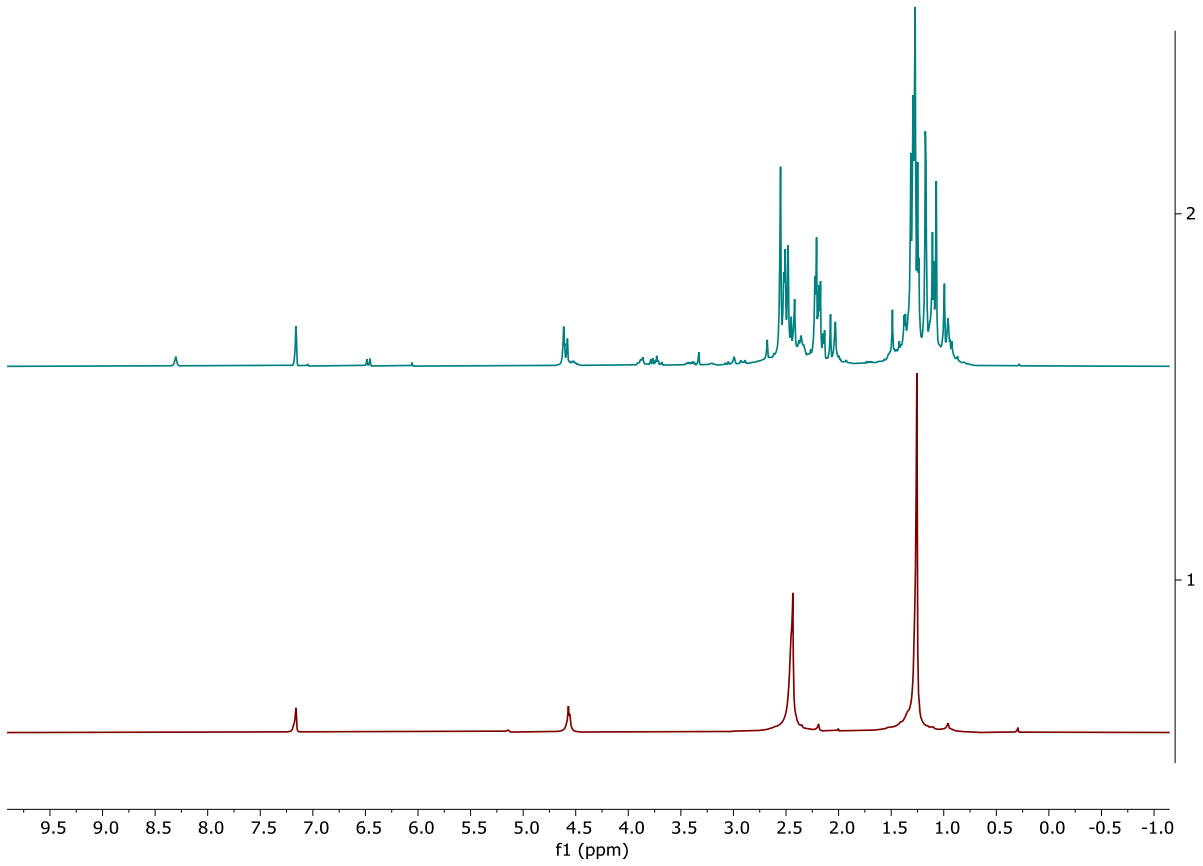

Figure 50. ^{1}H NMR spectra of **12** before (bottom) and after heating (top) at 130 °C for 24 hours. The resonance at around δ 7.16 is from the benzene-d_6 solvent residual protons.

The decomposition temperatures shown in Table 6 demonstrate that the L^3-containing complexes **16-21** are more thermally stable than the remaining complexes **7-15** that contain L^1 or L^2 ligands. To provide further insights into long-term stabilities, 25 mg samples of **16-21** were heated in sealed glass ampules near their sublimation temperatures (140 °C for **19** and **20**, 150 °C for **16-18** and **21**) for 24 h. The heated samples were analyzed by ^{1}H NMR spectroscopy for signs of decomposition. The ^{1}H NMR spectra of **17-19** and **21** after 24 h of heating were very similar to those prior to heating, suggesting that these complexes do not decompose under the heating conditions. Complexes **16** and **20** (Figure 51) showed about 10−20% of free L^3H after 24 h of heating, suggesting a small amount of decomposition. Accordingly, complexes containing the midsized Pr, Er, and Y ions have the highest thermal stabilities, whereas La^{3+} (largest ion) and Lu^{3+} (smallest ion) have slightly lower thermal stabilities. It is possible that the L^3 ligand has just the right steric profile to protect the Pr, Er, and Y ions from intramolecular and intermolecular reactions. The L^3 ligand may not be large enough to encapsulate the La^{3+} ion in **16** and may be too large to fit around the Lu^{3+} ion in **20**. Accordingly, achieving the highest thermal stability for a given lanthanide ion will likely require “tuning” the ligand structures to obtain optimum steric interactions. Fortunately, analogues of L^1–L^3 can be easily prepared with alkyl and amino substituents of varying steric profiles.

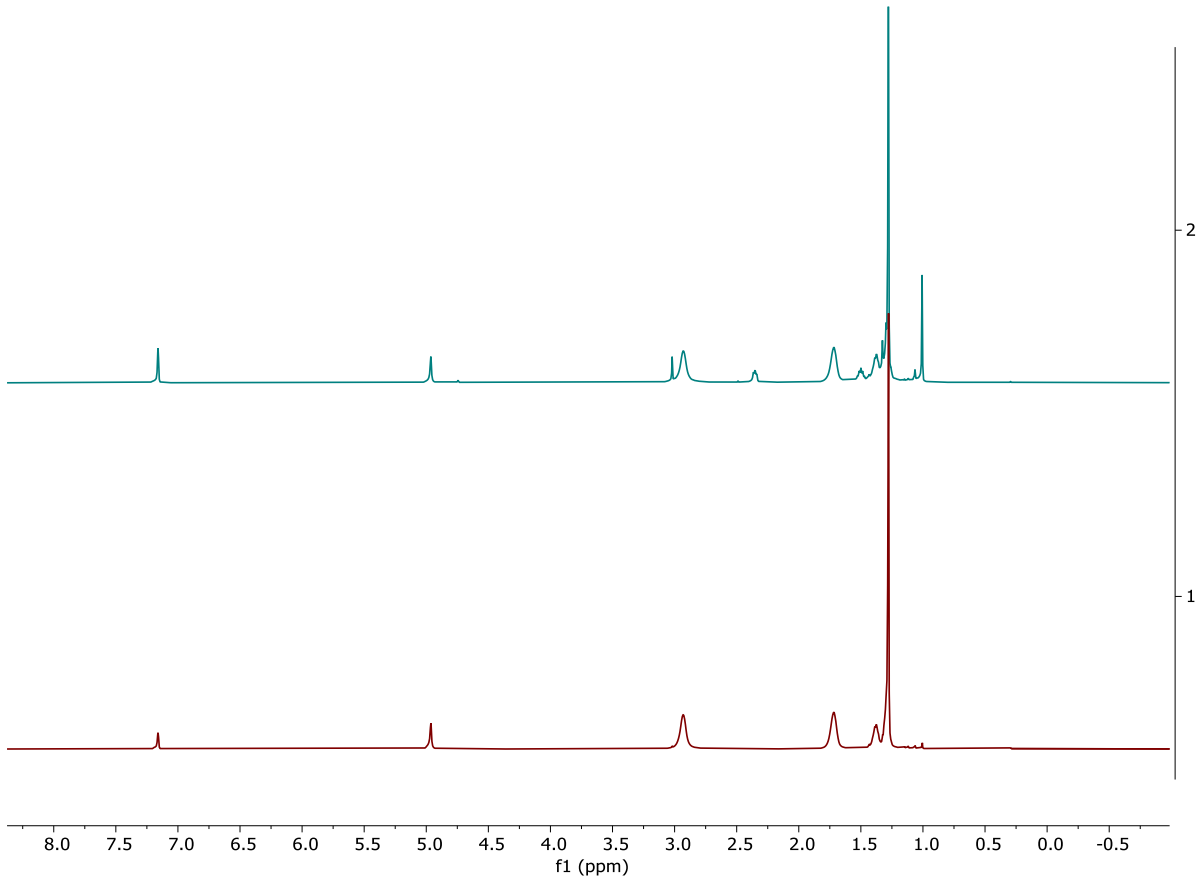

Figure 51. ^{1}H NMR spectra of **20** before (bottom) and after heating (top) at 140 °C for 24 hours. The resonance at around δ 7.16 is from the benzene-d_6 solvent residual protons.

Comparison of Precursor Properties with Those of Previously Reported Lanthanide ALD Precursors.

The L^3-containing complexes **16-21** are more thermally stable than **7-15**, which contain L^1 and L^2 ligands. However, the higher molecular weights of the L^3 ligands in **16-21**, relative to the ligands in **7-15**, lead to higher sublimation temperatures (140−160 °C at 0.5 Torr) in comparison to those found in L^1 complexes **7-14** (100−120 °C at 0.5 Torr). Complex **15** is dimeric, is the only complex containing L^2 ligands, and has a high sublimation temperature (160 °C at 0.5 Torr) and low decomposition temperature (180 °C).

Of the complexes reported here, **16-21** clearly have the best ALD precursor properties, because of their high thermal stabilities at the sublimation temperatures. It is difficult to compare the precursor properties of the compounds in the present work with those of precursors that have been previously used in the ALD of lanthanide-containing thin films, however, since precursor decomposition temperatures are rarely given. The decomposition temperature of a precursor is often close to the upper temperature limit of the ALD window in an ALD process.[158, 159] This similarity can be used to perform an initial comparison of previous precursors with **16-21**.

Among previous lanthanide complexes, precursors containing β-diketonate or cyclopentadienyl ligands have been the most widely used.[89, 201-203] Lanthanide complexes of the formula Ln(β-diketonate)$_3$ have very high thermal stabilities and can exhibit self-limited growth of oxides up to 400 °C.[185,89, 201-203] However, Ln(β-diketonate)$_3$ precursors are unreactive toward water and require ozone as a co-reactant for oxide growth.[185,89, 201-203] Ozone is highly reactive and causes oxidation of silicon substrates. Lanthanide cyclopentadienyl complexes also have very high thermal stabilities and water can be used as a co-reactant for the growth of oxide films.[59, 89, 126, 204, 205] For example, the growth of Er_2O_3 films with $Er(C_5H_4Me)_3$ and water exhibits an ALD window from about 250 to 350 °C on Si(100) substrates.[227] The growth of $PrAlO_3$ films using $Pr(C_5H_4iPr)_3$, $AlMe_3$, and water shows an ALD window from about 275 to 325 °C.[59] Accordingly, the thermal stabilities of lanthanide cyclopentadienyl precursors appear to be higher than those of **7-21**. However, the close similarity of the *pKa* values for water (*pKa* = 14.00, 15.7)[101] and cyclopentadiene (*pKa* = 16)[228] may lead to a low reactivity of lanthanide cyclopentadienyl precursors with water in oxide growth. Moreover, the ALD growth of some lanthanide cyclopentadienyl precursors with water does not exhibit self-limited growth.[155, 229] Finally, the ALD growth of Pr_2O_3 films using $Pr(C_5H_4iPr)_3$ and ozone showed an ALD window from 200 to

250 °C, suggesting that not all lanthanide cyclopentadienyl precursors have high upper temperature limits for self-limited growth.[230] Precursors containing alkoxide, bis(trimethylsilylamide), and amidinate ligands have been evaluated as precursors for the growth of lanthanide oxide films but exhibit problems that include lack of self-limiting growth, low decomposition temperatures, variable reactivity toward water, and impurity incorporation in the films.[89] Precursors containing new ligands such as guanidinate[157] and malonate[89] are promising. For example, the ALD growth of Er_2O_3 using the guanidinate precursor $Er(iPrNC(NMe_2)NiPr)_3$ and water exhibited an ALD window from about 175 to 275 °C.[157] The upper limit of the ALD window for $Er(iPrNC(NMe_2)NiPr)_3$ is similar to the decomposition temperatures of **16-21** herein.

3.3 Conclusions

In this work, we have described the synthesis, molecular structures, volatilities, and thermal stabilities of lanthanide complexes **7-21** that contain enaminolate ligands. Among the structurally characterized complexes, **7**−**9**, **14**, **19**, and **20** have monomeric molecular structures, whereas **13** and **15** adopt dimeric structures. Complexes **7**−**21** are volatile and sublime between 95 and 160 °C at 0.5 Torr. Complexes **7**−**14**, which contain NMe_2 groups in the L^1 ligand, sublime at the lowest temperatures (95−120 °C at 0.5 Torr), whereas complexes with L^2 (**15**) and L^3 ligands (**16**−**21**) sublime at 140−160 °Cat 0.5 Torr. The trend of increasing sublimation temperatures (**7**−**14** < **15**−**21**) approximately follows the trend of increasing molecular weights for the monomeric complexes. Interestingly, the dimeric complexes **13** and **15** sublime at similar temperatures to the monomeric complexes, suggesting that the dimers may sublime as monomers. Complexes containing L^1 (**7**−**14**) and L^2 ligands (**15**) decompose in heated capillary tubes at temperatures between 180 and 265 °C, whereas the complexes with L^3 ligands (**16-21**) decompose between 255 and 290 °C. The higher thermal stabilities of **16-21** are attributed to the large steric bulk of the

piperidinyl groups in L^3 ligands, which protects the lanthanide ions from intramolecular and intermolecular decomposition reactions better than the dimethylamino and pyrrolidinyl substituents in L^1 and L^2 ligands, respectively. Heating of **12** at 130 °C for 24 h led to complete decomposition, whereas similar treatment of **16-21** at their sublimation temperatures (140−150 °C) revealed a small amount of decomposition for **16** and **20** and no decomposition for **17**, **19**, and **21**. Accordingly, **16-21** have the best overall thin film precursor properties among the complexes described herein, in spite of their moderate sublimation temperatures (140−160 °C at 0.5 Torr).

3.4 Experimental Section

General Considerations.

All reactions and manipulations were carried out under an argon atmosphere using standard glovebox and Schlenk techniques, except that L^1H−L^3H ligands were synthesized under an ambient atmosphere. Tetrahydrofuran and diethyl ether were distilled from purple solutions of sodium/benzophenone ketyl under an argon atmosphere. Hexane was distilled from sodium under an argon atmosphere. Anhydrous $LaCl_3$, $ErCl_3$, $LuCl_3$, and YCl_3 were purchased from Strem Chemicals, Inc. Anhydrous $PrCl_3$ and $NdCl_3$ were purchased from ProChem Inc. All of the anhydrous lanthanide chlorides were used as received. Potassium hydride (30 wt % dispersion in mineral oil) was purchased from Sigma-Aldrich and was washed with hexane before use. 1-Bromopinacolone was purchased from Combi-Blocks, and triethylamine, dimethylamine, piperidine, and pyrrolidine were purchased from Sigma-Aldrich and were used as received. 1-(Dimethylamino)-3,3-dimethylbutan-2-one (L^1H),[231] 3,3dimethyl-1-(pyrrolidin-1-yl)butan-2-one (L^2H),[231] and 3,3-dimethyl-1(piperidin-1-yl)butan-2-one (L^3H)[232] were synthesized according to

published procedures, except that diethyl ether was used as the reaction solvent for L^1H and L^2H, instead of benzene. Yields for **7-21** are based upon the amounts of lanthanide(III) chloride starting materials.

^1H and $^{13}C\{^1H\}$ NMR spectra were recorded using an Agilent 400 MHz spectrometer in benzene-d_6 or toluene-d_8, as indicated. All spectra were recorded at ambient temperature unless otherwise noted. Infrared spectra were measured using a Shimadzu IR Tracer-100 spectrometer. Melting points and solid-state thermal decomposition temperatures were determined using an Electrothermal-IA-9000 series digital melting point apparatus with a heating rate of 5 °C/min. TGA data were obtained using a TA Instruments TGA Q-50 apparatus inside a nitrogen-filled glovebox with a ramp of 10 °C/min. Elemental analyses were performed by Galbraith Laboratories, Inc., Knoxville, TN.

Preparation of $Pr(L^1)_3(L^1H)$ (7).

A 100 mL Schlenk flask was charged with a magnetic stir bar, anhydrous $PrCl_3$ (0.432 g, 1.75 mmol), and tetrahydrofuran (10 mL). To this stirred solution at ambient temperature was slowly added a solution of KL^1 (prepared from L^1H (0.750 g, 5.25 mmol) and KH (0.231 g, 5.77 mmol) in tetrahydrofuran (25 mL)), followed by a solution of L^1H (0.250 g, 1.75 mmol) in tetrahydrofuran (5 mL). This solution was refluxed for 24 h. When the solution was cooled to room temperature, the volatile components were removed under reduced pressure and the resultant green-brown solid was dissolved in diethyl ether (40 mL). The solution was filtered through a 1 cm pad of Celite on a coarse glass frit and concentrated to about 15 mL under reduced pressure. The flask was then placed in a −30 °C freezer for 3 days. This procedure gave pale green X-ray-quality crystals of **7** (0.375, 30%): mp 128−130 °C, dec 206 °C; IR (cm^{-1}) 2947 (m), 1682 (m),

1616 (m), 1333 (s), 1332 (s), 1132 (s), 1036 (m), 918 (m), 869 (m), 578 (m), 515 (w), 422 (m). Anal. Calcd for $C_{32}H_{65}PrN_4O_4$: C, 54.07; H, 9.22; N, 7.88. Found: C, 52.96; H 9.24; N 7.70.

Preparation of Er(L^1)$_3$(L^1H) (8).

In a fashion similar to the preparation of **7**, treatment of anhydrous $ErCl_3$ (0.478 g, 1.75 mmol) with a solution of KL^1 (prepared from L^1H (0.75 g, 5.25 mmol) and KH (0.231 g, 5.77 mmol)) was followed by addition of a solution of L^1H (0.250 g, 1.75 mmol). In contrast to **7**, the reaction mixture was stirred at ambient temperature instead of refluxing. Crystallization from diethyl ether afforded **8** as pale orange X-ray-quality crystals (0.421 g, 33%): mp 107−110 °C, dec 229 °C; IR (cm^{-1}) 2947 (m), 1678 (m), 1618 (m), 1454 (m), 1334 (s), 1136 (s), 1033 (m), 922 (m), 723 (m), 694 (m), 590 (m), 465 (m). Anal. Calcd for $C_{32}H_{65}ErN_4O_4$: C, 52.14; H, 8.89; N, 7.60. Found: C, 50.42; H, 8.64; N, 7.25.

Preparation of Y(L^1)$_3$(L^1H) (9).

In a fashion similar to the preparation of **8**, treatment of anhydrous YCl_3 (0.342 g, 1.75 mmol) with a solution of KL^1 (prepared from L^1H (0.75 g, 5.25 mmol) and KH (0.231 g, 5.77 mmol)) was followed by a solution of L^1H (0.250 g, 1.75 mmol) to afford **9** (0.412 g, 36%) as yellow crystals from diethyl ether: mp 120−123 °C, dec 180 °C; ^{1}H NMR (benzene-d_6, 23 °C, δ) 4.55 (br s, 3 H, CH), 3.05 (br s, 2 H, CH_2), 2.39 (br s, 18 H, $N(CH_3)_2$), 2.24 (br s, 6 H, $N(CH_3)_2$), 1.25 (br s, 27 H, $C(CH_3)_3$), 0.94 (br s, 9 H, $C(CH_3)_3$); ^{13}C{1H} R (benzene- d_6, 23 °C, ppm) 167.00 (s, *C*-O), 109.80 (s, *C*HN), 63.63 (br s, $N(CH_3)_2$), 47.82 (s, $N(CH_3)_2$), 45.48 (s, CH_2N), 43.40 (s, $C(CH_3)_3$), 35.56 (s, $C(CH_3)_3$), 28.75 (br s, $C(CH_3)_3$), 26.47 (br s, $C(CH_3)_3$); IR (cm^{-1}) 2945 (m), 1680 (m), 1618 (m), 1450 (m), 1337 (s), 1138 (s), 922 (m), 869 (m), 723 (m), 696 (m), 590 (m), 521 (m), 430 (m). Anal. Calcd for $C_{32}H_{65}YN_4O_4$: C, 58.34; H, 9.94; N, 8.50. Found: C, 57.23; H, 9.98; N, 8.29.

Preparation of Pr(L^1)$_3$ (10).

A 0.300 g sample of **7** was placed in a 1 cm diameter glass tube and sublimed under reduced pressure (0.5 Torr) at 120 °C to afford **10** as a pale green solid (0.101 g, 42%): mp 133−136 °C, dec 220 °C; ^{1}H NMR (benzene-d_6, 23 °C, δ) 15.96 (br s), 9.55 (s), 6.74 (br s), −4.03 (br s), −22.49 (br s), −29.10 (br s); IR (cm^{-1}) 2949 (m), 1616 (w), 1458 (m), 1332 (s), 1134 (s), 1110 (m), 1041 (m), 918 (m), 867 (m), 581 (m), 424 (m). Anal. Calcd for $C_{24}H_{48}N_3O_3Pr$: C, 50.78; H, 8.52; N, 7.40. Found: C, 49.70; H, 8.78; N, 7.19.

Preparation of Er(L^1)$_3$ (11).

Similarly to the preparation of **10**, sublimation of 0.400 g of **8** at 110 °C/0.5 Torr afforded **11** as a pale orange solid (0.142 g, 44%): mp 93−95 °C, dec 265 °C; ^{1}H NMR (benzene-d_6, 23 °C, δ) 113.84 (br s), −47.83 (br s), −54.34 (br s); IR (cm^{-1}) 2947 (m), 1618 (m), 1454 (m), 1335 (s), 1136 (s), 1004 (m), 922 (m), 866 (w), 723 (m), 590 (m), 426 (m). Anal. Calcd for $C_{24}H_{48}ErN_3O_3$: C, 48.53; H, 8.15; N, 7.08. Found: C, 47.25; H, 8.33; N, 6.95.

Preparation of Y(L^1)$_3$ (12).

In a fashion similar to the preparation of **10**, sublimation of 0.400 g of **9** at 100 °C/0.5 Torr afforded **12** as a pale yellow solid (0.162 g, 52%): mp 111−115 °C, dec 188 °C; ^{1}H NMR (benzene-d_6, 23 °C, δ) 4.55 (s, 3 H, CH), 2.40 (s, 18 H, N(CH$_3$)$_2$), 1.25 (s, 27 H, C(CH$_3$)$_3$); ^{13}C{1H} NMR (benzene-d_6, 23 °C, ppm) 167.17 (s, *C*-O), 109.62 (s, *C*HN), 47.69 (s, N(*C*H$_3$)$_2$), 35.49 (s, *C*(CH$_3$)$_3$), 28.66 (s, C(*C*H$_3$)$_3$); IR (cm^{-1}) 2945 (m), 1618 (m), 1452 (m), 1336 (s), 1138 (s), 1002 (m), 923 (m), 866 (m). Anal. Calcd for $C_{24}H_{48}N_3O_3Y$: C, 55.91; H, 9.38; N, 8.15. Found: C, 54.67; H, 9.42; N, 8.02.

Preparation of $[Nd(L^1)_3]_2$ (13).

A 100 mL Schlenk flask was charged with a magnetic stir bar, anhydrous $NdCl_3$ (0.584 g, 2.33 mmol), and tetrahydrofuran (20 mL). To this stirred solution at ambient temperature was slowly added a solution of KL^1 (prepared in situ from L^1H (1.000 g, 6.98 mmol) and KH (0.336 g, 8.38 mmol)) in tetrahydrofuran (30 mL). This solution was refluxed for 20 h. The volatile components were removed under reduced pressure, and the resultant pale blue solid was subjected to sublimation at 120 °C/0.5 Torr to afford **13** as a pale blue solid (0.487 g, 37%). X-ray-quality crystals were grown by slow evaporation of a solution of sublimed **13** in hexane at 23 °C under an argon atmosphere: mp 73−76 °C, dec 210 °C; IR (cm^{-1}) 2949 (m), 1616 (m), 1454 (m), 1330 (s), 1134 (s), 918 (m), 869 (m), 580 (m), 424 (m). Anal. Calcd for $C_{48}H_{96}Nd_2N_6O_6$: C, 50.49; H, 8.47; N, 7.36. Found: C, 49.99; H, 8.51; N, 7.14.

Preparation of $Lu(L^1)_3$ (14).

In a fashion similar to the preparation of **13**, treatment of anhydrous $LuCl_3$ (0.655 g, 2.33 mmol) with a solution of KL^1 (prepared from L^1H (1.000 g, 6.98 mmol) and KH (0.336 g, 8.38 mmol) in tetrahydrofuran (30 mL)) was followed by stirring at ambient temperature for 20 h. Sublimation of the crude product at 95 °C/0.5 Torr afforded **14** (0.571 g, 40%) as white, X-rayquality crystals: mp 112−116 °C, dec 255 °C; ^{1}H NMR (benzene-d_6, 23 °C, δ) 4.60 (s, 3 H, CH), 2.38 (s, 18 H, $N(CH_3)_2$), 1.24 (s, 27 H, $C(CH_3)_3$); ^{13}C{1H} NMR (benzene- d_6, 23 °C, ppm) 167.61 (s, *C*O), 110.30 (s, *C*HN), 48.75 (s, $N(CH_3)_2$), 35.65 (s, $C(CH_3)_3$), 28.74 (s, $C(CH_3)_3$); IR (cm^{-1}) 2949 (m), 1618 (w), 1458 (m), 1334 (s), 1138 (s), 1010 (m), 921 (m), 867 (m), 592 (m). Anal. Calcd for $C_{24}H_{48}LuN_3O_3$: C, 47.92; H, 8.04; N, 6.98. Found: C, 48.06; H, 8.18; N, 6.91.

Preparation of $[La(L^2)_3]_2$ (15).

In a fashion similar to the preparation of **13**, treatment of anhydrous $LaCl_3$ (0.483 g, 1.97 mmol) with a solution of KL^2 (prepared from L^2H (1.000 g, 5.92 mmol) and KH (0.284 g, 7.09 mmol) in tetrahydrofuran (30 mL)) afforded **15** (0.628 g, 50%) as white, X-ray-quality crystals upon sublimation at 160 °C/0.5 Torr: mp 171 °C, dec 180 °C; ^{1}H NMR (benzene-d_6, 23 °C, δ) 4.74 (s, 6 H, CH), 2.87 (br m, 24 H, $N(CH_2)_2(CH_2)_2$), 1.80 (br m, 24 H, $(CH_2)_2(CH_2)_2$), 1.27 (s, 54 H, $C(CH_3)_3$); ^{13}C{1H} NMR (benzene- d_6, 23 °C, ppm) 166.53 (s, *C*O), 105.64 (s, *C*HN), 55.08 (s, $N(CH_2)_2(CH_2)_2$), 35.92 (s, $C(CH_3)_3$), 28.99 (s, $C(CH_3)_3$), 24.04 (s, $N(CH_2)_2(CH_2)_2$); IR (cm^{-1}) 2956 (m), 1606 (m), 1477 (w), 1344 (m), 1325 (s), 1143 (s), 1097 (m), 920 (m), 572 (m), 475 (w). Anal. Calcd for $C_{60}H_{108}La_2N_6O_6$: C, 55.98; H, 8.46; N, 6.53. Found: C, 54.24; H, 8.37; N, 6.36.

Preparation of $La(L^3)_3$ (16).

In a fashion similar to the preparation of **13**, treatment of anhydrous $LaCl_3$ (0.446 g, 1.82 mmol) with a solution of KL^3 (prepared from L^3H (1.000 g, 5.46 mmol) and KH (0.263 g, 6.55 mmol) in tetrahydrofuran (30 mL)) afforded **16** (0.490 g, 39%) as a white solid upon sublimation at 155 °C/0.5 Torr: mp 140−144 °C, dec 255 °C; ^{1}H NMR (benzene-d_6, 23°C, δ) 4.79 (s, 3 H, CH), 2.84 (br m, 12 H, $N(CH_2)_2(CH_2)_2(CH_2)$), 1.76 (br m, 12 H, $N(CH_2)_2(CH_2)_2(CH_2)$), 1.36 (br m, 6 H, $N(CH_2)_2(CH_2)_2(CH_2)$), 1.29 (s, 27 H, $C(CH_3)_3$); ^{13}C{1H} NMR (benzene- d_6, 23 °C, δ) 164.98 (s, *C*-O), 105.36 (s, *C*HN), 54.62 (s, $N(CH_2)_2(CH_2)_2(CH_2)$), 36.25 (s, $C(CH_3)_3$), 29.25 (s, $C(CH_3)_3$), 24.78 (s, $N(CH_2)_2(CH_2)_2(CH_2)$), 24.28 (s, $N(CH_2)_2(CH_2)_2(CH_2)$); IR (cm^{-1}) 2935 (s), 1576 (w), 1450 (w), 1335 (s), 1148 (m), 1093 (m), 1049 (m), 983 (m), 858 (m). Anal. Calcd for $C_{33}H_{60}LaN_3O_3$:C, 57.79; H, 8.82; N, 6.13. Found: C, 56.40; H, 8.94; N, 6.05.

Preparation of $Pr(L^3)_3$ (17).

In a fashion similar to the preparation of **13**, treatment of anhydrous $PrCl_3$ (0.450 g, 1.82 mmol) with a solution of KL^3 (prepared from L^3H (1.000 g, 5.46 mmol) and KH (0.263 g, 6.55 mmol) in tetrahydrofuran (30 mL)) afforded **17** (0.513 g, 41%) as a pale yellow-green solid upon sublimation at 150 °C/0.5 Torr: mp 124−128 °C, dec 280 °C; IR (cm^{-1}) 2930 (m), 1618 (w), 1456 (w), 1454 (w), 1329 (m), 1145 (m), 1099 (m), 1091 (m), 725 (m), 581 (m). Anal. Calcd for $C_{33}H_{60}PrN_3O_3$: C, 57.63; H, 8.79; N, 6.11. Found: C, 52.42; H, 8.30; N, 5.60.

Preparation of $Nd(L^3)_3$ (18).

In a fashion similar to the preparation of **13**, treatment of anhydrous $NdCl_3$ (0.456 g, 1.82 mmol) with a solution of KL^3 (prepared from L^3H (1.000 g, 5.46 mmol) and KH (0.263 g, 6.55 mmol) in tetrahydrofuran (30 mL)) afforded **18** (0.674, 54%) as a pale blue solid upon sublimation at 160 °C/0.5 Torr: mp 144−148 °C, dec 280 °C; IR (cm^{-1}) 2931 (s), 2852 (w), 1575 (w), 1454 (w), 1330 (s), 1147 (m), 1091 (m), 1053 (m), 981 (s), 860 (m), 570 (s). Anal. Calcd for $C_{33}H_{60}NdN_3O_3$: C, 57.35; H, 8.75; N, 6.08. Found: C, 55.84; H, 8.59; N, 6.03.

Preparation of $Er(L^3)_3$ (19).

In a fashion similar to the preparation of **13**, treatment of anhydrous $ErCl_3$ (0.498 g, 1.82 mmol) with a solution of KL^3 (prepared from L^3H (1.000 g, 5.46 mmol) and KH (0.263 g, 6.55 mmol) in tetrahydrofuran (30 mL)) afforded **19** (0.613 g, 47%) as pink, X-ray-quality crystals upon sublimation of the crude solid at 140 °C/0.5 Torr: mp 155−158 °C, dec 290 °C; IR (cm^{-1}) 2931 (m), 1613 (m), 1450 (m), 1331 (s), 1146 (s), 1096 (m), 1043 (m), 987 (m), 923 (s), 696 (m), 586 (s). Anal. Calcd for $C_{33}H_{60}ErN_3O_3$: C, 55.50; H, 8.47; N, 5.88. Found: C, 54.33; H, 8.75; N, 5.81.

Preparation of Lu(L^3)$_3$ (20).

In a fashion similar to the preparation of **13**, treatment of anhydrous $LuCl_3$ (0.512 g, 1.82 mmol) with a solution of KL^3 (prepared from L^3H (1.000 g, 5.46 mmol) and KH (0.263 g, 6.55 mmol) in tetrahydrofuran (30 mL)) afforded **20** (0.519 g, 40%) as a white solid upon sublimation at 140 °C/0.5 Torr: mp 167−172 °C, dec 272 °C; ^{1}H NMR (benzene-d_6, 23 °C, δ) 4.96 (s, 3 H, CH), 2.92 (br m, 12 H, N(CH_2)$_2$(CH_2)$_2$(CH_2)), 1.71 (br m, 12 H, N(CH_2)$_2$(CH_2)$_2$(CH_2)), 1.38 (br m, 6 H, N(CH_2)$_2$(CH_2)$_2$(CH_2)), 1.27 (s, 27 H, C(CH_3)$_3$); ^{13}C{1H} NMR (benzene-d_6, 23 °C, ppm) 167.05 (s, *C*-O), 106.37 (s, *C*HN), 56.52 (s, N(*C*H_2)$_2$(CH_2)$_2$(CH_2)), 35.83 (s, *C*(CH_3)$_3$), 28.65 (s, C(*C*H_3)$_3$), 24.34 (s, N(CH_2)$_2$(*C*H_2)$_2$(CH_2)), 22.80 (s, N(CH_2)$_2$(CH_2)$_2$(*C*H_2)); IR (cm^{-1}) 2932 (m), 1616 (m), 1450 (m), 1384 (m), 1332 (s), 1145 (s), 1093 (m), 1043 (m), 987 (m), 923 (s), 860 (m), 590 (s). Anal. Calcd for $C_{33}H_{60}LuN_3O_3$: C, 54.91; H, 8.38; N, 5.82. Found: C, 52.09; H, 8.11; N, 5.61.

Preparation of Y(L^3)$_3$ (21).

In a fashion similar to the preparation of **13**, treatment of anhydrous YCl_3 (0.355 g, 1.82 mmol) with a solution of KL^3 (prepared from L^3H (1.000 g, 5.46 mmol) and KH (0.263 g, 6.55 mmol) in tetrahydrofuran (30 mL)) afforded **21** (0.647 g, 56%) as a white solid upon sublimation at 160 °C/0.5 Torr: mp 152−155 °C, dec 280 °C; ^{1}H NMR (benzene-d_6, 23 °C, δ) 4.88 (s, 3 H, CH), 2.91 (br m, 12 H, N(CH_2)$_2$(CH_2)$_2$(CH_2)), 1.71 (br m, 12 H, N(CH_2)$_2$(CH_2)$_2$(CH_2)), 1.38 (br m, 6 H, N(CH_2)$_2$(CH_2)$_2$(CH_2)), 1.27 (s, 27 H, C(CH_3)$_3$); ^{13}C{1H} NMR (benzene-d_6, 23 °C, ppm) 166.48 (s, *C*-O), 106.12 (s, *C*HN), 55.92 (s, N(*C*H_2)$_2$(CH_2)$_2$(CH_2)), 35.64 (s, *C*(CH_3)$_3$), 28.72 (s, C(*C*H_3)$_3$), 24.40 (N(CH_2)$_2$(*C*H_2)$_2$(CH_2)), 22.99 (s, N(CH_2)$_2$(CH_2)$_2$(*C*H_2)); IR (cm^{-1}) 2933 (m), 1612 (m), 1450 (m), 1381 (m), 1333 (s), 1146 (s), 1043 (m), 985 (m), 860 (m), 587 (s). Anal. Calcd for $C_{33}H_{60}YN_3O_3$: C, 62.34; H, 9.51; N, 6.61. Found: C, 60.42; H, 9.47; N, 6.46.

CHAPTER 4

Thermal Atomic Layer Deposition of Er_2O_3 Thin Films using an Erbium Enaminolate Precursor

4.1 Introduction

As described in the introduction chapter of this thesis, lanthanide oxide films have been extensively researched in the past few decades because of their potential multi-functionality in various technological fields, including optics, semiconductors, and catalysis. Among the lanthanide oxides, Er_2O_3 has attracted increased attention because of its high dielectric constant ($\kappa[Er_2O_3] \sim 14$),[233] large bandgap energy (~7 eV),[234] conduction band offset on Si (~3.5 eV),[235, 236] thermodynamic stability at high temperatures such as 900 °C,[237] high refractive indices (~1.6-1.7),[238] transparency in the UV and visible range (>90%),[239] and the limited tendency of hydroxylation owing to the small ionic radius.[240] Because of these remarkable properties, Er_2O_3 films have been investigated as high κ materials in CMOS devices, antireflection coatings in solar cells, protective coatings, and passivation layers for III-V semiconductors.[30, 67, 236, 241-243] In addition, Er_2O_3 is found to have a much higher concentration of effective light-emitting centers (Er) (~10^{22}) than in typical Er-doped Si-based materials (~10^{18}–10^{19}/cm^3), hence is an excellent material for use in optoelectronic materials.[244]

Deposition of Er_2O_3 films has been studied previously using various chemical and physical vapor deposition techniques, namely, molecular beam epitaxy (MBE),[67, 241] reactive evaporation,[243] electron beam evaporation,[244] sputtering,[68, 238, 245] sol-gel methods,[246] laser ablation,[247] MOCVD,[18, 248-250] and ALD.[97, 151, 157, 181, 251] Among these techniques, ALD can be considered the most efficient technique in terms of precise thickness control, conformal growth on 3D geometry substrates, and film growth at relatively low temperatures. Yet, the number of ALD studies reported in the literature regarding the ALD of Er_2O_3 is limited. In 2004, Pavisaari reported

the first ALD growth of Er_2O_3 films by using the β-diketonate complex $Er(thd)_3$ and ozone.[97] The process gave nearly stoichiometric Er_2O_3 films with a growth rate of 0.25 Å/cycle, but the films were contaminated with carbon, hydrogen, and fluorine impurities. In another study, Pavisaari and coworkers studied the ALD behavior of an Er amidinate precursor, $Er[CH_3C(N^tBu)_2]_3$, by using water and ozone as co-reactants.[151] The $Er[CH_3C(N^tBu)_2]_3$ precursor was found to be unreactive towards water co-reactant, with no evidence of film growth. By contrast, the $Er[CH_3C(N^tBu)_2]_3$ /O_3 process gave nearly stoichiometric films with low impurity levels. In 2014, Blanquart compared the ALD growth behavior of Er_2O_3 with $Er(^iPrCp)_3$, $Er(MeCp)_2$(iPr-amd) (amd = amidinate), and $Er(^nBuCp)_3$ precursors using either water or ozone as co-reactants.[126] Here, all three precursors were reported to give self-limited ALD growth for the Er precursors. However, the films were found to be contaminated with 2-7% of carbon impurities for both co-reactants. In 2013, Xu reported explored a guanidinate Er precursor, $Er[Me_2NC(NPr^i)_2]_3$ for ALD of Er_2O_3 using water as the co-reactant.[157] Among the Er_2O_3 ALD studies carried out so far, only the latter process has reported true self-limiting growth behavior with respect to both water and Er precursor. However, longer water pulse lengths were required (≥2 s) to obtain the saturative growth behavior for water. Taken together, these observations emphasize the need for alternative ALD precursors and processes to deposit high purity Er_2O_3 films with mild co-reactants such as water to avoid the detrimental effects caused by strong oxidants like ozone such as damaging the underlying substrates and causing carbon conaminations to the films.

In this work, the ALD growth behavior of Er_2O_3 was explored using the novel erbium enaminolate precursor, tris(1-(dimethylamino)-3,3-dimethylbut-1-en-2-olate)erbium(III) (**11**), with the use of water as the co-reactant. Complex **11** is found to be thermally stable up to about 265 °C and sublimes at 110 °C at 0.05 Torr.[176] TGA trace of **11** has a single step weight loss up to

it's decomposition temperature and the 50% weight loss of the TGA of **11** is around 220 °C with approximate delivery temperature ~120 °C. The melting point of **11** ranges from 93-95 °C, so it is in its liquid form at the delivery temperature. Liquid precursors are considered favorable over solid precursors as liquid precursors can maintain a constant surface area which help to provide a constant precursor vapor pressure. In contrast, surface area of solids changes over the deposition time and hence cannot maintain a constant flux of precursor vapors which can cause problems in reproducibility of the growth process. Further, small solid particles can be carried away with the carrier gas causing contaminations to the films..[90] Importantly, these enaminolate ligands have a higher pK_a value (pK_a ~25)[212] than water (pK_a ~14)[101] and hence were hypothesized to react rapidly with water during Er_2O_3 ALD.

4.2 Results and discussion

ALD Growth Characteristics of Er_2O_3 using $Er(L^1)_3$ and Water

Er_2O_3 film deposition studies using **11** (Figure 52) and water were carried out mainly on Si(100) with native oxide (~2 nm) and thermal SiO_2 (300 nm) substrates. During the depositions, substrate temperature, precursor pulse lengths, and the number of ALD cycles were varied to explore the ALD growth behavior. The reaction chamber pressure was maintained at 3-8 Torr for the growth experiments.

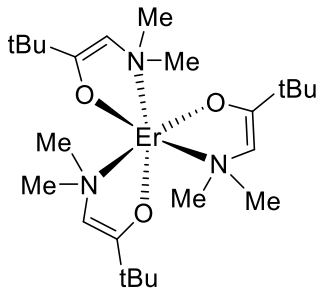

Figure 52. Er enaminolate precursor **11** used in this study.

Due to the favorable ALD precursor properties of **11** described earlier such as high volatility, moderate thermal stability, high reactivity with water, and low melting point, precursor **11** was envisioned as a promising ALD precursor. Hence, initial ALD studies were carried out using **11** along with water co-reactant to deposit Er_2O_3 films. Precursor **11** was delivered at the optimized delivery temperature of 125 °C and water was delivered at room temperature with the aid of high pure (99.999%, Airgas) N_2 carrier gas.

The key feature in ALD that stands out from other film deposition techniques is the self-limiting surface reactions taking place between the precursors and surface reactive sites. For each precursor used in ALD, there is a minimum amount of precursor dose that is needed to saturate the available surface reactive sites on the substrate. In order to probe the self-limiting growth behavior and to identify the optimum saturative precursor dose for each precursor, ALD experiments were carried out at 200 °C substrate temperature employing 1000 ALD cycles. The saturative growth behavior of **11** was evaluated first using the following pulse sequence: **11** (varied), N_2 purge (8.0 s), water (0.3 s), and N_2 purge (10.0 s). As depicted in Figure 53, saturative growth was observed at ≥4.0 s pulse length of **11** with a growth rate of 0.25 Å/cycle.

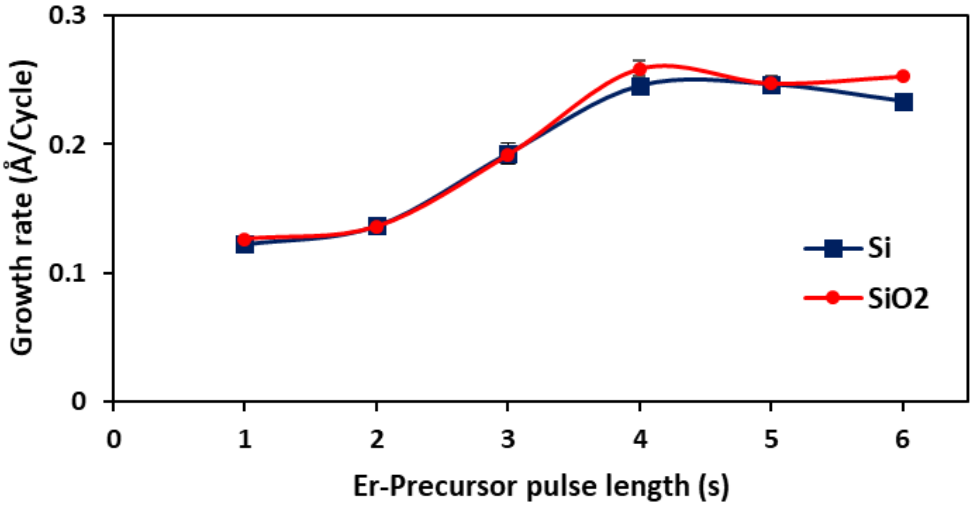

Figure 54. The growth rate of Er_2O_3 films on Si(100) and SiO_2 substrates at 200 °C after 1000 cycles as a function of pulse length of **11.**

Similarly, the self-limited growth behavior of the water precursor was evaluated next. The pulse sequence of **11** (5.0 s), N_2 purge (8.0 s), water (varied), and N_2 purge (10.0 s) was used for 1000 ALD cycles at 200 °C substrate temperature. As depicted in Figure 54, the growth rate became constant with a saturative growth rate of 0.25 Å/cycle after ≥0.2 s of water pulse length.

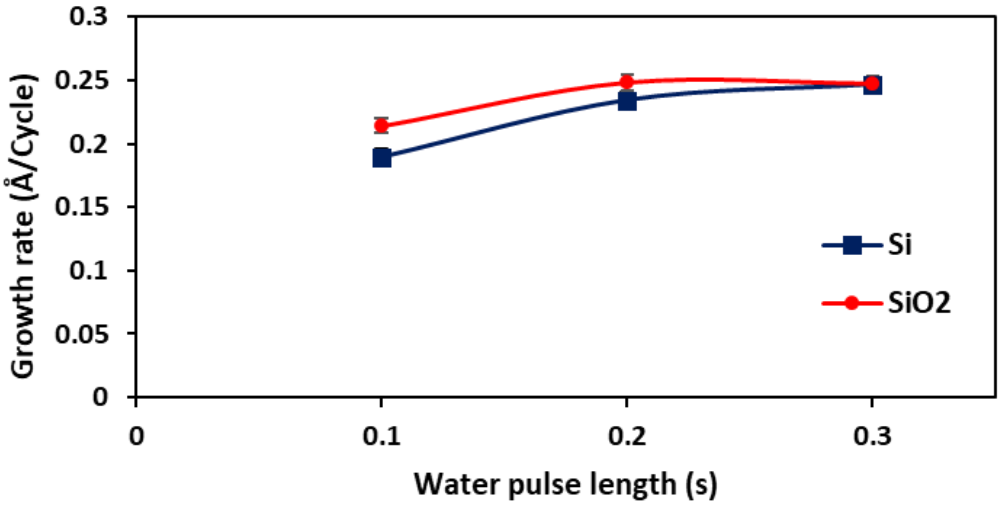

Figure 53. The growth rate of Er_2O_3 films on Si(100) and SiO_2 substrates at 200 °C after 1000 cycles as a function of water pulse length.

The majority of the Ln_2O_3 ALD processes reported in the literature have not shown true self-limited growth behavior for water. For instance, we have previously reported the ALD of Pr_2O_3 films using $Pr(iPrCp)_3$ and water, in which water did not show a saturative growth behavior, but rather a large thickness gradient across the film was observed.[59] Hence, the saturative growth behavior observed for both Er precursor **11** and water reported here is advantageous to obtain uniform Er_2O_3 thin films with high reproducibility.

This work only required 0.2 s of short water pulse length to obtain the saturative growth behavior. Short pulse lengths of water are favorable over longer pulse lengths for Ln_2O_3 film deposition, as the films themselves are hygroscopic.[11] Shortening the contact time of water vapor with the growing lanthanide oxide film could lead to a more controlled growth process.

To assess the dependence of the Er_2O_3 growth rate on the deposition temperature, ALD experiments were carried out in the temperature range of 150 to 275 °C, with 25 °C temperature increments. Depositions were carried out at optimized precursor pulse lengths (**11** (5.0 s)/N_2 purge (8.0 s)/Water (0.2 s)/N_2 purge (10.0 s)) with 1000 ALD cycles. As illustrated in Figure 55, the growth rate increased moderately from 0.20 Å/cycle at 150 °C to 0.25 Å/cycle at 175 °C and a constant growth of about 0.25 Å/cycle was maintained in the temperature range of 175 to 225 °C. This region with a constant growth rate can be considered as the ALD window for this process. The low growth rate observed below 175 °C is likely due to the insufficient thermal energy at deposition temperatures to overcome the energy required for surface reactions to take place. Above 225 °C, the growth rate decreased from 0.25 to about 0.15 Å/cycle. These lower growth rates detected above the ALD window could either be due to precursor decomposition before it reaches the reactor chamber as evidenced by solid-state decomposition of precursor **11** at 265 °C or due to the dehydration of surface-bound Er-OH groups, resulting in fewer surface reactive sites. The

presence of an ALD window is not necessary for an ALD process. Even outside the ALD window, self-limiting growth behavior can be maintained but with varying growth rates.[116]

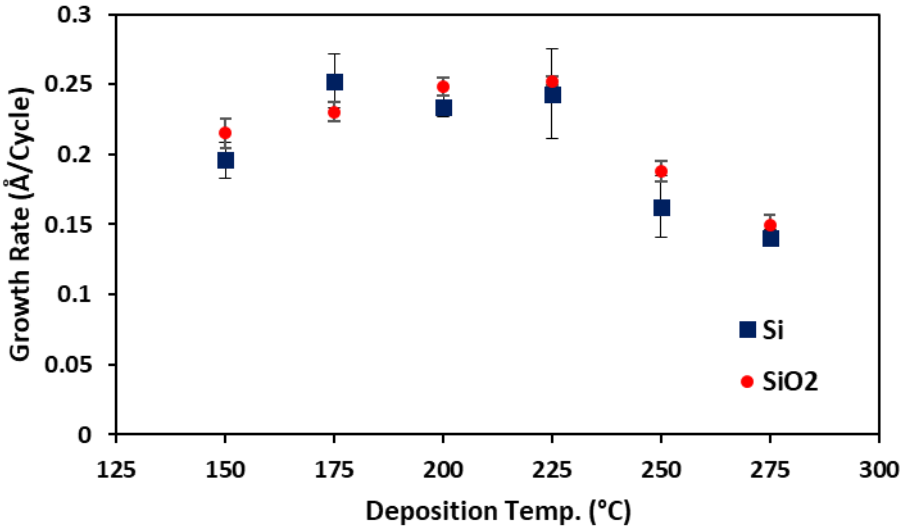

Figure 55. The growth rate of Er_2O_3 films on Si(100) and SiO_2 substrates as a function of substrate temperature.

The relationship between film thickness versus the number of ALD cycles was subsequently examined at 200 °C using the optimized precursor pulse lengths (5 s and 0.2 s for **11** and water, respectively). According to the data obtained (Figure 56), the film thicknesses varied linearly with the number of ALD cycles, which is a characteristic feature of an ideal ALD process. The slope of the linear regression analysis for these graphs indicated a growth rate of 0.31 and 0.29 Å/cycle on Si and SiO_2 substrates, respectively. This line did not pass through the origin, suggesting a nucleation delay of about 200 cycles. The growth rate of 0.3 Å/cycle observed in this work is similar to the growth rate of $Er(thd)_3/O_3$ process (0.25 Å/cycle),[97] but is considerably lower than the other Er_2O_3 ALD processes reported in the literature ($(CpMe)_3Er/H_2O$ ~1.5 Å/cycle,[252] $Er(NMe_2\text{-}Guan)_3/H_2O$ ~1.1 Å/cycle,[157] $Er[CH_3C(N^tBu)_2]_3/O_3$ ~0.51 Å/cycle[151]). However, the high reactivity of enaminolate precursor **11** used in this work towards mild oxygen source water

is advantageous compared to the $Er(thd)_3$ and $Er[CH_3C(N^tBu)_2]_3$ precursors that required ozone for the Er_2O_3 film growth.[97, 151]

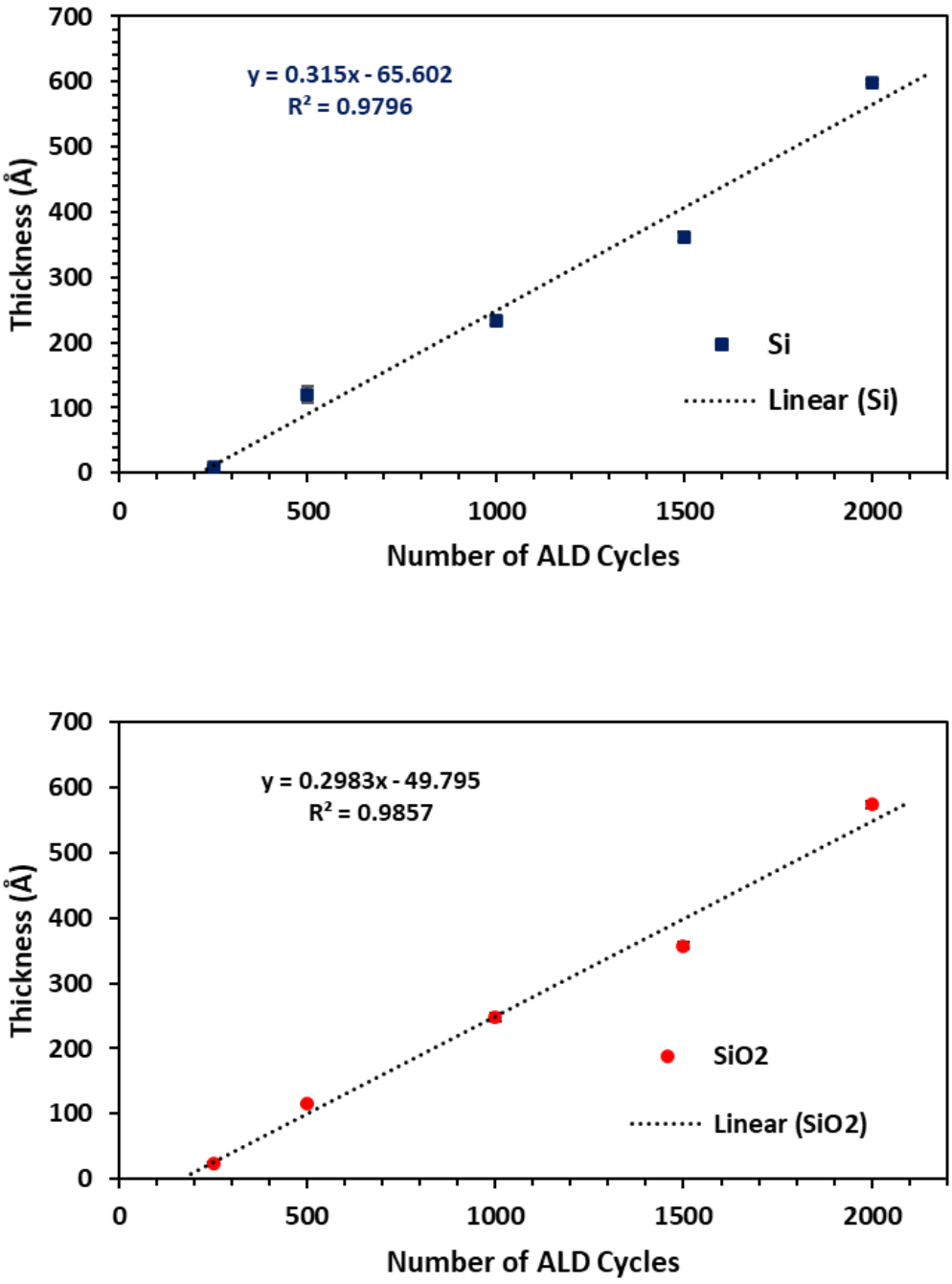

Figure 56. The dependence of Er_2O_3 film thicknesses on the number of ALD cycles on Si(100) (top) and SiO_2 (bottom) substrates at 200 °C substrate temperature.

As mentioned in the introductory chapter of this dissertation, the growth rate of an ALD process depends on several factors, including the reactivity of the precursor with the initial substrate surface and subsequent surface reactive sites, the reactivity of the surface-bound precursors with the incoming co-reactants, and the steric bulkiness of the precursors used. For water-based oxide ALD, the reactivity of the precursor molecules with water depends mainly on the pK_a of the ligands and the strength of the metal-ligand bonds. Metal precursors are expected to have high reactivity toward the water when the pK_a of the ligands is higher than that of water. Similarly, strong metal-ligand bonds are expected to have lower reactivity towards co-reactants and surface reactive sites. For instance, the pK_a of the β-diketone ligand is around 9 and is lower than that of water (~14).[101] Hence, the β-diketonate ligand does not act as a Bronsted base to abstract protons from water. Furthermore, the strong bonds between the Lewis acidic Ln^{3+} center and highly electronegative O donor atoms in diketonate ligands give strong Ln-O bonds. These factors result in lanthanide β-diketonate complexes being unreactive toward water during ALD to produce metal oxide films. In contrast, guanidinate and cyclopentadienyl lanthanide complexes can abstract protons from water due to higher pK_a values of guanidine (pK_a ~17) and cyclopentadiene (pK_a ~15) ligands than water.[157] Moreover, due to the strong oxophilic Ln^{3+} centers, lanthanide guanidinate complexes with Ln-N bonds and lanthanide cyclopentadienyl complexes with Ln-C bonds can be expected to react rapidly with mild oxygen sources such as water to form Ln-O bonds.[157]

The protonated enaminolate ligand used in this study has a pK_a around 23, which is higher than the pK_a of water.[212] Hence, enaminolate precursor **11** is expected to react rapidly with water. The relatively low growth rate observed for **11** in this work, compared to $Er(NMe_2\text{-Guan})_3]/H_2O$ process, may be attributed to the large size of the enaminolate precursor. Sterically crowded bulky

tert-butyl and dimethylamino groups present in the enaminolate ligands of **11** (Figure 57) could obstruct the surface reactive sites upon physisorption on the surface to a larger extent than the guanidinate and cyclopentadienyl precursors. As a result, the fraction of the surface reactive sites that get occupied during each ALD cycle by the precursor **11** is less. Hence, the growth per cycle becomes lower with **11**. Nevertheless, having a relatively low growth rate should not hinder the application of this process as long as it gives uniform and pure Er_2O_3 films.

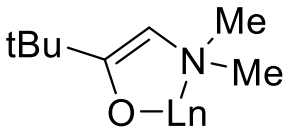

Figure 57. Schematic diagram of the sterically crowded chelate ring formed by the dimethyl substituted enaminolate ligand in **11**.

Film Analyses

Film Crystallinity

To determine the crystallinity of the as-deposited Er_2O_3 films, ~20-25 nm thick Er_2O_3 films grown at 150, 200, and 250 °C deposition temperatures on Si and SiO_2 substrates with 1000 ALD cycles were analyzed by GI-XRD. All of the films that were deposited at different temperatures were polycrystalline (Figure 58) and the reflections correspond to the cubic phase of Er_2O_3. The crystallinity of the films was enhanced considerably when the deposition temperature was increased from 150 to 250 °C. Moreover, the reduced full width at half maximum (FWHM) of the reflections observed at the higher deposition temperatures suggests the formation of larger crystallites. The latter behavior agrees with ~2 nm and ~6 nm crystallite size obtained using the Scherrer equation for the most intense (222) reflection for films deposited at 150 and 250 °C deposition temperatures, respectively.

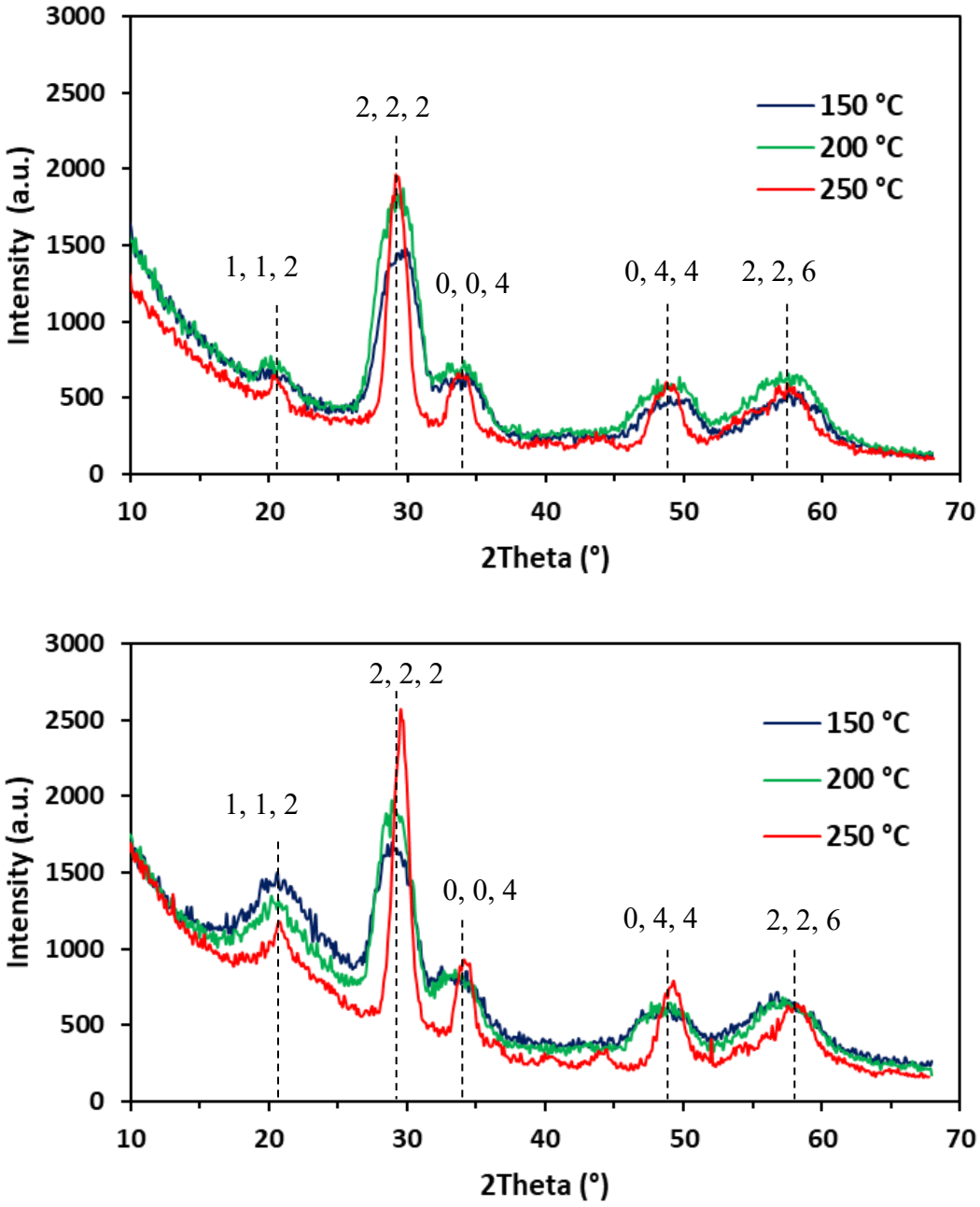

Figure 58. XRD patterns of ~ 20-25 nm as-deposited Er_2O_3 thin films deposited at 150, 200, and 250 °C on Si (top) and SiO_2 (bottom) substrates with 1000 cycles. The dotted lines represent the reference for cubic Er_2O_3 (COD 1010334 Er_2O_3).

Film Morphology

To analyze the film uniformity and texture, cross-sectional and top-down SEM analyses were carried out with films deposited on Si and SiO_2 substrates. Er_2O_3 films with 500, 1000, 1500, and 2000 cycles grown at 200 °C on Si substrates (Figure 59) were determined to be uniform and continuous according to the representative cross-sectional SEM images. A similar observation was obtained for films deposited on SiO_2 substrates. Further, as depicted in figure 60, SEM surface micrographs of ~ 37 nm thick Er_2O_3 films deposited on Si and SiO_2 at 200 °C gave nearly featureless, smooth, and continuous surfaces.

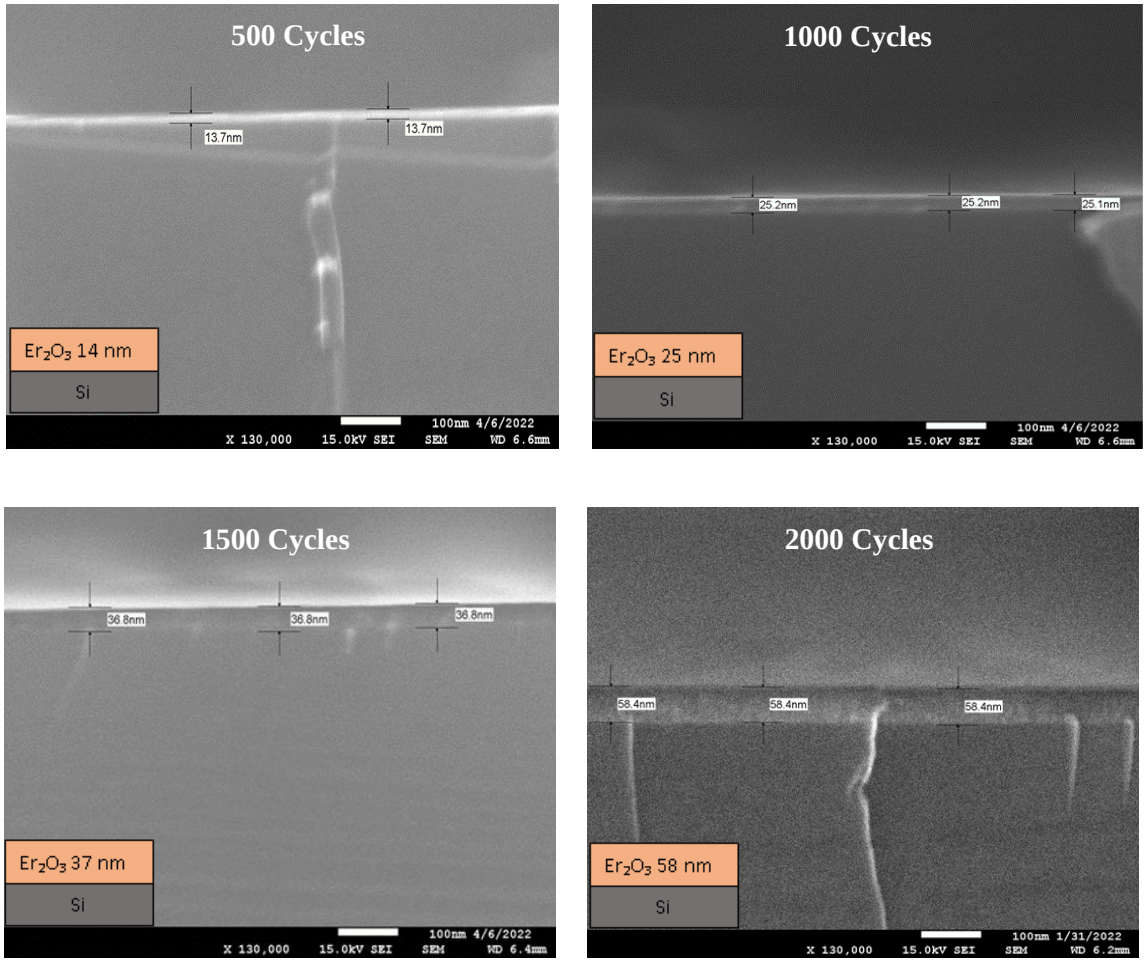

Figure 59. Cross-sectional SEM micrographs of Er_2O_3 thin films deposited with 500, 1000, 1500, and 2000 on Si substrates at 200 °C.

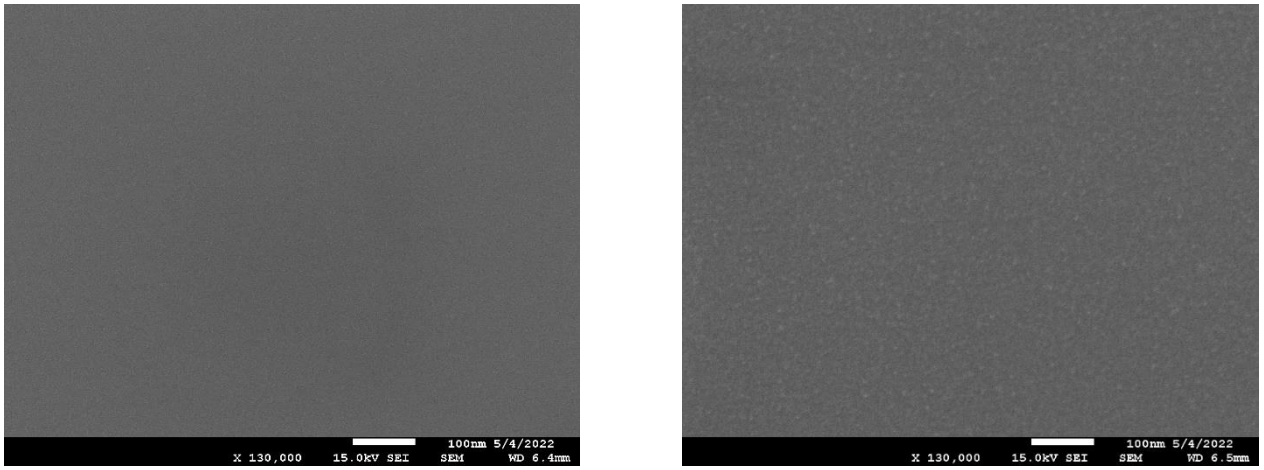

Figure 60. Surface SEM micrographs of Er_2O_3 thin films deposited with 1500 ALD cycles on Si (left) and SiO_2 (right) substrates at 200 °C.

Film Composition

To investigate the elemental composition and purity of the films, ~35 nm thick Er_2O_3 films deposited at 200 and 225 °C on Si substrates were subjected to X-ray photoelectron spectroscopic (XPS) analyses. Figure 61 shows the Er $4d_{5/2,}$ O 1s, C 1s, Si 2s, and Si 2p XPS binding energy spectra for the Er_2O_3 film deposited at 200 °C. All the ionizations are fitted using a Lorentzian-Gaussian function (fitting curves are not shown) and the binding energy of the C1s ionization (284.5 eV) of adventitious carbon present before sputtering the film surface was used as the reference to correct the binding energy shifting in ionizations that occur due to charging.

According to the spectra collected, the surface of the as-deposited Er_2O_3 film (0 min Ar sputter) consisted of Er, O, and C. The characteristic Er $4d_{5/2}$ ionization of Er_2O_3 film appeared at 168.14 eV binding energy (Figure 61 (a)) and the intensity of the ionization increased significantly after the removal of the surface layer by argon ion sputtering. Two ionizations were observed in the O 1s spectral region (Figure 61 (b)); the ionization at the lower binding energy side (528.8 eV) corresponds to the O 1s of Er_2O_3 while the ionizations at the higher binding energy side (531.17 eV) can be attributed to the formation $Er(OH)_3$. Interestingly, the O 1s spectra collected after 2 minutes of Ar ion sputtering show a drastic decrease in the intensity of the peak at the higher

binding side. The latter observation indicates the absence of $Er(OH)_3$ phases in the bulk of the Er_2O_3 film and only the surface layer of the film has reacted with the ambient moisture during the exposure of the film to the atmosphere. This observation is common for Ln_2O_3 films because of their hygroscopic nature.[68, 253] O 1s and Er $4d_{5/2}$ spectra with similar shapes and binding energies are reported in the literature for Er_2O_3 films.[68, 157, 244, 245] The carbon contaminants on the film surface were almost completely removed after 2 minutes of argon ion sputtering (Figure 61 (c)). This suggests the absence of carbon contamination in the film bulk due to incomplete removal of the ligands or precursor decomposition. No ionizations were observed at Si 2s (~151 eV) and N 1s (397 eV) core binding energy levels, which indicated the absence of Si and N in the film (Figure 61 (d) and (f)). All of these XPS data confirm the presence of pure Er_2O_3 in the bulk of the film.

It should be noted that there is a broad feature appearing around 100 eV binding energy in the Si 2p spectral region shown in Figure 61 (e). However, according to the Si 2s region shown in Figure 61 (d), there are no Si 2s signals that follow the same trend that appear in the Si 2p region. Hence, this broad feature is believed not to arise from Si. A similar broad feature in the Si 2p region was observed for Er_2O_3 films deposited using electron beam evaporation, which the authors claim arose from the Er MVV Auger ionization rather than from Si 2p.[244]

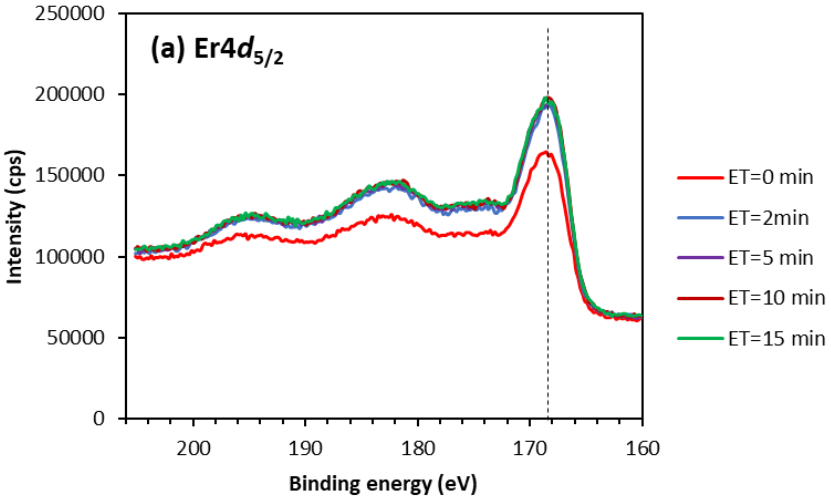
(a) Er4$d_{5/2}$
Intensity (cps)
250000
200000
150000
100000
50000
0
200
190
180
170
160
Binding energy (eV)
ET=0 min
ET=2min
ET=5 min
ET=10 min
ET=15 min

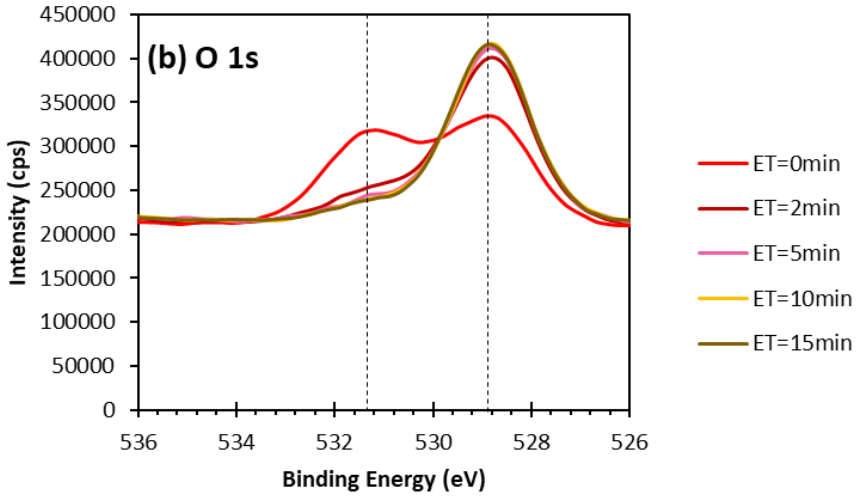
(b) O 1s
Intensity (cps)
450000
400000
350000
300000
250000
200000
150000
100000
50000
0
536
534
532
530
528
526
Binding Energy (eV)
ET=0min
ET=2min
ET=5min
ET=10min
ET=15min

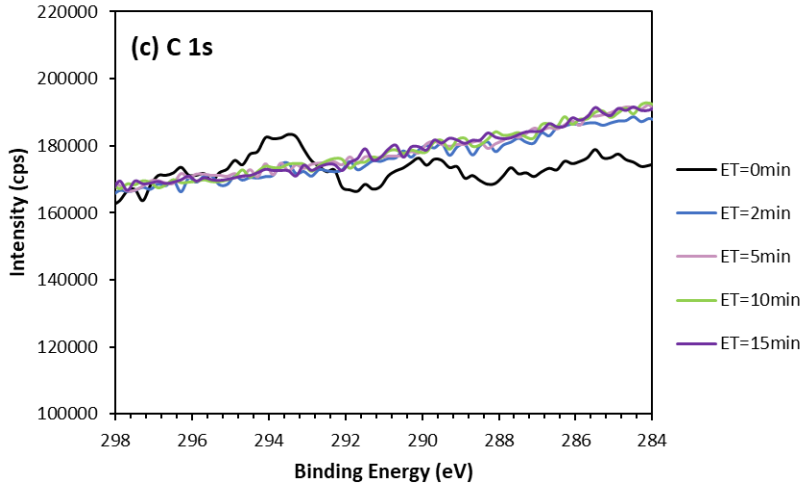
(c) C 1s
Intensity (cps)
220000
200000
180000
160000
140000
120000
100000
298
296
294
292
290
288
286
284
Binding Energy (eV)
ET=0min
ET=2min
ET=5min
ET=10min
ET=15min

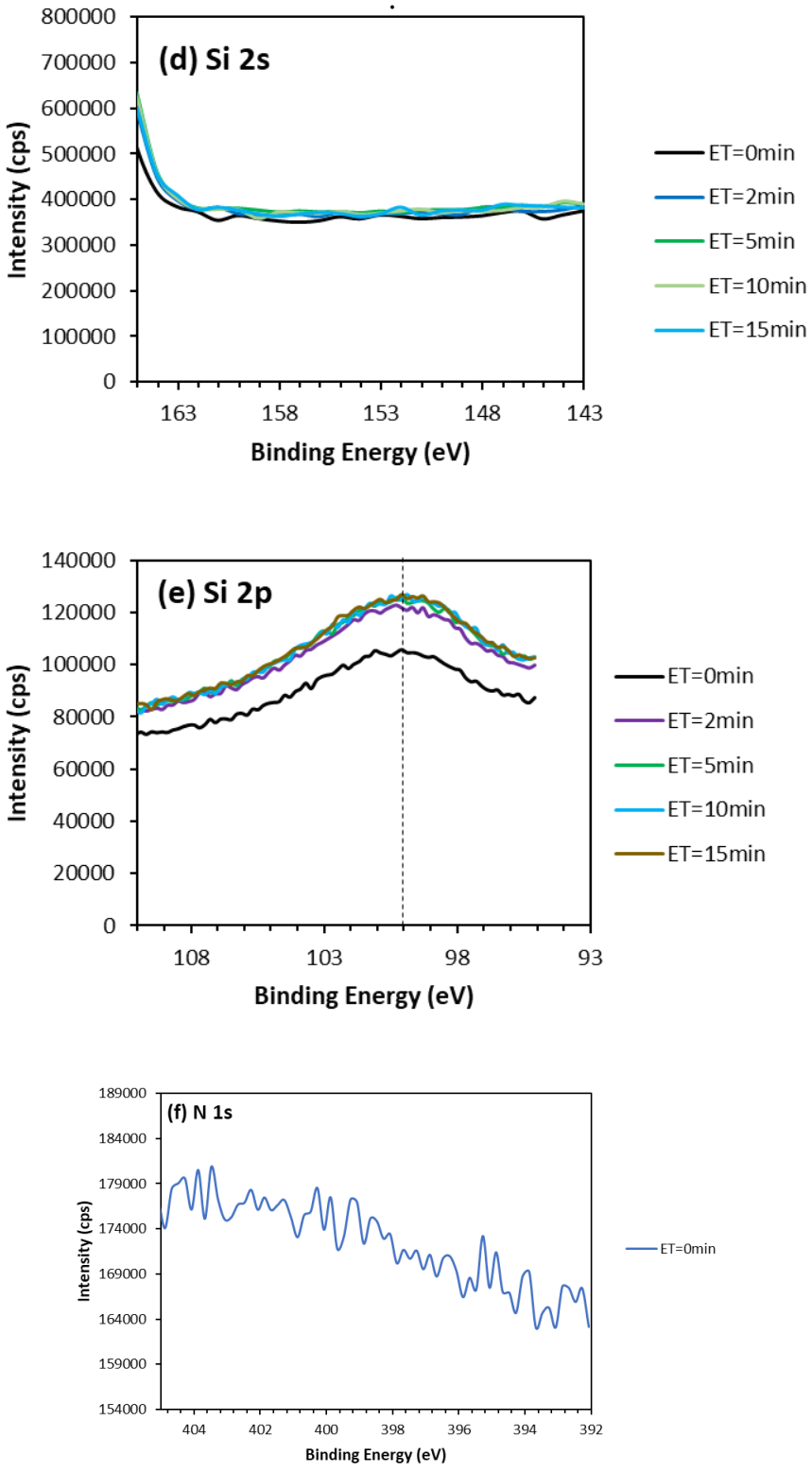

Figure 61. High-resolution XPS spectra of Er $4d_{5/2}$ (a), O 1s (b), C 1s (c), Si 2s (d), Si 2p (e), and N 1s (f) of the Er_2O_3 thin film grown on a Si substrate at 200 °C with 1500 cycles.

Figure 62 illustrates the depth profile obtained for a 35 nm thick Er_2O_3 film deposited on a Si substrate at 200 °C with 1000 cycles. Depth profiling was done by removing the surface layers by argon ion sputtering with 300 eV sputter energy. A uniform distribution of Er and O atoms throughout the film was observed and the bulk of the film is pure with no carbon, nitrogen, or silicon contamination. The average Er:O ratio observed from the XPS data for the film deposited at 200 °C is approximately 1:1.63, which is close to the Er:O atomic ratio of 1:1.5 for Er_2O_3. Similar XPS data were obtained for the Er_2O_3 film deposited at 225 °C on a Si substrate.

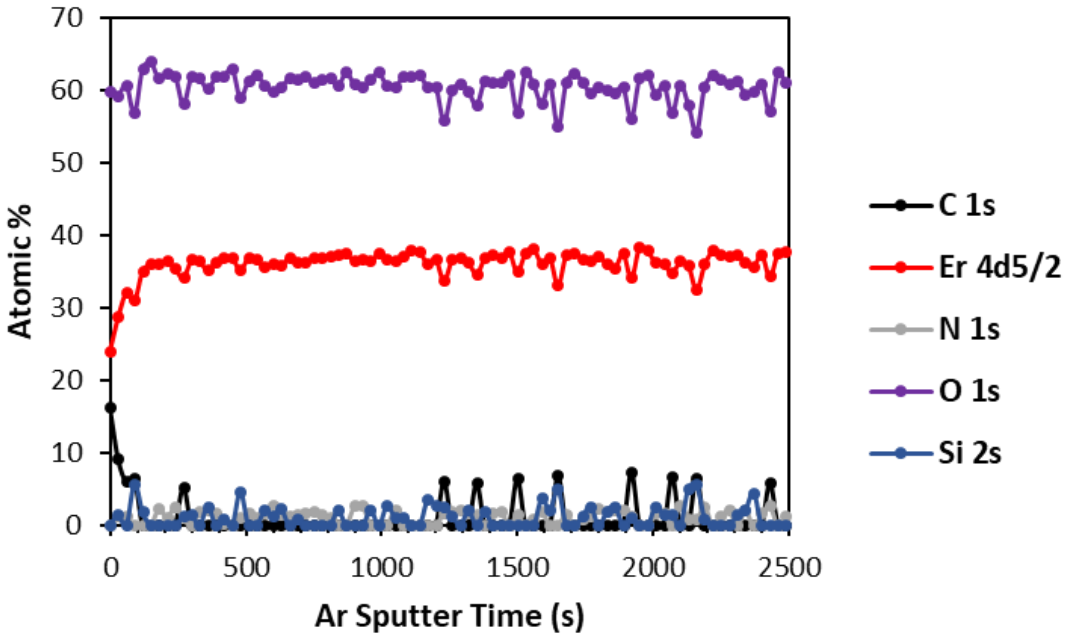

Figure 62. XPS depth profile of a 35 nm thick Er_2O_3 thin film grown on a Si substrate at 200 °C with 1500 cycles.

XRR and AFM Measurements

In many of thin film applications presence of atomically flat smooth surfaces is desired. Surface roughness is associated with the thin film deposition process and surface roughness has a significant impact on the optical, electrical, and mechanical performances of thin-film based devices. Hence, surface roughness is an important parameter that can be optimized to increase the performance of thin-film based devices.[254] In general, surface roughness of thin films changes with several parameters such as the thickness of the film, film deposition method, deposition temperature, and crystalline/amorphous nature of the film.[255] To determine the surface roughnesses of as-deposited 33 nm (by ellipsometry) Er_2O_3 films deposited at 200 °C on Si and SiO_2 substrates, atomic force microscopy (AFM) analyses were carried out. We would like to thank Dr. Rui Liu from the University of Wisconsin, Madison for conducting these AFM experiments (Figure 63). According to the AFM measurements obtained, root mean square (RMS) roughness values over 1 μm^2 x 1 μm^2 area on both Si and SiO_2 substrates were 1.76 and 0.75 nm, respectively. These RMS values suggest 33 nm Er_2O_3 film deposited by ALD at 200 °C substrate temperature on Si and SiO_2 substrates are smooth with only about 5.3% (on Si) and 2.2% (on SiO_2) roughness.

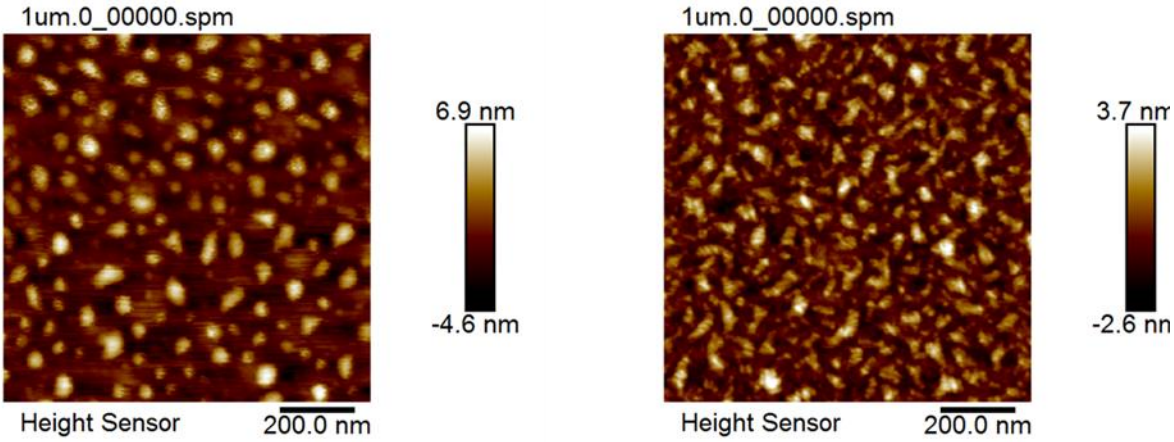

Figure 63. AFM images of 33 nm thick Er_2O_3 thin films grown on Si (left, rms = 1.76 nm) and SiO_2 (right, rms = 0.75 nm) substrates at 200 °C.

For further evaluation of film density, thickness, and roughness, X-ray reflectivity (XRR) measurements were collected on the same samples used for AFM. These XRR measurements were carried out by Prof. Donald Savage from the University of Wisconsin, Madison (Figure 64). XRR fitting data further confirmed the Er_2O_3 film thicknesses (31.3 nm on Si and 31.7 nm on SiO_2) determined using ellipsometry (33 nm on both Si and SiO_2) to be accurate. The Er_2O_3 film density extracted from XRR fitting data for the film deposited on Si was about 7.3 gm/cm^3 while the film deposited on SiO_2 was around 7.1 gm/cm^3. These density values extracted from XRR correspond to about 85% of the bulk Er_2O_3 density (8.64 gm/cm^3). In addition, XRR data also revealed smooth Er_2O_3 films with 0.575 nm (1.8%) and 1.0 nm (3.2%) roughness values for the 31 nm thick Er_2O_3 films on Si and SiO_2, respectively. The surface roughness of Er_2O_3 on a Si substrate obtained from XRR is in good agreement with the previously reported 0.598 nm roughness value of a 20 nm thick Er_2O_3 film deposited on Si by ALD.[157]

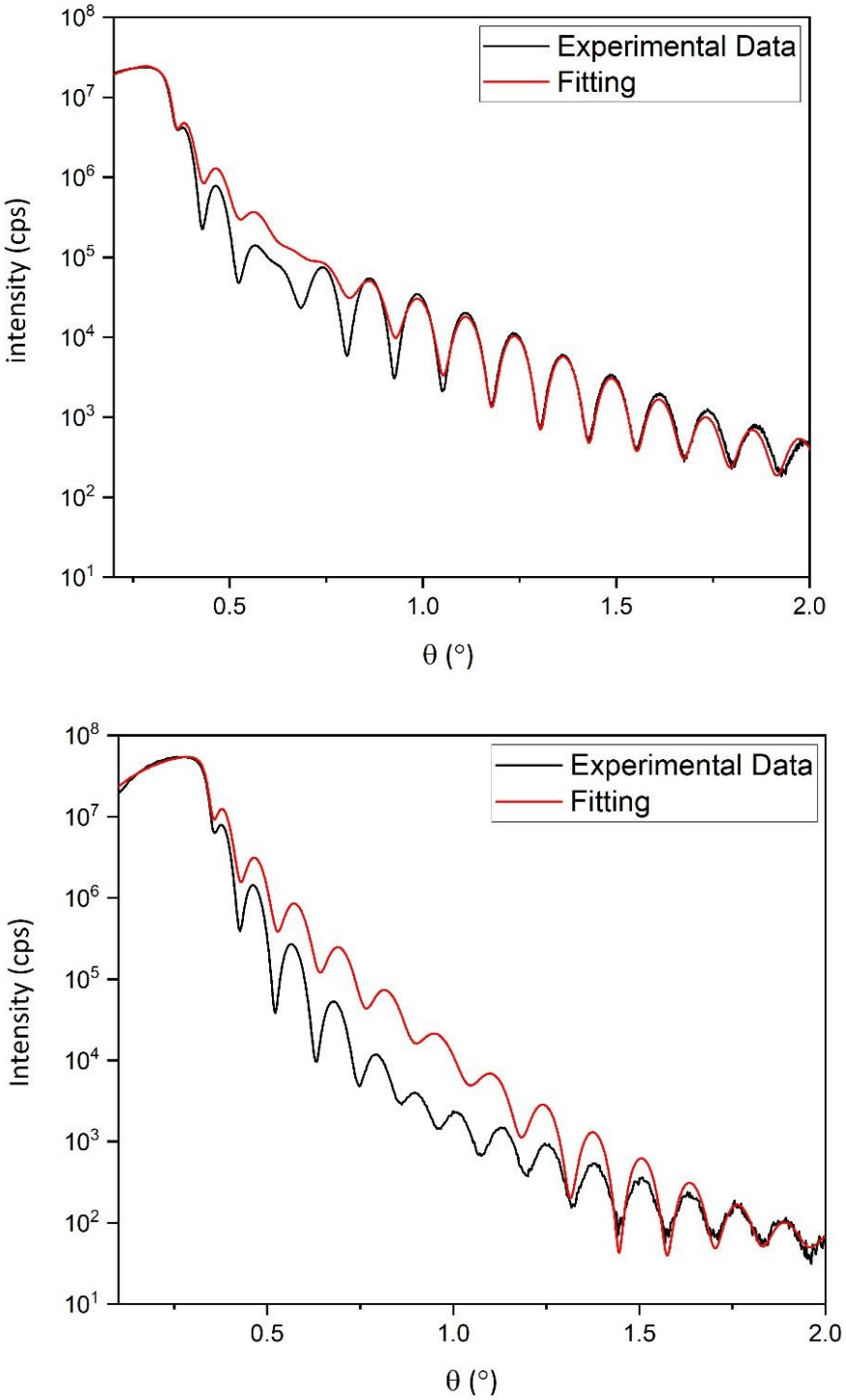

Figure 64. XRR fitting curves of 33 nm thick Er_2O_3 thin film grown on Si (top, density = 7.3 gm/cm^3) and SiO_2 (bottom, density = 7.1 gm/cm^3) substrates at 200 °C.

Growth Behavior of Er_2O_3 on Metallic and Other Non-metallic Substrates

To investigate the substrate selectivity of the ALD process reported here, the growth of Er_2O_3 films on substrates other than Si and SiO_2 was carried out at 200 °C using the optimized pulse sequence obtained for Si and SiO_2 substrates (**11** (5 s)/N_2 (8 s)/H_2O (0.2 s)/N_2 (10 s)). Depositions were conducted on Cu, Ru, TiN, Pt, and W substrates. Cross-sectional SEM micrographs revealed Er_2O_3 film depositions on all substrates with similar Er_2O_3 growth rates to that on Si and SiO_2 substrates (Figure 65), thereby indicating that Er_2O_3 can be grown on both metallic and amorphous substrates. This growth behavior of Er_2O_3 on metallic substrates can be useful for applications such as heat and corrosions resistant coatings and catalysis on metallic substrates.[256]

GI-XRD was carried out for films deposited on Cu, Ru, TiN, Pt, and W substrates described in the previous paragraph. Similar to the results observed with Si and SiO_2 substrates, films are polycrystalline cubic and crystal grains are randomly oriented. The corresponding GI-XRD patterns are shown in Figure 66.

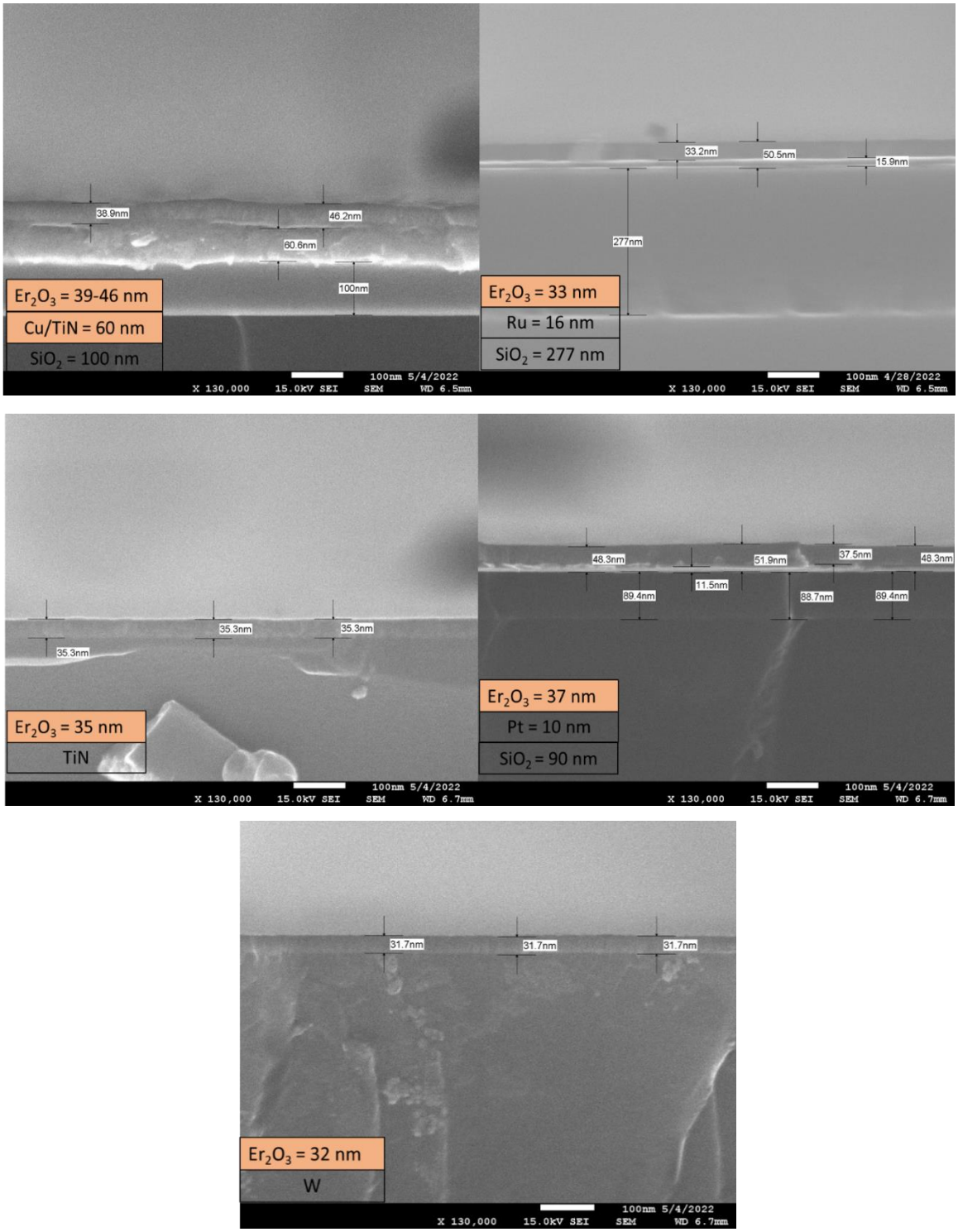

Figure 65. SEM images of Er_2O_3 thin films grown on (a) Cu, (b) Ru, (c) TiN, (d) Pt, and (e) W substrates at 200 °C with 1500 ALD cycles.

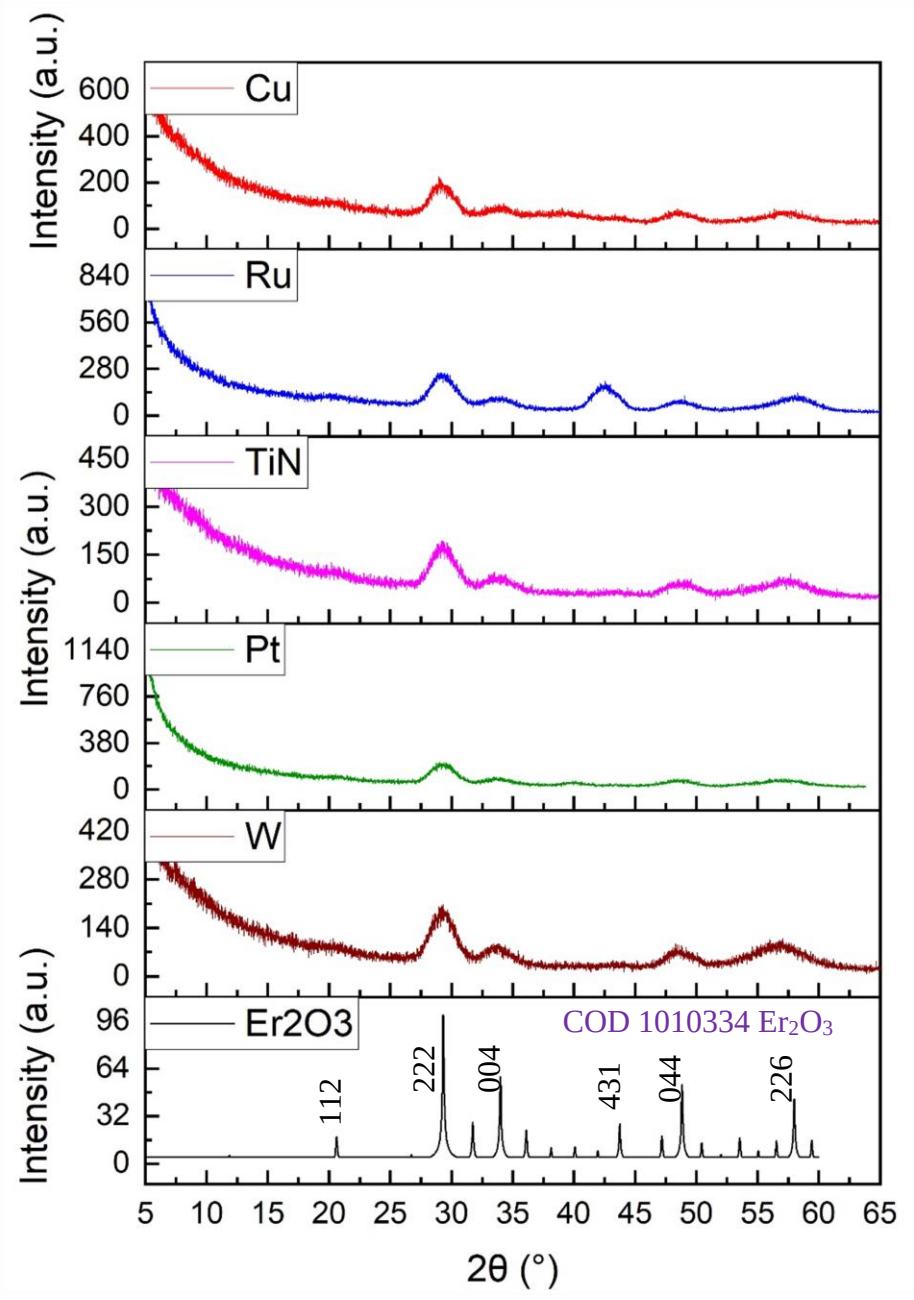

Figure 66. GI-XRD pattern of as-deposited Er_2O_3 thin films grown on Cu, Ru, TiN, Pt, and W substrates at 200 °C with 1500 ALD cycles.

Growth Behavior of Er_2O_3 on Single Crystal Substrates

The crystalline nature of Er_2O_3 films was further investigated on single-crystal substrates, and depositions were carried out on single crystal $SrTiO_3$ (001) and C-plane sapphire (0001) substrates. $SrTiO_3$ substrates (STO) were subjected to annealing (1000 °C) prior to depositions to obtain the TiO_2-terminated phase, whereas C-plane sapphire substrates were annealed (1400 °C) to obtain atomically smooth surfaces. Annealing of both substrates (STO and sapphire) was carried out following previously established procedures.[257, 258]

The motivation behind this work was to study the epitaxial growth of Er_2O_3 films with preferred 00L or 000L orientation on atomically smooth single-crystal STO (001) and sapphire (0001) substrates, respectively. However, as shown in Figures 67 and 68, Er_2O_3 films deposited on both substrates were polycrystalline and did not show an epitaxial relationship with the substrates at the deposition temperature of 200 °C. Even though the films grown on these single-crystal substrates did not follow the crystal orientation of the substrate exactly, film grown on STO (001) showed a 004 preferred texture around 2Theta = 34°.

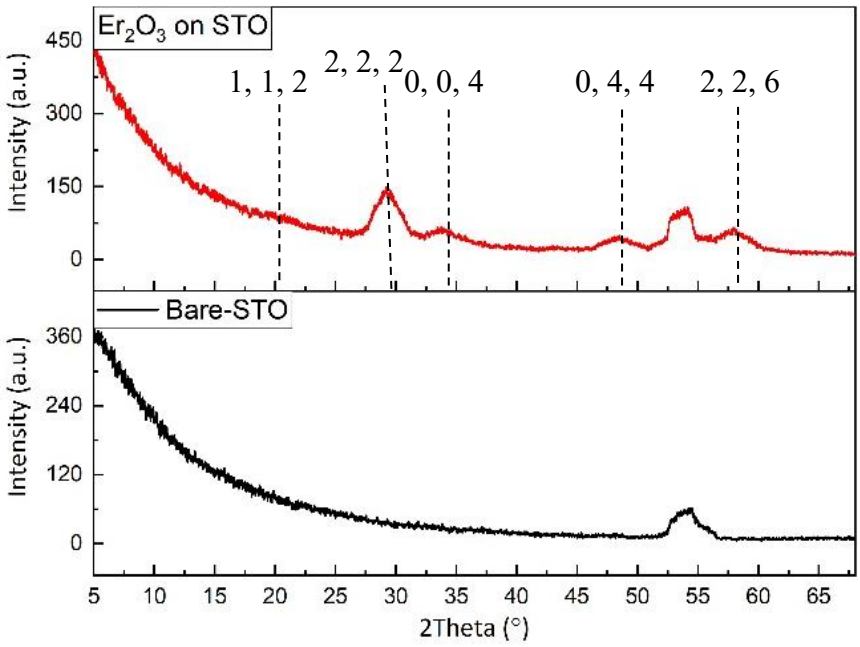

Figure 67. GI-XRD patterns of as-deposited Er_2O_3 thin films grown on STO substrate at 200 °C with 1500 ALD cycles.

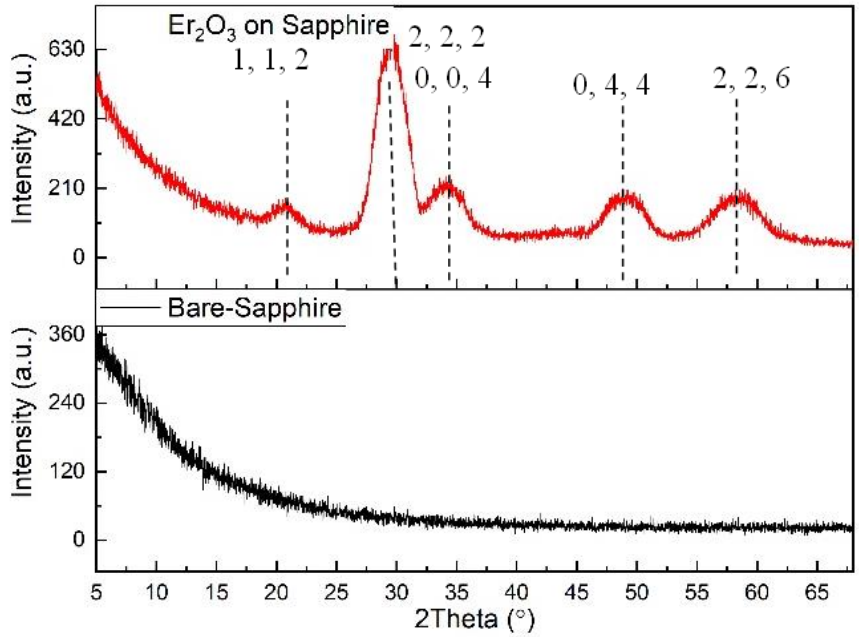

Figure 68. GI-XRD patterns of as-deposited Er_2O_3 thin films grown on sapphire substrates at 200 °C with 1500 ALD cycles.

4.3 Conclusions

This study has successfully demonstrated the ALD growth of Er_2O_3 films using the novel Er-enaminolate complex **11** and water as precursors. Self-limited growth was established for both **11** and water, with a growth rate of about 0.25 Å/cycle within the ALD window of 175-225 °C, using the pulse sequence of precursor **11** (5 s), N_2 (8 s), water (0.2 s), N_2 (10 s) on Si and SiO_2 substrates. This process showed a linear relationship between the thickness and the number of deposition cycles. There was a nucleation delay of up to about 200 cycles, after which the thickness increased linearly with the increase in the number of cycles. The as-deposited Er_2O_3 films showed polycrystalline nature according to GI-XRD and XPS analyses of the films revealed high-quality films with no carbon or silicon contaminations in the bulk of the film. Atomic percentages of elements abstracted from the XPS data suggest an Er:O ratio of 1:1.63, a value close to the Er:O ratio in Er_2O_3. Furthermore, XRR and AFM data suggest the presence of smooth film surfaces with low RMS roughness values. SEM micrographs of the films deposited on all the substrates studied (Si, SiO_2, Cu, Ru, TiN, Pt, W) show uniformly thick films. This ALD process can be considered as one of the very few Ln_2O_3 processes reported in the literature that demonstrate self-limited growth for both metal precursor and water co-reactant. These lanthanide enaminolate precursors are a viable alternative to lanthanide β-diketonate precursors, which show no reactivity towards water, and also for lanthanide precursors containing Si in the ligand backbone, which can cause Si contamination in the films. Hence, the ALD process established in this work using precursor **11** and water can be used to obtain high purity Er_2O_3 films in order to study and expand the potential applications of Er_2O_3 films, such as high κ materials and optoelectronic materials. The proven ability of this process to deposit Er_2O_3 on metallic substrates makes this process useful to

deposit Er_2O_3 as anti-reflection, heat, and corrosion-resistant coating on different types of substrates.

4.4 Experimental Section

ALD experiments were carried out using a Picosun R-75BE ALD reactor within the temperature range of 150-275 °C. Depositions were carried out mainly on thermal SiO_2 (~300 nm) on Si and Si with native oxide (~2 nm) substrates. Additional depositions were carried out on PVD grown Cu/TiN (~60 nm)/SiO_2 (100 nm)/Si, Ru (~16nm)/SiO_2, TiN, Pt (~10 nm/SiO_2), W, and single-crystal $SrTiO_3$ (STO) and sapphire substrates. Depositions on all of the substrates except on STO and sapphire were carried out without prior cleaning. STO and sapphire substrates were subjected to cleaning procedures reported in the literature, before depositions.[257, 258] ALD reactor chamber pressure was maintained at 3-8 Torr during the depositions and ultra-high purity nitrogen (99.999%, Airgas) was used as both the carrier and purge gas. Erbium precursor **11** was synthesized on large scale following the procedure described in Chapter 3. Freshly sublimed Er precursor **11** was delivered using a Picosolid booster at 125 °C optimized temperature and water was delivered using a conventional vapor draw bubbler at 23 °C.

Film thickness was measured using spectroscopic ellipsometry (J. A. Woollam Co. Alpha-SE) with a wavelength of 632.8 nm and an incident angle of 65° and was confirmed by cross-sectional SEM (JEOL-6510LV) and XRR. XRR measurements were performed at the University of Wisconsin-Madison by Prof. Donald Savage using a PANalytical Empyrean X-ray diffractometer with CuK_α radiation. Film crystallinity was determined by grazing-incidence X-ray diffraction using Bruker D8 Advance diffractometer with Cu Kα radiation at 1.54 Å wavelength and an incident angle of $\omega = 0.5°$ with the detector (2θ) scan range of 5-68°. Surface morphology was explored using a Bruker icon AFM operated in the tapping mode and AFM experiments were

performed at the University of Wisconsin-Madison, by Dr. Rui Liu. XPS analysis was carried out to determine the film composition using a NEXSA, ThermoFisher Scientific spectrometer, equipped with a monochromatic Al K_α (1486.7 eV) X-ray source operating at 12kV and 6 mA.

CHAPTER 5

Conclusions

The main focus of this dissertation work was to introduce new classes of volatile and thermally stable lanthanide complexes that can be employed to deposit Ln_2O_3 films by ALD together with water as a co-reactant. We hypothesized that ligand systems with weak Bronsted acid character (high pK_a) will make lanthanide complexes with appropriate reactivity with mild oxidants such as water. Further, when finding ligand systems, priority was given to bidentate ligand systems owing to their increased ability to saturate the coordination spheres of large lanthanide ions via the additional donor atom and to increase the thermal stability via chelation. Accordingly, this dissertation reports the synthesis, characterization, and ALD precursor property evaluation of two new classes of lanthanide complexes using *tert*-butyl hydrazonate and enaminolate ligand systems and demonstrates the ALD growth behavior of Er_2O_3 thin films using a newly synthesized Er-enaminolate precursor.

Chapter 2 describes the synthesis, characterization, and precursor property evaluation of a series of lanthanide complexes (La, Pr, Gd, Er, Lu, and Y) using *tert*-butyl hydrazonate ligand. These particular lanthanides were selected to probe the structural and precursor property variation across the early (La, Pr), mid (Gd), and late (Lu) lanthanide ions. Y^{3+} complexes were synthesized due to their similar chemical behavior and properties to those of mid to late lanthanides. Six new complexes were synthesized and all were volatile and sublimed in the 155-185 °C temperature range at low pressure. These complexes are thermally stable and melted along with decomposition at their corresponding decomposition temperatures (~290 °C for **2-6** and ~250 °C for **1**). The *tert*-butyl groups in the complexes were highly disordered. Due to the highly disordered ligands around the lanthanide centers, visualizing the exact structures was difficult but all complexes subjected to

single-crystal X-ray diffraction showed similar diffraction patterns. All complexes were monomeric. TGA traces of the complexes showed single-step weight losses. Complex **6** (Y) was thermally stable for 24 h at and above its sublimation temperature of 160 and 190 °C and for 1 h at 275 °C, hence is a promising precursor for the ALD of Y_2O_3.

Chapter 3 introduces the new lanthanide complexes synthesized using enaminolate ligands. Similar to Chapter 2, a series of selected complexes were synthesized to cover the lanthanide series. The ligand substituents on the N atoms were varied to tune the volatility and thermal stability. A total of 15 complexes was synthesized and characterized for structure and precursor properties. Complexes **7-21** are volatile. Complexes with dimethyl-substituted L^1 ligands showed the highest volatility (sublimation temperatures of 95-120 °C at 0.5 Torr) and pyrrolidine (L^2) and piperidine (L^3) substituted complexes (sublimation temperatures of 140-160 °C at 0.5 Torr) had lower but similar volatilities to each other. However, complexes with L^3 ligands showed the highest thermal stabilities, and complexes with L^2 had the lowest thermal stabilities. Complexes **7-9** crystalized as neutral ligand adduct complexes due to the hydrolysis during crystallization and loss of the neutral ligand was observed during TGA, which gave two-step weight losses for **7-9**. Complexes **10-12** obtained by both direct sublimation of the crude and the neutral ligand adduct complexes were free of the neutral ligand as expected, and TGA traces of **10-12** have single-step weight losses. Complexes **7-21** are air and moisture sensitive. Due to the high pK_a of the enaminolate ligands[47] compared to water and one of the Ln-ligand bonds being a more reactive Ln-N bond, these complexes are expected to react with water to deposit Ln_2O_3 films.

Chapter 4 of this dissertation demonstrates the ALD growth behavior of lanthanide enaminolate complexes introduced in Chapter 3 with water co-reactant. As a starting point, the growth of Er_2O_3 films was explored owing to their high application potential among all lanthanide

oxides. Additionally, Er_2O_3 is less hygroscopic than earlier lanthanide oxides. Complex **11** ($Er(L^1)_3$) was selected as the most favorable precursor among $Er(L^1)_3$, $Er(L^2)_3$, and $Er(L^3)_3$ because of the higher volatility (low T_{sub}), sufficient thermal stability (T_{dec} ~ 260 °C), and the lower melting point of $Er(L^1)_3$ compared to $Er(L^3)_3$. Depositions were carried out primarily on Si and SiO_2 substrates and delivery temperatures for **11** and water were 125 and 25 °C, respectively. Complex **11** was a liquid at the delivery temperature. Depositions were carried out in the temperature range of 150-275 °C and ALD widow of 175-225 °C was observed with a constant growth rate of 0.25 Å/cycle. Saturative growth behavior was observed for both precursor **11** and water at ≥4.0 s and 0.2 s precursor pulse lengths, respectively. A linear relationship between the thickness and the number of ALD cycles was observed with a slope of 0.3 Å/cycle. Nucleation delays of about 200 cycles were observed on both Si and SiO_2 substrates. As-deposited films were polycrystalline by GI-XRD and XPS revealed pure films with <1% carbon or nitrogen contaminations. Based on the XPS depth profile, elements were distributed uniformly throughout the film. XRR and AFM data revealed deposition of smooth films with a density of around 7.3 gm/cm^3. Cross-sectional SEM images revealed Er_2O_3 films with uniform thicknesses. Depositions on single crystalline substrates did not show epitaxial growth, however, the preferred 004 texture was observed on single-crystal STO (001) substrates along with other randomly oriented grains. Growth of Er_2O_3 was observed on metallic substrates as well. Deposition carried out on metallic substrates had similar results to those on Si and SiO_2.

CHAPTER 6

Future Directions

Expanding the ALD of Binary and Ternary Lanthanide Oxide Films with Hydrazonate and Enaminolate Complexes

Herein, precursor properties of two novel lanthanide precursor classes (hydrazonates and enaminolates) were introduced and their precursor properties were evaluated. Both precursor classes have favorable precursor properties. However, for the time being, only ALD of Er_2O_3 was studied in this dissertation using the $Er(L^1)_3$ enaminolate precursor **11**. Since promising results were obtained with **11**, future ALD studies can be expanded to study the ALD growth behavior of other Ln_2O_3 films using the remaining enaminolate precursors introduced in Chapter 3.

One of the key drawbacks that limit some of the application of lanthanide oxides, especially with the early lanthanide oxides, is their hygroscopic nature. This can be overcome by the incorporation of inert metal oxide such as Al_2O_3 into lanthanide oxides.[204, 259-261] There are multiple studies reporting the ALD of ternary lanthanide oxide films ($LnMO_3$) which exhibit similar or improved properties such as high dielectric constants, high chemical and thermal stability, and 2DEG properties relative to that of binary lanthanide oxides.[52, 112, 262-264] We have previously demonstrated the ALD of $PrAlO_3$ to study the solid phase epitaxy of $PrAlO_3$ grown on $SrTiO_3$ single crystal substrates to explore its 2DEG properties.[59] Similarly, future ALD studies can be carried out to obtain stoichiometric $LnAlO_3$ films, starting from $ErAlO_3$.

Further, ALD studies can be carried out to test the ALD growth behavior of Ln_2O_3 using *tert*-butyl hydrazonate complexes introduced in Chapter 2. Particularly, $Y(^{tBu}Hyd)_3$ which showed good volatility and long-term thermal stability will be the best point to start.

Improving the Precursor Properties of Lanthanide Enaminolate Complexes

The enaminolate ligand skeleton has some useful characteristics that make it an ideal ligand system for lanthanide ALD precursor development. It is a bidentate ligand. Hence, thermal stability of metal complexes may be increased via chelation. More importantly, the high pK_a value of enaminolate ligand system compared to water, makes the enaminolate complexes highly reactive towards the water to deposit oxides, which helps to avoid ALD processes that require harsh co-reactants such as ozone. Further, the higher pK_a value of the enaminolate ligand system compared to ligand systems such as cyclopentadieneyl and alkoxide, that have relatively lower pK_a values of around 15.7 and 16, respectively suggest higher reactivity of lanthanide enaminolate complexes towards water than lanthanide complexes with cyclopentadienyl, and alkoxide ligands.

Hence, improving the volatility and thermal stability of lanthanide enaminolate complexes will be useful to expand the applications of lanthanide-containing oxides. Heteroleptic complexes are reported to have improved precursor properties compared to their homoleptic counterparts.[208, 265, 266] In heteroleptic complexes, the central metal atom is bonded to more than one type of ligand classes. Heteroleptic metal complexes can be advantageous as ALD precursors as they can combine the best precursor properties of each ligand classes into one molecule. Heteroleptic rare earth complexes synthesized with the combination of amidinate and cyclopentadienyl ligands are such examples.[208] For instance, Y(^{i}PrCp)$_2$(^{i}Pr-AMD) heteroleptic complex is a liquid at room temperature and the temperature required to obtain 1 Torr vapor pressure is around 168 °C. The homoleptic counter parts of Y(^{i}PrCp)$_2$(^{i}Pr-AMD), Y(^{i}PrCp)$_3$ and Y(^{i}Pr-AMD)$_3$ are solids at the room temperature and temperatures of ≥ 200 °C are required to obtain 1 Torr vapor pressure.[267] Above observation suggest that heteroleptic complexes may have advantageous ALD precursor properties such as increased volatility and lower melting points compared with the homoleptic

counter parts. Accordingly, it is worth attempting to synthesize heteroleptic complexes consisting of enaminolate ligands along with other suitable ligands. Particularly, lanthanide complexes with L^3 enaminolate ligands gave good thermal stabilities but their volatilities were relatively low and most of them have high melting points. Precursors that are liquids during the delivery temperature are advantageous as they maintain a constant surface area throughout the deposition process and hence provide a constant flux of precursor vapors. Surface area of solid precursors constantly change as the particle size of solids change with the heating. Therefore, precursor vapor pressure produced by solid precursors can change during the deposition process. The substitution of one of the three L^3 ligands in $Er(L^3)_3$ complexes introduced in Chapter 3 with a substituted Cp ligand may result in lanthanide complexes with low melting points and improved volatility (Figure 69).

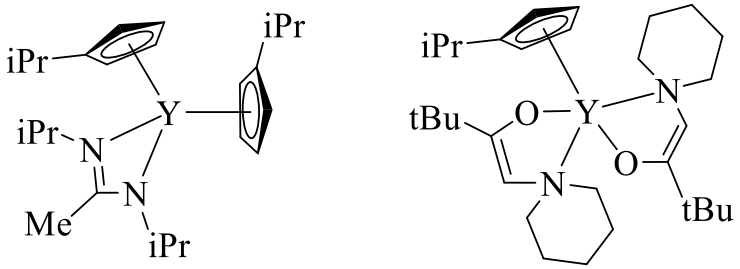

Figure 69. Heteroleptic $Y(^iPrCp)_2(^iPr\text{-}AMD)$ known in literatue (left) and proposed heteroleptic $Y(L^3)_2(^iPrCp)$ complex (right).

APPENDIX

Permission/License Agreements for Copyrighted Material

CCC RightsLink

Home | Help | Live Chat | Sign in | Create Account

Evaluation of Volatility and Thermal Stability in Monomeric and Dimeric Lanthanide(III) Complexes Containing Enaminolate Ligands

ACS Publications

Author: Navoda Jayakodiarachchi, Paul G. Evans, Cassandra L. Ward, et al

Publication: Organometallics

Publisher: American Chemical Society

Date: May 1, 2021

Copyright © 2021, American Chemical Society

PERMISSION/LICENSE IS GRANTED FOR YOUR ORDER AT NO CHARGE

This type of permission/license, instead of the standard Terms and Conditions, is sent to you because no fee is being charged for your order. Please note the following:

- Permission is granted for your request in both print and electronic formats, and translations.
- If figures and/or tables were requested, they may be adapted or used in part.
- Please print this page for your records and send a copy of it to your publisher/graduate school.
- Appropriate credit for the requested material should be given as follows: "Reprinted (adapted) with permission from {COMPLETE REFERENCE CITATION}. Copyright {YEAR} American Chemical Society." Insert appropriate information in place of the capitalized words.
- One-time permission is granted only for the use specified in your RightsLink request. No additional uses are granted (such as derivative works or other editions). For any uses, please submit a new request.

If credit is given to another source for the material you requested from RightsLink, permission must be obtained from that source.

BACK CLOSE WINDOW

REFERENCES

1. Cotton, S. A. Scandium, yttrium & the lanthanides: Inorganic & coordination chemistry. In *encyclopedia of inorganic and bioinorganic chemistry*; John Wiley & Sons, 2011. DOI: 10.1002/9781119951438.eibc0195.

2. Cotton, S. A. Lanthanide and actinide chemistry. John Wiley & Sons Ltd: The Atrium, Southern Gate, Chichester, West Sussex PO19 8SQ, England, 2006.

3. Greenwood, N. N.; Earnshaw, A. The lanthanide elements. In *chemistry of the elements*, 2nd ed.; Pergamon Press: Oxford, U.K., 1997; pp 1227-1249.

4. Wells Jr., W. H.; Wells, V. L. The lanthanides, rare earth elements. In *patty's toxicology*; John Wiley & Sons, 2012. DOI: 10.1002/0471435139.tox043.pub2.

5. Peters, J. A.; Djanashvili, K.; Geraldes, C. F. G. C.; Platas-Iglesias, C. The chemical consequences of the gradual decrease of the ionic radius along the Ln-series. *Coord. Chem. Rev*. **2020**, *406*, 213146.

6. Päiväsaari, J.; Niinistö, J.; Myllymäki, P.; Dezelah, C.; Winter, C. H.; Putkonen, M.; Nieminen, M.; Niinistö, L. Atomic layer deposition of rare earth oxides. In *rare earth oxide thin films*, Fanciulli, M.; Scarel, G., Eds. Springer Berlin Heidelberg: Berlin, Heidelberg, 2007; pp 15-32.

7. Malba, C. M. Synthesis and characterization of lanthanide based luminescent materials. Ph.D. Dissertation, University of Venice, **2013**.

8. Martinez-Gomez, N. C.; Vu, H. N.; Skovran, E. Lanthanide chemistry: From coordination in chemical complexes shaping our technology to coordination in enzymes shaping bacterial metabolism. *Inorg. Chem*. **2016**, *55*, 10083-10089.

9. Asuigui, D. R.; Atif, R.; Swanson, J.; Glaser, P.; Garskaite, E.; Žarkov, A.; Stoll, S. L. Synthesis of lanthanide chalcogenide nanoparticles. In *Nanomaterials via Single-Source Precursors*, Apblett, A. W.; Barron, A. R.; Hepp, A. F., Eds.; Elsevier: 2022; pp 219-243.

10. Eyring, L., The binary lanthanide oxides: synthesis and identification. In *synthesis of lanthanide and actinide compounds*, Meyer, G.; Morss, L. R., Eds.; Springer Netherlands: Dordrecht, **1991**; pp 187-224.

11. Külah, E.; Marot, L.; Steiner, R.; Romanyuk, A.; Jung, T. A.; Wäckerlin, A.; Meyer, E. Surface chemistry of rare- earth oxide surfaces at ambient conditions: reactions with water and hydrocarbons. *Sci. Rep*. **2017**, *7*, 43369-43369.

12. Zhao, Y.; Toyama, M.; Kita, K.; Kyuno, K.; Toriumi, A. Moisture-absorption-induced permittivity deterioration and surface roughness enhancement of lanthanum oxide films on silicon. *Appl. Phys. Lett*. **2006**, *88*, 072904.

13. Nieminen, M.; Putkonen, M.; Niinistö, L. Formation and stability of lanthanum oxide thin films deposited from *β*-diketonate precursor. *Appl. Surf. Sci*. **2001**, *174*, 155-166.

14. Elers, K. E.; Blomberg, T.; Peussa, M.; Aitchison, B.; Haukka, S.; Marcus, S. Film uniformity in atomic layer deposition. *Chem. Vap. Deposition.* **2006**, *12*, 13-24.

15. Jeon, S.; Hwang, H. Effect of hygroscopic nature on the electrical characteristics of lanthanide oxides (Pr_2O_3, Sm_2O_3, Gd_2O_3, and Dy_2O_3). *Appl. Phys. Lett.* **2003**, *93*, 6393-6395.

16. Hoekstra, H. R.; Gingerich, K. A. High-pressure B-Type polymorphs of some rare-earth sesquioxides. *Science* **1964**, *146*, 1163-1164.

17. Warshaw, I.; Roy, R. Polymorphism of the rare earth sesquioxides. *J. Phys. Chem. A* **1961**, *65*, 2048-2051.

18. Bonnet, G. L., M.; Colson, J. C.; Larpin, J. P. Characterization of thin solid films of rare earth oxides formed by the metallo-organic chemical vapour deposition technique, for high temperature corrosion applications. *Thin Solid Films* **1995**, *261*, 31-36.

19. Coutures, J. P.; Rand, M. H. Melting temperatures of refractory oxides - Part II: Lanthanoid sesquioxides. *Pure Appl. Chem*. **1989**, *61*, 1461-1482.

20. Tseng, K.-P.; Yang, Q.; McCormack, S. J.; Kriven, W. M. High-entropy, phase-constrained, lanthanide sesquioxide. *J. Am. Ceram. Soc*. **2020**, *103*, 569-576.

21. Yang, C.; Fan, H.; Qiu, S.; Xi, Y.; Fu, Y. Microstructure and dielectric properties of La_2O_3 films prepared by ion beam assistant electron-beam evaporation. *J. Non-Cryst. Solids* **2009**, *355*, 33-37.

22. Chin, W. C.; Cheong, K. Y.; Hassan, Z. Sm_2O_3 gate dielectric on Si substrate. *Mater. Sci. Semicond. Process*. **2010**, *13*, 303-314.

23. Engström, O.; Raeissi, B.; Hall, S.; Buiu, O.; Lemme, M. C.; Gottlob, H. D. B.; Hurley, P. K.; Cherkaoui, K. Navigation aids in the search for future high-k dielectrics: Physical and electrical trends. *Solid State Electron*. **2007**, *51*, 622-626.

24. Hubbard, K. J.; Schlom, D. G. Thermodynamic stability of binary oxides in contact with silicon. *J. Mater. Res*. **1996**, *11*, 2757-2776.

25. Medenbach, O.; Dettmar, D.; Shannon, R.; Fischer, R.; Yen, W. Refractive index and optical dispersion of rare earth oxides using a small-prism technique. *J. Opt. A: Pure Appl. Opt.* **2001**, *3*, 174-177.

26. Zhao, X.; Wang, X.; Lin, H.; Wang, Z. Electronic polarizability and optical basicity of lanthanide oxides. *Physica B: Condensed Matter* **2007**, *392*, 132-136.

27. Swatowska, B.; Stapinski, T.; Drabczyk, K.; Panek, P. The role of antireflective coatings in silicon solar cells–the influence on their electrical parameters. *Opt. Appl*. **2011**, *41*, 487-492.

28. Zhao, J.; Green, M. A. Optimized antireflection coatings for high-efficiency silicon solar cells. *IEEE Trans. Electron Devices* **1991**, *38*, 1925-1934.

29. Rozhkov, V. A.; Petrov, A. I. Antireflective cerium and samarium oxide coatings for silicon photoelectric devices. *Russ. Phys. J*. **1994**, *37*, 815-818.

30. Rozhkov, V. A.; Rodionov, M. A. Antireflection properties of erbium oxide films. *Tech. Phys. Lett.* **2005**, *31*, 77-78.

31. Rozhkov, V. A.; Trusova, A. Y. Energy barriers at the interfaces in the MIS system Me-Yb_2O_3-Si. *Tech. Phys.* **1999**, *44*, 404-408.

32. Atyaoui, M.; Dimassi, W.; Atyaoui, A.; Elyagoubi, J.; Ouertani, R.; Ezzaouia, H. Improvement in photovoltaic properties of silicon solar cells with a doped porous silicon layer with rare earth (Ce, La) as antireflection coatings. *J. Lumin*. **2013**, *141*, 1-5.

33. Moore, G. E. Cramming more components onto integrated circuits, *Electronics*, **1965**, 114-117.

34. Liu, H.-X.; Ma, F. Analysis of off-state leakage current characteristics and mechanisms of nanoscale MOSFETs with a high- k gate dielectric. *Chin. Phys. Lett*. **2012**, *29*, 127301.

35. Wong, H.; Iwai, H. J. M. E. On the scaling issues and high-κ replacement of ultrathin gate dielectrics for nanoscale MOS transistors. *Microelectron. Eng.* **2006**, *83*, 1867-1904.

36. Wilk, G. D.; Wallace, R. M.; Anthony, J. M. High-κ gate dielectrics: current status and materials properties considerations. *J. Appl. Phys*. **2001**, *89*, 5243-5275.

37. Parker, C. G.; Lucovsky, G.; Hauser, J. R. Ultrathin oxide-nitride gate dielectric MOSFET's. *IEEE Electron Device Lett*. **1998**, *19*, 106-108.

38. Wiemer, C.; Lamagna, L.; Fanciulli, M. Atomic layer deposition of rare-earth-based binary and ternary oxides for microelectronic applications. *Semicond. Sci. Technol*. **2012**, *27*, 074013.

39. Goh, K. H.; Haseeb, A. S. M. A.; Wong, Y. H. Lanthanide rare earth oxide thin film as an alternative gate oxide. *Mater. Sci. Semicond. Process*. **2017**, *68*, 302-315.

40. Xue, D.; Betzler, K.; Hesse, H. Dielectric constants of binary rare-earth compounds. *J. Phys.: Condens. Matter* **2000**, *12*, 3113-3118.

41. Pavunny, S. P.; Scott, J. F.; Katiyar, R. S. Lanthanum gadolinium oxide: a new electronic device material for CMOS logic and memory devices. *Materials* **2014**, *7*, 2669-2696.

42. Minh, N. Q. Solid oxide fuel cell technology—features and applications. *Solid State Ion*. **2004**, *174*, 271-277.

43. Ormerod, R. M. Solid oxide fuel cells. *Chem. Soc. Rev*. **2003**, *32*, 17-28.

44. Jacobson, A. J. Materials for solid oxide fuel cells. *Chem. Mater*. **2010**, *22*, 660-674.

45. Han, M.; Tang, X.; Yin, H.; Peng, S. Fabrication, microstructure and properties of a YSZ electrolyte for SOFCs. *J. Power Sources* **2007**, *165*, 757-763.

46. Solovyev, A. A.; Shipilova, A. V.; Ionov, I. V.; Kovalchuk, A. N.; Rabotkin, S. V.; Oskirko, V. O. Magnetron-Sputtered YSZ and CGO Electrolytes for SOFC. *J. Electron. Mater*. **2016**, *45*, 3921-3928.

47. Dong, Y.; Li, D.; Feng, X.; Dong, X.; Hampshire, S. A high-strength Sm-doped CeO_2 oxide-ion conducting electrolyte membrane for solid oxide fuel cell application. *RSC Advances* **2013**, *3*, 17395-17401.

48. Naiqing, Z.; Kening, S.; Derui, Z.; Dechang, J. Study on properties of LSGM electrolyte made by tape casting method and applications in SOFC. *J. of Rare Earths* **2006**, *24*, 90-92.

49. Han, P.; Worrell, W. L. Mixed (oxygen ion and p-type) conductivity in yttria-stabilized zirconia containing terbia. *J. Electrochem. Soc*. **1995**, *142*, 4235-4246.

50. Wang, Y.; Niranjan, M. K.; Jaswal, S. S.; Tsymbal, E. Y. First-principles studies of a two-dimensional electron gas at the interface in ferroelectric oxide heterostructures. *Phys. Rev. B* **2009**, *80*, 165130.

51. Lee, S. W. Two-dimensional electron gas at $SrTiO_3$-based oxide heterostructures via atomic layer deposition. *J. Nanomater*. **2016**, 1-9.

52. Ohtomo, A.; Hwang, H. Y. A high-mobility electron gas at the $LaAlO_3/SrTiO_3$ heterointerface. *Nature* **2004**, *427*, 423-426.

53. Dong, Y.; Zhang, L.; Li, C.; Liu, Y.; Shao, P.; Lei, J.; Wang, R.; Wu, D.; Chen, D.; Zhang, R.; Zheng, Y. Stable pH sensitivity of $LaAlO_3/SrTiO_3$ interfacial electronic gas. *Curr. Appl. Phys.* **2022**, *34*, 55-58.

54. Reyren, N.; Thiel, S.; Caviglia, A. D.; Kourkoutis, L. F.; Hammerl, G.; Richter, C.; Schneider, C. W.; Kopp, T.; Rüetschi, A. S.; Jaccard, D.; Gabay, M.; Muller, D. A.; Triscone, J. M.; Mannhart, J. Superconducting interfaces between insulating oxides. *Science* **2007**, *317*, 1196-1199.

55. Kim, T.; Kim, S. I.; Joo, S.; Kim, S.; Jeon, J.; Hong, J.; Doh, Y. J.; Baek, S. H.; Koo, H. C. A possible superconductor-like state at elevated temperatures near metal electrodes in an $LaAlO_3/SrTiO_3$ interface. *Sci. Rep*. **2018**, *8*, 11558.

56. Cen, C.; Thiel, S.; Mannhart, J.; Levy, J. Oxide nanoelectronics on demand. *Science* **2009**, *323*, 1026-1030.

57. Vasylechko, L.; Stepchuk, R.; Prots, Y.; Rosner, H. Concentration and temperature-induced phase transitions in $PrAlO_3$-$SrTiO_3$ system. *Nanoscale Res. Lett*. **2016**, *11*, 1-6.

58. Annadi, A.; Putra, A.; Srivastava, A.; Wang, X.; Huang, Z.; Liu, Z.; Venkatesan, T.; Ariando, A. Evolution of variable range hopping in strongly localized two-dimensional electron gas at $NdAlO_3/SrTiO_3$ (100) heterointerfaces. *Appl. Phys. Lett*. **2012**, *101*, 231604.

59. Waduge, W. L. I.; Chen, Y.; Zuo, P.; Jayakodiarachchi, N.; Kuech, T. F.; Babcock, S. E.; Evans, P. G.; Winter, C. H. Solid-phase epitaxy of perovskite high dielectric $PrAlO_3$ films grown by atomic layer deposition for use in two-dimensional electronics and memory devices. *ACS Appl. Nano Mater.* **2019**, *2*, 7449-7458.

60. Carvalho, F.; Ramanathan, L. Rare earth oxide coatings to decrease high temperature degradation of chromia forming alloys. *Mater. Res.* **2004**, *7*, 135-139.

61. Sun, Y.; Xiang, H.; Dai, F.-Z.; Wang, X.; Xing, Y.; Zhao, X.; Zhou, Y. Preparation and properties of CMAS resistant bixbyite structured high-entropy oxides RE_2O_3 (RE = Sm, Eu, Er, Lu, Y, and Yb): promising environmental barrier coating materials for Al_2O_{3f}/Al_2O_3 composites. *J. Adv. Ceram.* **2021**, *10*, 596-613.

62. Lopato, L. M. Highly refractory oxide systems containing oxides of rare-earth elements. *Ceram. Int.* **1976**, *2*, 18-32.

63. Doleker, K. M.; Karaoglanli, A. C. Comparison of oxidation behavior of YSZ and $Gd_2Zr_2O_7$ thermal barrier coatings (TBCs). *Surf. Coat. Technol.* **2017**, *318*, 198-207.

64. Cârâc, G.; Bund, A.; Thiemig, D. Electrocodeposition and characterization of cobalt lanthanide oxides composite coatings. *Surf. Coat. Technol.* **2007,** *202*, 403-411.

65. Makhlouf, A. S. H. Current and advanced coating technologies for industrial applications. In *Nanocoatings and Ultra-Thin Films,* Makhlouf, A. S. H.; Tiginyanu, I., Eds. Woodhead Publishing: 2011, 3-23.

66. Jensen, K. F. Chemical vapor deposition. In *Microelectronics Processing*, American Chemical Society, 1989; pp 199-263.

67. Chen, S.; Zhu, Y. Y.; Xu, R.; Wu, Y. Q.; Yang, X. J.; Fan, Y. L.; Lu, F.; Jiang, Z. M.; Zou, J. Superior electrical properties of crystalline Er_2O_3 films epitaxially grown on Si substrates. *Appl. Phys. Lett.* **2006**, *88*, 222902.

68. Li, X.; Wu, P.; Qiu, H.; Chen, S.; Song, B. Crystallization behavior and mechanical properties of erbium oxide coatings fabricated by pulsed magnetron sputtering. *Thin Solid Films* **2012**, *520*, 2316-2320.

69. Sanghun, J.; Kiju, I.; Hyundoek, Y.; Hyelan, L.; Hyunjun, S.; Sangmu, C.; Taesung, J.; Hyunsang, H. Excellent electrical characteristics of lanthanide (Pr, Nd, Sm, Gd, and Dy) oxide and lanthanide-doped oxide for MOS gate dielectric applications, *Tech. Dig. - Int. Electron Devices Meet.* **2001**, 20.6.1-20.6.4.

70. Schubert, J.; Trithaveesak, O.; Zander, W.; Roeckerath, M.; Heeg, T.; Chen, H. Y.; Jia, C. L.; Meuffels, P.; Jia, Y.; Schlom, D. G. Characterization of epitaxial lanthanum lutetium oxide thin films prepared by pulsed-laser deposition. *Appl. Phys. A* **2008**, *90*, 577-579.

71. Pisecny, P.; Husekova, K.; Frohlich, K.; Harmatha, L.; Soltys, J.; Machajdik, D.; Espinos, J. P.; Jergel, M.; Jakabovic, J. Growth of lanthanum oxide films for application as a gate dielectric in CMOS technology. *Mater. Sci. Semicond. Process*. **2004**, *7*, 231-236.

72. Milanov, A. P.; Toader, T.; Parala, H.; Barreca, D.; Gasparotto, A.; Bock, C.; Becker, H.-W.; Ngwashi, D. K.; Cross, R.; Paul, S.; Kunze, U.; Fischer, R. A.; Devi, A. Lanthanide oxide thin films by metalorganic chemical vapor deposition employing volatile guanidinate precursors. *Chem. Mater*. **2009**, *21*, 5443-5455.

73. Edleman, N. L.; Wang, A.; Belot, J. A.; Metz, A. W.; Babcock, J. R.; Kawaoka, A. M.; Ni, J.; Metz, M. V.; Flaschenriem, C. J.; Stern, C. L.; Liable-Sands, L. M.; Rheingold, A. L.; Markworth, P. R.; Chang, R. P. H.; Chudzik, M. P.; Kannewurf, C. R.; Marks, T. J. Synthesis and characterization of volatile, fluorine-free *β*-ketoiminate lanthanide mocvd precursors and their implementation in low-temperature growth of epitaxial CeO_2 buffer layers for superconducting electronics. *Inorg. Chem.* **2002**, *41*, 5005-5023.

74. Aspinall, H. C.; Gaskell, J.; Williams, P. A.; Jones, A. C.; Chalker, P. R.; Marshall, P. A.; Bickley, J. F.; Smith, L. M.; Critchlow, G. W. Growth of praseodymium oxide thin films by liquid injection MOCVD using a novel praseodymium alkoxide precursor. *Chem. Vap. Deposition* **2003**, *9*, 235-238.

75. Shalini, K.; Shivashankar, S. A. Oriented growth of thin films of samarium oxide by MOCVD. *Bull. Mater. Sci*. **2005**, *28*, 49-54.

76. Losurdo, M.; Giangregorio, M. M.; Capezzuto, P.; Bruno, G.; Malandrino, G.; Fragalà, I. L.; Armelao, L.; Barreca, D.; Tondello, E. Structural and optical properties of nanocrystalline Er_2O_3 thin films deposited by a versatile low-pressure MOCVD approach. *J. Electrochem. Soc.* **2008**, *155*, G44-G50.

77. Kim, H.; Lee, H.-B.-R.; Maeng, W. J. Applications of atomic layer deposition to nanofabrication and emerging nanodevices. *Thin Solid Films* **2009**, *517*, 2563-2580.

78. Leskelä, M.; Ritala, M. Atomic layer epitaxy in deposition of various oxide and nitride thin films. *J. Phys. IV France* **1995**, *05*, 937-951.

79. George, S. M. Atomic layer deposition: an overview. *Chem. Rev*. **2010**, *110*, 111-131.

80. Parsons, G. N.; Elam, J. W.; George, S. M.; Haukka, S.; Jeon, H.; Kessels, W. M. M.; Leskelä, M.; Poodt, P.; Ritala, M.; Rossnagel, S. M. History of atomic layer deposition and its relationship with the american vacuum society. *J. Vac. Sci. Technol. A* **2013,** *31*, 050818.

81. Mistry, K.; Allen, C.; Auth, C.; Beattie, B.; Bergstrom, D.; Bost, M.; Brazier, M.; Buehler, M.; Cappellani, A.; Chau, R.; Choi, C. H.; Ding, G.; Fischer, K.; Ghani, T.; Grover, R.; Han, W.; Hanken, D.; Hattendorf, M.; He, J.; Hicks, J.; Huessner, R.; Ingerly, D.; Jain, P.; James, R.; Jong, L.; Joshi, S.; Kenyon, C.; Kuhn, K.; Lee, K.; Liu, H.; Maiz, J.; McIntyre, B.; Moon, P.; Neirynck, J.; Pae, S.; Parker, C.; Parsons, D.; Prasad, C.; Pipes, L.; Prince, M.; Ranade, P.; Reynolds, T.; Sandford, J.; Shifren, L.; Sebastian, J.; Seiple, J.; Simon, D.; Sivakumar, S.; Smith, P.; Thomas, C.; Troeger, T.; Vandervoorn, P.; Williams, S.; Zawadzki, K. In a 45nm logic technology with high-k metal gate transistors, strained silicon, 9 Cu interconnect layers, 193 nm dry patterning, and 100% Pb-free packaging. *IEEE Tech. Dig. IEDM* **2007**, 247-250.

82. Cremers, V.; Puurunen, R. L.; Dendooven, J. Conformality in atomic layer deposition: current status overview of analysis and modeling. *Appl. Phys. Rev.* **2019**, *6*, 021302.

83. Mallick, B. C.; Hsieh, C.-T.; Yin, K.-M.; Gandomi, Y. A.; Huang, K.-T. Review on atomic layer deposition: current progress and future challenges. *ECS J. Solid State Sci. Technol.* **2019**, *8*, N55-N78.

84. Ritala, M.; Leskelä, M. Atomic layer deposition. In *handbook of thin films materials: deposition and processing of thin films*, Academic Press, 2001; pp 103-159.

85. Johnson, R. W.; Hultqvist, A.; Bent, S. F. A brief review of atomic layer deposition: from fundamentals to applications. *Mater. Today* **2014**, *17*, 236-246.

86. Knoops, H. C. M.; Potts, S. E.; Bol, A. A.; Kessels, W. M. M. Atomic layer deposition. In *handbook of crystal growth: thin films and epitaxy*, 2nd ed.; Elsevier, 2015; 1101-1134.

87. Knisley, T. J.; Kalutarage, L. C.; Winter, C. H. Precursors and chemistry for the atomic layer deposition of metallic first row transition metal films. *Coord. Chem. Rev*. **2013**, *257*, 3222-3231.

88. Hatanpää, T. Precursor chemistry for atomic layer deposition. Ph.D. Thesis, University of Helsinki, Finland, 2019.

89. Devi, A. 'Old Chemistries' for new applications: perspectives for development of precursors for MOCVD and ALD applications. *Coord. Chem. Rev*. **2013**, *257*, 3332-3384.

90. Koponen, S. E.; Gordon, P. G.; Barry, S. T. Principles of precursor design for vapour deposition methods. *Polyhedron* **2016**, *108*, 59-66.

91. Jones, A. C.; Aspinall, H. C.; Chalker, P. R. Chemical vapor deposition of metal oxides for microelectronics applications. In *chemical vapor deposition: precursors, processes and applications*, the royal society of chemistry, 2009; pp 357-412.

92. Pochekutova, T. S.; Khamylov, V. K.; Fukin, G. K.; Petrov, B. I.; Shavyrin, A. S.; Arapova, A. V.; Lazarev, N. M.; Faerman, V. I.; Kulikova, T. I.; Baranov, E. V.; Khamaletdinova, N. M. Synthesis, structures, thermal behavior and vapor pressures of new strontium and barium *β*-diketonate complexes [M(*t*BuCOCHCOCF$_3$)$_2$(18-crown-6)] and [M(*t*BuCOCHCOC$_3$F$_7$)$_2$(18-crown-6)] (M = Sr, Ba). *Polyhedron* **2020,** *177*, 114263.

93. Lesikar, L. A.; Gushwa, A. F.; Richards, A. F. Synthesis, characterization, and steric hindrance comparisons of selected transition and main group metal *β*-ketoiminato complexes. *J. Organomet. Chem.* **2008**, *693*, 3245-3255.

94. Sedai, B.; Heeg, M. J.; Winter, C. H. Magnesium complexes containing *β*-ketiminate and *β*-diketiminate ligands with dimethylamino substituents on the ligand core nitrogen atoms. *J. Organomet. Chem.* **2008**, *693*, 3495-3503.

95. Griffiths, M. B. E.; Dubrawski, Z. S.; Bačić, G.; Japahuge, A.; Masuda, J. D.; Zeng, T.; Barry, S. T. Controlling the thermal stability and volatility of organogold(I) compounds for vapor deposition with complementary ligand design. *Eur. J. Inorg. Chem.* **2019**, *46*, 4927-4938.

96. King, J.; Block, B.; Popoff, I. Phosphinylmethylphosphinates as chelating ligands. *Inorg. Chem.* **1965**, *4*, 198–202.

97. Päiväsaari, J.; Putkonen, M.; Sajavaara, T.; Niinistö, L. Atomic layer deposition of rare earth oxides: erbium oxide thin films from *β*-diketonate and ozone precursors. *J. Alloys Compd*. **2004**, *374*, 124-128.

98. Beer, S. M. J.; Krusenbaum, A.; Winter, M.; Vahlas, C.; Devi, A. Study on structural and thermal characteristics of heteroleptic yttrium complexes as potential precursors for vapor phase deposition. *Eur. J. Inorg. Chem*. **2020**, *2020*, 3587-3596.

99. Arunasalam, V. C.; Drake, S. R.; Hursthouse, M. B.; Malik, K. M. A.; Miller, S. A. S.; Mingos, D. M. P. Synthesis, structure and characterisation of magnesium and calcium *β*-diketonate complexes $[Ca_3(tmhd)_6]$ and $[Ca_2(tmhd)_4(EtOH)_2]$(Htmhd = 2,2,6,6-tetramethylheptane-3,5-dione). *J. Chem. Soc., Dalton Trans*. **1996**, 2435-2442.

100. Han, J. H.; Park, B. K.; Chung, T.-M. Atomic layer deposition of pure In_2O_3 films for a temperature range of 200–300 °C using heteroleptic liquid $In(DMAMP)_2(O^iPr)$ precursor. *Ceram. Int*. **2020**, *46*, 3139-3143.

101. Silverstein, T. P.; Heller, S. T. pKa Values in the undergraduate curriculum: What is the real pKa of water? *J. Chem. Educ.* **2017**, *94*, 690-695.

102. Xu, X.; Antal Jr, M. J. Kinetics and mechanism of isobutene formation from T-butanol in hot liquid water. *AlChE J.* **1994,** *40*, 1524-1534.

103. Mai, L.; Boysen, N.; Subaşı, E.; Arcos, T. d. l.; Rogalla, D.; Grundmeier, G.; Bock, C.; Lu, H.-L.; Devi, A. Water assisted atomic layer deposition of yttrium oxide using tris(N,N′-diisopropyl-2-dimethylamido-guanidinato) yttrium(iii): process development, film characterization and functional properties. *RSC Advances* **2018**, *8*, 4987-4994.

104. de Rouffignac, P.; Park, J.-S.; Gordon, R. G. Atomic layer deposition of Y_2O_3 thin films from yttrium tris(N,N-diisopropylacetamidinate) and water. *Chem. Mater*. **2005**, *17*, 4808-4814.

105. Adeniyi, A. A.; Conradie, J. Influence of substituents on the reduction potential and pKa values of *β*-diketones tautomers: A theoretical study. *Electrochim. Acta* **2019**, *297*, 947-960.

106. Hongtao Wang, H. W., J.; Gordon, R. G.; Lehn, J. M.; Li, H.; Hong, D.; Shenaic, D. V. Atomic layer deposition of lanthanum-based ternary oxides. *Electrochem. Solid-State Lett*. **2009**, *12*, 13-15.

107. Urs, U.; Shalini, K.; Cameron, T.; Shivashankar, S.; Guru Row, G. Low-temperature structure of a twinned crystal of tris(2,4-pentanedionato)(1,10-phenanthroline)samarium(III). *Acta Cryst.* **2001**, *57*, 457-458.

108. Erasmus, C.; Boeyens, J. Crystal structure of the praseodymium *β*-diketonate of 2,2,6,6-tetramethyl-3,5-heptanedione, $Pr_2(thd)_6$. *Acta Cryst*. **1970**, *26*, 1843-1854.

109. Eisentraut, K. J.; Sievers, R. E. Thermogravimetric studies of metal *β*-diketonates. *J. Inorg. Nucl. Chem.* **1967**, *29*, 1931-1936.

110. Zhang, T.; Gu, H.; Ding, F.; Qu, F.; Dai, S. Synthesis, characterization and thermostability of tris(2,2,6,6-tetramethyl-3,5-heptanedionato)yttrium(III). *J. of Rare Earths* **2012**, *30*, 1041-1047.

111. Päiväsaari, J.; Putkonen, M.; Niinistö, L. A comparative study on lanthanide oxide thin films grown by atomic layer deposition. *Thin Solid Films* **2005**, *472*, 275-281.

112. Kosola, A.; Päiväsaari, J.; Putkonen, M.; Niinistö, L. Neodymium oxide and neodymium aluminate thin films by atomic layer deposition. *Thin Solid Films* **2005**, *479*, 152-159.

113. Cheng, J.-B.; Li, A.-D.; Shao, Q.-Y.; Ling, H.-Q.; Wu, D.; Wang, Y.; Bao, Y.-J.; Wang, M.; Liu, Z.-G.; Ming, N.-B. Growth and characteristics of La_2O_3 gate dielectric prepared by low pressure metalorganic chemical vapor deposition. *Appl. Surf. Sci.* **2004**, *233*, 91-98.

114. He, W.; Schuetz, S.; Solanki, R.; Belot, J.; McAndrew, J. Atomic layer deposition of lanthanum oxide films for high-κ gate dielectrics. *Electrochem. Solid-State Lett*. **2004**, *7*, G131-G133.

115. Jones, A. C.; Aspinall, H. C.; Chalker, P. R.; Potter, R. J.; Kukli, K.; Rahtu, A.; Ritala, M.; Leskelä, M. Recent developments in the MOCVD and ALD of rare earth oxides and silicates. *J. mater. sci. eng. B* **2005**, *118*, 97-104.

116. Sønsteby, H. H.; Yanguas-Gil, A.; Elam, J. W. Consistency and reproducibility in atomic layer deposition. *Nat. Commun.* **2020**, *38*, 020804.

117. Wilkinson, G.; Birmingham, J. M. Cyclopentadienyl compounds of Sc, y, La, Ce and some lanthanide elements. *J. Am. Chem. Soc*. **1954**, *76*, 6210-6210.

118. Burns, J. H.; Baldwin, W. H.; Fink, F. H. Crystal structure of neodymium tris(methylcyclopentadienide). *Inorg. Chem.* **1974**, *13*, 1916-1920.

119. Stults, S. D.; Andersen, R. A.; Zalkin, A. Structural studies on cyclopentadienyl compounds of trivalent cerium: tetrameric $(MeC_5H_4)_3Ce$ and monomeric $(Me_3SiC_5H_4)_3Ce$ and $[(Me_3Si)_2C_5H_3]_3Ce$ and their coordination chemistry. *Organometallics* **1990**, *9*, 115-122.

120. Kondo, H.; Matsui, H.; Furuta, K.; Sakashita, M.; Zaima, S. Formation of Pr Oxide Films by atomic layer deposition using $Pr(EtCp)_3$ precursor. *Jpn. J. Appl. Phys*. **2010**, *49*, 04DA14.

121. Rodrigues, I.; Xue, T. Y.; Roussel, P.; Visseaux, M. (t-BuC_5H_4)$_3$Nd: A triscyclopentadienyl rare earth compound as non-classical isoprene polymerization pre-catalyst. *J. Organomet. Chem.* **2013**, *743*, 139-146.

122. Angadol, M. A.; Woen, D. H.; Windorff, C. J.; Ziller, J. W.; Evans, W. J. tert-Butyl(cyclopentadienyl) ligands will stabilize nontraditional +2 rare-earth metal ions. *Organometallics* **2019**, *38*, 1151-1158.

123. Kadokura, H. Method for preparation of tris(ethylcyclopentadienyl)lanthanide and method for manufacturing oxide thin film by vapor growth method using tris(ethylcyclopentadienyl)lanthanide. JP2002338590A, 2002.

124. Alkorta, I.; Elguero, J.; Gallo, R. A theoretical study of the limits of the acidity of carbon acids in phase transfer catalysis in water and in liquid ammonia. *J Open Chemistry. Cent. Eur. J. Chem.* **2013**, *11*, 1711-1722.

125. Ngo, T.; Posadas, A.; McDaniel, M.; Ferrer, D.; Bruley, J.; Breslin, C. M.; Demkov, A.; Ekerdt, J. Epitaxial growth of $LaAlO_3$ on $SrTiO_3$-buffered Si (001) substrates by atomic layer deposition. *J. Cryst. Growth* **2013**, *363*, 150–157.

126. Blanquart, T.; Kaipio, M.; Niinistö, J.; Gavagnin, M.; Longo, V.; Blanquart, L.; Lansalot, C.; Noh, W.; Wanzenböck, H. D.; Ritala, M.; Leskelä, M. Cyclopentadienyl precursors for the atomic layer deposition of erbium oxide thin films. *Chem. Vap. Deposition* **2014**, *20*, 217-223.

127. Andersen, R. A.; Templeton, D. H.; Zalkin, A. Structure of tris(bis(trimethylsilyl)amido)neodymium(III), Nd[N(Si(CH_3)$_3$)$_2$]$_3$. *Inorg. Chem.* **1978**, *17*, 2317-2319.

128. Schuetz, S. A.; Day, V. W.; Sommer, R. D.; Rheingold, A. L.; Belot, J. A. Anhydrous lanthanide schiff base complexes and their preparation using lanthanide triflate derived amides. *Inorg. Chem.* **2001**, *40*, 5292-5295.

129. Kaupo Kukli, K. R., M.; Pilvi, T.; Sajavaara, T.; Leskela¨, M.; Jones, A. C.; Aspinall, H. C.; Gilmer, D. C.; Tobin, P. J. Evaluation of a praseodymium precursor for atomic layer deposition of oxide dielectric films. *Chem. Mater*. **2004**, *16*, 5162-5168.

130. He, W.; Schuetz, S. A.; Solanki, R.; Belot, J.; McAndrew, J. Atomic layer deposition of lanthanum oxide films for high-k gate dielectrics. *Electrochem. Solid-State Lett*. **2004**, *7*, 131-133.

131. de Rouffignac, P.; Gordon, R. G. Atomic layer deposition of praseodymium aluminum oxide for electrical applications. *Chem. Vap. Deposition* **2006**, *12*, 152-157.

132. Fraser, R. R.; Mansour, T. S. Acidity measurements with lithiated amines: steric reduction and electronic enhancement of acidity. *J. Org. Chem.* **1984**, *49*, 3442-3443.

133. Chalker, P. R.; Marshall, P. A.; Potter, R. J.; Joyce, T. B.; Jones, A. C.; Taylor, S.; Noakes, T. C. Q.; Bailey, P. Thermal stability of hafnium silicate dielectric films deposited by a dual source liquid injection MOCVD. *J. Mater. Sci. Mater. Electron.* **2004**, *15*, 711-714.

134. Gordon, R. G.; Becker, J.; Hausmann, D.; Suh, S. Vapor deposition of metal oxides and silicates: possible gate insulators for future microelectronics. *Chem. Mater.* **2001**, *13*, 2463-2464.

135. Boyle, T. J.; Tribby, L. J.; Bunge, S. D. Synthesis and structural characterization of a series of carboxylic acid modified cerium(III) alkoxides. *Eur. J. Inorg. Chem.* **2006**, *2006*, 4553-4563.

136. Westin, G.; Moustiakimov, M.; Kritikos, M. Synthesis, characterization, and properties of three europium 2-propoxides: $[Eu_4(OiPr)_{10}(HOiPr)_3]_2HOiPr$, $Eu_5O(OiPr)_{13}$, and $EuAl_3(OiPr)_{12}$. *Inorg. Chem.* **2002**, *41*, 3249-3258.

137. Bradley, D. C.; Chudzynska, H.; Frigo, D. M.; Hammond, M. E.; Hursthouse, M. B.; Mazid, M. A. Pentanuclear oxoalkoxide clusters of scandium, yttrium, indium and ytterbium, X-ray crystal structures of $[M_5(\mu_5\text{-}O)(\mu_3\text{-}OPri)_4(\mu_2\text{-}OPri)_4(OPri)_5]$ (M = In, Yb). *Polyhedron* **1990**, *9*, 719-726.

138. Stecher, H. A.; Sen, A.; Rheingold, A. L. Synthesis, structure, and reactivity of tricoordinate cerium(III) aryloxides. The first structurally characterized monomeric $Ln(OR)_3$ complexes. *Inorg. Chem.* **1988**, *27*, 1130-1132.

139. Anwander, R.; Munck, F. C.; Priermeier, T.; Scherer, W.; Runte, O.; Herrmann, W. A. Volatile donor-functionalized alkoxy derivatives of lutetium and their structural characterization. *Inorg. Chem.* **1997**, *36*, 3545-3552.

140. Herrmann, W. A.; Anwander, R.; Denk, M. Lanthanoiden-Komplexe, III. Flüchtige Neodym- und Yttrium-Alkoxide mit neuen sperrigen Chelatliganden. *Chem. Ber.* **1992**, *125*, 2399-2405.

141. Aspinall, H. C.; Bickley, J. F.; Gaskell, J. M.; Jones, A. C.; Labat, G. Precursors for MOCVD and ALD of rare earth oxides−complexes of the early lanthanides with a donor-functionalized alkoxide ligand. *Inorg. Chem.* **2007**, *46*, 5852−5860.

142. Aspinall, H. C.; Gaskell, J. M.; Loo, Y. F. Jones, A. C.; Chalker, P. R.; Potter, R. J.; Smith, L. M.; Critchlow, G. W. Growth of neodymium oxide thin films by liquid injection MOCVD using a new neodymium alkoxide precursor. *Chem. Vap. Deposition* **2004**, *10*, 301-305.

143. Loo, Y. F.; Potter, R. J.; Jones, A. C.; Aspinall, H. C.; Gaskell, J. M.; Chalker, P. R.; Smith, L. M.; Critchlow, G. W. Growth of gadolinium oxide thin films by liquid injection MOCVD using a new gadolinium alkoxide precursor. *Chem. Vap. Deposition* **2004**, *10*, 306-310.

144. Gervasini, A.; Auroux, A. Thermodynamics of adsorbed molecules for a new acid-base topo chemistry of alumina. *J. Phys. Chem*. **1993**, *97*, 2628-2639.

145. Thapa, B.; Schlegel, H. B. Improved pKa prediction of substituted alcohols, phenols, and hydroperoxides in aqueous medium using density functional theory and a cluster-continuum solvation model. *J. Phys. Chem. A* **2017**, *121*, 4698-4706.

146. Jinhee Kwon, J. D., M.; Halls, M. D.; Langereis, E.; Chabal, Y. J.; Gordon, R. G. In situ infrared characterization during atomic layer deposition of lanthanum oxide. *J. Phys. Chem. C* **2009**, *113*, 654–660.

147. Milanov, A. P.; Fischer, R. A.; Devi, A. Synthesis, characterization, and thermal properties of homoleptic rare-earth guanidinates: promising precursors for MOCVD and ALD of rare-earth oxide thin films. *Inorg. Chem*. **2008**, *47*, 11405-11416.

148. Kaur, P.; Mai, L.; Muriqi, A.; Zanders, D.; Ghiyasi, R.; Safdar, M.; Boysen, N.; Winter, M.; Nolan, M.; Karppinen, M.; Devi, A. Rational development of guanidinate and amidinate based cerium and ytterbium complexes as atomic layer deposition precursors: synthesis, modeling, and application. *Chem. Eur. J.* **2021**, *27*, 4913-4926.

149. Bordwell, F. G.; Ji, G. Z. Effects of structural changes on acidities and homolytic bond dissociation energies of the hydrogen-nitrogen bonds in amidines, carboxamides, and thiocarboxamides. *J. Am. Chem. Soc.* **1991**, *113*, 8398-8401.

150. Drozdov, F.; Kotov, V. Guanidine: a simple molecule with great potential: from catalysts to biocides and molecular glues. *Ineos open* **2021**, *3*, 200-213.

151. Päiväsaari, J.; Dezelah, I. C. L.; Back, D.; El-Kaderi, H. M.; Heeg, M. J.; Putkonen, M.; Niinistö, L.; Winter, C. H. Synthesis, structure and properties of volatile lanthanide complexes

containing amidinate ligands: application for Er_2O_3 thin film growth by atomic layer deposition. *J. Mater. Chem.* **2005**, *15*, 4224.

152. Wang, X.; Dong, L.; Zhang, J.; Liu, Y.; Ye, P. D.; Gordon, R. G. Heteroepitaxy of La_2O_3 and $La_{2-x}Y_xO_3$ on GaAs (111) by atomic layer deposition: achieving low interface trap Density. *Nano Lett.* **2013**, *13*, 594-599.

153. Wang, H.; Wang, J.-J.; Gordon, R.; Lehn, J.-S. b. M.; Li, H.; Hong, D.; Shenai, D. V. Atomic layer deposition of lanthanum-based ternary oxides. Electrochem. *Solid-State Lett.* **2009**, *12*, G13-G15.

154. Ngo, T. Q.; Posadas, A.; McDaniel, M. D.; Ferrer, D. A.; Bruley, J.; Breslin, C.; Demkov, A. A.; Ekerdt, J. G. Epitaxial growth of $LaAlO_3$ on $SrTiO_3$-buffered Si (001) substrates by atomic layer deposition. *J. Cryst. Growth* **2013**, *363*, 150-157.

155. de Rouffignac, P.; Gordon, R. G. Atomic layer deposition of praseodymium aluminum oxide for electrical applications. *Chem. Vap. Deposition* **2006**, *12*, 152-157.

156. Milanov, A. P.; Fischer, R. A.; Devi, A. Synthesis, characterization, and thermal properties of homoleptic rare-earth guanidinates: Promising precursors for MOCVD and ALD of rare-earth oxide thin films. *Inorg. Chem.* **2008**, *47*, 11405-11416.

157. Xu, K.; Chaudhuri, A. R.; Parala, H.; Schwendt, D.; Arcos, T. d. l.; Osten, H. J.; Devi, A. Atomic layer deposition of Er_2O_3 thin films from Er tris-guanidinate and water: process optimization, film analysis and electrical properties. *J. Mater. Chem. C* **2013**, *1*, 3939-3946.

158. Wiedmann, M. K.; Karunarathne, M. C.; Baird, R. J.; Winter, C. H. Growth of Tantalum(V) Oxide Films by Atomic Layer Deposition Using the Highly Thermally Stable Precursor Ta(N*t*Bu)(*i*PrNC(Me)N*i*Pr)$_2$(NMe$_2$). *Chem. Mater.* **2010**, *22*, 4400-4405.

159. Dezelah, C. L.; El-Kadri, O. M.; Kukli, K.; Arstila, K. Baird, R. J.; Lu, J.; Niinistö, L.; Winter, C. H. A low valent metalorganic precursor for the growth of tungsten nitride thin films by atomic layer deposition. *J. Mater. Chem.* **2007**, *17*, 1109-1116.

160. Guha, S.; Cartier, E.; Gribelyuk, M. A.; Bojarczuk, N. A.; Copel, M. C. Atomic beam deposition of lanthanum- and yttrium-based oxide thin films for gate dielectrics. *Appl. Phys. Lett*. **2000**, *77*, 2710-2712.

161. Leskelä, M.; Ritala, M. Rare-earth oxide thin films as gate oxides in MOSFET transistors. *J. Solid State Chem*. **2003**, *171*, 170-174.

162. Ghazy, A.; Safdar, M.; Lastusaari, M.; Aho, A.; Tukiainen, A.; Savin, H.; Guina, M.; Karppinen, M. Luminescent $(Er,Ho)_2O_3$ thin films by ALD to enhance the performance of silicon solar cells. *Sol. Energy Mater. Sol. Cells* **2021**, *219*, 110787.

163. Majdi, M. R.; Danaee, I.; Afghahi, S. S. S. Preparation and anti-corrosive properties of cerium oxide conversion coatings on steel X52. *Mater. Res.* **2017**, *20*, 445-451.

164. Pearson, R. G. Hard and soft acids and bases, HSAB, part 1: fundamental principles. *J. Chem. Educ.* **1968**, *45*, 581.

165. Kemp, K. C.; Fourie, E.; Conradie, J.; Swarts, J. C. Ruthenocene-containing β-diketones: Synthesis, pKa′ values, keto–enol isomerization kinetics, and electrochemical aspects. *Organometallics* **2008**, *27*, 353-362.

166. Huang, W.; Upton, B. M.; Khan, S. I.; Diaconescu, P. L. Synthesis and characterization of paramagnetic lanthanide benzyl complexes. *Organometallics* **2013**, *32*, 1379-1386.

167. Kalutarage, L. C.; Martin, P. D.; Heeg, M. J.; Winter, C. H. Synthesis, structure, and solution reduction reactions of volatile and thermally stable mid to late first row transition metal complexes containing hydrazonate ligands. *Inorg. Chem*. **2013**, *52*, 5385-5394.

168. Mudavakkat, V. H.; Atuchin, V. V.; Kruchinin, V. N.; Kayani, A.; Ramana, C. V. Structure, morphology and optical properties of nanocrystalline yttrium oxide (Y_2O_3) thin films. *Opt. Mater*. **2012**, *34*, 893-900.

169. Korzenski, M. B.; Lecoeur, P.; Mercey, B.; Chippaux, D.; Raveau, B.; Desfeux, R. PLD-Grown Y_2O_3 Thin Films from Y metal: An advantageous alternative to films deposited from yttria. *Chem. Mater*. **2000**, *12*, 3139-3150.

170. Bosze, E. J.; Hirata, G. A.; McKittrick, J. An analysis of Y_2O_3:Eu^{3+} thin films for thermographic phosphor applications. *J. Lumin*. **2011**, *131*, 41-48.

171. Simonenko, T. L.; Simonenko, N. P.; Mokrushin, A. S.; Simonenko, E. P.; Glumov, O. V.; Mel'nikova, N. A.; Murin, I. V.; Kalinina, M. V.; Shilova, O. A.; Sevastyanov, V. G.; Kuznetsov, N. T. Microstructural, electrophysical and gas-sensing properties of CeO_2–Y_2O_3 thin films obtained by the sol-gel process. *Ceram. Int*. **2020**, *46*, 121-131.

172. Morozumi, T.; Matsuoka, R.; Nakamura, T.; Nabeshima, T. Solvent-dependent fac/mer-isomerization and self-assembly of triply helical complexes bearing a pivot part. *Chem. Sci*. **2021**, *12*, 7720-7726.

173. Lima, C. F. R. A. C.; Taveira, R. J. S.; Costa, J. C. S.; Fernandes, A. M.; Melo, A.; Silva, A. M. S.; Santos, L. M. N. B. F. Understanding M–ligand bonding and mer-/fac-isomerism in tris(8-hydroxyquinolinate) metallic complexes. *Phys. Chem. Chem. Phys.* **2016**, *18*, 16555-16565.

174. Hatanpää, T.; Kukli, K.; Ritala, M.; Leskelä, M. Crystal structures and thermal properties of some rare earth alkoxides with tertiary alcohols. *J. Therm. Anal. Calorim*. **2011**, *105*, 61-71.

175. Aspinall, H. C.; Bacsa, J.; Jones, A. C.; Wrench, J. S.; Black, K.; Chalker, P. R.; King, P. J.; Marshall, P.; Werner, M.; Davies, H. O.; Odedra, R. Ce(IV) complexes with donor-

functionalized alkoxide ligands: improved precursors for chemical vapor deposition of CeO_2. *Inorg. Chem*. **2011**, *50*, 11644-11652.

176. Jayakodiarachchi, N.; Evans, P. G.; Ward, C. L.; Winter, C. H. Evaluation of volatility and thermal stability in monomeric and dimeric lanthanide(III) complexes containing enaminolate ligands. *Organometallics* **2021**, *40*, 1270-1283.

177. Lim, B. S.; Rahtu, A.; Park, J.-S.; Gordon, R. G. Synthesis and characterization of volatile, thermally stable, reactive transition metal amidinates. *Inorg. Chem*. **2003**, *42*, 7951-7958.

178. Seitz, M.; Oliver, A. G.; Raymond, K. N. The lanthanide contraction revisited. *J. Am. Chem. Soc.* **2007**, *129*, 11153-11160.

179. Quadrelli, E. A., Lanthanide contraction over the 4f series follows a quadratic decay. *Inorg. Chem.* **2002**, *41*, 167-169.

180. Muthaiah, S.; Bhatia, A.; Kannan, M. Stability of metal complexes. In *stability and applications in coordination compounds*. IntechOpen, 2020; pp 1-18.

181. Xu, R.; Tao, Q.; Yang, Y.; Takoudis, C. G. Atomic layer deposition and characterization of stoichiometric erbium oxide thin dielectrics on Si(100) using $(CpMe)_3Er$ precursor and ozone. *Appl. Surf. Sci*. **2012**, *258*, 8514-8520.

182. Jo, S. J.; Ha, J. S.; Park, N. K.; Kang, D. K.; Kim, B.-H. 5 nm thick lanthanum oxide thin films grown on Si(100) by atomic layer deposition: the effect of post-annealing on the electrical properties. *Thin Solid Films* **2006**, *513*, 253-257.

183. Fuson, R. C.; Gray, H.; Gouza, J. J. Acyloins from t-Butylglyoxal. *J. Am. Chem. Soc.* **1939**, *61*, 1937-1940.

184. Wang, B.; Huang, W.; Chi, L.; Al-Hashimi, M.; Marks, T. J.; Facchetti, A. High-k gate dielectrics for emerging flexible and stretchable electronics. *Chem. Rev*. **2018**, *118*, 5690-5754.

185. Leskelä, M.; Kukli, K.; Ritala, M. Rare-earth oxide thin films for gate dielectrics in microelectronics. *J. Alloys Compd*. **2006**, *418*, 27-34.

186. Miikkulainen, V.; Leskelä, M.; Ritala, M.; Puurunen, R. L. Crystallinity of inorganic films grown by atomic layer deposition: overview and general trends. *J. Appl. Phys*. **2013**, *113*, 021301.

187. Lopes, J. M. J.; Özben, E. D.; Roeckerath, M.; Littmark, U.; Lupták, R.; Lenk, S.; Luysberg, M.; Besmehn, A.; Breuer, U.; Schubert, J.; Mantl, S. Amorphous ternary rare-earth gate oxides for future integration in MOSFETs. *J Microelectron. Eng*. **2009**, *86*, 1646–1649.

188. Mannhart, J.; Blank, D. H. A.; Hwang, H. Y.; Millis, A. J.; Triscone, J. M. Two-dimensional electron gases at oxide interfaces. *MRS Bull*. **2008**, *33*, 1027-1034.

189. Brinkman, A.; Huijben, M.; van Zalk, M.; Huijben, J.; Zeitler, U.; Maan, J. C.; van der Wiel, W. G.; Rijnders, G.; Blank, D. H.; Hilgenkamp, H. Magnetic effects at the interface between non-magnetic oxides. *Nat. Mater.* **2007**, *6*, 493-496.

190. Thiel, S.; Hammerl, G.; Schmehl, A.; Schneider, C. W.; Mannhart, J. Tunable quasi-two-dimensional electron gases in oxide heterostructures. *Science* **2006**, *313*, 1942-1945.

191. Ariando; Wang, X.; Baskaran, G.; Liu, Z. Q.; Huijben, J.; Yi, J. B.; Annadi, A.; Barman, A. R.; Rusydi, A.; Dhar, S.; Feng, Y. P.; Ding, J.; Hilgenkamp, H.; Venkatesan, T. Electronic phase separation at the $LaAlO_3/SrTiO_3$ interface. *Nat. Commun.* **2011**, *2*, 188-194.

192. Bohr, M. T.; Chau, R.; Ghani, T.; Mistry, K. The high-κ solution. *IEEE Spectrum* **2007**, *44*, 29-35.

193. Biswas, A.; Yang, C.-H.; Ramesh, R.; Jeong, Y. H. Atomically flat single terminated oxide substrate surfaces. *Prog. Surf. Sci*. **2017**, *92*, 117-141.

194. Catalano, S.; Gibert, M.; Fowlie, J.; Íñiguez, J.; Triscone, J. M.; Kreisel, J. Rare-earth nickelates $RNiO_3$: thin films and heterostructures. *Rep. Prog. Phys*. **2018**, *81*, 046501.

195. Pénard, A.-L.; Gacoin, T.; Boilot, J.-P. Functionalized sol–gel coatings for optical applications. *Acc. Chem. Res*. **2007**, *40*, 895-902.

196. Liu, X.; Wen, F.; Karapetrova, E.; Kim, J. W.; Ryan, P. J.; Freeland, J. W.; Terilli, M.; Wu, T. C.; Kareev, M.; Chakhalian, J. In-situ fabrication and transport properties of (111) $Y_2Ir_2O_7$ epitaxial thin film. *Appl. Phys. Lett*. **2020**, *117*, 041903.

197. Gaita-Ariño, A.; Luis, F.; Hill, S.; Coronado, E. Molecular spins for quantum computation. *Nat. Chem*. **2019**, *11*, 301-309.

198. Jha, A. K.; Matsumoto, K. Superconductive REBCO Thin Films and Their Nanocomposites: The Role of Rare-Earth Oxides in Promoting Sustainable Energy. *Front. Phys.* **2019**, *7*, 1-21.

199. Zeng, Z.; Xu, Y.; Zhang, Z.; Gao, Z.; Luo, M.; Yin, Z.; Zhang, C.; Xu, J.; Huang, B.; Luo, F.; Du, Y.; Yan, C. Rare-earth-containing perovskite nanomaterials: design, synthesis, properties, and applications. *Chem. Soc. Rev*. **2020**, *49*, 1109-1143.

200. Jang, J.; Moon, D.; Lee, H.-J.; Lee, D.; Choi, D.; Bae, D.; Yuh, H.; Moon, Y.; Park, Y.; Yoon, E. Incorporation of air-cavity into sapphire substrate and its effect on GaN growth and optical properties. *J. Cryst. Growth* **2015**, *430*, 41-45.

201. Tiitta, M.; Niinistou, L. Volatile metal *β*-diketonates: ALE and CVD precursors for electroluminescent device thin films. *Chem. Vap. Depos.* **1997**, *3*, 167-182.

202. Hansen, P.-A.; Fjellvåg, H.; Finstad, T.; Nilsen, O. Structural and optical properties of lanthanide oxides grown by atomic layer deposition (Ln = Pr, Nd, Sm, Eu, Tb, Dy, Ho, Er, Tm, Yb). *Dalton Trans*. **2013**, *42*, 10778-10785.

203. Sønsteby, H. H.; Østreng, E.; Fjellvåg, H.; Nilsen, O. Deposition and x-ray characterization of epitaxial thin films of $LaAlO_3$. *Thin Solid Films* **2014**, *550*, 90-94.

204. Zhao, L.; Liu, H.-X.; Wang, X.; Fei, C.-X.; Feng, X.-Y.; Wang, Y.-T. Effects of annealing ambient on the characteristics of $LaAlO_3$ films grown by atomic layer deposition. *Nanoscale Res. Lett*. **2017**, *12*, 1-7.

205. Oh, I.-K.; Kim, K.; Lee, Z.; Ko, K. Y.; Lee, C.-W.; Lee, S. J.; Myung, J. M.; Lansalot-Matras, C.; Noh, W.; Dussarrat, C.; Kim, H.; Lee, H.-B.-R. Hydrophobicity of rare earth oxides grown by atomic layer deposition. *Chem. Mater*. **2015**, *27*, 148-156.

206. Jones, A. C.; Aspinall, H. C.; Chalker, P. R.; Potter, R. J.; Manning, T. D.; Loo, Y. F.; O'Kane, R.; Gaskell, J. M.; Smith, L. M. MOCVD and ALD of high-k dielectric oxides using alkoxide precursors. *Chem. Vap. Deposition* **2006**, *12*, 83-98.

207. Edelmann, F. T. Lanthanide amidinates and guanidinates in catalysis and materials science: A continuing success story. *Chem. Soc. Rev*. **2012**, *41*, 7657-7672.

208. Seppälä, S.; Niinistö, J.; Blanquart, T.; Kaipio, M.; Mizohata, K.; Räisänen, J.; Lansalot-Matras, C.; Noh, W.; Ritala, M.; Leskelä, M. Heteroleptic cyclopentadienyl-amidinate precursors for atomic layer deposition (ALD) of Y, Pr, Gd, and Dy oxide thin films. *Chem. Mater*. **2016**, *28*, 5440-5449.

209. Daly, S. R.; Kim, D. Y.; Yang, Y.; Abelson, J. R.; Girolami, G. S. Lanthanide N,N-dimethylaminodiboranates: highly volatile precursors for the deposition of lanthanide-containing thin films. *J. Am. Chem. Soc*. **2010**, *132*, 2106-2107.

210. Daly, S. R.; Kim, D. Y.; Girolami, G. S. Lanthanide N,N-dimethylaminodiboranates as a new class of highly volatile chemical vapor deposition precursors. *Inorg. Chem*. **2012**, *51*, 7050-7065.

211. Vlaisavljevich, B.; Miró, P.; Koballa, D.; Todorova, T. K.; Daly, S. R.; Girolami, G. S.; Cramer, C. J.; Gagliardi, L. Volatilities of actinide and lanthanide N,N-dimethylaminodiboranate chemical vapor deposition precursors: a DFT study. *J. Phys. Chem. C* **2012**, *116*, 23194-23200.

212. Bordwell, F. G.; Harrelson, J. A.; Lynch, T. Y. Homolytic bond dissociation energies for the cleavage of α-nitrogen-hydrogen bonds in carboxamides, sulfonamides, and their derivatives. The question of synergism in nitrogen-centered radicals. *J. Org. Chem.* **1990**, *55*, 3337-3341.

213. Pipko, S. E.; Balitzky, Y. V.; Sinitsa, A. D.; Gololobov, Y. G. Peculiarities of structure and properties of phosphorus-containing cations with two intramolecular donor-acceptor bonds N→P. Synthesis of the first 5-coordinated P-cation with P-N bond. *Tetrahedron Lett*. **1994**, *35*, 165-168.

214. Van Vliet, M. R. P.; Van Koten, G.; Buysingh, P.; Jastrzebski, J. T. B. H.; Spek, A. L. Reactivity of 1-aza-4-oxo-1,3-butadienes (α-imino ketones) toward diorganozinc reagents: regio- and chemoselective transfer of organo groups in the $ZnR_2/R^1N=C(R^2)C(R^3)=O$ system and x-ray structure of [cyclic] $[EtZn(Et)(tert\text{-}Bu)NC(H)=C(Me)O]_2$. *Organometallics* **1987**, *6*, 537-546.

215. Van Vliet, M. R. P.; Jastrzebski, J. T. B. H.; Van Koten, G.; Vrieze, K.; Spek, A. L. Novel reactions of substituted 1-aza-4-oxobutadienes (α-iminoketones) with diorganozinc reagents. Selective ethyl transfer in the $Et^2Zn/t\text{-}BuN=C(H)\text{-}C(Me)=O$ system and x-ray crystal structure of $[EtZn(Et)(t\text{-}Bu)N=C(H)\text{-}C(Me)O]_2$. *J. Organomet. Chem*. **1983**, *251*, c17-c21.

216. Cozzi, P. G.; Veya, P.; Floriani, C.; Chiesi-Villa, A.; Rizzoli, C. *β*-Keto amino enolates binding to transition metals: synthesis and structure of the ion-pair form and its mono- and bidentate coordination to zirconium and nickel. *Organometallics* **1994**, *13*, 1528-1532.

217. Aspinall, H. C.; Bickley, J. F.; Gaskell, J. M.; Jones, A. C.; Labat, G.; Chalker, P. R.; Williams, P. A. Precursors for MOCVD and ALD of rare earth oxides−complexes of the early lanthanides with a donor-functionalized alkoxide ligand. *Inorg. Chem*. **2007**, *46*, 5852-5860.

218. Kilimann, U.; Schäfer, M.; Herbst-Irmer, R.; Edelmann, F. T. Cyclooctatetraenyl-komplexe der frühen übergangsmetalle und lanthanoide: III. cyclooctatetraenyl-lanthanoidtriflate und -iodide: Neue ausgangsmaterialien für die organolanthanoid-chemie. *J. Organomet. Chem.* **1994**, *469*, C10-C14.

219. Li, Z.; Xue, M.; Yao, H.; Sun, H.; Zhang, Y.; Shen, Q. Enol-functionalized N-heterocyclic carbene lanthanide amide complexes: Synthesis, molecular structures and catalytic activity for addition of amines to carbodiimides. *J. Organomet. Chem.* **2012**, *713*, 27-34.

220. Liu, R.; Zheng, P.; Weng, L.; Zhou, X.; Liu, C. Insertion of ketenes into lanthanocene n-butylamide and imidazolate complexes. *J. Organomet. Chem.* **2008**, *693*, 1614-1620.

221. Zhang, C.; Lin, Y.; Chen, Z.; Zhou, X. Insertion reactions of PhEtCCO and PhNCO into Ln-S (Ln = Er, Y, Yb) bond of $[Cp_2Ln(\mu\text{-}SEt)]_2$. *J. Rare Earths* **2006**, *24*, 9-14.

222. Zhang, C.; Liu, R.; Zhou, X.; Chen, Z.; Weng, L.; Lin, Y. Insertion reaction of ketene into the metal−sulfur bond: synthesis and characterization of $[Cp_2Ln(\mu\text{-}\eta^1\text{:}\eta^2\text{-}OC(SEt)CPh_2)]_2$ (Ln = Yb, Er, Sm, Y) and $[Cp_2Er(\mu\text{-}\eta^1\text{:}\eta^2\text{-}OC(SEt)CPhEt)]_2$. *Organometallics* **2004**, *23*, 3246-3251.

223. Deacon, G. B.; Junk, P. C.; Moxey, G. J. Mono-, di-, tri- and tetranuclear rare earth complexes obtained using a moderately bulky aryloxide ligand. *Chem. Asian J.* **2009**, *4*, 1717-1728.

224. Barnhart, D. M.; Clark, D. L.; Gordon, J. C.; Huffman, J. C.; Vincent, R. L.; Watkin, J. G.; Zwick, B. D. Synthesis, properties, and x-ray structures of the lanthanide η^6-arene-bridged aryloxide dimers $ln_2(O\text{-}2,6\text{-}^{i}Pr_2C_6H_3)_6$ and their lewis base adducts $Ln(O\text{-}2,6\text{-}^{i}Pr_2C_6H_3)_3(THF)_2$ (Ln = Pr, Nd, Sm, Gd, Er, Yb, Lu). *Inorg. Chem.* **1994**, *33*, 3487-3497.

225. Feng, J.; Yu, J.-B.; Song, S.-Y.; Sun, L.-N.; Fan, W.-Q.; Guo, X.-M.; Dang, S.; Zhang, H.-J. Near-infrared luminescent xerogel materials covalently bonded with ternary lanthanide [Er(III), Nd(III), Yb(III), Sm(III)] complexes. *Dalton Trans*. **2009**, 2406-2414.

226. Rogachev, A. Y.; Mironov, A. V.; Troyanov, S. I.; Kuzmina, N. P.; Nemukhin, A. V. Synthesis, crystal structures and theoretical study of mixed ligand complexes of lanthanides acetylacetonates with o-phenanthroline and 2,2′-dipyridyl: the unexpected inverted electrostatic trend in stability. *J. Mol. Struct*. **2006**, *789*, 187-194.

227. Päiväsaari, J.; Niinistö, J.; Arstila, K.; Kukli, K.; Putkonen, M.; Niinistö, L. High growth rate of erbium oxide thin films in atomic layer deposition from $(CpMe)_3Er$ and water precursors. *Chem. Vap. Deposition* **2005**, *11*, 415-419.

228. Streitwieser, A.; Nebenzahl, L. L. Carbon acidity. LII. equilibrium acidity of cyclopentadiene in water and in cyclohexylamine. *J. Am. Chem. Soc*. **1976**, *98*, 2188-2190.

229. Sbrockey, N. M.; Luong, M.; Gallo, E. M.; Sloppy, J. D.; Chen, G.; Winkler, C. R.; Johnson, S. H.; Taheri, M. L.; Tompa, G. S.; Spanier, J. E. $LaAlO_3/SrTiO_3$ epitaxial heterostructures by atomic layer deposition. *J. Electron. Mater*. **2012**, *41*, 819-823.

230. Rao, V. P.; Besancon, B.; Omarjee, V.; Dussarrat, C. Development of lanthanide precursors as dopants for advanced high-k materials. *ECS Transactions* **2010**, *33*, 145-156.

231. Frenzel, T.; Beale, J. M.; Kobayashi, M.; Zenk, M. H.; Floss, H. G. Stereochemistry of enzymic formation of the berberine bridge in protoberberine alkaloids. *J. Am. Chem. Soc*. **1988**, *110*, 7878-7880.

232. Hoard, D. W.; Moher, E. D.; Turpin, J. A. Synthesis of (R)-(−)-1-Piperidino-3,3-dimethylbutan-2-ol: Application in the molar scale asymmetric ethylation of trans-crotonaldehyde. *Org. Process Res. Dev*. **1999**, *3*, 64-66.

233. Losurdo, M.; Giangregorio, M. M.; Bruno, G.; Yang, D.; Irene, E. A.; Suvorova, A. A.; Saunders, M. Er_2O_3 as a high-K dielectric candidate. *Appl. Phys. Lett.* **2007**, *91*, 091914.

234. Giangregorio, M.; Losurdo, M.; Sacchetti, A.; Capezzuto, P.; Bruno, G. Metalorganic chemical vapor deposition of Er_2O_3 thin films: Correlation between growth process and film properties. *Thin Solid Films* **2009**, *517*, 2606-2610.

235. Zhu, Y. Y.; Xu, R.; Chen, S.; Fang, Z. B.; Xue, F.; Fan, Y. L.; Yang, X. J.; Jiang, Z. M. Epitaxial growth of Er_2O_3 films on oxidized Si(111) and Si(001) substrates. *Thin Solid Films* **2006**, *508*, 86-89.

236. Mikhelashvili, V.; Eisenstein, G.; Edelmann, F. Structural properties and electrical characteristics of electron-beam gun evaporated erbium oxide films. *Appl. Phys. Lett.* **2002**, *80*, 2156-2158.

237. Ono, H.; Katsumata, T. Interfacial reactions between thin rare-earth-metal oxide films and Si substrates. *Opt. Express 16* **2001**, *78*, 1832-1834.

238. Zhu, Y.; Fang, Z.; Liu, Y. Structural and optical properties of Er_2O_3 films. *J. Rare Earths* **2010**, *28*, 752-755.

239. Hubbard, K. M.; Espinoza, B. F. Corrosion-resistant erbium oxide coatings by organometallic chemical vapor deposition. *Thin Solid Films* **2000**, *366*, 175-180.

240. Scarel, G.; Svane, A.; Fanciulli, M. Scientific and technological issues related to rare earth oxides: an introduction. in rare earth oxide thin films, Springer, Berlin Heidelberg, **2007**; pp 1-14.

241. Qiao, L.; He, G.; Hao, L.; Lu, J.; Gao, Q.; Zhang, M.; Fang, Z. Interface optimization of passivated Er_2O_3/Al_2O_3/InP MOS capacitors and modulation of leakage current conduction mechanism. *IEEE Trans. Electron Devices* **2021**, *68*, 2899-2905.

242. Wang, X.; Zhu, Y. L.; He, M.; Lu, H. B.; Ma, X. L. Structural and microstructural analyses of crystalline Er_2O_3 high-k films grown on Si(001) by laser molecular beam epitaxy. *Acta Mater*. **2011**, *59*, 1644-1650.

243. Fang, Z. B.; Chen, S.; Zhu, Y. Y.; Wu, Y. Q.; Fan, Y. L.; Wang, Y. Y.; Jiang, Z. M. Structural and electrical characterization of ultrathin Er_2O_3 films grown on Si(001) by reactive evaporation. *Nanotechnology* **2007**, *18*, 155205.

244. Kamineni, H. S.; Kamineni, V. K.; Moore, R. L.; Gallis, S.; Diebold, A. C.; Huang, M.; Kaloyeros, A. E. Optical and structural characterization of thermal oxidation effects of erbium thin films deposited by electron beam on silicon. *J. Appl. Phys.* **2012**, *111*, 013104.

245. Chen, F. H.; Her, J. L.; Shao, Y. H.; Matsuda, Y. H.; Pan, T. M. Structural and electrical characteristics of high-kappa Er_2O_3 and Er_2TiO_5 gate dielectrics for a-IGZO thin-film transistors. *Nanoscale Res. Lett.* **2013**, 8-18.

246. Morelhão, S. L.; Brito, G. E. S.; Abramof, E. Characterization of erbium oxide sol–gel films and devices by grazing incidence X-ray reflectivity. *J. Alloys Compd.* **2002**, *344*, 207-211.

247. Sánchez, F.; Queralt, X.; Ferrater, C.; Aguiar, R.; Varela, M. Deposition of Er_2O_3 thin films on Si(100) by laser ablation. *Vacuum* **1994**, *45*, 1129-1130.

248. Giangregorio, M. M.; Losurdo, M.; Sacchetti, A.; Capezzuto, P.; Bruno, G. Metalorganic chemical vapor deposition of Er_2O_3 thin films: correlation between growth process and film properties. *Thin Solid Films* **2009**, *517*, 2606-2610.

249. Xu, K.; Dang, V.-S.; Ney, A.; Arcos, T. d. l.; Devi, A. Nanostructured Er_2O_3 thin films grown by metalorganic chemical vapour deposition. *J. Nanosci. Nanotechnol.* **2014**, *14*, 5095-5102.

250. Singh, M. P.; Thakur, C. S.; Shalini, K.; Bhat, N.; Shivashankar, S. A. Structural and electrical characterization of erbium oxide films grown on Si(100) by low-pressure metalorganic chemical vapor deposition. *Appl. Phys. Lett*. **2003**, *83*, 2889-2891.

251. Chen, P.-Y.; Posadas, A. B.; Kwon, S.; Wang, Q.; Kim, M. J.; Demkov, A. A.; Ekerdt, J. G. Cubic crystalline erbium oxide growth on GaN(0001) by atomic layer deposition. *J. Appl. Phys.* **2017**, *122*, 215302.

252. Päiväsaari, J.; Niinistö, J.; Arstila, K.; Kukli, K.; Putkonen, M.; Niinistö, L. High growth rate of erbium oxide thin films in atomic layer deposition from $(CpMe)_3Er$ and water precursors. *Chem. Vap. Deposition* **2005**, *11*, 415-419.

253. Jeon, S.; Hwang, H. Effect of hygroscopic nature on the electrical characteristics of lanthanide oxides (Pr_2O_3, Sm_2O_3, Gd_2O_3, and Dy_2O_3). *J. Appl. Phys*. **2003**, *93*, 6393-6395.

254. Rabady, R.; Avrutsky, I. Reduced surface roughness of solid thin films prepared by alternating-bias, radio-frequency magnetron sputtering. *J. Opt. Soc. Am. B* **2003**, *20*, 2174-2178.

255. Cao, Y.; Zhou, C. Thickness dependence of surface roughness and magnetic properties of FeNiCr thin films. *J. Magn. Magn. Mater.* **2013**, *333*, 1-7.

256. Díaz, B.; Światowska, J.; Maurice, V.; Seyeux, A.; Normand, B.; Härkönen, E.; Ritala, M.; Marcus, P. Electrochemical and time-of-flight secondary ion mass spectrometry analysis of ultra-thin metal oxide (Al_2O_3 and Ta_2O_5) coatings deposited by atomic layer deposition on stainless steel. *Electrochim. Acta.* **2011**, *56*, 10516-10523.

257. Chen, Y.; Yusuf, M. H.; Guan, Y.; Jacobson, R. B.; Lagally, M. G.; Babcock, S. E.; Kuech, T. F.; Evans, P. G. Distinct nucleation and growth kinetics of amorphous $SrTiO_3$ on (001) $SrTiO_3$ and SiO_2/Si: A step toward new architectures. *ACS Appl. Mater. Interfaces* **2017**, *9*, 41034-41042.

258. Yoshimoto, M.; Maeda, T.; Ohnishi, T.; Koinuma, H.; Ishiyama, O.; Shinohara, M.; Kubo, M.; Miura, R.; Miyamoto, A. Atomic-scale formation of ultrasmooth surfaces on sapphire substrates for high-quality thin-film fabrication. *Appl. Phys. Lett*. **1995**, *67*, 2615-2617.

259. Feng, X.-Y.; Liu, H.-X.; Wang, X.; Zhao, L.; Fei, C.-X.; Liu, H.-L. The Study of electrical properties for multilayer La_2O_3/Al_2O_3 dielectric stacks and $LaAlO_3$ dielectric film deposited by ALD. *Nanoscale Res. Lett*. **2017**, *12*, 1-4.

260. Adelmann, C.; Swerts, J.; Richard, O.; Conard, T.; Popovici, M.; Meersschaut, J.; Afanas'ev, V. V.; Breuil, L.; Cacciato, A.; Opsomer, K.; Brijs, B.; Tielens, H.; Pourtois, G.; Bender, H.; Jurczak, M.; Houdt, J. V.; Elshocht, S. V.; Kittl, J. A. Lanthanide aluminates as dielectrics for non-volatile memory applications: material aspects. *J. Electrochem. Soc*. **2011**, *158*, H778-H784.

261. Adelmann, C.; Swerts, J.; Richard, O.; Conard, T.; Popovici, M.; Afanas'ev, V. V.; Breuil, L.; Cacciato, A.; Opsomer, K.; Brijs, B.; Tielens, H.; Pourtois, G.; Bender, H.; Detavernier, C.; Jurczak, M.; Van Elshocht, S.; Kittl, J. A. Introducing lanthanide aluminates as dielectrics for nonvolatile memory applications: a material scientist's view. *ECS Transactions* **2010**, *33*, 31-42.

262. Kukli, K.; Ritala, M.; Pore, V.; Leskelä, M.; Sajavaara, T.; Hegde, R. I.; Gilmer, D. C.; Tobin, P. J.; Jones, A. C.; Aspinall, H. C. Atomic layer deposition and properties of lanthanum oxide and lanthanum-aluminum oxide films. *Chem. Vap. Deposition* **2006**, *12*, 158-164.

263. Annadi, A.; Putra, A.; Liu, Z. Q.; Wang, X.; Gopinadhan, K.; Huang, Z.; Dhar, S.; Venkatesan, T.; Ariando. Electronic correlation and strain effects at the interfaces between polar and nonpolar complex oxides. *Phys. Rev. B* **2012**, *86*, 085450.

264. McDaniel, M. D.; Ngo, T. Q.; Hu, S.; Posadas, A.; Demkov, A. A.; Ekerdt, J. G. Atomic layer deposition of perovskite oxides and their epitaxial integration with Si, Ge, and other semiconductors. *Appl. Phys. Rev*. **2015**, *2*, 041301.

265. Beer, S. M J.; Krusenbaum, A.; Winter, M.; Vahlas, C.; Devi, A. Study on structural and thermal characteristics of heteroleptic yttrium complexes as potential precursors for vapor phase deposition. *Eur. J. Inorg. Chem*. **2020**, *2020*, 3587–3596.

266. Golalikhani, M.; James, T.; Van Buskirk, P.; Noh, W.; Lee, J.; Wang, Z.; Roeder, J. F. Atomic layer deposition of CeO_2 using a heteroleptic cyclopentadienyl-amidinate precursor. J. *Vac. Sci. Technol. A* **2018**, *36*, 051502.

267. Dussarrat, C.; Blasco, N.; Noh, W.; Lee, J.; Greer, J.; Teramoto, T.; Kamimura, S.; Gosset, N.; Ono, T. Thermal atomic layer deposition of yttrium oxide films and their properties in anticorrosion and water repellent coating applications. *Coatings* **2021,** *11*, 497.

ABSTRACT

ATOMIC LAYER DEPOSITION (ALD) OF LANTHANIDE OXIDE FILMS: SYNTHESIS, CHARACTERIZATION, AND PRECURSOR PROPERTY EVALUATION OF NEW CLASSES OF LANTHANIDE COMPLEXES AND THERMAL ALD OF ERBIUM OXIDE THIN FILMS

by

NAVODA AMALI JAYAKODIARACHCHI

December 2022

Advisor: Prof. Charles H. Winter

Major: Chemistry (Inorganic)

Degree: Doctor of Philosophy

Lanthanide oxide-containing thin films are groups of materials with high application potential in numerous fields, including microelectronic, photovoltaic, catalysis, and surface-coating applications. These oxides are refractory materials with high melting points and thermodynamic stabilities, hence, are useful as heat and corrosion-resistant coatings. Further, due to the high refractive indices of lanthanide oxides, they are widely used in optics and photovoltaics. Most importantly, with the continuous downscaling of semiconductor devices, search of alternative high-κ gate dielectric materials for gate oxides in transistors is ongoing. Owing to the high dielectric constants and large band gaps inherent to lanthanide oxides, they have gained increased attention as potential alternative candidates for gate dielectrics in transistors.

Traditional vapor phase thin film deposition methods include PVD and CVD. PVD is a line-of-site technique and difficult to achieve conformal thin film growth in high-aspect ratio features. CVD has a better conformal coverage than PVD on planar substrates. However, both of these techniques lack the required precision for film growth in high aspect ratio nanoscale 3-dimensional architectures. By contrast, the ALD technique deposits films with perfect surface

conformality and nanometer-scale thickness control on both planar and non-planar architectures and in high aspect ratio features. However, the lack of lanthanide precursors with desired ALD precursor properties that can react with mild oxidants has made the thermal ALD of lanthanide oxide films difficult. Moreover, several established ALD processes for lanthanide oxide ALD are plagued by low growth rates, lack of self-limited growth, impurity incorporation, high surface roughness, or the need for highly reactive oxygen sources.

The research herein seeks to develop new ALD precursors and processes for lanthanide oxide thin film growth with the scope of increasing the applications of lanthanide-containing oxide thin films for future nanoscale technologies. Accordingly, two new precursor classes for lanthanide(III) ions were introduced employing hydrazonate and enaminolate ligand systems (Chapters 2 and 3). All of the complexes were synthesized using salt metathesis approaches and were purified by sublimation or solvent crystallizations. Diamagnetic lanthanide complexes (La^{3+}, Lu^{3+}, and Y^{3+}) were fully characterized by ^{1}H and $^{13}C\{^{1}H\}$ NMR and all of the complexes were characterized using IR spectroscopy, melting points, and CHN microanalyses. Variable temperature NMR spectra were obtained for selected diamagnetic complexes to understand the solution state behavior. Single crystal XRD studies were carried out for selected complexes to understand the solid-state structures. Volatility and thermal stability evaluation to determine the potential of these precursors for ALD was carried out using sublimation, TGA, melting point, thermal decomposition temperature analysis, and long-term thermal stability tests. All of the new complexes sublimed, demonstrating their volatile nature. Hydrazonate complexes showed lower volatilities compared to enaminolate complexes, which could be attributed to the large molecular weight of the *tert*-butyl hydrazonate ligand compared to the L^1 and L^2 enaminolate ligands. Hydrazonate complexes have acceptable thermal stabilities for use in ALD. The thermal stabilities

of enaminolate complexes varied with the ligand substituents. L^1 and L^3 enaminolate complexes are predicted to have sufficient thermal stabilities to use in ALD.

Smooth, continuous, and high-purity Er_2O_3 films were deposited successfully using the Er-enaminolate precursor, $Er(L^1)_3$ (Chapter 4). Water was used as the co-reactant. Films were characterized using several techniques such as SEM, GI-XRD, SE, XRR, AFM, and XPS. The plot of thickness versus number of cycles was linear and slope this linear plot gave a growth rate of about 0.3 Å/cycle. Self-limited growth behavior was observed for both Er-precursor and water at ≥4 s and ≥0.2 s pulse lengths, respectively. Being able to find a precursor system that shows adequate reactivity toward a mild oxygen source is one of the greatest achievements in this work. This Er_2O_3 ALD process further demonstrates the potential of using other enaminolate complexes reported in Chapter 3 for the deposition of other lanthanide oxides as future work.

AUTOBIOGRAPHICAL STATEMENT

NAVODA AMALI JAYAKODIARACHCHI

Education

Ph.D., Inorganic Chemistry, Wayne State University, Detroit, Michigan (2016-2022)
Advisor: Professor Charles H. Winter
B.Sc., Chemistry Special, University of Sri Jayewardenepura, Sri Lanka (2010-2014)
Advisor: Professor Champa Jayaweera

Publications

1. Waduge, W. L. I.; Chen, Y.; Zuo, P.; Jayakodiarachchi, N.; Kuech, T. F.; Babcock, S. E.; Evans, P. G.; Winter, C. H., Solid-Phase Epitaxy of Perovskite High Dielectric $PrAlO_3$ Films Grown by Atomic Layer Deposition for Use in Two-Dimensional Electronics and Memory Devices. *ACS Applied Nano Materials* **2019,** *2* (11), 7449-7458.

2. Jayakodiarachchi, N.; Evans, P. G.; Ward, C. L.; Winter, C. H., Evaluation of Volatility and Thermal Stability in Monomeric and Dimeric Lanthanide(III) Complexes Containing Enaminolate Ligands. *Organometallics* **2021,** *40* (9), 1270-1283.

3. Jayakodiarachchi, N.; Ward, C. L.; Evans, P. G.; Winter, C. H. Synthesis and Characterization of Lanthanide(III) Complexes Containing Hydrazonate Ligands, and Evaluation of Their Volatility and Thermal Stability. *Manuscript in preparation.*

4. Jayakodiarachchi, N.; Devereaux, Z. J.; Liu, R.; Evans, P. G.; Savage, D.; Winter, C. H. Atomic Layer Deposition and Characterization of Erbium Oxide Thin Films Using Volatile Erbium Enaminolate Precursor and Water. *Manuscript in preparation.*

Honors and Awards

Outstanding Teaching Award, Wayne State University, 2016